The Hong Kong Polytechnic University

Department of Applied Biology and Chemical Technology

Synthesis and Characterization of Gold Nanoparticles Capped with Tiopronin-Derivatives and Pyrrolidinium Ionic Liquids

LAM Kin Ming

A Thesis Submitted

in

Partial Fulfillment of the Requirements

for

the Degree of Doctor of Philosophy

June, 2010

Certificate of Originality

I hereby declare that this thesis is my own work and that, to the best of my knowledge and belief, it reproduces no material previously published or written, nor material that has been accepted for the award of any other degree or diploma, except where due acknowledgement has been made in the text.

Lam Kin Ming

June, 2010

Abstract

Nanoparticles have widespread applications in many areas and are a new generation of advanced materials. Among the different kinds of nanoparticles, gold nanoparticle is one of the most widely studied and utilized. The easy preparation, higher stability, low toxicity and unique properties make the gold nanoclusters the material of choice in many applications. The objective of this study is to synthesize and characterize a series of gold nanoparticles capped by different ligands.

In the first part of the thesis, the preparation and characterization of several tiopronin derivatives and their gold nanoparticles were demonstrated. The tiopronin derivatives were designed by modifying their hydrophobic segment or the amino acid residue based on the parent tiopronin. The phenyl, ethyl, alanine, proline and leucine derivatives were synthesized. All, except the phenyl-, tiopronin derivatives gave stable, water-soluble and very small gold nanoparticles. The gold nanoparticles were characterized by IR, UV-visible, transmission electron microscopy, luminescence spectroscopy and thermogravimetric analysis.

In the second part of the thesis, the ligand exchange reaction involving the tiopronin derivatives on the small gold nanoclusters was studied. The difference in structure of the derivatives did not introduce much discrimination on the extent and kinetics of the ligand exchange reactions. However, introduction of negative charges on the ligand monolayer on gold nanoparticles by pH adjustment significantly reduced the extent of exchange reaction at the initial stage and allowed the investigation of ligand exchange

occurring at the higher energy metal surface defective sites. A difference in the exchange kinetics among different tiopronin derivatives was observed at pH 6.5. The initial stage for all exchange processes with tiopronin derivatives can generally be described by the second order Langmuir diffusion-limited model. This confirms the diffusion nature of the ligand exchange reaction between tiopronin and its derivatives on gold surface before equilibrium was established.

In the third part of the thesis, the preparation of gold nanoparticles by direct reduction with tetrabutylammonium borohydride in neat pyrrolidinium-based bis(trifluoromethanesulfonyl)imide ionic liquids was studied. The average size of the gold nanoparticles prepared was 4 – 8 nm in diameter. The size-dispersity and colloid stability were improved when the nanoclusters were synthesized in longer alkyl chain pyrrolidinium ionic liquids. The presence of bromide only produced spherical nanoparticles while chloride could induce the formation of thread-like structure. A lower reaction temperature generally leads to a wider spread of average particle size of the gold nanoparticles.

Acknowledgements

I would like to express my greatest gratitude to my supervisor Prof. K. Y. Wong for his supervision, guidance, valuable advices, endless support and encouragement throughout the course of my study, and for his valuable comments on the draft of this thesis.

Meanwhile, I would like to give my sincere thanks also to all my colleagues in Y 606, who have offered me assistance, suggestions and a joyful environment throughout my study: Dr. W. L. Wong, Dr. Gary K. C. Cheung, Dr. Lawrence Y. S. Lee, Dr. Dias P. H. Chan, Dr. Bill K. P. Ho, Dr. Joseph H. L. Pang, Dr. L. Zou, Dr. Y. J. Lu, Dr. Kelvin W. H. Chung, Dr. Elaine F. Y. Chan, Mr. N. Sun, Mr. M. H. So, Mr. W. L. Cheung, and Miss K. Y. Chow.

Special thanks are also given to Dr. Clement C. K. Wong, Dr. W. Lu, Mr. T. K. Cheung, Mr. Roy Ho, and Mr. M. N. Yeung for their helpful support and advices.

Last but not least, I would also like to express my greatest gratitude to my beloved family for their unconditional love and understanding during my postgraduate study.

Table of Contents

List of Abbreviations

Au@MBG	2-Mercaptobutanoyl glycine-capped gold nanoparticles
Au@MPA	2-Mercaptopropionyl alanine-capped gold nanoparticles
Au@MPL	2- Mercaptopropionyl leucine-capped gold nanoparticles
Au@MPP	2- Mercaptopropionyl proline-capped gold nanoparticles
Au@MPEG	α -Mercaptophenylethanoyl glycine-capped gold nanoparticles
Au@tiopronin	Tiopronin-capped gold nanoparticles
C_{14} / C_{10}	Binary mixture of *N*-methyl-*N* -tetradecylpyrrolidinium halide in *N*-decyl-*N*-methylpyrrolidinium bis(trifluoromethanesulfonyl)imide
DDI water	Double deionized water
DMAP	Dimethylaminopyridine
k_{obs}	Pseudo first order rate constant
MBG	2-Mercaptobutanoyl glycine
MPA	2-Mercaptopropionyl alanine
MPL	2- Mercaptopropionyl leucine
MPP	2- Mercaptopropionyl proline
MPEG	α -Mercaptophenylethanoyl glycine
$NaBH_4$	Sodium borohydride
$PyC_n[AuBr_4]$	*N* -alkyl-*N*-methylpyrrolidinium tetrabromoaurate(III)
$PyC_n[AuCl_4]$	*N* -alkyl-*N*-methylpyrrolidinium tetrachloroaurate(III)
PyC_nBr	*N* -alkyl-*N*-methylpyrrolidinium bromide
PyC_nCl	*N* -alkyl-*N*-methylpyrrolidinium chloride
$PyC_n[Tf_2N]$	*N* -alkyl-*N*-methylpyrrolidinium bis(trifluoromethanesulfonyl)imide

$PyC_{10}[AuBr_4]$	*N* -decyl-*N*-methylpyrrolidinium tetrabromoaurate(III)
$PyC_{10}[AuCl_4]$	*N* -decyl-*N*-methylpyrrolidinium tetrachloroaurate(III)
$PyC_{10}Br$	*N* -decyl-*N*-methylpyrrolidinium bromide
$PyC_{10}Cl$	*N* -decyl-*N*-methylpyrrolidinium chloride
$PyC_{10}[Tf_2N]$	*N* -decyl-*N*-methylpyrrolidinium bis(trifluoromethanesulfonyl)imide
$PyC_{14}[AuBr_4]$	*N* -methyl-*N*-tetradecylpyrrolidinium tetrabromoaurate(III)
$PyC_{14}[AuCl_4]$	*N* -methyl-*N*-tetradecylpyrrolidinium tetrachloroaurate(III)
$PyC_{14}Br$	*N* -methyl-*N*-tetradecylpyrrolidinium bromide
$PyC_{14}Cl$	*N* -methyl-*N*-tetradecylpyrrolidinium chloride
$PyC_6[AuBr_4]$	*N* -hexyl-*N*-methylpyrrolidinium tetrabromoaurate(III)
$PyC_6[AuCl_4]$	*N* -hexyl-*N*-methylpyrrolidinium tetrachloroaurate(III)
PyC_6Br	*N* -hexyl-*N*-methylpyrrolidinium bromide
PyC_6Cl	*N* -hexyl-*N*-methylpyrrolidinium chloride
$PyC_6[Tf_2N]$	*N* -hexyl-*N*-methylpyrrolidinium bis(trifluoromethanesulfonyl)imide
$PyC_8[AuBr_4]$	*N* -methyl-*N*-octylpyrrolidinium tetrabromoaurate(III)
$PyC_8[AuCl_4]$	*N* -methyl-*N*-octylpyrrolidinium tetrachloroaurate(III)
PyC_8Br	*N* -methyl-*N*-octylpyrrolidinium bromide
PyC_8Cl	*N* -methyl-*N*-octylpyrrolidinium chloride
$PyC_8[Tf_2N]$	*N*-methyl-*N*-octylpyrrolidinium bis(trifluoromethanesulfonyl)imide
SAM	Self-assemble monolayer
$TBABH_4$	etrabutylammonium borohydride
TMSP-Na	3-(trimethylsilyl)propionic-2,2,3,3,-d_4 acid, sodium salt

Chapter 1

Introduction

1.1. Background

Gold is the 79th element in the periodic table and belongs to the noble transition metal family. In fact, gold is amid the few metallic elements that has been known by human beings since the ancient time. Its extreme chemical inertness and the forever luster render the metal to play an important role in jewelry and monetary business. The contribution of gold to chemistry was not recognized until the successful preparation of different gold complexes and the demonstration of their catalytic activity towards C-C, C-N and C-O bond formations.[1]

In recent decades, the successful preparation of gold nanoparticles by facile procedures and the discovery of their numerous unique properties have triggered intense interests to investigate these new materials in various area. On the other hand, much effort is still devoted to the synthesis of new nanostructures in order to achieved desirable properties.

Because of the interest in biological applications of gold nanoparticles, studies on water-soluble gold nanoparticles are growing rapidly. On the other hand, the strong urges for greener and environmentally benign reaction conditions have driven research directions towards the preparation of nanomaterials in new solvent media such as ionic liquids. The background and recent development in these two area will be discussed in the following sections.

1.1.1. Properties of gold nanoparticles

Nanomaterials usually refer to substances the size of which are within the range of 1 – 100 nm. Under such a small size regime, the behavior of the materials is in between the molecular and the bulk state. Properties that are very different from the bulk materials also arise due to the extremely small dimension.

Gold nanoparticles, which are mostly black-coloured powder when dried, are visibly very different from the shiny golden appearance of their bulk state. Such discrepancy demonstrates the distinctive optical properties of nano-sized gold. When excited by incident electromagnetic wave, the free conduction electrons in 5 – 20 nm gold nanoparticles express a collective oscillation and polarization at 525 – 530 nm,[2] which corresponds to the surface plasmon resonance (SPR).[3] This accounts for the wine red colour of the nanoparticle solution observed. The SPR wavelength depends strongly on size,[4] shape[5] and the local environment[6] around the nanoparticles. The plasmon band shifts to longer wavelength when the dimension of the particles increases. A second SPR peak at ~ 700 nm emerges in addition to the usual band at 525 nm when anisotropic morphologies like rod-shaped nanoparticles are present. This is due to the absorption by the electrons oscillating along and perpendicular to the major axis of the rod.

However, when the particle size (< 3 nm) approaches the de Broglie wavelength of the valence electrons (~ 1 nm),[7] the clusters will behave electronically as a quantum box according to the rules of quantum mechanics and the well-known ‘quantum size effect’ arises.[3] The continuum band structure and the plasmon resonance disappear because of

the formation of discrete energy levels with the energy spacing between levels becomes larger than the thermal energy (~ 26 meV).[7,8]

The quantization of electronic states renders the gold nanoparticles unique electrical properties. Splitting into discrete energy states in smaller nanoparticles leads to redox-like charging behavior.[9] This is manifested in the single electron tunneling experiment between a small gold nanocluster and a tip probe.[10] Differential pulse voltammetry on larger size particles (~ Au140) showed 13 to 15 well-resolved quantized double layer charging peaks,[11,12] while a significant HOMO-LUMO gap was found for extremely small gold nanoclusters (Au38).[12] The experimental results unambiguously demonstrated the presence of discontinuous energy states in nanoclusters and the widened separation in energy levels separation upon the decrease in particle size.

Other than the unique optical and electrical properties, the small size also imparts the gold nanoparticles an extremely high surface to volume ratio. This provides numerous unsaturated sites and contributes to the nanoparticles' high activity towards catalysis. They are found to play an active role in different reactions, for instance, oxidation,[13] hydrogenation[14] and epoxidation.[15]

1.1.2. Some applications of gold nanoparticles

Over the past decades, gold nanoparticles have found applications in various aspects, such as catalysis, biological studies, bio-medicine, and sensor development.

1.1.2.1 Gold nanoparticles and catalysis

Since the first report on the potential catalytic activity of gold for the hydrochlorination of ethyne by Hutchings *et al*,[16] much effort has been devoted to explore the catalytic applications of this well-known 'inert' metal in a variety of important chemical reactions. It was found that the catalytic activity of gold nanoparticles was strongly influenced by the their dimension. A small size regime is required for a high catalytic performance.[17]

Propene epoxidation by supported gold catalyst with hydrogen as sacrificial reductant is a widely studied system. The report by Haruta[18] on the gas phase epoxidation of propene by oxygen in the presence of hydrogen demonstrated for the first time successful propene oxide formation with supported nano-gold catalyst. However, only a low conversion was achieved in exchange for a higher selectivity toward epoxide formation. Later studies resulted in a better selectivity control and higher conversion by using Ti-dope MCM-41 as solid support,[19] silylation technique,[20] and titanium substituted silicalite adulterated with gold nanoclusters smaller than 2 nm.[21]

Oxidation of other alkenes by gold catalyst has also attracted much attention. Ethene can be successfully transformed into vinyl acetate in the presence of nano-sized palladium-gold bimetallic catalyst.[22,23] Styrene was converted into its epoxide with high selectivity by nanocrystalline gold catalyst using air, with benzaldehyde and acetophenone formed as the side products.[24,25] The epoxide yield was improved when tert-butylhydroperoxide (TBHP)[26] and titania[27] as the catalyst support were used in the catalytic reaction. Recently, Caps *et al*. demonstrated the use of hydrogen peroxide

instead of TBHP to achieve a higher selectivity towards the epoxide product.[28,29]

Supported gold catalyst is also active towards the oxidative transformation of alkanes.[30,31] Cyclohexane was oxidized into cyclohexanone and cyclohexanol by oxygen with gold on alumina. A reduction in gold content from 0.6% to 0.2% resulted in a four-fold increase in the turnover frequency of the reaction.[32] Dependence on additive in methane oxidation by gold catalyst was illustrated in Hutching and co-workers' study in which benzene was the preferred product instead of C_2 hydrocarbons when hydrogen peroxide was added.[33]

Gold nanoparticles encapsulated in polymer or trapped on solid supports were also found active in the catalytic oxidation of aliphatic and aromatic alcohols,[34] diols,[35] benzylic alcohol,[36,37] amines[38] and glucose[39] in the presence of dioxygen. These laboratory scale catalytic reactions have been gradually translated into industrial capacity in recent years.

1.1.2.2 Gold nanoparticles for biomedical application

Gold nanoparticles find their applications in the area of biological research, such as nanoclusters arrangement on DNA templates,[40] labels for microscopy[41] and bioelectronics.[42,43] In recent years, gold nanoparticles were reported to readily enter into living cells upon suitable surface functionalization.

Citrate-capped gold nanoparticles[44,45] were widely used in experiments on nanoclusters uptake by cells. Particles with size in the range of 14 – 74 nm can enter into cells.

Meanwhile, the weakly-bound citrate layer enables the derivatization of the gold nanoparticles with specific functionalities, which promotes the uptake of these nanoclusters by the cells[46] or induces certain cellular responses.[47] The electrostatic interaction between the negatively charged citrate-capped gold nanoparticles and positively charged transferrin facilitated the entry of the nanoconjugate into cells through endocytosis pathway.[48] Other than the water soluble citrate-capped nanoparticles, the cetyltrimethylammonium bromide (CTAB) passivated gold nanoparticles also facilitate cell uptake of the nanoclusters, possibly by imparting the clusters' water solubility and ability to cross the hydrophobic phospholipids bilayer of the cell membrane.[49]

In addition to assisting the nanoclusters assimilation by cells, gold nanoparticles capped with different functionalities served as a valuable tool in various biological applications. Gold nanoparticles functionalized with bio-molecules like oligonucleotides,[50] peptides,[51] anti-bodies[52] and lipids[53] were employed in mRNA and small molecules detection, nuclear translocation, imaging, and cholesterol binding.

1.1.2.3 Gold nanoparticles as sensor

Gold nanoparticles can function as sensitive sensor for various analytes. It is because nanoclusters possess certain specific optical and electrochemical properties, which allow sensitive detection of many small molecules.

The strong interaction between the surface plasmon and the incident electromagnetic wave, usually in the form of light, is the foundation of the optical sensing by gold

nanoparticles. Localized surface plasmon resonance (LSPR) based AuNPs sensor involves the direct use of the surface plasmon to detect the binding events on the clusters' surface. A number of studies have demonstrated the detection of different analytes by LSPR-type gold nanoclusters sensors, including gelatin,[54] phospholipids,[55] serum[56] and pesticides.[57] Other than the LSPR mode, enhanced surface plasmon resonance is also a convenient analytical tool. He *et al*.[58] has applied the method in the detection of DNA hybridization, resulting in an over 1000-fold enhancement in sensitivity. In addition, it has been employed in the detection of single nucleotide polymorphisms in genomic DNA,[59] and in the form of biochips for analyzing low molecular weight molecules[60] and acetylcholine esterase inhibitors.[61]

The higher surface to volume ratio and the quantum size effect of gold nanoparticles significantly lower the overpotential of many analytically important electrochemical reactions and render reversibility to some redox reactions.[62] These features enable gold nano-colloids to function as electrochemical sensors. In some occasions, gold colloids served as a bridging component to facilitate the electron transfer between electrode and the redox-active centre buried inside the analyte-specific enzyme.[63-66] On the other hand, gold colloids can function as an immobilization platform for analyte specific enzymes like periplasmic glucose receptors,[67] horseradish peroxidase,[68] microperoxidase-11,[69] and tyrosinase.[70] The adsoption of enzymes on the high surface area colloid surface allows a higher loading of these proteins on a small area with retention of their activity and specificity towards the analytes, enabling higher sensitivity detection.

1.1.3. Conventional methods for preparing gold nanoparticles

The first report of gold colloids formation was by Michael Faraday[71] dated back to 150 years ago which involved the two-phase reduction of tetrachloroaurate ion in aqueous solution with phosphorus in carbon disulfide. However, great interests in preparing gold colloids was initiated nearly a hundred years later when Turkevich revisited Faraday's work and developed a protocol for the aqueous preparation of citrate-capped gold nanoparticles[72]. Based on Turkevich protocol, Fern[73] achieved the size-controlled preparation of monodisperse gold nanoparticles with different diameters (16 – 147 nm) by controlling the reductant-to-stabilizer ratio. Even though citrate can only bind weakly to the gold surface, the lower passivating ability allows easy functionalization by other stronger ligands which provide higher stability to the metal colloids. Other than citrate, phosphines can also be used to prepare gold nanoclusters with extremely small size and defined stoichiometry. The phosphine-capped gold nanoparticles prepared by McPartlin[74] and Schmid[75,76] were less than 2 nm in dimension, and possessed a composition of $Au_{11}(PPh_3)_7(SCN)_3$ and $Au_{55}(PPh_3)_{12}Cl_6$ respectively.

In 1994, Brust *et al.*[77] synthesized alkanethiolate-capped gold nanoparticles by direct reduction of gold salt in toluene containing alkanethiols and tetrabutylammonium bromide with aqueous sodium borohydride solution under biphasic condition. The nanoparticles formed were of extremely small size (1 – 2 nm) with narrow dispersity. The high stability of the thiolated-capped gold nanoclusters originated from the strong gold-sulfur interaction which allowed the colloids to be stored as solid for several years without appreciable deterioration. Due to the easy preparation, high stability, reversible dissolution character, and the functionalization potential of the thiolate monolayer on

the metallic core, the thiolated-protected gold nanoclusters has attracted much attention and facilitated further investigations on nano-materials.

1.2. Ligand exchange reaction in gold nanoparticles

1.2.1. Nature and kinetics of ligand exchange reaction between free thiols and gold nanoparticles

Since the passivating ligand monolayer is the most accessible part of the entire nanoparticles, its composition accounts for the properties expressed by the nanoclusters. To adjust the behavior of this layer, ligand exchange is one of the most convenient strategies.

Ligand exchange is a very important process that occurs on the surface of metals and semi-conductors.[78] It is one of the most commonly employed approaches to functionalize the metallic substrates to impart them the ability to serve as valuable agents in catalysis and sensing.

The exchange events on the surface of noble metals, like gold, silver and platinum, have been extensively studied in order to understand the kinetics and the thermodynamics that control the resultant binary monolayer formed.

The mechanisms for ligand exchange reactions occurring on gold surface resemble the three most common mechanistic routes describing ligand substitution in conventional inorganic complexes.[79] They are the associative, dissociative and interchange mechanisms. However, the predominant mechanism involved is largely determined by the morphology of the metallic substrate. For instant, dissociative mechanism was strongly favored over the associative route for the ligand exchange on platinum

electrode surface.[80] This was supported by the similar rates for the ligand desorption and the exchange reaction obtained in some studies.[81,82]

The pioneering work by Murray and co-workers[83] on ligand exchange in thiolate-passivated gold nanoparticles revealed significant differences in the exchange behavior between the three dimensional nanoclusters and the flat metallic surface. It was found that the ligand exchange between free thiol and the bound-thiol on gold nanoparticles possesses several characteristics. Firstly, the exchange is in 'one-to-one' basis, i.e. a single incoming ligand was introduced for every departed bound thiol, and it is also this characteristic that makes the process to be associative in nature. No spontaneous desorption of thiol is observed. Another feature is that the bound thiolates were detached as thiols after exchanging for the incoming ligands. In addition, a two-stage exchange can generally be observed in nanoparticles: a fast reaction was followed by a much slower process. This is largely due to the exchange of ligands on different surface morphologies with varying energy states. The exchange kinetics are generally complex and cannot be described in terms of simple first order and second order process. The most common approach to investigate the exchange kinetics of ligand exchange in gold nanoparticles is the initial rate estimation. It is because the reverse reaction can be neglected upon a low fraction of in-coming ligand exchanged. More importantly, the kinetic data obtained in the early period can be well-approximated by the overall second order which indicated that the exchange reaction at the beginning stage is first order with respect to both the incoming ligand and the nanoparticles concentration. The recent report by Kassam *et al*.[84] demonstrated that the entire course of the ligand exchange process between dodecanethiol and decanethiol-capped gold nanoparticles can be well described by the second-order

Langmuir diffusion-limited process equation:

$$\Theta(t) = \frac{Ak\sqrt{t}}{1 + k\sqrt{t}}$$

where Θ(t) refers to the fractional surface cover of incoming ligand at time equals to t, A is the final incoming ligand surface coverage and k is the rate constant. The exchange rate was found to be independent of the free thiol loading ratio.

The effects on the ligand exchange kinetics as a result of the various metal core and surface monolayer status have been extensively investigated by many researchers with different spectroscopic means, such as fluorescence, NMR, EPR and ESI-MS.

Donkers *et al*.[85] demonstrated a strong link between the ligand electronic effects and the initial stage kinetics for the ligand exchange of p-substituted arylthiol with phenylethanethiol-capped gold nanoparticles, as reflected by Hammett plot. The relationship was also proven to be core-size independent (Au_{38} and Au_{140}).[86]

Apart from the electronic effect by the ligand, the charge from the gold core also exerted significant effect towards ligand exchange process. Song *et al*.[87] reported that a gradual increase in the ligand exchange rate was accompanied by progressive accumulation of positive charge in gold nanoclusters. This is similar to the observed higher ligand exchange rate with electron-withdrawing ligands and charged 2D-gold substrate.[88]

Since alkanethiol-capped gold nanoparticles were the most well-studied system, most reports concerning ligand exchange kinetics were largely dedicated to this class of

clusters. Due to the growing demand for gold nanoparticles in biomedical research, detailed study on ligand exchange kinetics in aqueous medium is highly desirable.

1.2.2. Application of ligand exchange reaction

Ligand exchange is an important route to incorporate different functionalities onto the surface of gold nanoparticles. There has been substantial reports demonstrated the modification of monolayer properties by incorporation of functional structure through ligand exchange reaction.

The earliest ligand exchange study by Murray *et al*.[89] demonstrated the introduction of thiols functionalized with polar or reactive groups at the ω-terminal into the monolayer of the as-prepared alkanethiol-capped gold nanoparticles. To probe the electrochemistry of the nanoparticles, thiol linker-tagged electro-active groups like ferrocene,[90] anthraquinone,[91] phenothiazine[92] and C_{60} fullerene[93] were introduced by ligand exchange.

As the need for bio-compatible gold nanoclusters grows, water-soluble ligands are introduced to the passivating monolayer of as-prepared gold nanoparticles to enhance their solvation in this highly polar environment. Thiolated PEG,[94] sulfonated[95] and quaternary ammonium[96] tagged thiols were implanted onto the particle surface by substituting the bound thiolated or the phopshine ligand.

The preparation and operation of gold nanoparticles-based molecular beacon sensor rely heavily on ligand exchange reaction. To prepare the beacon, thiol ligands equipped with

photoactive fluorophores such as porphyrin,[97] ethidium[98], dansyl[99] and pyrene[100] are tethered onto the very small gold nanoclusters through place exchange reaction. Under the short distance linkage, the luminescence from the fluorophore was completely quenched by the strong and broad-range absorption of the nanoparticles. When serving as sensor, the progress of assay was monitored by the recovery of luminescence from the fluorophore-tagged ligands detached in the ligand exchange reaction with the target(s).[101,102] The final extent of exchange can be modulated through manipulating the amount of mercapto terminal available for binding.[103]

In addition, ligand exchange reaction has been widely employed in the preparation of peptide functionalized gold nanoparticles[104,105] to enable the nanoclusters to function as pseudo-enzyme.[106,107] Similar catalytic activity for gold nanoparticles in chemical transformations are also realized by introducing catalyst-modified ligand to the monolayer via place exchange reaction.[107,108]

1.3. Gold nanoparticles synthesized in aqueous medium

1.3.1. Polar ligands for gold nanoparticles

As gold nanoparticles are promising tools in biological delivery processes and bio-assays, fabrication of gold nanoparticles which are water-soluble has been an active research area. In recent years, many reports concerning the use of different polar ligands and hydrophilic group-substituted thiols for the preparation of water-soluble gold nanoclusters have appeared.

Earlier researches employed simple polar thiols to passivate the gold nanoparticles formed and to impart the metal clusters a higher water-solubility. Examples of these simple thiols are 3-mercaptopropionic acid,[109] mercaptosuccinic acid[110] and p-substituted thiolphenols. [111-114] The use of short peptides, sugar and amino acids, like glutathione,[115] methionine,[116] thiolated-mannose[117] and cysteine[118] carrying a naturally equipped or artificially added mercapto group have also been reported. Positively charged ω-ammonium head group was also utilized in several reports[119,120] to achieve high water-solubility of the nanoclusters.

In order to better passivate the nanoparticles in water, the ligands employed has gradually shifted from simple molecules to a variety of steric ligands. The most commonly employed steric ligand is polymer. Thiolated poly(ethylene glycols), [94,121,122] poly(amidoamine) type dendrimers[123,124] and amphiphilic polymer[125] have all been employed. Although higher stability can always be achieved with ligands which are more sterically hindered, the protection provided by small thiol-contained molecules is

still sufficient enough to yield highly stable, water-soluble and isolable passivated gold nanoclusters. In addition, these small molecules are generally naturally available or more easily prepared when compare with their more complicated polymeric counterparts.

1.3.2. Au@tiopronin system by Murray

In 1999, Murray and co-workers[126] synthesized the tiopronin-passivated gold nanoparticles (Au@tiopronin). Tiopronin is a drug for curing cystinuria. It contains two polar functionalities – amide and carboxyl – which render the compound high solubility in water. When synthesized in a single acetic acid/methanol phase with gold salt, 3 equivalents of tiopronin and 20 equivalent of sodium borohydride, vast quantity of extremely small gold nanoclusters (~ 1.8 nm) were formed with narrow dispersity. Due to its simple preparation, excellent water-solubility and stability against coagulation, the novel Au@tiopronin has been applied in various studies, such as nanoparticles enhanced surface plasmon resonance based molecular sensing,[127] nanoparticles-assisted cell uptake,[128] antigen-anti-body interactions assay,[129] electric conductivity measurement of nanoparticles coated crystals[130] etc. The simple molecular structure and the functionalizable carboxyl group in tiopronin ligand greatly facilitate the derivatization of the nanocluster for desired purposes.[127,128]

One of the most important characteristics of Au@tiopronin is its ability to emit at near-infra red (NIR) region (700 – 900 nm) upon excited at ~ 360 nm. The broad emission profile[131] indicated a collection of radiative pathways involved. Such discovery promoted the fabrication of near-IR emitting gold nanoparticles passivated

with polar ligands, like glutathione,[132] lipolic acid,[133] thiolated PEG[134] and amino-dendrimer.[124] Since biological tissues express a much smaller interference at the near-infra red spectral region,[135] the NIR emitting gold nanoparticles are promising new fluorophores for future bioassays.

Based on the substantial interests towards water-soluble gold nanoparticles capped with simple small molecules, further research and modification of the novel Au@tiopronin system is highly desirable.

1.4. Gold nanoparticles synthesized in room temperature ionic liquids

1.4.1. Ionic liquids – the green solvent

$[EtNH_3][NO_3]$ is the first reported room temperature ionic liquid dated back to the early 20th century. The subsequent alkyl-substituted imidazolium and pyridinium based trihaloaluminate ionic liquids, emerged during the 70s to 80s,[136,137] had limited usage due to their high sensitivity to moisture. In 1992, Wilkes and Zawarotko [138] introduced the air stable 1,3-dialkylimidazolium based ionic liquids, with tetrafluoroborate and hexafluorophosphate as the anions. Since the discovery of the ambient conditions stable ionic liquids, much attention has been attracted to utilize this family of non-volatile liquid as medium for reactions.

The extraordinary low melting point of the ionic liquids, compared with the conventional non-organic based ionic compounds, originates from the inferior packing of the cations and anions.[139] The low volatility,[140] specific miscibility properties[141] and high solubility towards a wide range of substances, like inorganic salts[142] and bio-molecules,[143] make ionic liquids a new generation of environmentally friendly reaction medium. In recent years, the successful incorporation of biodegradable components, like amino acid cations,[144,145] and alkylsulfate chain[146] further makes ionic liquid more environmentally benign.

Many studies demonstrated that ionic liquids can lead to enhanced reaction efficiency and selectivity, which directly help reduce energy consumption and waste production in

chemical reactions. Catalytic hydrogenation of cyclohexene[147] and olefins[148] with respectively rhodium or cobalt-based catalyst in ionic liquids showed an enhanced reaction rate and selectivity when compared to conventional organic solvents. Direct immobilization of metal catalysts to ionic liquids enabled one-phase catalytic reaction[149,150] and easy recovery of product by simple extraction. This strategy greatly minimizes the materials and energy required for the work-up process and the loss of catalyst, achieving a greener transformation. Recent development of functional ionic liquids possessing a 'dual-role' character – serving as both the reaction medium and catalyst – vastly promotes the reaction efficiency and reduces reagent or catalyst consumption[1,151].

1.4.2. Preparation of gold nanoparticles in ionic liquids.

Gold nanoparticles can be prepared in ionic liquids from the corresponding gold salt by various reduction methods. These methods can be roughly classified into either physical or chemical approach.

For physical approach, the reduction of gold salt to zero-valence gold is entirely attributed to physical phenomena or with indirect assistance from chemical reagents. Larger size and less regularly-shaped gold nanoparticles can be obtained by applying electron beam[152,153] to an ionic liquid solution containing gold salt. The use of low energy electron beam method produced gold nanoparticles of 100 – 200 nm in diameter in 1-butyl-3-methylimidazolium bis(trifluoromethanesulfonyl)imide ionic liquid [BMIm][Tf_2N]. When gamma radiation was applied to the gold salt contained [$Me_3NC_2H_4OH$][Zn_2Cl_5] ionic liquid, the reduced zinc ions generated by irradiation

gradually reduce the gold precursor in the medium to produce the nano-colloids. The gold nano-species formed by gamma radiation are generally irregular in morphology. The use of laser ablation,[154] which nanoclusters were formed upon the laser beam struck onto the gold plate immersed in the ionic liquid, produced relatively more spherical nanoparticles. The dimension of the nanoclusters formed varied upon a change in laser beam frequency and the ionic liquid used. In general, the size of the nanoparticles became smaller when a higher energy beam and shorter alkyl chain imidazolium cation were utilized in the preparation.

The principle of gold nanoparticles preparation with sputter deposition[155] is highly similar to that by laser ablation. In both techniques, nanoparticles were obtained by the clustering of gold atoms scratched off with higher energy electron or argon beam. The nano-colloids formed by sputter deposition were highly spherical in morphology with very small size and dispersity. Smallest nano-clusters were formed with the acyclic quaternary ammonium imide ionic liquid[155]. In addition, larger particles were observed with higher silver content in the Au-Ag alloy nanoclusters formed.

Ultrasound can effectively promoted the synthesis of gold nanoparticles in ionic liquids with the presence of hydrogen peroxide.[156] The gold colloids produced were 2.7 to 9.5 nm in diameter under different gold-to-thiol-functionalized ionic liquid loading ratio. Electrodeposition with ionic liquid composed of cyano-aurate anion and imidazolium cation gave nano-sized gold species of 20 – 100 nm in dimension and leaf-like structures.[156]

Chemical reduction approach was more commonly employed in preparing ionic liquid

passivated gold nanoparticles. The nanoclusters produced with thiol-functionalized ionic liquids were of 2 – 5 nm in diameters. They were formed by direct reduction of gold salt in the aqueous solution of the thiolated ionic liquids with sodium borohydride,[157,158] methanolic borohydride,[159] and super-hydride in THF.[160] The gold nano-colloids produced were generally spherical in morphology and some can be made soluble directly into the hydrophobic ionic liquids[160] or after anion metathesis.[158] An extra quantity of N-methylimidazole added significantly enhanced the stability of the gold nanoparticles formed in imidazolium ionic liquid by borohydride reduction.[161]

The cationic moiety of the ionic liquid, such as the imidazolium and the quaternary ammonium head group, can be grafted to polymer chain like PAMAM to give a water-soluble ionomer. The size of the ionomer passivated gold nanoparticles produced by direct borohydride reduction varied over 1 – 30 nm[162]. Except the most popular borohydride reduction, gold nanoclusters can be produced directly from the reductive functional groups incorporated to the cation of the ionic liquids.[163,164] The nanoparticles produced were generally small with spherical morphology. Other frequently employed reductants like citrate,[165] oleic acid,[166] and carbon monoxide.[167]

Except the physical reduction approaches, gold nanoparticles synthesized in ionic liquids always require a secondary solvent, like water and other organic solvents, when chemical reduction protocols are used. This may be due to the poor solubility of sodium borohydride in ionic liquid and problems associated with agitation. Considering a greener synthesis and simpler preparation, the development of better protocols for nanoparticles preparation solely in ionic liquid is highly anticipated.

1.5 Aims and objectives

Since there has been a strong desire for applying gold nanoparticles in biomedicine, further investigation on water-soluble gold nanoparticles is needed. As mentioned previously, the relatively simple and highly functionalizable Au@tiopronin system facilitated its utilization in various aspects. Preparation of tiopronin derivatives and their respective gold nanoparticles may help to provide a wider collection of useful water-soluble gold nanoparticles to serve different purposes.

The preparation and characterization of several tiopronin derivatives and also their respective gold nanoparticles will be discussed in Chapter 2. Meanwhile, because of the strong reliance on ligand exchange reaction in many assay protocols and functionalization of nanoparticles, the ligand exchange kinetics of the prepared tiopronin-derivative-capped gold nanoparticles in aqueous medium was examined and the results obtained will be discussed in Chapter 3.

In order to establish a greener and genuine single-phase preparation of gold nanoparticles in ionic liquid, a one-pot synthesis protocol of gold nanoclusters in pyrrolidinium-based ionic liquid with ionic liquid solvated quaternary ammonium borohydride under various reaction conditions was examined. The results obtained will be discussed in Chapter 4.

Chapter 2

Synthesis and characterization of gold nanoparticles capped with tiopronin-derivatives

2.1 Introduction

Tiopronin, a drug molecule for modulating cystine precipitation and excretion in cystinuria and rheumatoid arthritis, is one of those polar thiols employed for the preparation of water-soluble gold nanoparticles in the early days. Since then, more polar mercapto compounds, especially peptides bearing thiol functionality, were employed to stablize gold nanoparticles as these capping agents are more compatible with the biological environment. Many researches are dedicated to control the morphology, dispersity, size and usability of the water-soluble nanoparticles by manipulating the ligand concentration or metal salt to ligand concentration ratio in the synthetic procedures. However, a systematic variation of the peptide structure and its relationship with the properties of the gold nanoparticels as synthesized, remain unknown in the literature. This chapter summarizes our attempts to synthesize tiopronin derivaties through a systematic variation of the structure and the properties of the gold nanoparticles with these peptide derivatives as capping ligands.

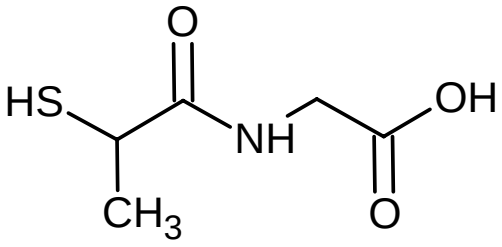

Figure 2.1 Strucutre of tiopronin

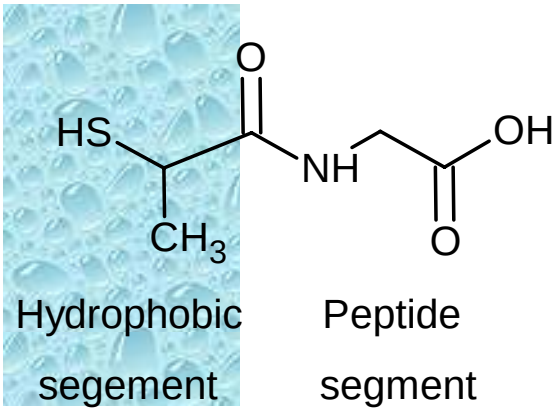

Figure 2.2 Structural characteristic of tiopronin

Tiopronin is a simple peptide molecule consisting of a more hydrophobic alkyl segment and a hydrophilic peptide segment (Figure 2.1). One can easily modify its structure by replacing with different alkyl side chains and amino acids. Therefore, in this study, some tiopronin-derivatives were prepared by adopting modifications to the two segments of the tiopronin backbone: the mercapto-containing hydrophobic segment, and the peptide segment. (Figure 2.2)

For the hydrophobic segment, the mercapto group in all derivatives was always kept one carbon distance away from the amide group in order to preserve the key character of the tiopronin skeleton. Variation was performed by introducing different alkyl substituents to replace the original methyl group. In this study, an ethyl and phenyl derivatives were synthesized. The final derivatives formed, as shown in Figure 2.4, were used in the synthesis of gold nanoparticles with the standard protocol by Murray.[168]

The peptide part, in fact, allows more room for structural modification, since there are altogether 21 amino acids and many other suitable small polar molecules for selection. However, in order to maintain a close similarity to the parent tiopronin backbone to facilitate the comparison, only three amino acids were considered in this study – alaine, proline and leucine. The structure of these three amino acids is shown in Figure 2.3. As shown in the Figure 2.4, incorporation of alanine and leucine render a secondary amide group in the final derivative molecule, which is similar to the tiopronin in terms of structural characteristics. Introducing proline, however, gives the final molecule a sterically hindered cyclic tertiary amide structure in which formation of hydrogen bonding through the amide moiety was prevented. Significant difference in monolayer

properties between the nanoclusters capped by these tiopronin derivatives and the original Au@tiopronin are therefore anticipated.

The gold nanoparticles capped with the aforementioned tiopronin-derivatives were synthesized with Murray's protocol[168] and they were characterized with various spectroscopic means and gravimetric analysis. The following abbreviations will be used to represent the various tiopronin-derivative capped gold nanoparticles:

Au@MBG - 2-Mercaptobutanoyl glycine capped gold nanoparticles

Au@MPEG - α-Mercaptophenylethanoyl glycine capped gold nanoparticles

Au@MPA - 2-Mercaptopropionyl alanine capped gold nanoparticles

Au@MPP - 2-Mercaptopropionyl proline capped gold nanoparticles

Au@MPL - 2-Mercaptopropionyl leucine capped gold nanoparticles

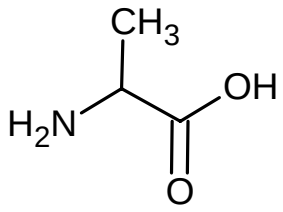

Alanine

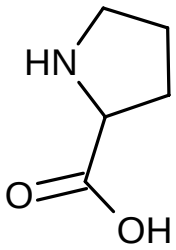

Proline

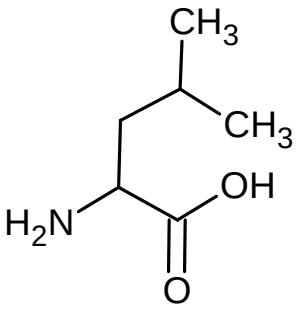

Leucine

Figure 2.3 Structure of alanine, proline and leucine

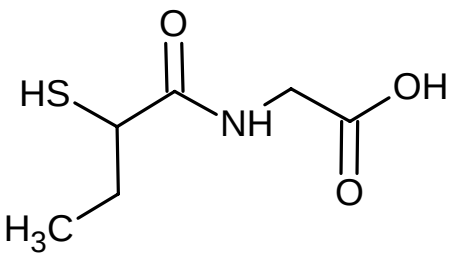

2-Mercaptobutanoyl glycine
(MBG)

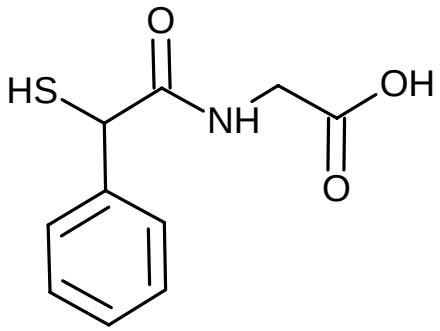

2-Mercapto-2-phenylethanoyl glycine
(MPEG)

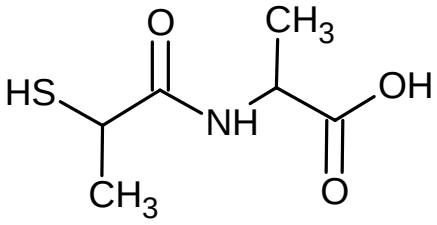

2-Mercaptopropionyl alanine
(MPA)

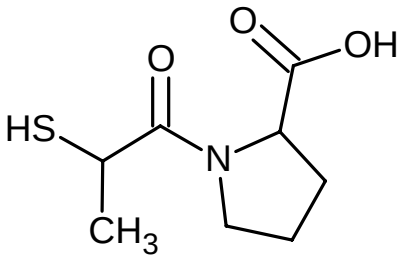

2-Mercaptopropionyl proline
(MPP)

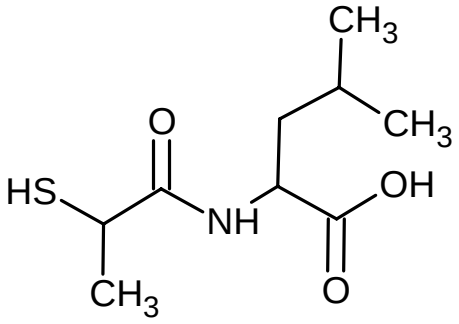

2-Mercaptopropionyl leucine
(MPL)

Figure 2.4 Molecular structure of tiopronin-derivatives synthesized in this study

2.2 Experimental section

The synthetic route of the tiopronin derivatives is illustrated in Scheme 2.1. Details for the preparation of all intermediates and the final derivatives are given in the subsequent sections of this chapter.

2.2.1 Materials

Hydrogen tetrachloroaurate-trihydrate ($HAuCl_4$ $3H_2O$), tiopronin, α-bromo-α-phenylacetic acid, 2-bromopropionyl chloride, 2-bromobutanoyl chloride, triethylamine, glycine ethyl ester hydrochloride, DL-alanine ethyl ester hydrochloride, DL-proline methyl ester hydrochloride, DL-leucine, potassium thioacetate, sodium bicarbonate, dimethylaminopyridine (DMAP), anhydrous magnesium sulphate and sodium hydroxide were purchased from Aldrich. Dichloromethane, acetone, methanol, glacial acetic acid, hydrochloric acid and ethyl acetate were obtained from Tedia. Sodium borohydride was acquired from Acros. Deionized water of resistance 18 MΩ was produced with a Millipore system.

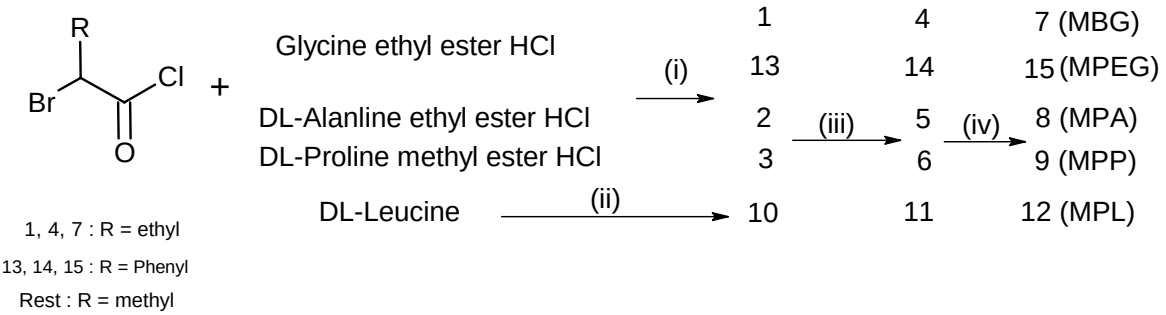

(i) Trimethylamine, DMAP, CH_2Cl_2 ii) a) 1 M NaOH $_{(aq)}$ b) 1 M HCl $_{(aq)}$
(iii) Potassium thioacetate, acetone iv) a) NaOH, methanol, under N_2, b) 1 M HCl

Scheme 2.1 Synthetic scheme for all tiopronin-derivatives and the intermediates.

For compounds 1 – 12, pleases refer to section 2.2.2

2.2.2 Synthesis of tiopronin-derivatives

2.2.2.1 Synthesis of 2-bromobutanoyl glycine ethyl ester (1)

To a stirred suspension of glycine ethyl ester hydrochloride (1.39 g, 10 mmol), triethylamine (1.21 g, 12 mmol) and DMAP in dichloromethane (100 mL) was added 2-bromobutanoyl chloride (1.76 g, 9.5 mmol, in 100 mL of dichloromethane) in a dropwise manner within 3 hours. After stirring overnight, the sample was washed twice with 1 M hydrochloric acid followed by saturated sodium bicarbonate solution. The organic phase was dried with anhydrous magnesium sulphate, filtered and rotary evaporized to give **1** as a white solid (1). Yield: 80% , ^{1}H NMR (400 MHz, $CDCl_3$), δ /ppm: 7.00 (b, 1H), 4.45 (t, 1H), 4.35 (q, 2H), 4.17 (d, 2H), 2.16 – 2.31 (dq, 2H), 1.40 (t, 3H), 1.16 (t, 3H).

2.2.2.2 Synthesis of 2-bromopropionyl alanine ethyl ester (2)

2-Bromopropionyl alanine ethyl ester was synthesized with 2-bromopropionyl chloride and DL-alanine ethyl ester similar to that described above for **1**. Yield: 74%. ^{1}H NMR (400 MHz, $CDCl_3$), δ /ppm: 7.05 (b, 1H), 4.65 (q, 1H), 4.52 (q, 1H), 4.33 (q, 2H), 2.01 (d, 3H), 1.56 (d, 3H), 1.41 (t, 3H).

2.2.2.3 Synthesis of 2-bromopropionyl proline methyl ester (3)

2-Bromopropionyl DL-proline methyl ester was synthesized with 2-bromopropionyl

chloride and DL-proline methyl ester by experimental procedures similar to those described for **1**. Yield: 85%. ^{1}H NMR (400 MHz, $CDCl_3$), δ/ppm: 4.55 (q, 1H), 4.48 (t, 1H), 3.74 (s, 3H), 3.55 (m, 2H), 2.38 (m, 2H), 1.98 (m, 2H), 1.97 (d, 3H).

2.2.2.4 Synthesis of 2-(acetylthio)butanoyl glycine ethyl ester (4)

1 (2.52 g, 10 mmol) was added to a stirred acetone solution (50 mL) of potassium thioacetate (1.26 g, 11 mmol). Potassium bromide immediately precipitated out as a white solid once **1** was added. The reaction mixture was stirred overnight, and acetone was removed the next day. The residue was washed with dichloromethane, dissolved in deionized water and then extracted with dichloromethane. The organic fractions were collected and then dried with anhydrous magnesium sulphate, filtered and rotary evaporized to give **4** as a yellowish solid. Yield: 98%. ^{1}H NMR (400 MHz, $CDCl_3$), δ /ppm: 6.76 (b, 1H), 4.33 (q, 2H), 4.12 (d, 2H), 4.06 (t, 1H), 2.50 (s, 3H), 1.87 – 2.16 (dq, 2H),1.39 (t, 3H), 1.12 (t, 3H).

2.2.2.5 Synthesis of 2-(acetylthio)propionyl alanine ethyl ester (5)

2-(Acetylthio)propionyl alanine ethyl ester was synthesized from **2** by procedures similar to those for **4**. Yield: 99%. ^{1}H NMR (400 MHz, $CDCl_3$), δ/ppm: 7.02 (b, 1H), 4.63 (q, 1H), 4.32 (q, 2H), 4.21 (q, 1H), 2.50 (ds, 3H), 1.58 (d, 3H), 1.50 (dd, 3H), 1.38 (t, 3H).

2.2.2.6 Synthesis of 2-(acetylthio)propionyl proline methyl ester (6)

2-(Acetylthio)propionyl proline methyl ester was prepared from **3** by procedures similar to those for **4**. Yield: 97%. ^{1}H NMR (400 MHz, $CDCl_3$), δ/ppm: 4.45 (m, 1H), 4.39 (q, 1H), 3.70 (s, 3H), 3.41 – 3.52 (m, 2H), 2.34 (s, 3H), 2.41 – 2.02 (m, 4H), 1.45 (d, 3H).

2.2.2.7 Synthesis of 2-mercaptobutanoyl glycine (MBG) (7)

To **4** (2.47 g, 10 mmol) in degassed methanol at 0℃ under nitrogen was added 22 mL of 1 M aqueous sodium hydroxide (22 mmol) under dropwise condition. After stirred for 1 h under nitrogen, HCl (1 M, 10 mL) was added and the solvent was removed under vacuum. 1 M HCl (10 mL) was added to the residue. The aqueous phase was extracted twice with ethyl acetate, dried with anhydrous magnesium sulphate, filtered and rotary evaporized to give **7** as a white solid, Yield: 85%. ^{1}H NMR (400 MHz, D_2O), δ/ppm: 3.99 (d, 2H), 3.41 (q, 1H), 1.72 – 1.84 (dq, 2H), 0.94 (t, 3H).

2.2.2.8 Synthesis of 2-mercaptopropionyl alanine (MPA) (8)

2-Mercaptopropionyl alanine was synthesized from **5** by the experimental procedures described for **7**. Yield: 87%. ^{1}H NMR (400 MHz, D_2O), δ/ppm: 4.15 (q, 1H), 3.44 (q, 1H), 1.28 (d, 3H), 1.25 (d, 3H).

2.2.2.9 Synthesis of 2-mercaptopropionyl proline (MPP) (9)

2-Mercaptopropionyl proline was synthesized from **6** by procedures similar to those described for **7**. Yield: 88%. ^{1}H NMR (400 MHz, CD_3CN), δ/ppm: 4.37 (m, 1H),

3.61 – 3.69 (m, 3H), 2.26 (d, 1H), 1.95 – 2.17 (m, 4H), 1.43 (d, 3H).

2.2.2.10 Synthesis of 2-bromopropionyl leucine (10)

To a chilled 5-mL aqueous mixture of sodium hydroxide (0.2 g, 5 mmol) and DL-leucine (0.65 g, 5 mmol), 2-bromopropionyl chloride (0.85 g, 5 mmol) and 1 M sodium hydroxide solution (5 mL) were added alternately in a dropwise manner. After the addition has been completed, the mixture was stirred at 0 ^{o}C for 30 min and then at room temperature for 1 h. The pH of the crude mixture was adjusted to 3 with 1 M HCl. The aqueous fraction was extracted twice with ethyl acetate. The organic fractions were then dried with anhydrous magnesium sulphate, filtered and rotary evaporated to give **10** as a white solid. Yield: 65%. ^{1}H NMR (400 MHz, $CDCl_3$), δ /ppm: 6.72 (b, 1H), 4.60 (q, 1H), 4.44 (q, 1H), 1.88 (d, 3H), 1.75 (m, 2H), 1.65 (m, 1H), 0.96 (d, 6H).

2.2.2.11 Synthesis of 2-(acetylthio)propionyl leucine (11)

2-(Acetylthio)propionyl leucine was synthesized from **10** by procedures similar to those described for **4**. Yield: 97% (pale yellow solid). ^{1}H NMR (400 MHz, $CDCl_3$), δ /ppm: 6.63 (b, 1H), 4.56 (q, 1H), 4.11 (q, 1H), 2.36 (s, 3H), 1.69 (t, 2H), 1.58 (m, 1H), 1.46 (d, 3H), 0.94 (d, 6H).

2.2.2.12 Synthesis of 2-mercaptopropionyl leucine (MPL) (12)

2-Mercaptopropionyl leucine was synthesized from **11** by the experimental procedures

similar to those described for **7**. The product precipitated out as a white solid from the aqueous reaction mixture once hydrochloric acid was added. Yield: 85%. ^{1}H NMR (400 MHz, $CDCl_3$), δ /ppm: 6.72 (b, 1H), 4.60 (q, 1H), 4.44 (q, 1H), 1.88 (d, 3H), 1.75 (m, 2H), 1.65 (m, 1H), 0.96 (d, 6H).

2.2.2.13 Synthesis of α-bromophenylethanoyl glycine ethyl ester (13)

α-Bromophenylacetic acid (2.15 g, 10 mmole) and thionyl chloride (1.09 mL, 15 mmole) were dissolved in dichloromethane. A few drops of DMF were added and the mixture was refluxed for 2 hrs. Afterwards, excess thionyl chloride and solvent were removed by rotary evaporation. The remaining freshly prepared acyl chloride was used without further purification. The acyl chloride formed was immediately diluted with 10 mL of dried dichloromethane and added in a dropwise manner to a stirred dichloromethane solution (50 mL) of glycine ethyl ester hydrochloride (1.39 g, 10 mmole) and triethylamine (3.48 mL, 25 mmole). A white solid of trimethylamine hydrochloride formed during the process. After the addition had been completed, the reaction mixture was stirred for 3 hrs. Then, the crude mixture was washed with saturated ammonium chloride and sodium carbonate solution alternately twice. The organic fractions were collected, dried over magnesium sulfate and filtered. The solvent was rotary evaporated to give **13** as a white solid. Yield 97% . ^{1}H NMR (400 MHz, CD_3CN) : δ /ppm: 7.67 (d, 2H), 7.54 (t, 2H), 7.49 (s, 1H), 6.82 (b, 1H), 5.69 (s, 1H), 4.26 (q, 2H), 4.04 (d, 2H), 1.35 (t, 3H)

2.2.2.14 Synthesis of α-(acetylthio)phenylethanoyl glycine ethyl ester (14)

α-(Acetylthio)phenylethanoyl glycine ethyl ester was synthesized from **13** by the experimental procedures similar to those described for **4**. Yield: 99% (pale yellow solid).

^{1}H NMR (400 MHz, CD_2Cl_2), δ /ppm: 7.54 (d, 2H), 7.48 (t, 2H), 7.45 (s, 1H), 6.82 (b, 1H), 5.39 (s, 1H), 4.30 (q, 2H), 4.10 (d, 2H), 2.51 (s, 3H), 1.38 (t, 3H)

2.2.2.15 Synthesis of α-(mercapto)phenylethanoyl glycine (MPEG) (15)

α-(Mercapto)phenylethanoyl glycine was synthesized from **14** by the experimental procedures similar to those described for **7**. Yield: 99% (off-white solid).

^{1}H NMR (400 MHz, CD_2Cl_2), δ /ppm : 7.56 (d, 2H), 7.47 (t, 2H), 7.44 (s, 1H), 7.10 (s, 1H), 4.86 (s, 1H), 4.19 (d, 2H), 2.70 (d, 1H)

2.2.3 Synthesis of gold nanoparticles capped with tiopronin derivatives

Murray's method for the preparation of gold-tiorpronin nanoparticles Au@tiopronin was adopted for synthesizing tiopronin-derivatives capped gold nanoparticles in this study[168].

$HAuCl_4$ 0.31 g (0.79 mmol) of $HAuCl_4$ was dissolved in 35 ml of methanol / glacial acetic acid mixture (6 : 1). Tiopronin-derivative (2.37 mmol) (Au : thiol = 1 : 3) was added. The colour of the solution changed immediately from bright yellow to deep orange and finally pale yellow, due to the formation of Au(I)-thiolate complex. $NaBH_4$ (0.60 g, 15.8 mmol) in 15 ml of water was added dropwisely upon vigorous stirring. After the addition of hydride had been completed, the reaction mixture was stirred for 1 hr. Finally, the reaction solution was vacuum evaporated to give a black residue. Double deionized water (DDI water) was added to the residue and this solution was adjusted to pH = 1 with concentrated hydrochloric acid.

2.2.3.1 Purification of gold nanoparticles

Crude Au@MBG, Au@MPA and Au@MPP solutions, after adjusting the pH to 1 with hydrochloric acid, were then charged into a dialysis tubing (MWCO = 6 – 8 k). The nanoparticle solutions were dialyzed for 3 days with DDI water and the water outside dialysis tubing were changed every 10 – 12 hrs. After dialysis has been completed, the purified nanoparticle solutions were lyophilized under vacuum.

As Au@MPEG could hardly be redissolved in any common solvents, attempt to purify

the crude solid failed and it was obtained as a black solid with no further investigation.

Crude Au@MPL was purified by two different procedures – acid-base-diethyl ether wash, or base-acid-water-dialysis. For the first approach, the crude residue was dissolved in 30 ml of diethyl ether, acidified with 1M HCl, then washed several times with DDI water (30 ml) to remove the inorganic salt. Then 0.5M sodium hydroxide solution (20 ml) was added to the ether solution. Transfer of nanoparticles to the alkaline aqueous phase occurred, and the ether fraction was removed. The aqueous phase was washed with fresh ether several times. Finally, the nanoparticles were dissolved into the ethereal phase again by acidifying the alkaline aqueous phase with 1M hydrochloric acid. The above process was repeated three times and finally the nanoparticles were precipitated from the solution by acidifying the alkaline nanoparticle aqueous solution with 1M HCl. The precipitated nanoparticles were filtered and a black solid was obtained.

The second approach also employed an acid-base wash procedure, but with dialysis. The crude nanoparticles residue, after vacuum removal of solvent, was made alkaline by adding 1M sodium hydroxide solution until pH reached 12. Then the alkaline nanoparticle solution was loaded to a dialysis tubing (MWCO = 6 – 8k) and dialyzed against 5L of 0.2M sodium hydroxide solution for 48 hours. The alkaline solution outside the tubing was changed every 12 hrs. After the alkaline dialysis, the pH of the nanoparticle solution in the tubing was adjusted to pH 1 with 2 M hydrochloric acid. Then the particle solution was dialyzed against DDI water for 3 days with the water outside tubing changed every 12 hours. The purified nanoparticle solution was lyophilized to give a black solid.

2.2.4 Characterization of tiopronin-derivatives capped gold nanoparticles

2.2.4.1 UV-visible spectroscopy

The UV-visible spectra of all tiopronin-derivative capped gold nanoparticles were obtained with a HP 8453 spectrophotomer. The stability of the gold colloids in various concentrations of electrolyte solution was also investigated by observing the change in their UV-visible spectra. The electrolyte tested were cesium chloride, sodium chloride and lithium chloride. The spectral change over the wavelength region of 350 – 700 nm and the absorbance at 525 nm was monitored.

2.2.4.2 Transmission electron microscopy (TEM)

Samples for TEM were prepared by putting a drop of the nanoparticle solution to a carbon-coated copper grid. Excess solution was removed from the grid with the tip of a piece of filter paper. The grid was then allowed to dry under ambient condition overnight, TEM measurement were performed with a JEOL model JEM 2010 transmission electron microscope operating at 200 kV, equipped with a GATAN MSC 794 CCD camera. The average size and the size distribution of each type of nanoparticles were obtained by counting 100 – 200 particles in a randomly selected area.

2.2.4.3 Nuclear magnetic resonance (NMR)

Nuclear magnetic resonance spectra for all intermediates, tiopronin-derivatives and nanoparticles were obtained with a Bruker 400 MHz spectrometer at room temperature.

2.2.4.4 Thermogravimetric analysis (TGA) / differential scanning calorimetry (DSC)

Thermogravimetric analysis and differential scanning calorimetry were conducted simultaneously with a Netzch TGA/DSC STA449C Jupiter® system. For each run, about 3.5 – 5 mg of nanoparticle powder was loaded in an alumina crucible and was heated under ambient atmosphere from 30℃ to 860℃ with a constant heating rate of 10℃ per minute.

2.2.4.5 Infra-red spectroscopy

The infra-red spectra for solid thiol ligands and lyophilized gold nanoparticles powder were acquired as KBr disc. The spectra were collected at a resolution of 4 cm^{-1}. Attenuated total reflectance infra-red (ATR-IR) spectra for aqueous thiol ligands and gold nanoparticles were obtained by measuring a thin liquid film of the solution placed on the instrument bound zinc selenide crystal.

2.2.4.6 X-ray photoelectron spectroscopy (XPS)

X-ray photoelectron spectra for all tropronin-derivative capped gold nanoparticles were obtained using a Physical Electronics 5600 multi-technique system, operating with monochromatic Al K_α line (1486.6 eV). The operating voltage and power are 14 kV and 350 W respectively. The signal from each sample was collected at fixed analyzer transmission (FAT) mode. Pass energy is 188 and 23 eV for survey and narrow scans respectively. Binding energy was referenced to the carbon 1s orbital signal at 285 eV. The nanoparticle powder was pressed on a 3 x 3 mm indium foil or carbon tape for measurement.

2.2.4.7 Excitation and emission profiles

The excitation and emission spectra for the tiopronin-derivative capped gold nanoparticles were acquired with a Horiba-JobinYvon Fluorolog-3 spectrophotometer equipped with a 450W xenon arc lamp and a R928P detector operated at room temperature. The five aqueous solutions of nanoparticles were freshly prepared and gave an absorbance of 0.3 at 520 nm. The excitation and emission slit width were 4 nm and a cut-off filter of 550 nm was always placed between the sample and detector to eliminate the scattering of light.

2.3 Results and discussion

2.3.1 Synthesis of gold nanoparticles capped with tiopronin derivatives

When the tiopronin-derivatives capped gold nanoparticles were synthesized according to Murray's protocol,[168] the colourless gold-thiolate solution formed turned immediately to deep tanned brown colour once the borohydride solution was added. This is similar to that reported for Au@tiopronin. However, when acid was added to the crude nanoparticle residue tor protonating the terminal carboxyl group of the bound ligands, while Au@MBG and AuMPA still gave a clear deep tanned solution, the crude Au@MPP and Au@MPL precipitated out as brown fluffy solid when the solution became acidic. Both of these two fluffy solids can be redissolved in alkaline solution completely and be precipitated from and dispersed again into aqueous phase through alternate addition of acid and base. Since MPP and MPL both contain a bulky hydrophobic structure near their terminal carboxyl group, the carboxyl groups of any excess ligands entrapped in the monolayer and of bound thiols may then be shielded from the surrounding medium and form an extensive network through hydrogen bonded carboxylic group when there is a high proton concentration[169] in solution. This may lead to poor solvation of the nanoparticles and caused precipitation.

The MPEG/$HAuCl_4$ solution gave a dull tanned colour for a very short while after a few drops of borohydride solution were added. Upon more reductant solution was added, the colour of reaction mixture turned reddish and finally some black precipitates were formed. The precipitates can hardly be re-dissolved in any solvents. Therefore, the as formed 'Au@MPEG' was not further investigated.

2.3.2 Purification of gold nanoparticles formed

The nanoparticles passivated by MBG and MPA remained stable in the entire dialysis process. Both of these two nanoparticle solutions remained clear and tanned in colour. After lyophilic treatment, spongy brownish black solid formed. These solids can be re-dispersed in water promptly to give a clear tanned solution again.

Au@MPP, as mentioned in the previous section, precipitated out when the crude nanoparticle residue was acidified with hydrochloric acid. During dialysis of this colloid suspension against DDI water, the precipitates slowly dispersed back into water inside the tubing. When the DDI water outside was changed periodically within the three day period, dispersion of nanoparticles became more obvious. Finally, nearly all Au@MPP particles were re-dispersed to produce a clear tanned solution, the same as that for Au@MBG and Au@MPA. Lyophilizing this nanoparticles solution gave also a spongy brownish black solid which can be re-dispersed in water easily to yield a clear brown solution. The precipitation under highly acidic conidition may be due to the interaction of bound and unbound MPP in the self-assemble monolayer (SAM) on the nanoparticle surface. Since the resulting ‘clean’ Au@MPP did not precipitate out from a solution with pH 1 and large excess of sodium acetate, a only possible reason to account for the observed coagulation of newly formed clusters is the presence of unbound MPP.

As discussed in section 2.2.4, Au@MPL can be purified by two different approaches. These two routes produced Au@MPL with very different solubilizing properties. The first approach (acid-base-ether) employed the concept of purifying the nanoparticles through ‘phase-transfer’. Au@MPL prepared with this approach can be dispersed in

organic solvents like diethyl ether and dichloromethane. The nanoparticles can be dispersed easily in aqueous medium when it was made basic and coagulated once the solution was made acidic (≤ pH 3). Coagulated particles can be transferred into the ethereal phase completely. A brownish clear solution was obtained regardless whether the particles were dispersed in ether or an alkaline solution. After several times of 'phase-transfer' wash followed by acid precipitation, a brown-black solid was obtained. It can be re-dissolved readily in organic solvents like ether, dichloromethane and methanol but not in pure water.

The second approach (base-acid-water-dialysis), however, yielded Au@MPL with very different solublizing properties compared to the first method. In the beginning, the crude particles were also not dispersable in strongly acidic solution. When these crude colloids were dialysed in a basic condition, the particles were in the solublized form and gave a clear tanned solution throughout the process. No significant coagulation was found. After prolonged basic solution dialysis, acid was added to protonate the carboxyl groups of the passivating ligand. Precipitation of particles was not observed. The purified Au@MPL can be lyophilized to give fluffy brown-black solid similar to other tiopronin-derivatives capped gold nanoparticles.

As MPL has a relatively low solubility in water, the coagulation of newly-formed Au@MPL may be due to the presence of unbound MPL entrapped in the monolayer on the surface of the particles. The interaction between ligands, together with the low solubility of MPL in water, make the departure of unbound ligand difficult.

The high solubility of the unbound MPL-entrapped Au@MPL in non-polar solvent, like

diethyl ether, may also be attributed to the strong interaction between carboxyl groups. At low pH, the protonated carboxyl groups on bound and unbound MPL interacted strongly through hydrogen bonding. This largely reduced the amount of carboxyl groups available for solvation. The more exposed hydrophobic isopropyl group in the leucine residue then became more accessible towards the solvent molecules instead, making the nanoparticles to exhibit a hydrophobic behavior.

When the solution pH was raised, the particles could be dispersed freely in water. This may be due to the negative charges contributed by the deprotonated carboxyl groups. Based on this observation, it is believed that using an alkaline solution for dialysis can liberate any free MPL ligands entrapped in the monolayer and finally out of the dialysis tubing. After a long period of alkaline solution dialysis, the Au@MPL nanoparticles were found to remain dispersible even if the solution was made to a pH $\leq$ 1. This supports the above postulation for the hydrophobic properties of Au@MPL purified by the first approach.

2.3.3 UV-visible spectroscopy

UV-visible spectroscopy was employed to investigate the surface plasmon of the gold nanoparticles passivated with the tiopronin-derivatives. The tanned colour of all derivative capped nanoparticle solutions, which is a result of light scattering by the clusters, indicates that they do not possess a surface plasmon resonance (SPR) absorption (~520 nm). From the UV-visible spectra obtained (Figure 2.5), the absence of SPR peak is consistent with the solution colour. Absorption remained low beyond 650 nm, but it increased gradually from 650 nm to 450 nm and abruptly when in the spectral region < 450 nm. The UV-visible spectra for all nanoparticles are in general featureless. These information suggested that the tiopronin-derivative capped gold nanoclusters should fall within the size range of 1.4 - <3 nm.[170,171]

The stability of the tiopronin-derivative capped gold nanoclusters in different concentrations of monovalent cation salt solution was investigated by UV-visible spectroscopy, as some nanoparticles are sensitive to electrolyte concentration and precipitated out at high salt content which would cause changes to their SPR band. According to the Hofmeister series[172] which has long been used to correlate the aggregation or stabilization behavior of colloids in aqueous solution, some common cations are placed in order based on their degree of hydration as follows:

$$NH_4^+ > Cs^+ > Rb^+ > K^+ > Na^+ > H^+ > Li^+ \sim Ca^{2+} > Mg^{2+}$$

(Chaotropic cations) (Kosmotropic cations)

Chaotropic cations, due to their low hydration ability, tend to disrupt the ordered water

structure at the local particle surface[173] which leads to the coagulation of colloids in aqueous phase. In the above series, cesium, sodium and lithium ion represent cations possessing different degree of hydration, so their chloride salts were used in our investigation. All the tiopronin derivative capped gold particles were placed in the aqueous solution of the above three salts over the concentration range of 5 x 10^{-4} to 5 M. The change in the absorbance at 525 nm of their respective UV-visible profile were recorded and plotted against salt concentration (Figures 2.6 – 2.8).

The UV-visible spectra of all tiopronin-derivative capped nanoparticles remained featureless over the spectral range of 400 – 1000 nm (not shown). No emergence of surface plasmon peak, a strong indicator of particles coagulation, was observed over the entire concentration range. No visible change to the tanned colour and solution turbidity were noted. The absorbance at 525nm dropped only slightly as the salt concentration increased.

It can be seen that all tiopronin-derivative capped nanoparticles showed a very good stability towards a wide electrolyte concentration range. They also exhibited a high tolerance towards the chaotropic cations like cesium.

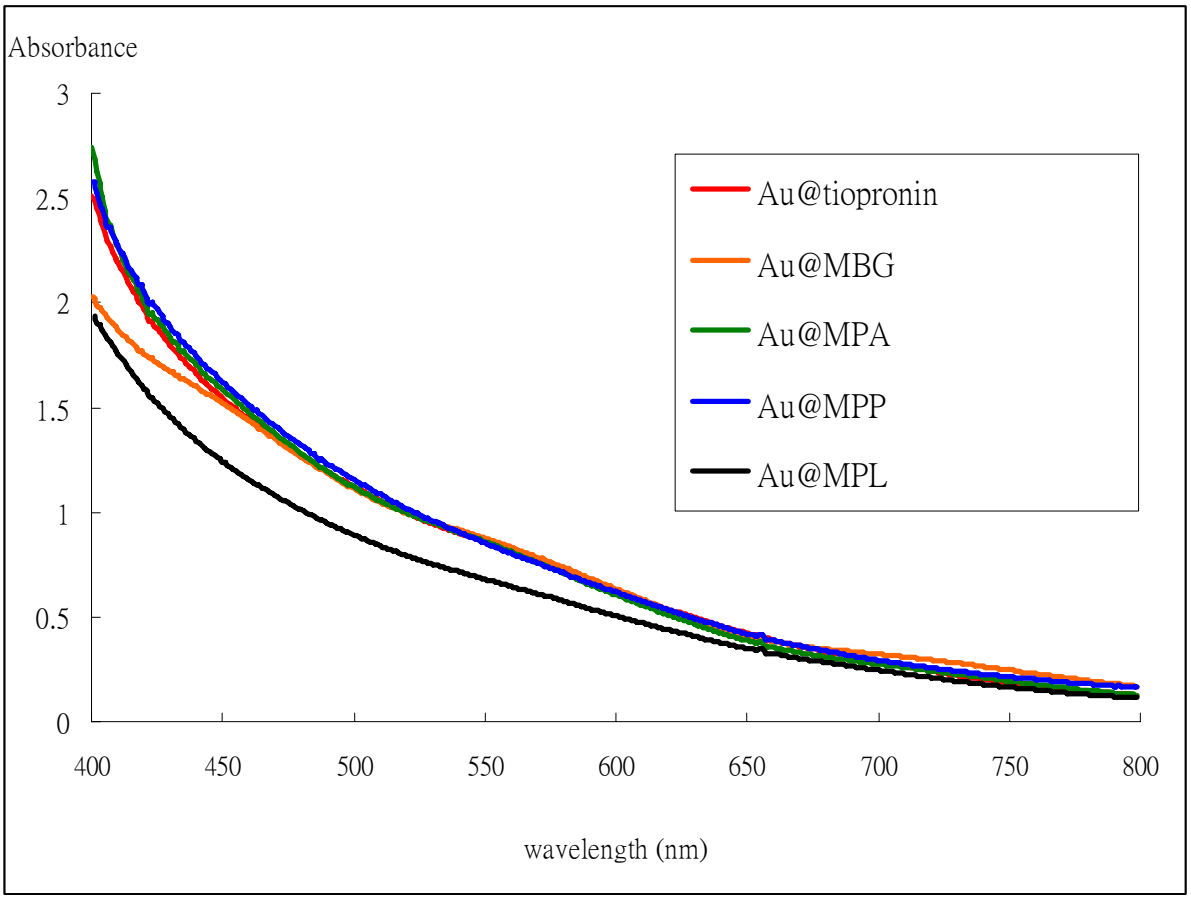

Figure 2.5 UV-visible spectra for Au@MBG, Au@MPA, Au@MPP, and Au@MPL (Au@MPL was prepared by base-acid-dialysis purification)

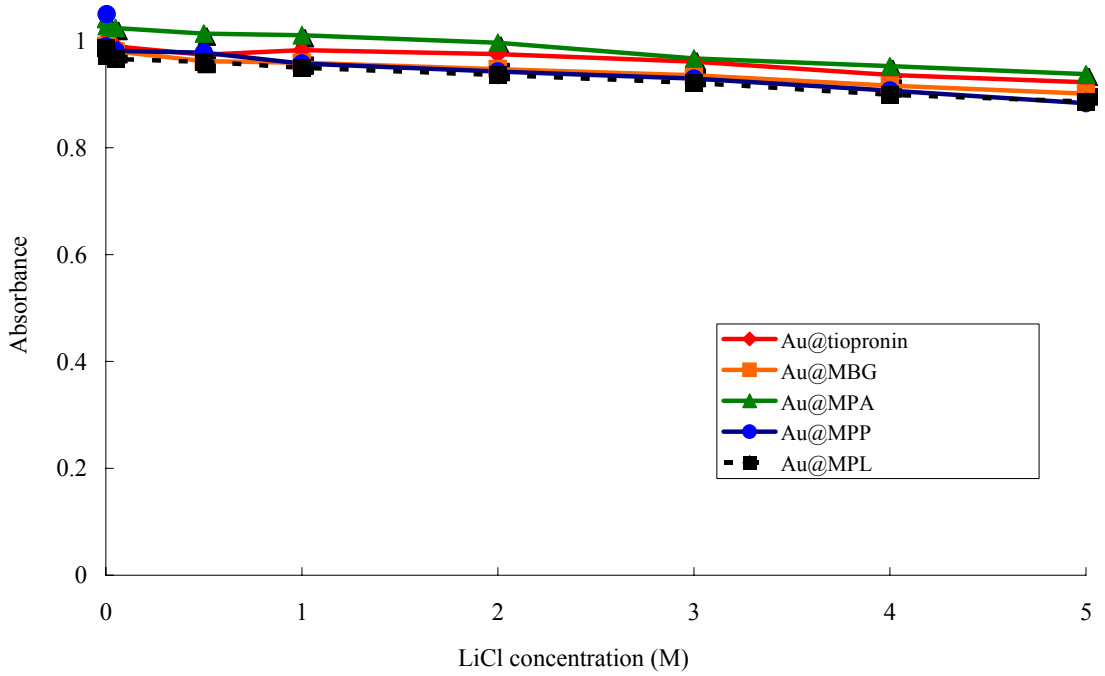

Figure 2.6 The influence of lithium ion concentration on the stability of thetiopronin-derivative capped gold nanoparticles in aqueous solution.Au@MPL was prepared by base-acid-water-dialysis. (Absorbancemonitored at 525 nm, no significant SPR band observed at this wavelength)

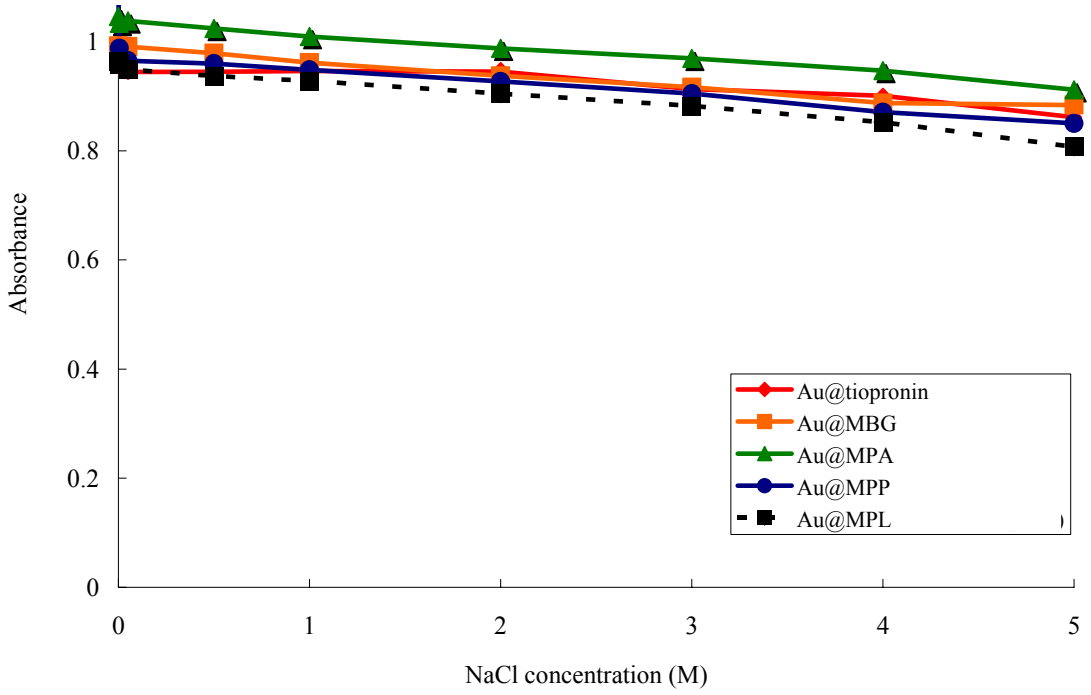

Figure 2.7 The influence of sodium ion concentration on the stability of the tiopronin-derivative capped gold nanoparticles in aqueous solution. Au@MPL was prepared by base-acid-water-dialysis. (Absorbance monitored at 525 nm, no significant SPR band observed at this wavelength)

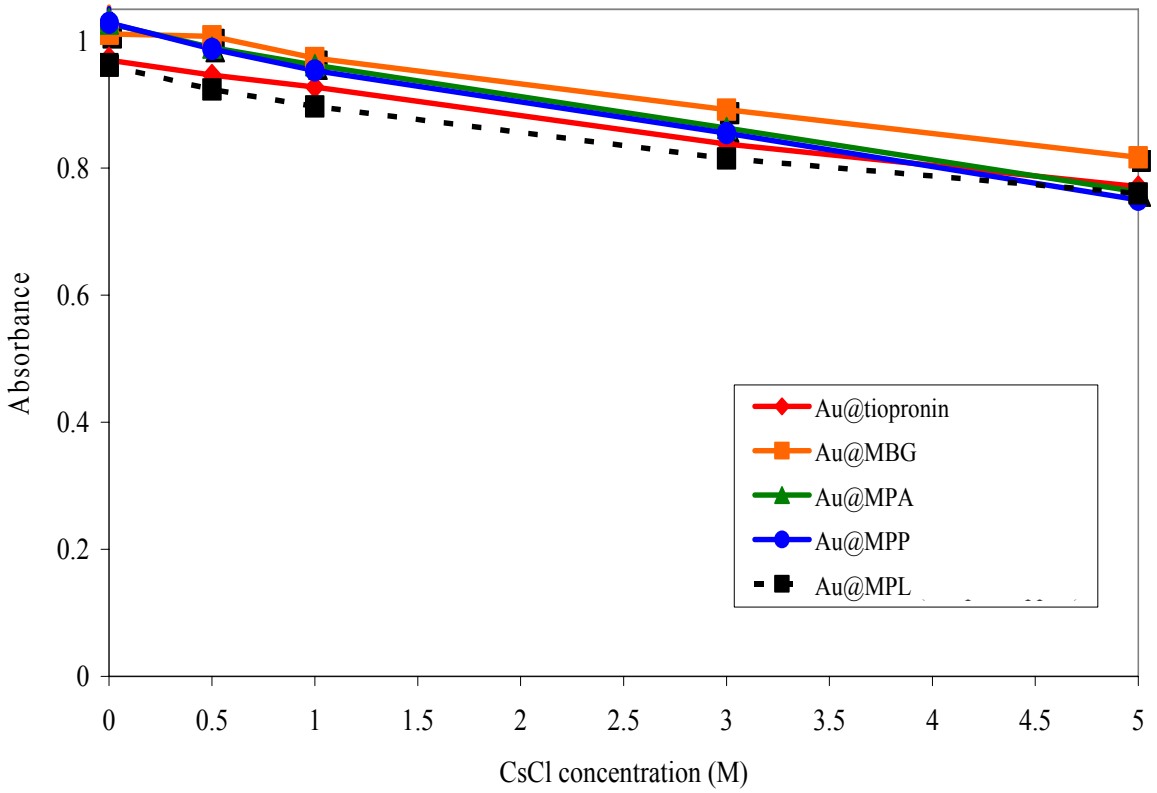

Figure 2.8 The influence of cesium ion concentration on the stability of the tiopronin-derivative capped gold nanoparticles in aqueous solution. Au@MPL was prepared by base-acid-water-dialysis. (Absorbance monitored at 525 nm, no significant SPR band observed at this wavelength).

2.3.4 Transmission electron microscopy (TEM)

Transmission electron microscopic images and the size distributions (Figures 2.9 – 2.12) of all tiopronin-derivative capped nanoparticles were obtained. It was found that all tiopronin derivatives gave spherical gold nanoparticles with an average size of 1.8 – 2.0 nm. The size distribution of the particles remains quite narrow. All these size-characteristics are highly similar to the Au@tiopronin system and are consistent with the UV-visible spectra obtained.

Figure 2.13 shows the TEM image of the Au@MPL nanoparticles dispersed in diethyl ether after the acid-base-ether purification. It was found that their size and distribution are very similar to those prepared through the base-acid-water-dialysis purification approach.

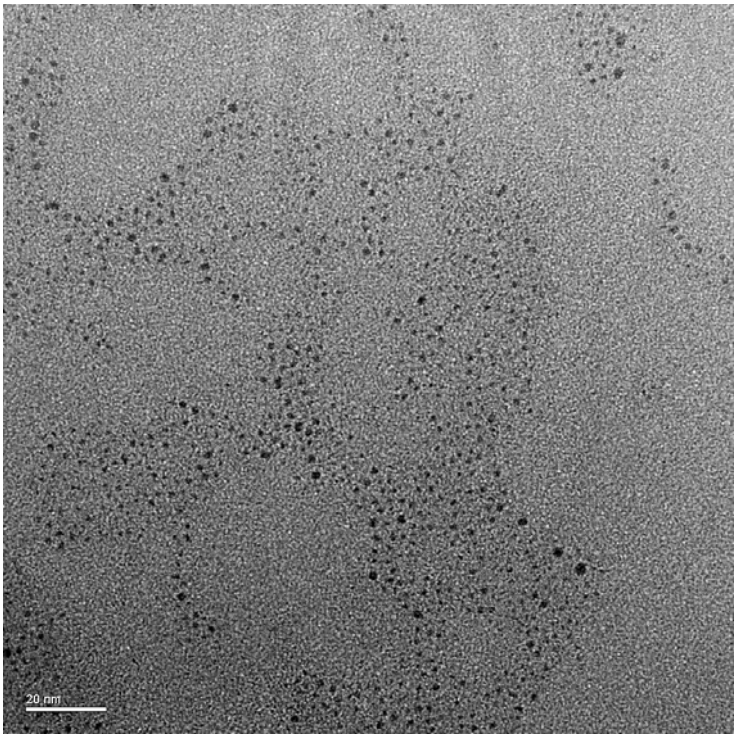

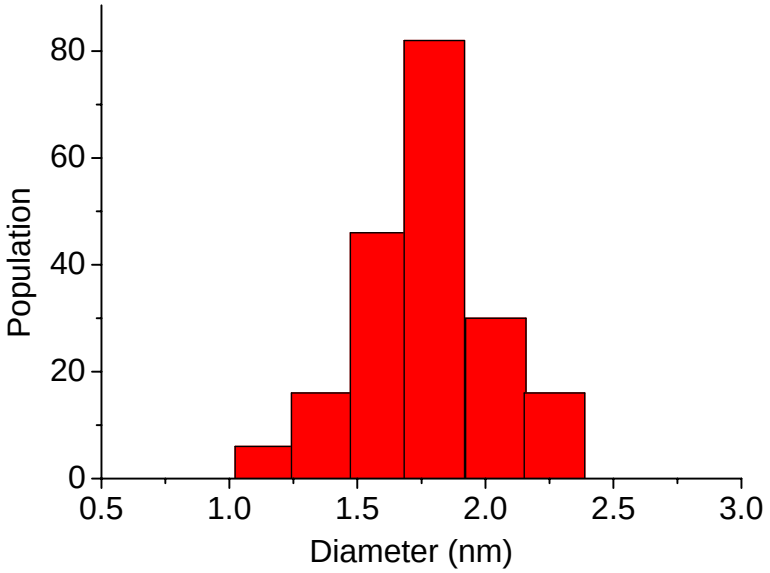

Figure 2.9 Transmission electron microscopic image and size distribution of Au@MBG (1.8 +/- 0.6 nm)

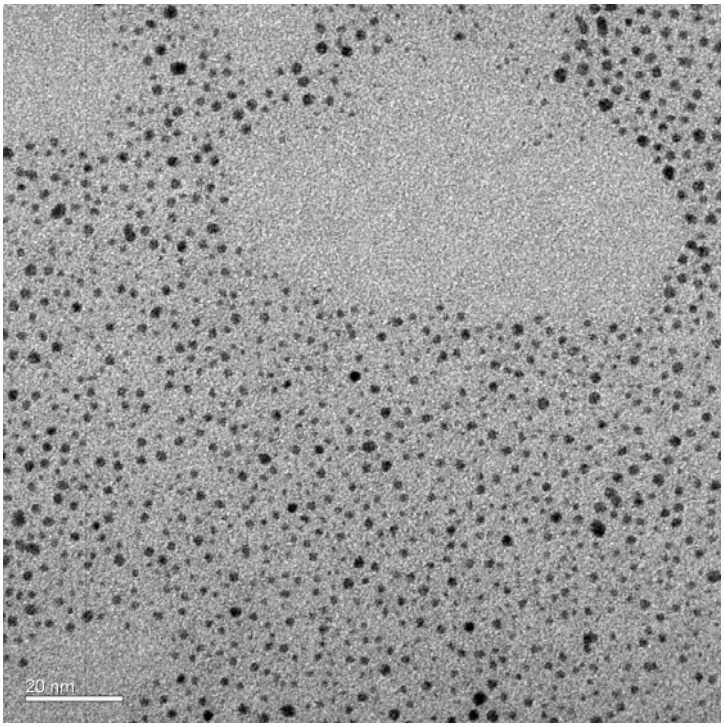

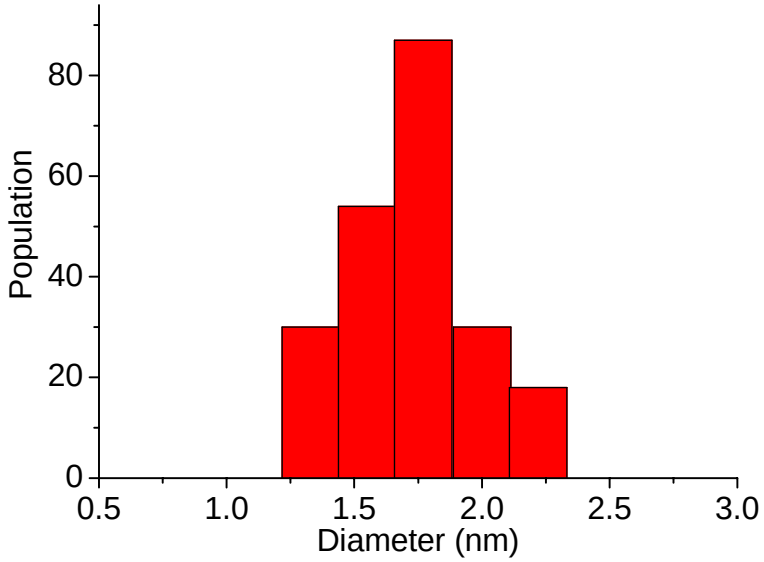

Figure 2.10 Transmission electron microscopic image and size distribution of Au@MPA (1.8 +/- 0.6 nm).

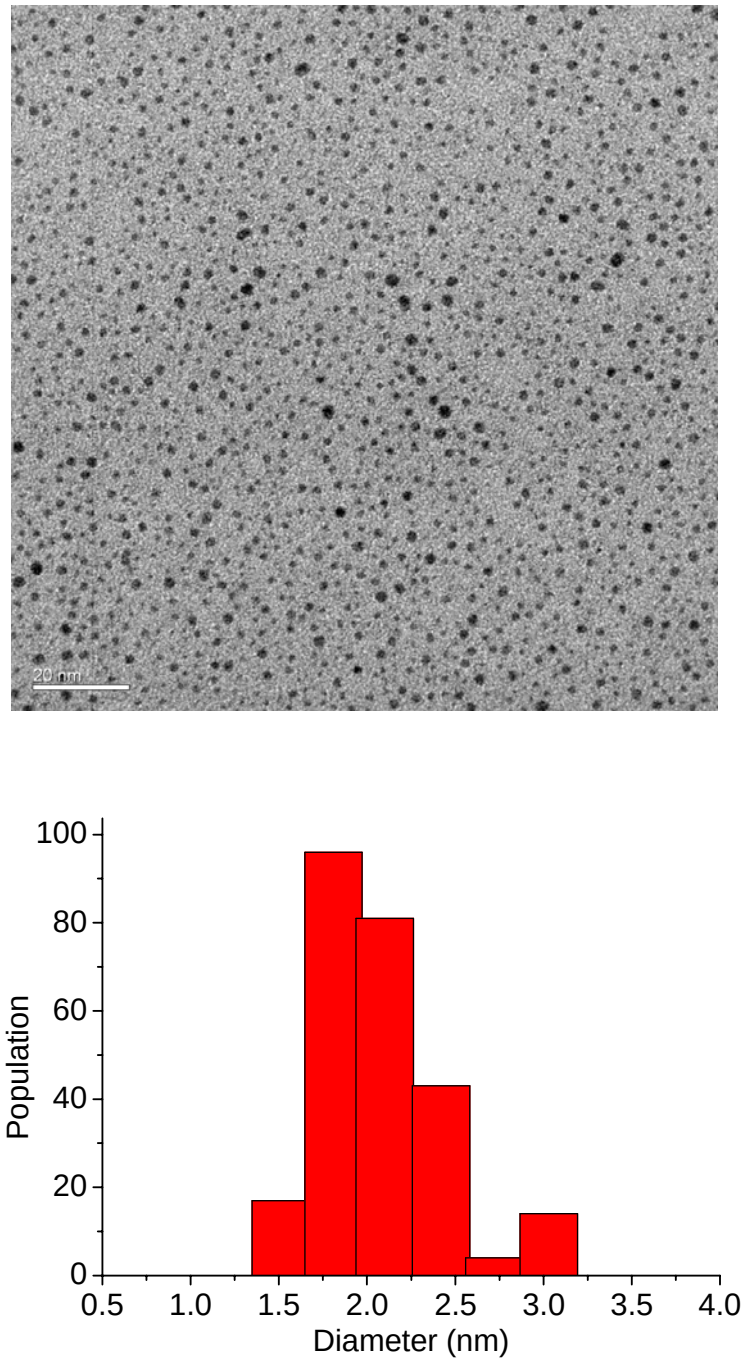

Figure 2.11 Transmission electron microscopic image and size distribution of Au@MPP (2.0 ±0.6 nm).

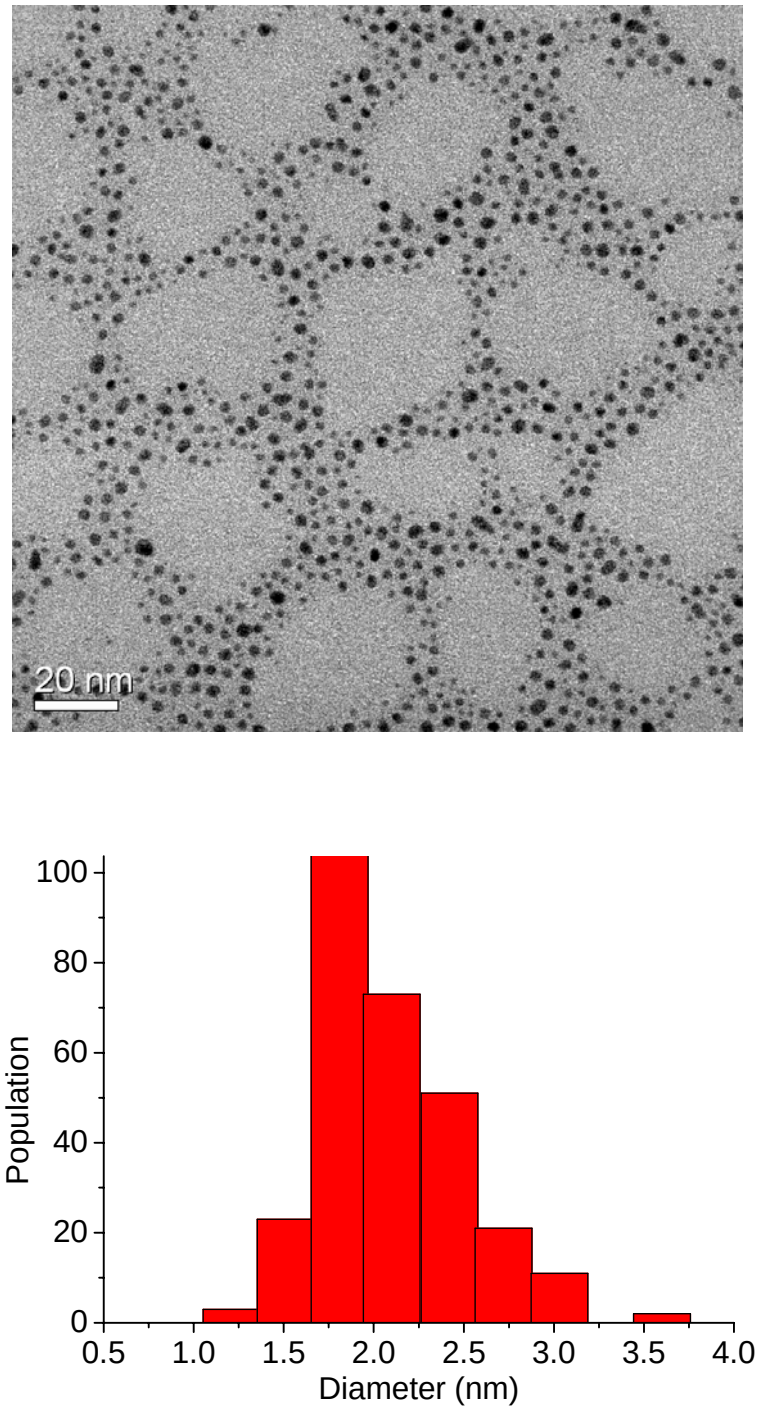

Figure 2.12 Transmission electron microscopy image and size distribution of Au@MPL purified by base-acid-water dialysis (2.0 +/- 0.8 nm).

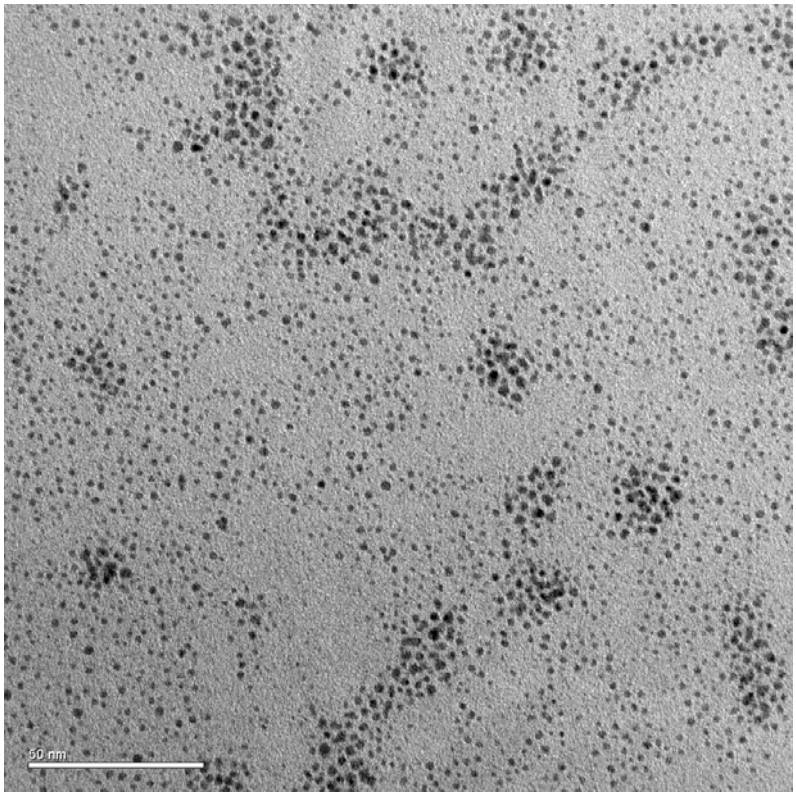

Figure 2.13 Transmission electron microscopic image for Au@MPL purified by repetitive acid-base-diethyl ether wash (acid-base-ether purification). The nanoparticles were dispersed in diethyl ether after purification and a drop of this solution was put onto the copper grid

2.3.5 Nuclear magnetic resonance (NMR) spectroscopy

The nuclear magnetic resonance spectra for the gold nanoparticles in deuterated water clearly demonstrated the successful attachment of the tiopronin-derivative ligands to the surface of the nanoparticles (Figures 2.14 – 2.18). The spectra of nanoparticles consist of broad peaks appearing at chemical shifts similar to the corresponding free ligands. The emergence of broad signal instead of a distinct and sharp peak can be attributed to the huge magnetic field inhomogeneity at local chemical environment (like terrance, edge, vertex)[174] where the capping ligands are located. Therefore, a distribution of chemical shift was found. Meanwhile, peaks corresponding to those protons which located in close proximity to the gold surface were highly suppressed. This is especially apparent for the methine proton bound directly to the thiol group linked sp^3 carbon. All NMR spectra for the particles showed no sharp peaks, an indication of the absence of free thiols. This suggested that the nanoparticles obtained after dialysis are of high purity.

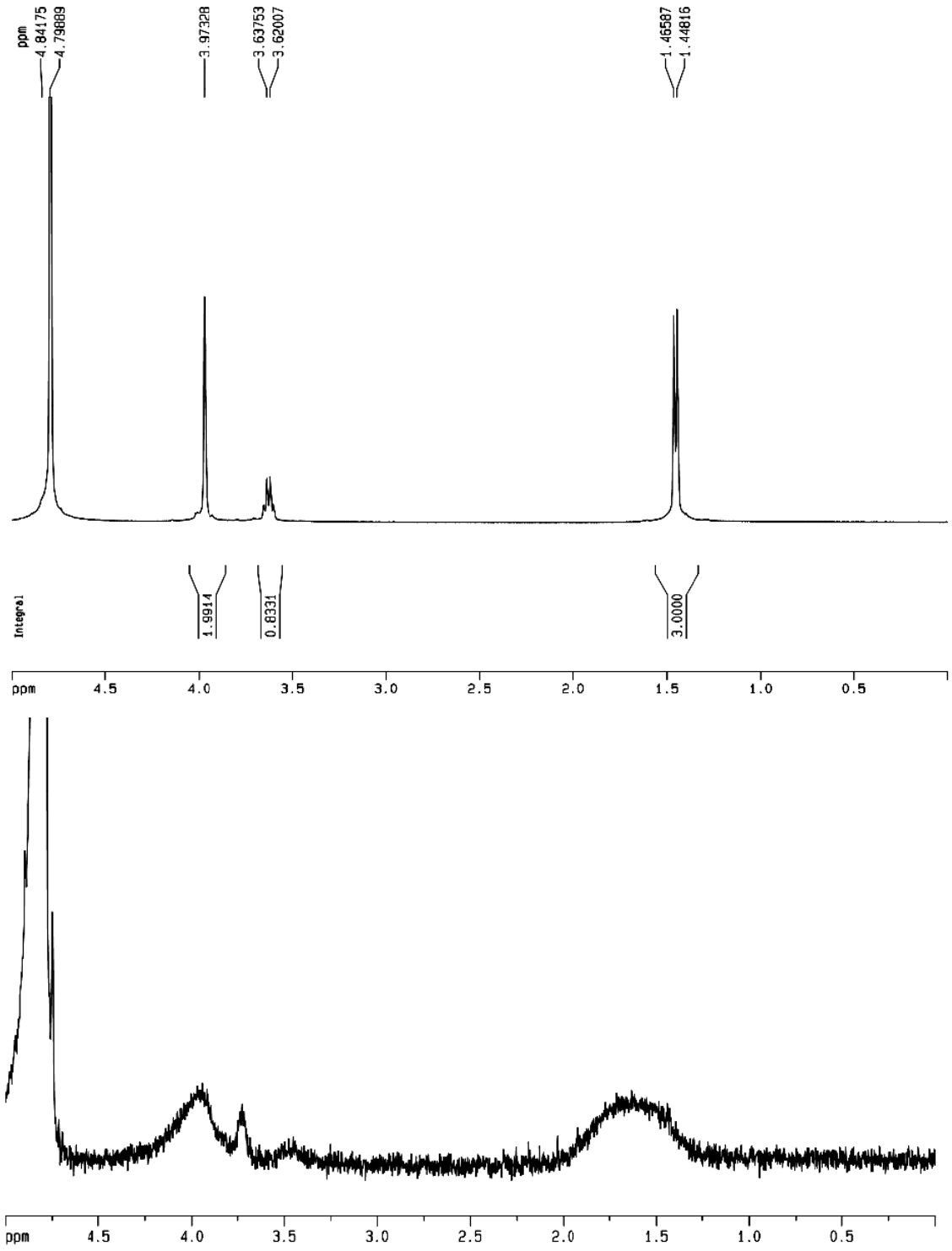

Figure 2.14 [1]HNMR spectrum for (top) tiopronin and (bottom) tiopronin-capped gold nanoparticles Au@tiopronin.

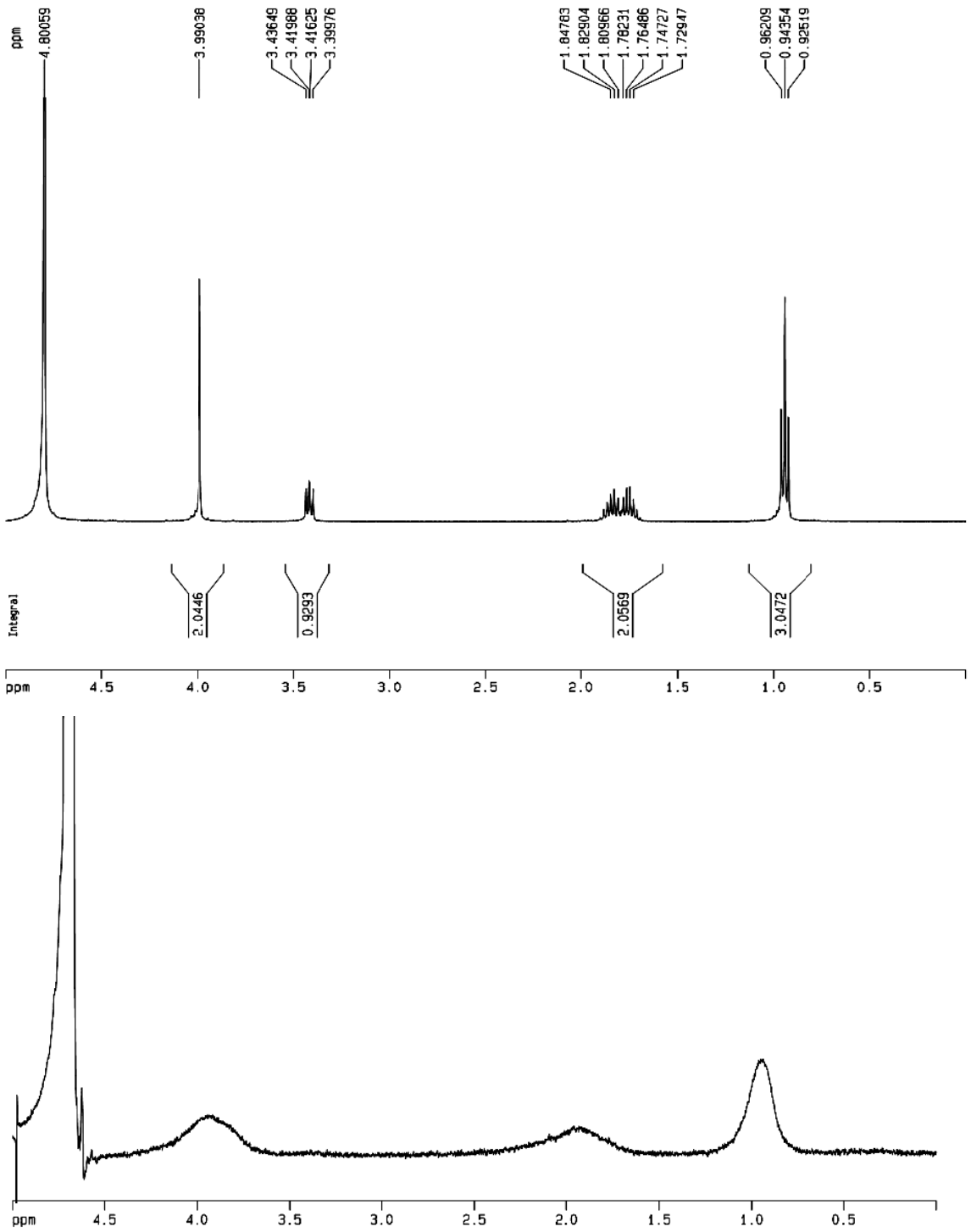

Figure 2.15 ^{1}H NMR for (top) 2-mercaptobutanoyl glycine (MBG) and (bottom) 2-mercaptobutanoyl glycine capped gold nanoparticles (Au@MBG).

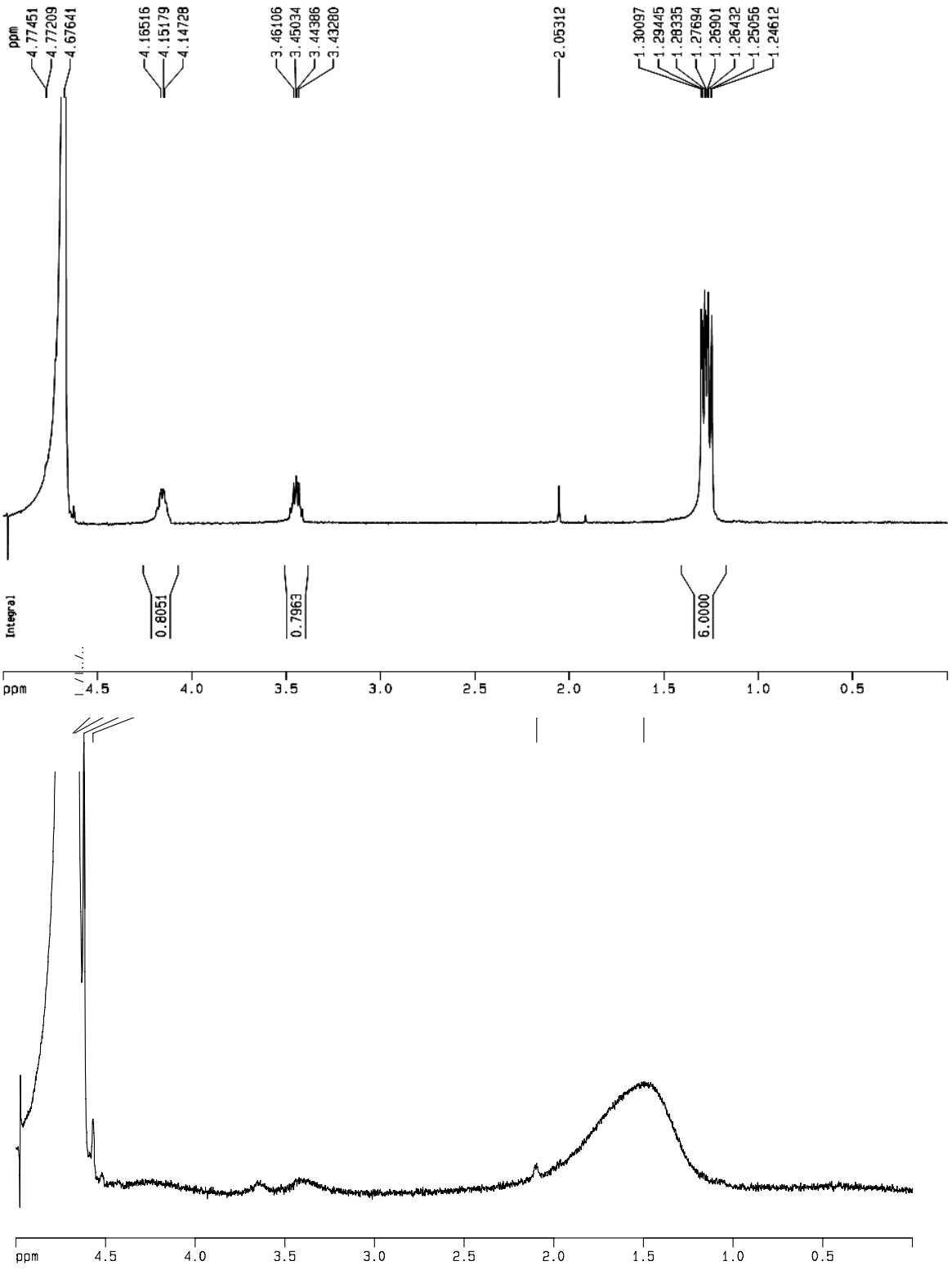

Figure 2.16 ^{1}H NMR for (top) 2-mercaptopropionyl alanine (MPA) and (bottom) 2-mercaptopropionyl alanine-capped gold nanoparticles (Au@MPA).

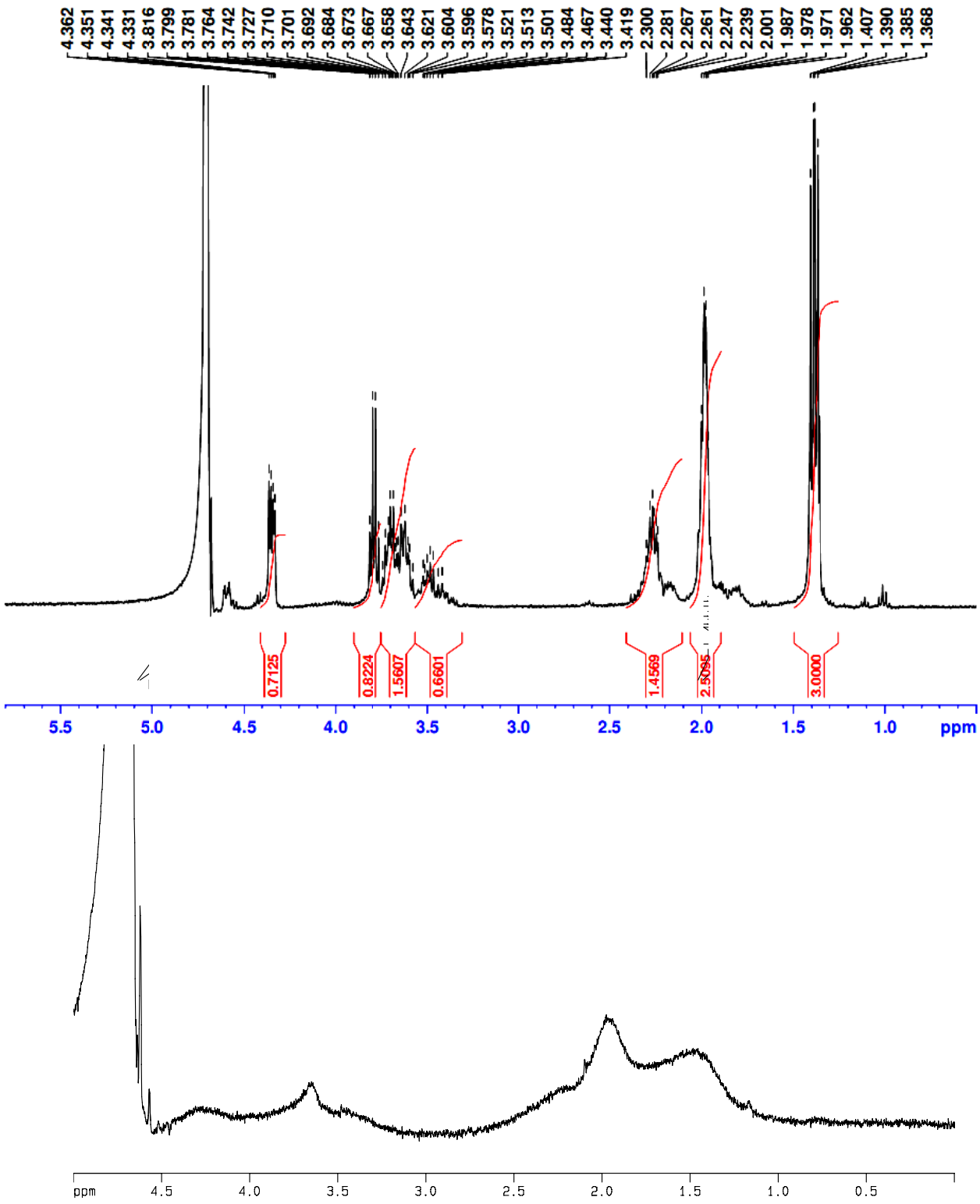

Figure 2.17 ^{1}HNMR spectrum for (top) 2-mercaptopropionyl proline (MPP) and (bottom) 2-mercaptopropionyl proline capped gold nanoparticles (Au@MPP).

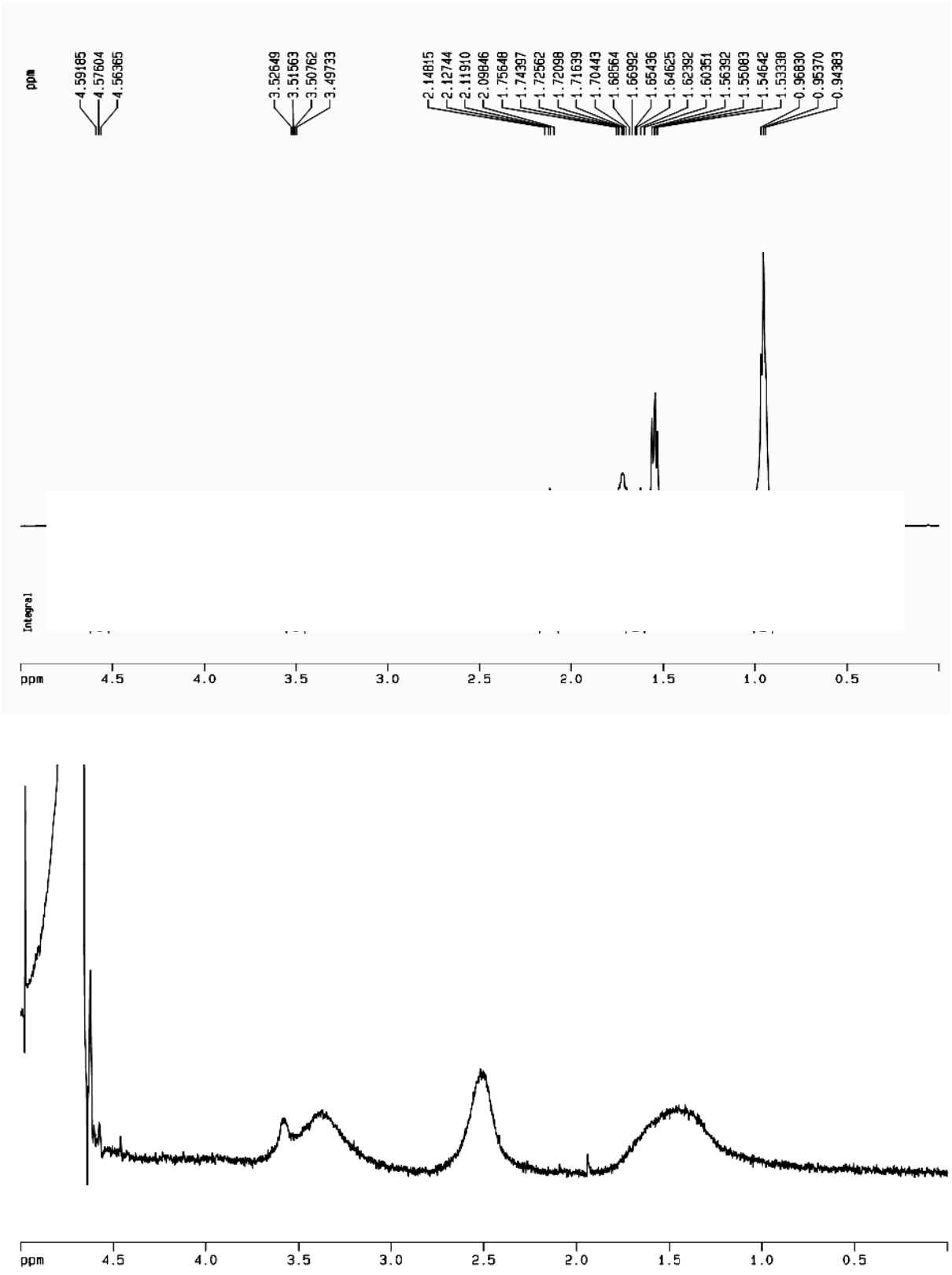

Figure 2.18 ^{1}H NMR for (top) 2-mercaptopropionyl leucine (MPL) and (bottom) 2-mercaptopropionyl leucine-capped gold nanoparticles (Au@MPL).

2.3.6 Thermogravimetric Analysis (TGA) / Differential Scanning Calorimetry (DSC)

Thermogravimetric analysis and differential scanning calorimetry can provide information on the organic content, phase-transition, and organization events of the materials tested. For self assemble monolayer (SAM) protected nanoparticles, they provide information on the intra- and intermolecular interaction and the arrangement of surface-bound ligands

Figures 2.19 to 2.24 and Table 2.1 show the TGA and DSC profiles and a summary of the mass loss of all the tiopronin-derivative capped gold nanoparticles. The loss in mass (<100%) for most samples at 50 – 100℃ corresponds to the removal of accompanied moisture in the sample. The DSC profile for all samples at 50 – <200℃ gave a very small but sharp endothermic peak. Taking the Au@tiopronin system as reference, similar tiny sharp projection from the DSC profile baseline at this temperature (Figure 2.19) represents the melting of the crystalline region[175] which is close to the normal melting point of the tiopronin (93 - 98℃). Since the TGA profile showed almost no change at the same temperature zone, melting transition is very likely to be the explanation for the observed small endothermic peak. When moved beyond 200℃, a sudden drop in sample weight occurred (first stage mass loss). The process occurred promptly over a short temperature range. However, even when such a large change in mass occurred, the heat transfer to the sample, as reflected by the DSC profile, was quite small. In general, there is a correlation between the TGA and DSC active events, so a considerable heat change is expect to appear when apparent decomposition

occurs.[175] The discrepancy may be explained by that the DSC measurement was carried out at the same time as the TGA process under normal air atmosphere. The heat released from the oxidative decomposition of the carbonaceous content in air may be taken for sustaining the spontaneous destruction event. Therefore, no net heat flow was observed. Meanwhile, for nanoparticles capped by structurally complicated derivatives like MPP and MPL, the DSC profiles are significantly different from those capped with MPA, MBG and tiopronin. The DSC profile of Au@MPP and Au@MPL showed less abrupt (always less than -3 mW / mg) but more complicated changes.

As the temperature increased, the gold nanoparticles capped with MBG and MPA showed an extremely sharp and intense peak in their DSC profile. This sudden change coincides with the second sudden drop in mass content period of the sample (second stage mass loss). The mass change in this temperature region for nearly all candidates (with the exception of lower value of ~ 11 % for Au@MPP) is around 25 – 33 %, which matches quite closely to the weight fraction of the amide linkage (20 – 26%) relative to the total molecular weight of the respective derivative ligand. The second sharp decrease in TGA profile is therefore interpreted as the destruction of amide bond. Amide linkage is well known for its ability to form extensive hydrogen bonding. The close proximity of derivative molecules in the SAM leads to a strong hydrogen bond cross-liked network. Therefore, a higher temperature (~ 500 ℃) for its demolition was observed in all particles studied. The enhanced endothermic heat change as shown by the very sharp and high intensity peak in DSC profile further support the breakage of the strongly interacting amide moiety.

The Au@MPL purified with acid-base-ether purification approach yielded particles

with 57% higher in organic content than those purified with the base-acid-water dialysis approach. This further supports that the organic solubility of Au@MPL purified by phase-transfer acid-base-ether wash in section 2.3.2 is caused extra ligand entrapment in the SAM on the gold clusters' surface.

The average organic content of tiopronin-derivative capped gold nanoparticles is ~ 33.5%. Taking the average molecular weight of all derivative as 188, an average Au : S of the derivatives capped gold nanoparticles equal to 1.89 can be obtained.

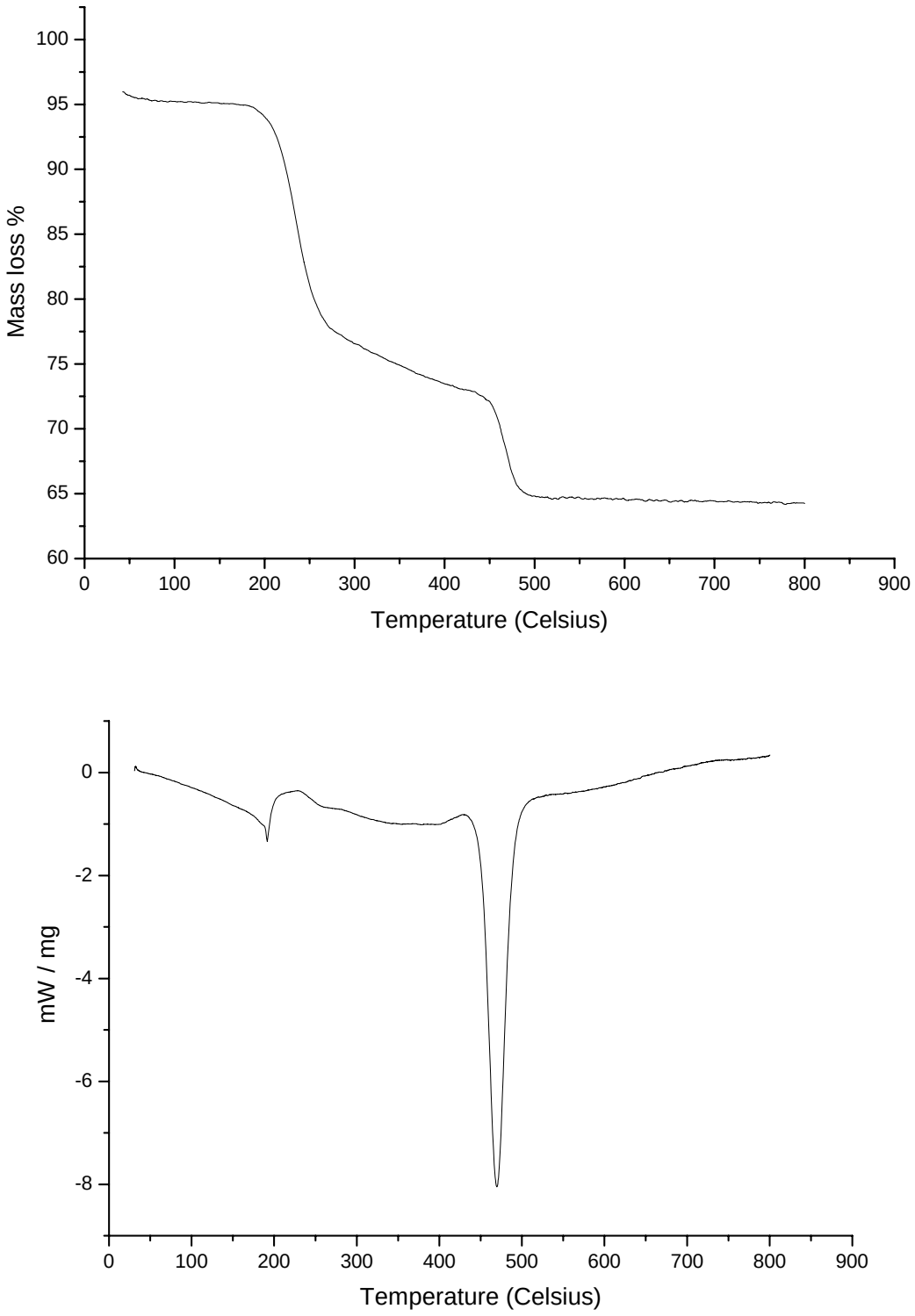

Figure 2.19 Thermogravimetric (top) and differential scanning calorimetric (bottom) profiles of Au@tiopronin.

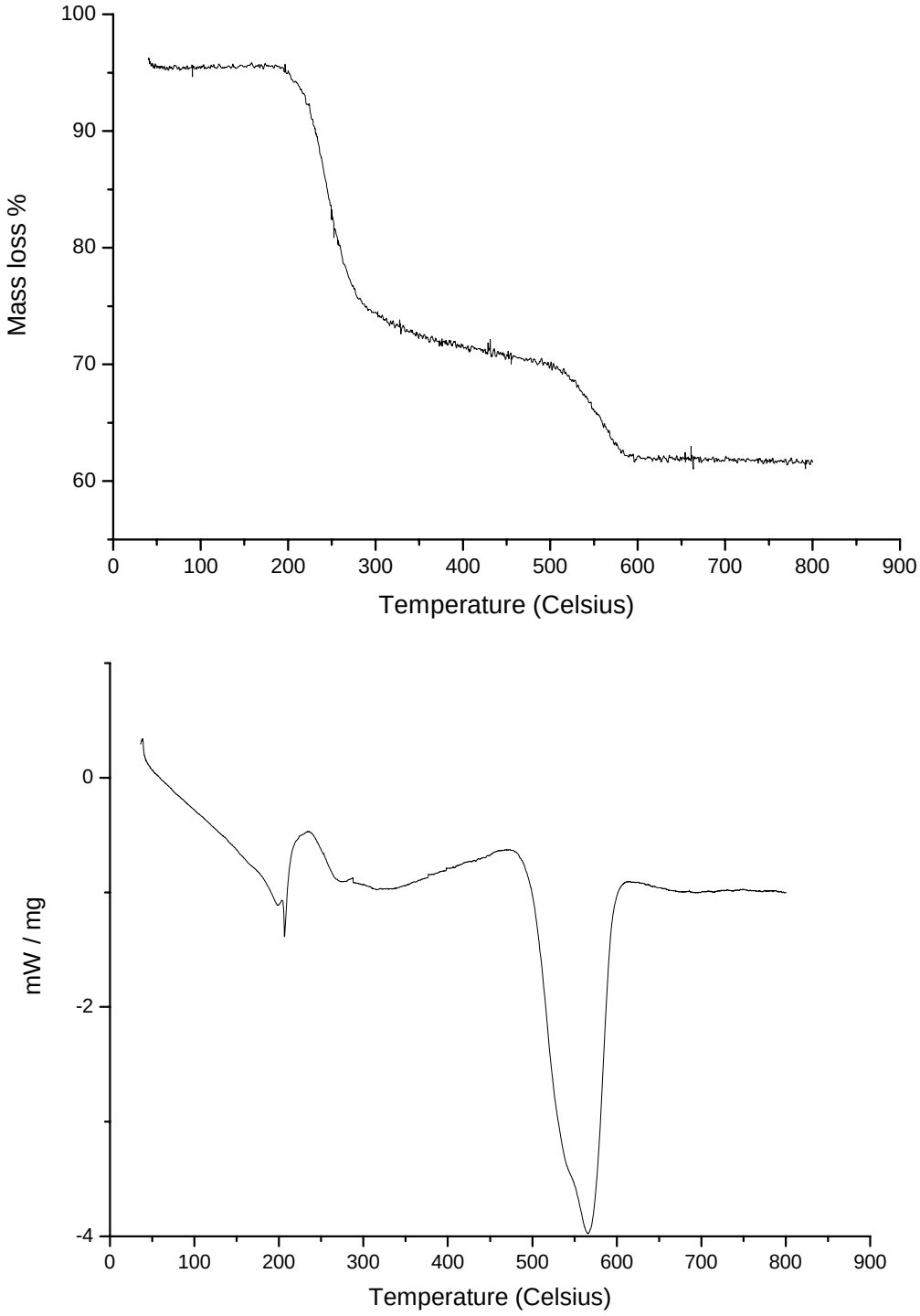

Figure 2.20 Thermogravimetric (top) and differential scanning calorimetric (bottom) profiles of Au@MBG.

.

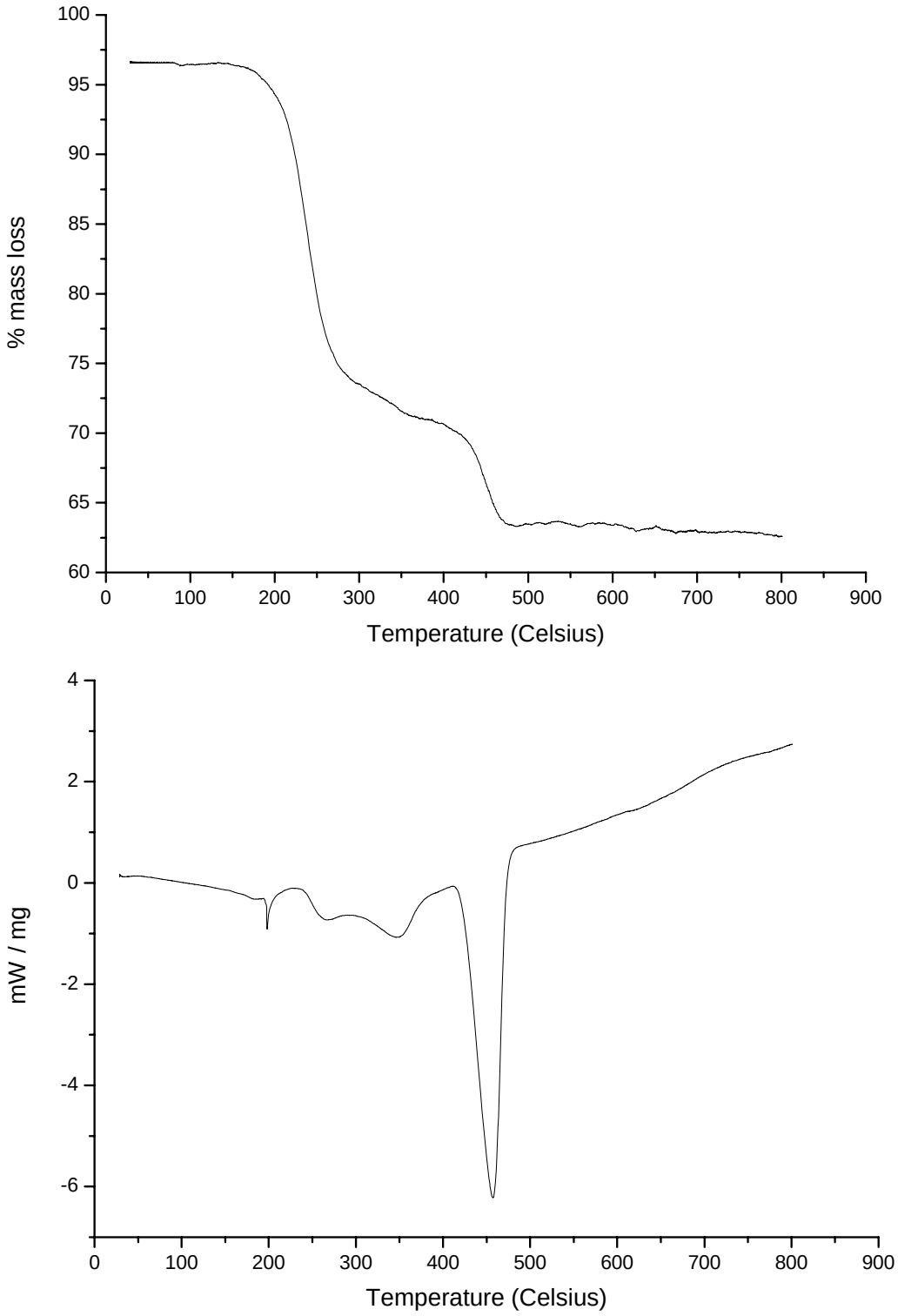

Figure 2.21 Thermogravimetric (top) and differential scanning calorimetric (bottom) profiles of Au@MPA.

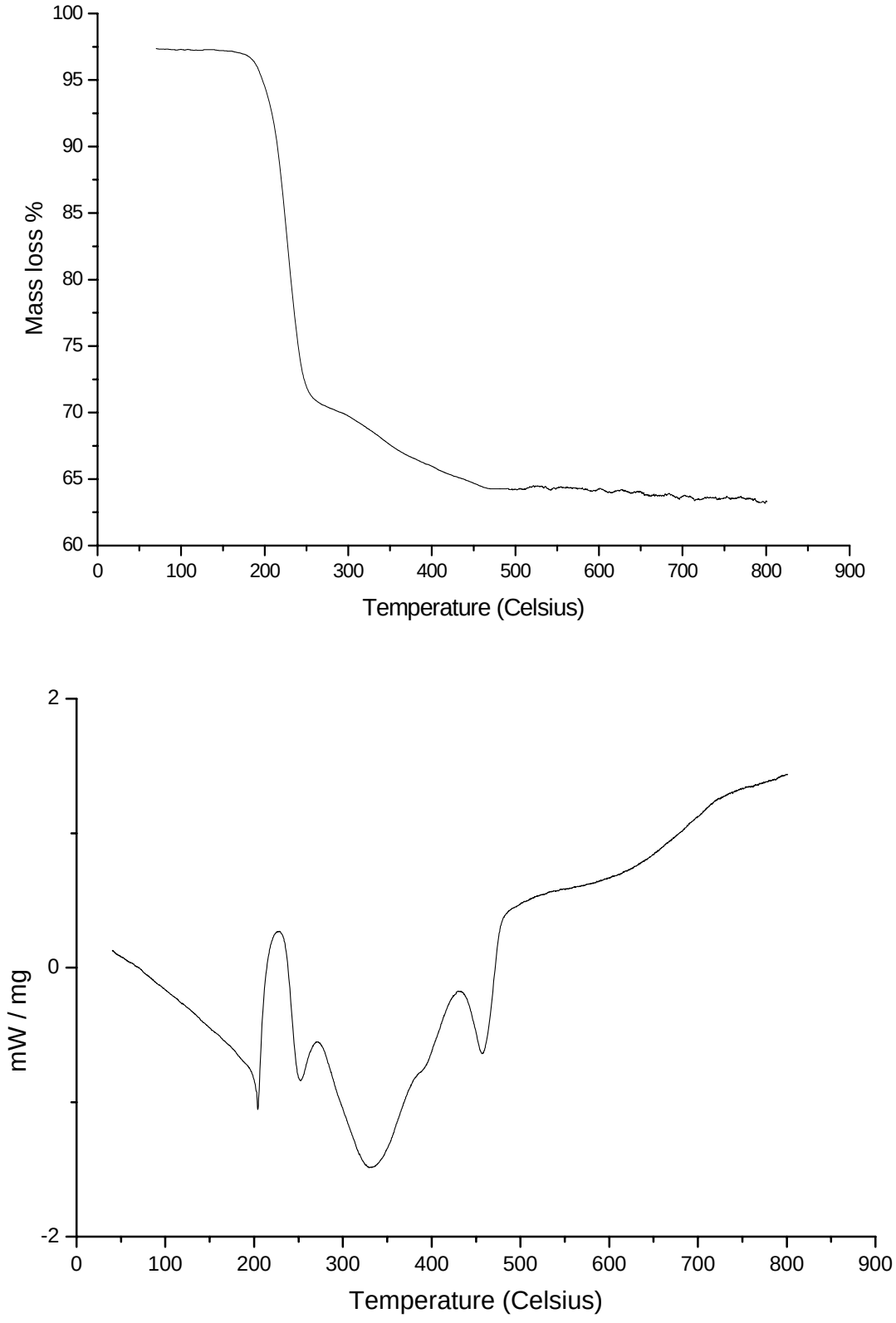

Figure 2.22 Thermogravimetric (top) and differential scanning calorimetric (bottom)profiles of Au@MPP.

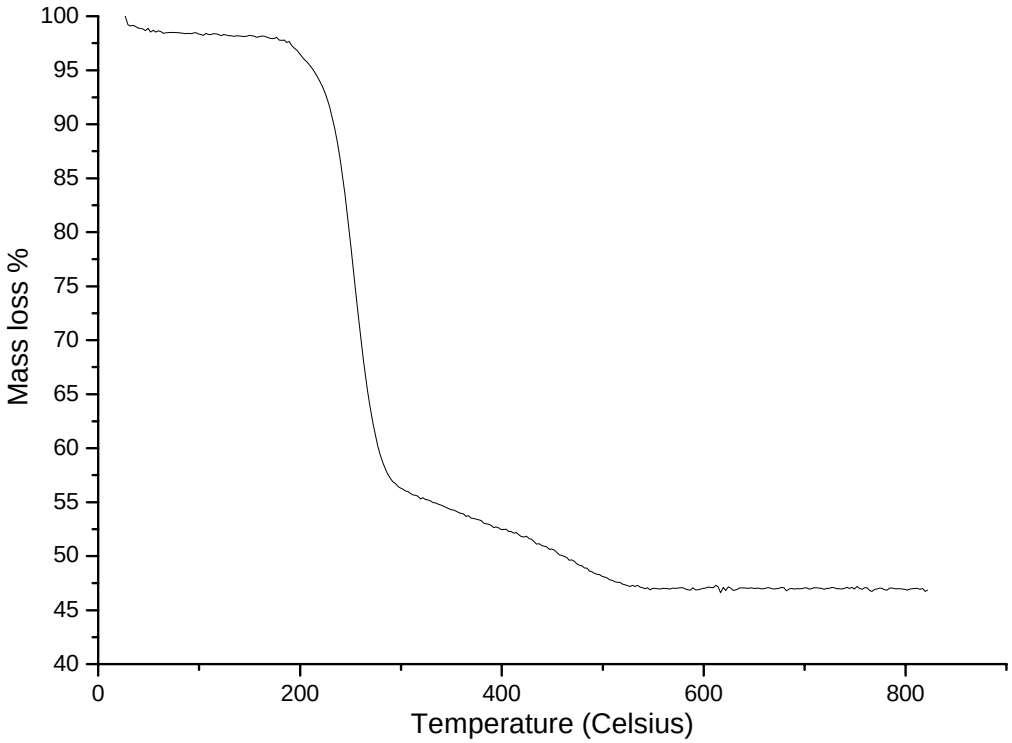

Figure 2.23 Thermogravimetric profile of Au@MPL purified by acid-base-ether approach.

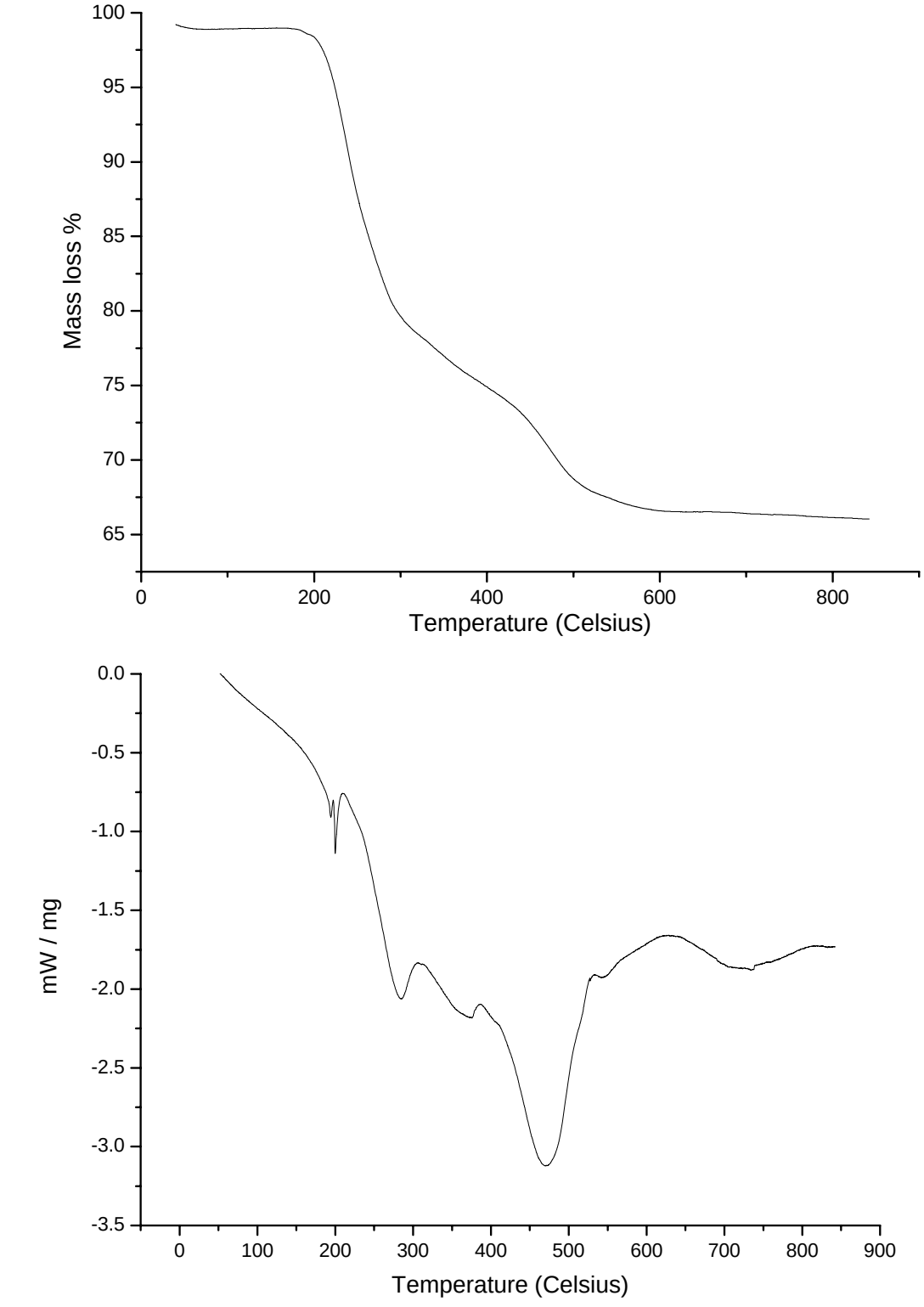

Figure 2.24 Thermogravimetric (top) and differential scanning calorimetric (bottom) profiles of Au@MPL (purified by base-acid-dialysis approach).

Table 2.1 Percentage mass loss of tiopronin-derivative capped gold nanoparticles at different stages and their total organic content (%).

[a] *First stage mass loss refers to the percentage of mass loss at the first significant mass drop period.*

Nanoparticles	Moisture (%)	Mass loss at first stage [a] (%)	Mass loss at second stage [b] (%)	Total organic content (%) [c]
Au@tiopronin	5	20	11 (33.7)	32.6
Au@MBG	4.5	23.5	10 (28.5)	35.08
Au@MPA	3.5	25	8.5 (24.5)	34.7
Au@MPP	3	30	4 (11.4)	35.05
Au@MPL (acid-base-ether)	1.8	46	5.3 (10.1)	52.2
Au@MPL (base-acid-water dialysis)	1	24	9 (27)	33.3

[b] *Second stage mass loss refers to the percentage of mass loss at the second significant mass drop period (the number in parenthesis refers to the fraction of mass loss (%) at second stage relative to total organic content).*

[c] *Total organic content calculated by: (first stage mass loss (%) + second stage mass loss(%)) / (100 – moisture content(%)).*

2.3.7 Infra-red spectroscopy

In order to investigate the interaction between the bound ligands in the nanoparticles, the IR spectra of the nanoclusters were obtained from the powdered particles as KBr disc or as a thin film aqueous solution (Figures 2.26 and 2.28). The attenuated total reflectance infra-red (ATR-IR) spectra for aqueous thin film solution are generally weaker in intensity and poorer in resolution. Spectra for the free ligands in their solid and dissolved form were also acquired as reference. (Figures 2.25 and 2.27 and Table 2.2)

The carboxyl C=O stretching (~ 1730 - 1760 cm^{-1}) for free ligands shifted to a lower frequency from solid to solvated form. Since extensive hydrogen-bonding exists between the free ligands and the water molecules in solution, lowering of the stretching frequency is expected. The carboxyl C=O bands of all ligands bound to the nanoparticles showed nearly the same stretching frequency regardless of whether the nanoparticles are in their solid or solvated form. Furthermore, the C=O stretching frequency for the surface bound and aqueous free ligands are very similar. Therefore, it is likely that the carboxyl groups are involved in hydrogen bonding in the SAM of the solid clusters. Similar observation has been reported for some synthetic oligo-peptides capped gold nanoparticles.[176] Another feature of the carboxyl groups in bound ligands is that they always exist as monomeric form. No dimerization, even when the nanoparticles are in solid state in which the carboxyl groups between different nanoparticles may be in close contact, was observed. This can be confirmed by their similar C=O stretching frequency which is close to the general monomeric carboxyl group (1724 cm^{-1}), rather than the dimeric counterpart (1683 cm^{-1}).

The IR spectra for solid free ligands differ from those anchored on nanoclusters in solid form. The sharp amide N-H stretching peak observed at ~ 3300 cm^{-1} in solid state ligands became very broad when they were attached to the gold nanoparticles. Together with the emergence of a small peak at ~ 3050 cm^{-1} in the spectra, which corresponds to the first harmonic N-H in-plane bending, the presence of extensive hydrogen bonding in solid derivatives capped gold nanoparticles can be confirmed.[177]

Previous study[176] on gold nanoparticles-bound-oligoamides indicated that the buried amide groups are not sensitive to the external medium polarity, and the amide I and II signals for the clusters exhibited no obvious shift even the nanoparticles were solvated in highly polar solvents like acetonitrile. Such phenomenon occurs only when there are several amide bonds found on a single ligand molecule as in oligoamide. Meanwhile, they should all be deeply buried and held strongly by intermolecular hydrogen bonding in the monolayer. For the tiopronin-derivative capped nanoparticles studied here, minor shift can be found in the amide I and II signals when the powdered nanoparticles were solvated in water. The amide II signal was absent from the Au@MPP spectrum due to the presence of cyclic tertiary amide structure.

It was noted that the amide I band shifted slightly to lower frequency whereas the amide II band was shifted to higher frequency when the solid tiopronin-derivative capped nanoparticles were dissolved in water. Such trend was also observed in a previous study by Fabris *et al*[176] on gold nanoparticles with synthetic oliopeptides as capping ligands. They explained the observation by the intermolecular hydrogen bonds which existed between the amide groups of passivating ligands. The drop in amide I C=O stretching

frequency is due to the reduced electron density of carbonyl oxygen because of enhanced interaction. However, the amide II band, which appears at ~ 1510 cm^{-1} when the amide is not hydrogen-bonded, shifts to a higher frequency (~1540 cm^{-1})[178] when the amides become hydrogen-bond ligated due to the more constrained amide N-H bending.[179]

In the present study, the reduced hydrogen-bonding between amide groups in solid state nanoparticles, as manifested by the lower stretching frequency (~1535 – 1538 cm^{-1}), may imply a more constrained SAM structure. According to the literature[180] the amide which is one methylene away from the mercapto group shows the least hydrogen bonded character compared to those that are further away. This is due to the twisted conformation of amide in exchange for better ligand coverage and finally a higher stability of the entire particles.[181] The degree of freedom of the bound ligands in SAM may somehow be enhanced when the nanoparticles are solvated. This facilitates the monolayer to adopt a better conformation in order to achieve a higher degree of hydrogen bonding and so is the stability. Therefore, the amide II frequency of the tiopronin derivatives on solvated particles increased compared to the solid form.

MPL ligand is soluble in basic aqueous solution but not in pure water or in acidic solution. In its ATR-IR spectrum obtained by dissolving the compound in a pH = 9 ammonium chloride solution, a small peak at 1400 cm^{-1} and an intense peak at 1590 cm^{-1} correspond respectively to the symmetric and asymmetric stretching of the deprotonated carboxylate group (COO^-)[182] were observed. The asymmetric stretching of the carboxylate group of MPL in alkaline solution shifted significantly to a frequency even lower than the amide I peak at 1625 cm^{-1}. The amide II signal appeared to have merged with the carboxylate asymmetric stretching signal and manifested as a flat

shoulder extended from 1550 cm^{-1} to 1520 cm^{-1}. Despite the above observation, the IR spectrum of solid MPL is very similar to other protonated tiopronin derivatives. The high similarity of the IR spectra of solid MPL, aqueous Au@MPL and solid Au@MPL suggests that MPL is in its protonated form in solvated Au@MPL. With the IR spectra and the observed water solubility for free and nanoparticle-bound protonated MPL, it can be seen that attachment on gold nanoparticles completely changed the solvation characters of MPL.

The band centred at 1460 cm^{-1} corresponds to the CH_2 deformation mode of the isopropyl side chain of leucine. This band is obvious in spectra for MPP and MPL with aliphatic methylene structures. The same pattern can also be found in Au@MPP and Au@MPL.

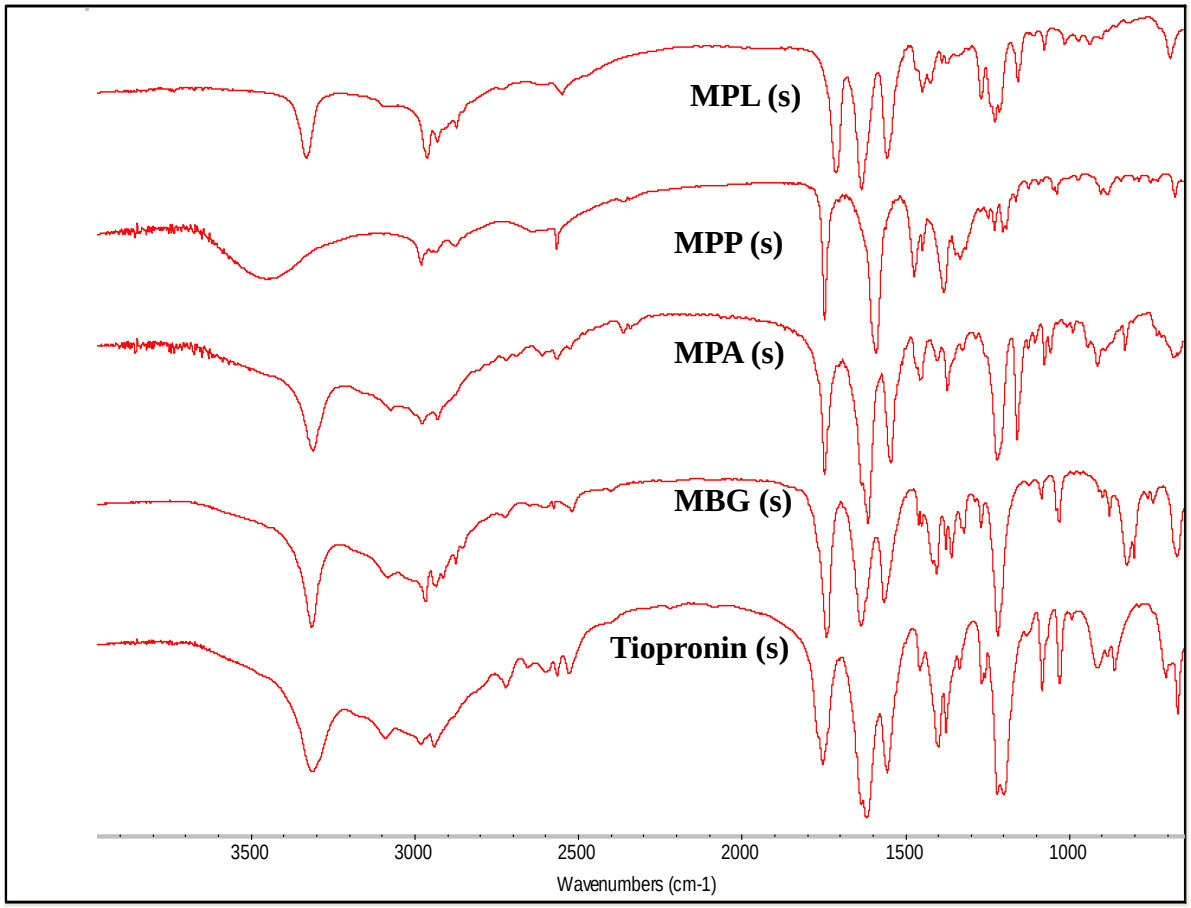

Figure 2.25 Infra-red spectra for solid tiopronin and tiopronin derivatives – MBG, MPA, MPP and MPL.

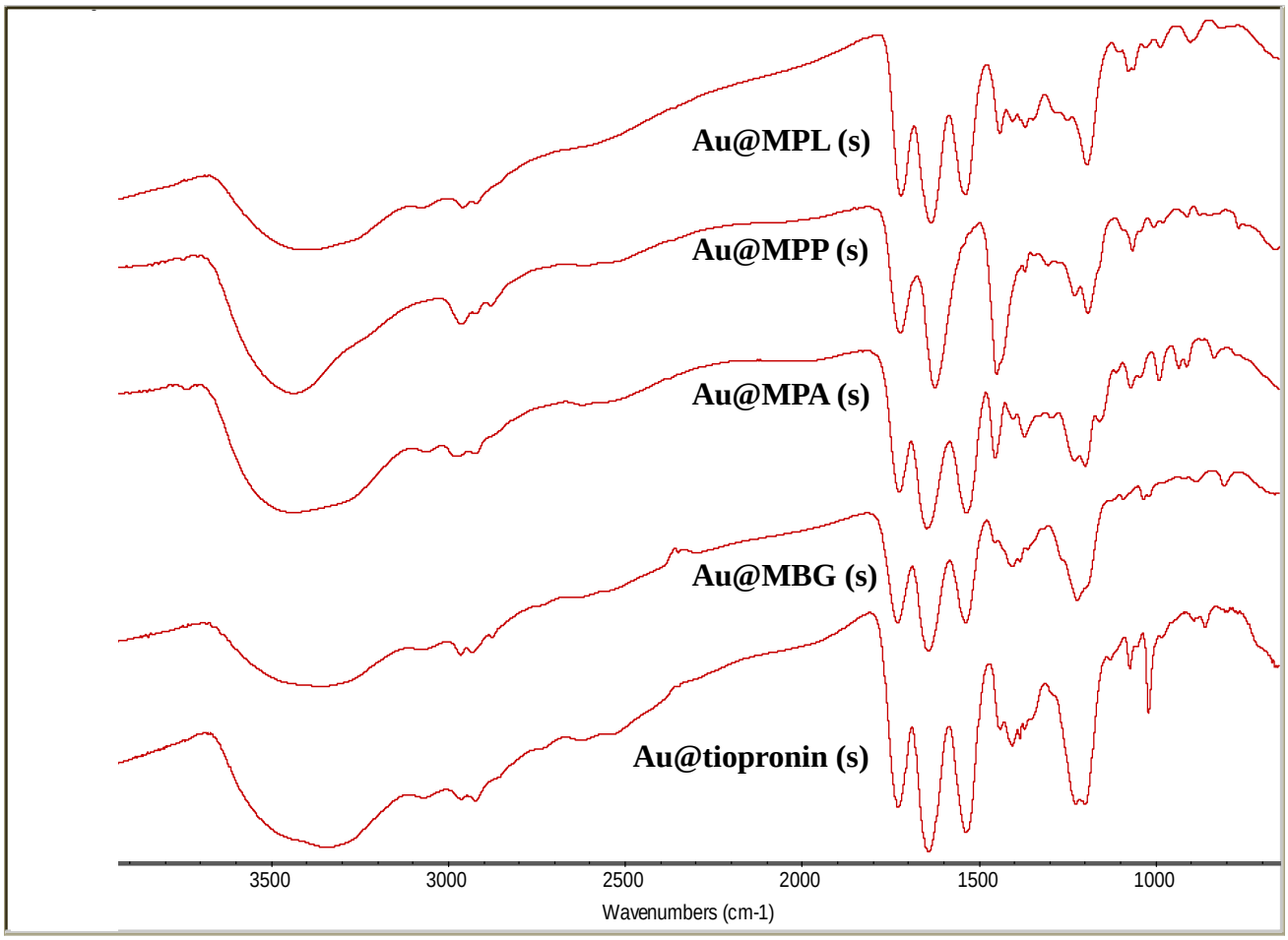

Figure 2.26 Infra-red spectra for solid Au@tiopronin and tiopronin-derivative capped gold nanoparticles – Au@ MBG, Au@MPA, Au@MPP and Au@MPL.

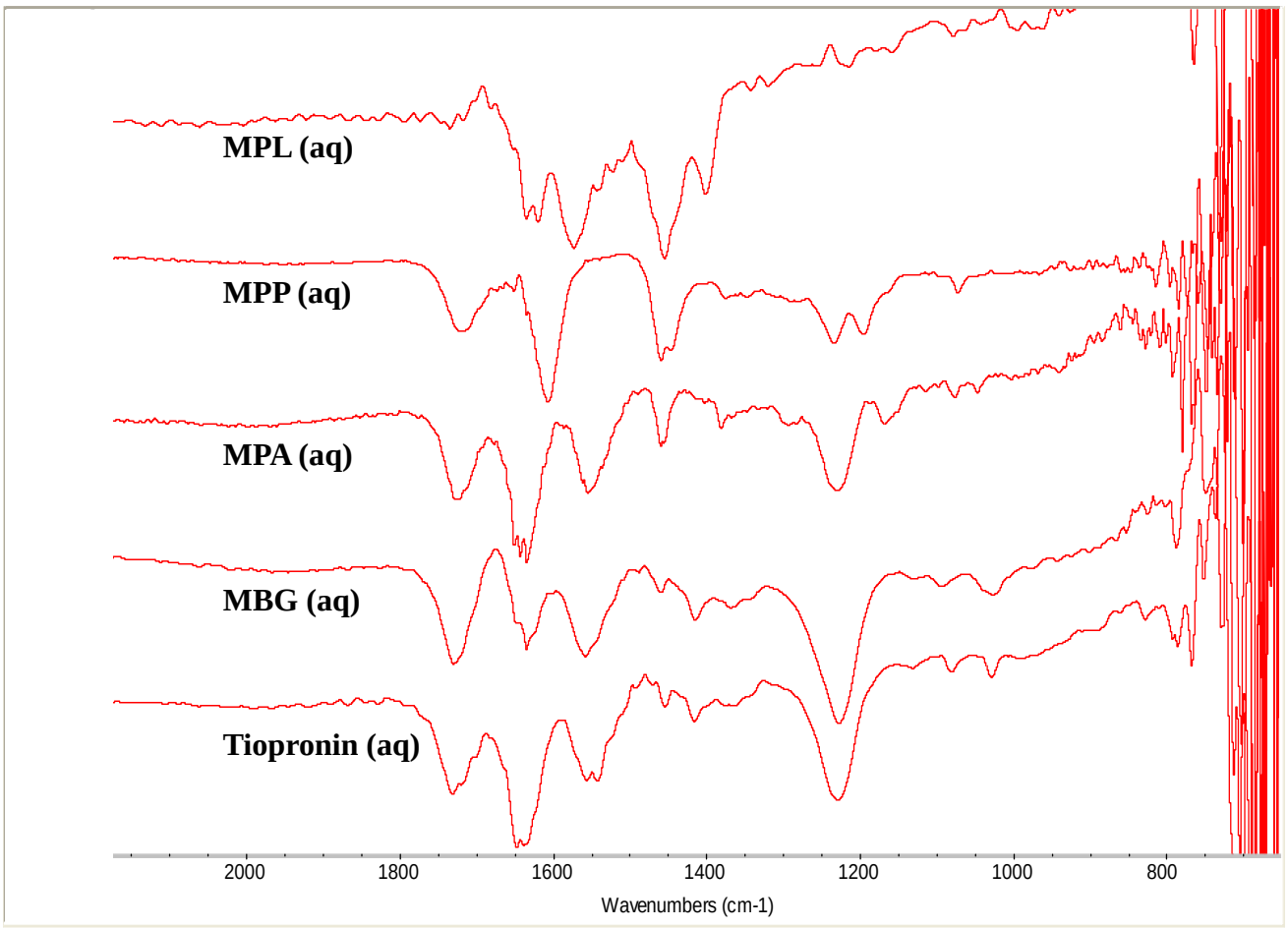

Figure 2.27 Attenuated total reflection infra-red (ATR-IR) spectra for aqueous tiopronin and its derivatives – MBG, MPA, MPP and MPL (the ATR-IR spectra for MPL was acquired in pH 9 buffer).

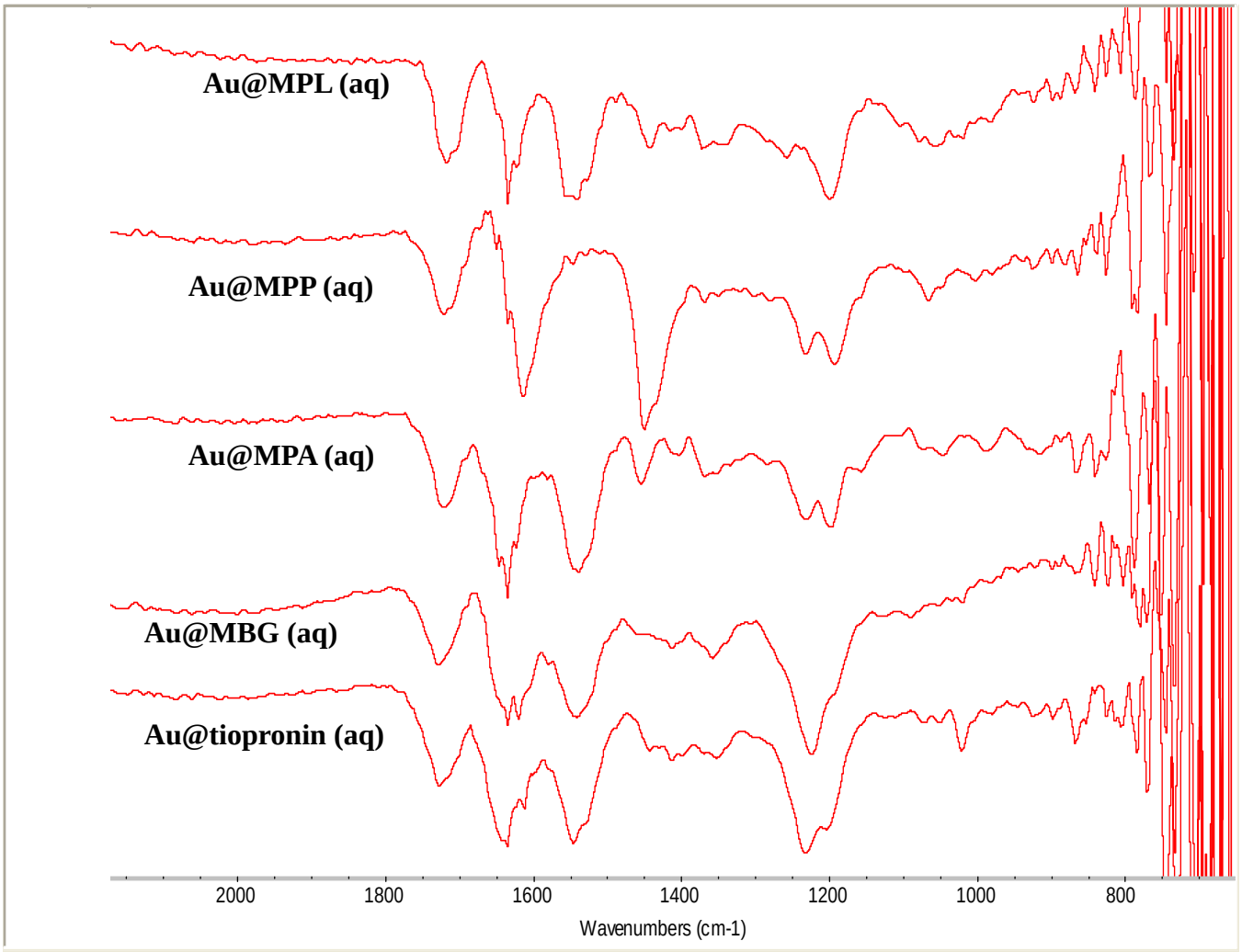

Figure 2.28 Attenuated total reflection infra-red (ATR-IR) spectra for aqueous Au@tiopronin and tiopronin-derivative capped gold nanoparticles – Au@MBG, Au@MPA, Au@MPP and Au@MPL.

Table 2.2. The carboxyl C=O stretching, amide I and amide II band frequency for solid and solvated tiopronin derivatives and their capped gold nanoparticles.

tiopronin (s)	1753.4	1619.3	1556.3
Au@tiopronin (s)	1728	1643.1	1535.9
Au@tiopronin (aq)	1727.7	1640	1546.5
tiopronin (aq)	1730	1655	1547
MBG (s)	1740.4	1636.5	1565.4
Au@MBG (s)	1730.6	1643	1538
Au@MBG (aq)	1730	1627	1542
MBG (aq)	1730.5	1635	1558
MPA (s)	1737.5	1615.5	1545
Au@MPA (s)	1725	1646	1535
Au@MPA (aq)	1722	1636	1539.5
MPA (aq)	1728	1645	1555
MPP (s)	1730	1620	-
Au@MPP (s)	1723.5	1625	-
Au@MPP (aq)	1722	1614.5	-
MPP (aq)	1720.5	1607.8	-
MPL (s)	1712.5	1635	1557
Au@MPL (s)	1720	1635	1538
Au@MPL (aq)	1717.7	1617	1541
MPL (aq, pH = 9)	1590 $(COO^-)_{asy}$	1625	1520-1550

2.3.8 X-ray photoelectron spectroscopy (XPS)

The XPS spectra for individual tiopronin derivative capped gold nanoparticles in the gold and sulfur region are shown in Figures 2.29 to 2.33.

The binding energy for the Au 4f $_{7/2}$ and Au 4f $_{5/2}$ electrons of all tiopronin-derivative capped gold nanoparticles are in the region of ~ 84 – 84.5 eV and ~ 88 eV respectively (Table 2.3). In most reports, the Au 4f $_{7/2}$ signal is always the band of interest and is used to probe the oxidation state of gold.

The usual binding energy for the Au 4f $_{7/2}$ electron in 2D (e.g. flat gold film) and 3D (e.g. nanoparticles) gold (0) system is 83.9 eV[183] while that for the Au 4f $_{5/2}$ is 87.5 eV.[77] The 4f $_{7/2}$ binding energy for nearly all tiopronin-derivative capped nanoparticles in this study (84.3 – 84.7 eV) are obviously higher than the normal gold (0) species. A shift to a higher binding energy implies a lower negative charge content, as is expected for small gold cluster which are relatively electron deficient. This may imply that the gold cores are partially oxidized, though this does not necessarily indicate the presence of formal gold(I) species. Although the binding energy found for the Au 4f $_{7/2}$ of Au@MBG is very similar to that for some general Au(I)-thiolate complexes (~ 84.7 eV), the $4f_{7/2}$ signal for gold(I) thiolated complex should be more positive when the thiolate is from very polar molecules like thiomalate. The binding energy can be pushed up to 84.9 to 85.5 eV.[184] Therefore, it can be inferred that the gold species in Au@MBG remain mostly in the zero valence state and the $4f_{7/2}$ signal found is still somewhat lower than its gold(I) counterpart. Cystine-coated gold nanoparticles give a Au $4f_{7/2}$ binding energy as high as 85.05 eV, which is even much higher than the Au@MBG in

the present study.[185].

In fact, the binding energy for the $4f_{7/2}$ band of nanoparticles depends very much on the size, nature of the ligand bound and the quantity of the ligand attached. Such relationship can be seen in some reports.[170,183]. Gold nanoparticles capped with alkanethiol of different chain length (C_nSH, n = 4, 5, 9, 12) showed nearly the same Au $4f_{7/2}$ binding energy as that of bulk gold (84 eV). However, when the size of the particles was reduced to 2.5 nm or below, the $4f_{7/2}$ binding energy shifted slightly to more positive values.[170] When the nanoparticles were capped with polar substituted aryl thiols, an increase in binding energy for the $4f_{7/2}$ could also be observed, even if the particle size is greater than 3 nm. Therefore, capping ligand can exert a considerable influence on the gold cluster they attached to. Shifting to 85 eV or above can be achieved when very small size gold clusters are attached with very polar ligands like glutathione[184]. The positive shift found in small size and polar thiol attached gold nanoparticles is due to the depletion of d charge in the metal core.[186] This has been proven by the charge neutralization experiment of polar ligand-bound nanoparticles.[187] The $4f_{7/2}$ band of the polar ligand-capped nanoparticles shifted to a more negative value, which is similar to that for bulk gold, when the depleted charge on gold clusters was compensated from an external source.

All tiopronin-derivatives prepared in this study contain an amide and a carboxyl group which are located closely to each other in the ligand molecule and in a very short distance from the gold surface. Therefore, the depletion of charge density in the gold core may be intensified, leading to a more positive binding energy for the $4f_{7/2}$ band. From the TEM and TGA study, the size and organic content of all tiopronin

derivative-capped gold nanoparticles and Au@tiopronin are similar. The effect of size and ligand quantity on the $4f_{7/2}$ band shifting should be very similar in all cases. The possible cause to account for the slight variation in binding energy may, therefore, be due to the extent of electron withdrawing ability of different tiopronin derivatives towards the gold core.

The presence of polar functionalities on the ligand exerts electron withdrawing effect and minimizes the negative charge in the metallic core through the sulfur atom. Therefore, other than the Au 4f band, shifting of binding energy of the sulfur 2p band is also anticipated. The asymmetric S 2p band for all tiopronin-derivative capped gold nanoparticles is due to the spin-orbital splitting of $2p_{3/2}$ and $2p_{1/2}$. The $2p_{3/2}$ is usually employed for studying the charge status on sulfur.

The sulfur $2p_{3/2}$ signal for all tiopronin-derivative capped gold nanoparticles locates in a narrow range (162.7 – 163.2 eV). The values found are more positive than the usual binding energy for sulfur of thiol bound to gold (~162.1 eV).[188] Similar to the case for Au $4f_{7/2}$, the positive shifting of S 2p band is due to the attachment of polar thiol. In many reports the S $2p_{3/2}$ value is close to 163 eV for thiolated ligands that contain carboxyl and amide moieties.[189] Furthermore, the acquired binding energy values for all nanoparticles are smaller than the values for free thiol (163.5 – 164.2 eV) and elemental sulfur,[190] implying that no residual free thiol can be found after purification and the sulfur atom on the ligand holds a higher negative charge.

The average gold to sulfur ratio for tiopronin-derivatives capped gold nanoparticles acquired with XPS is 1.76, which is similar to the average value 1.89 obtained by TGA .

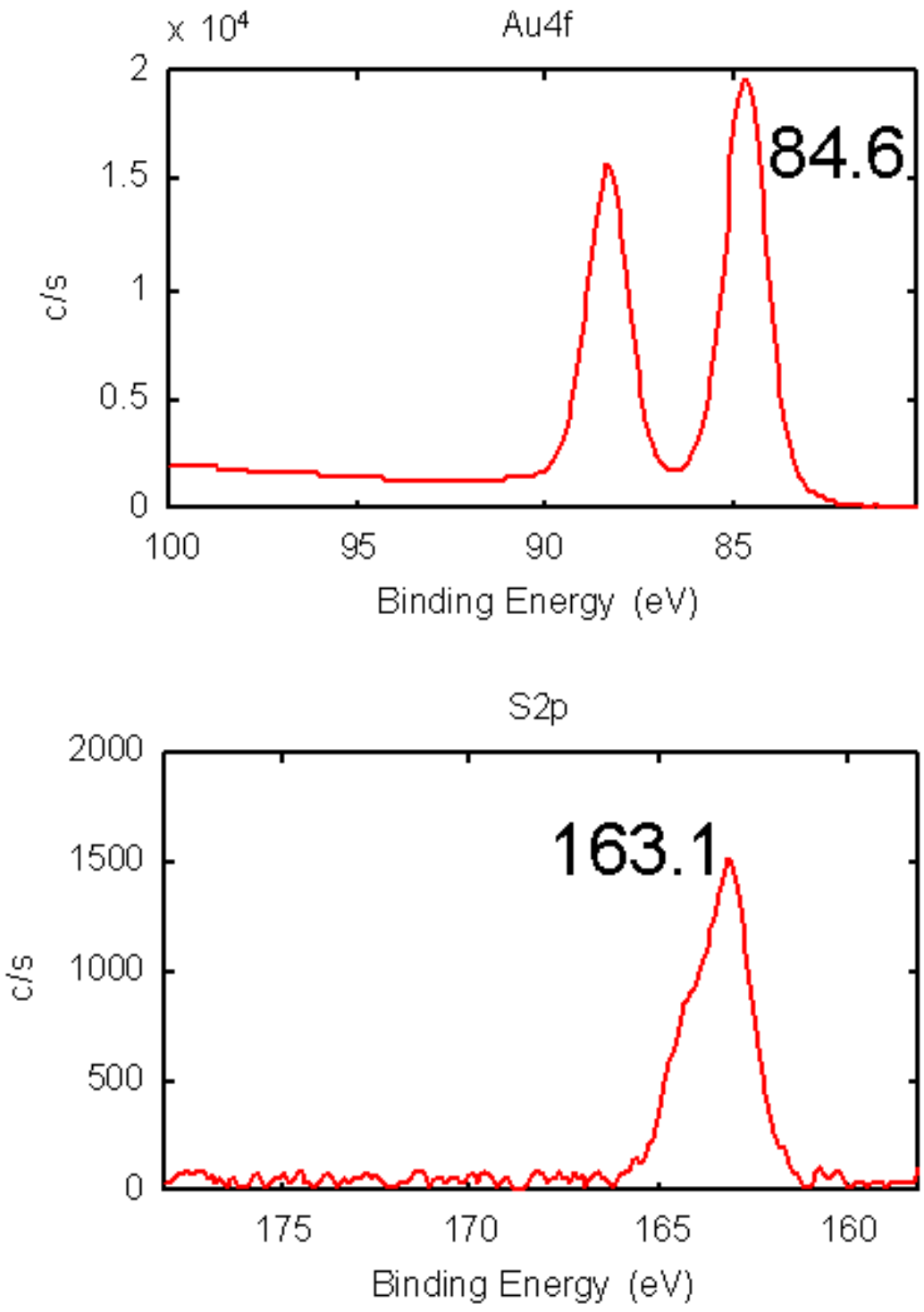

Figure 2.29XPS spectra of Au and S region of Au@tiopronin (values for Au $4f_{7/2}$ and S $2p_{3/2}$ highlighted).

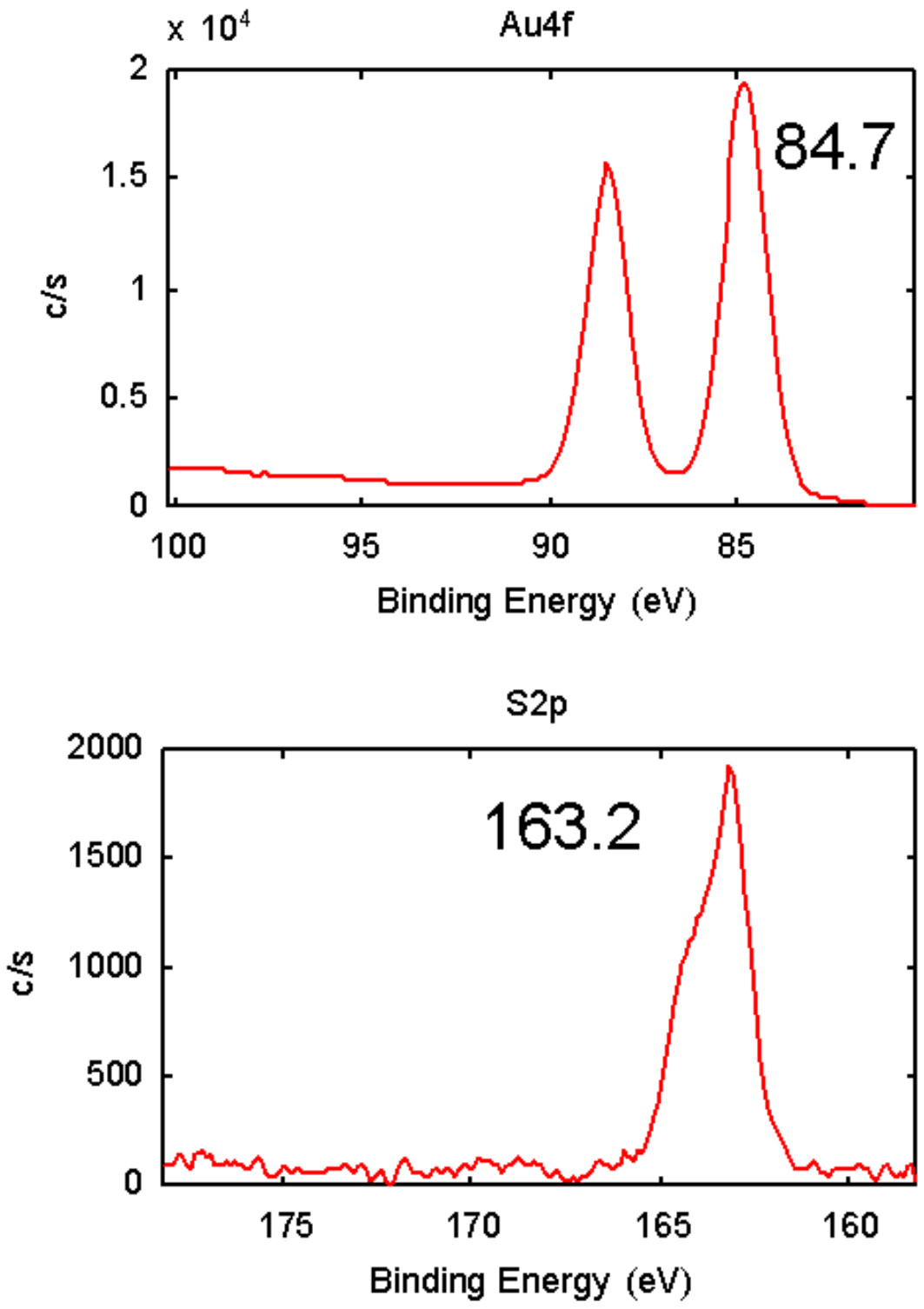

Figure 2.30 XPS spectra of Au and S region of Au@MBG(values for Au $4f_{7/2}$ and S $2p_{3/2}$ highlighted).

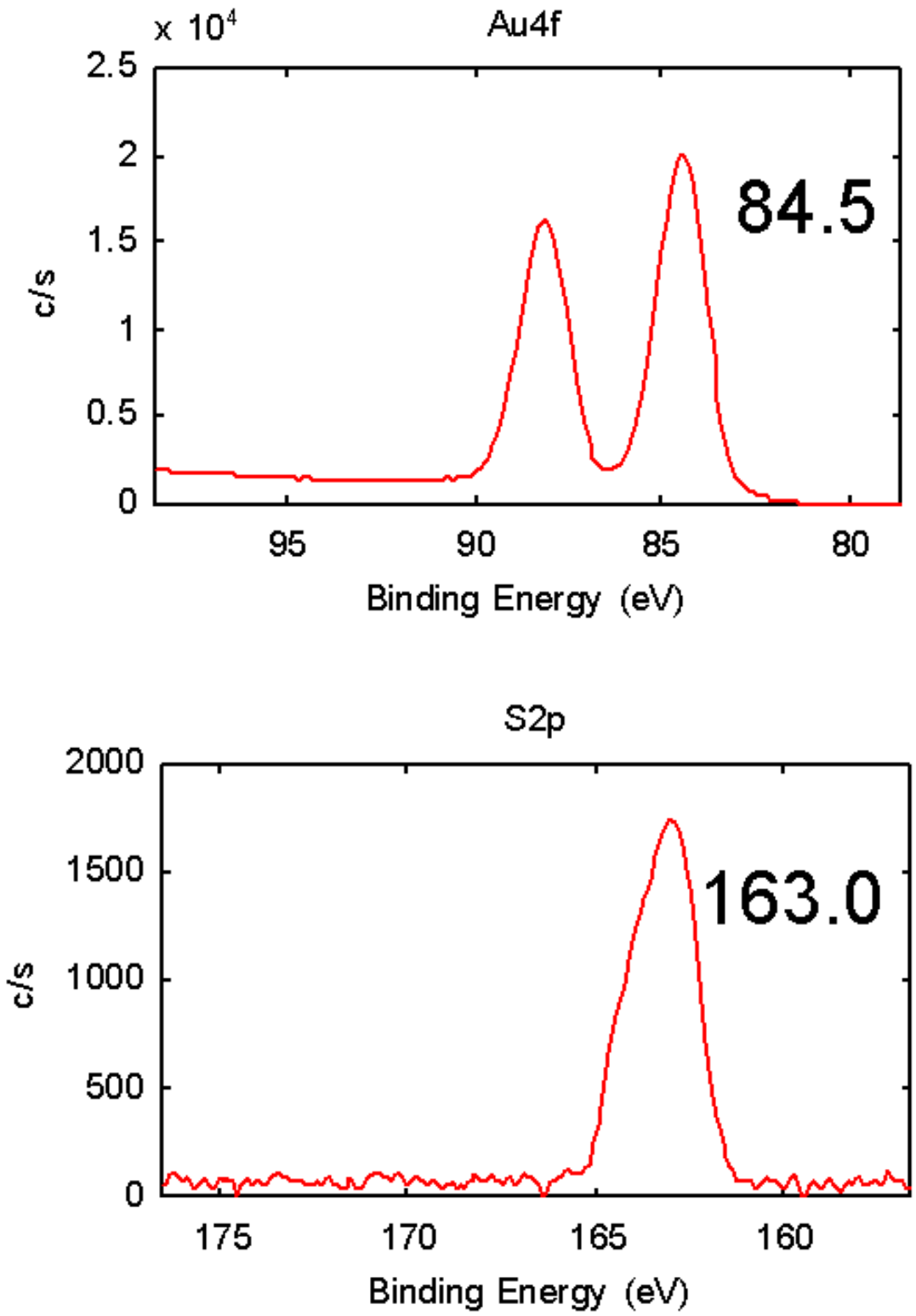

Figure 2.31 XPS spectra of Au and S region of Au@MPA(values for Au $4f_{7/2}$ and S $2p_{3/2}$ highlighted).

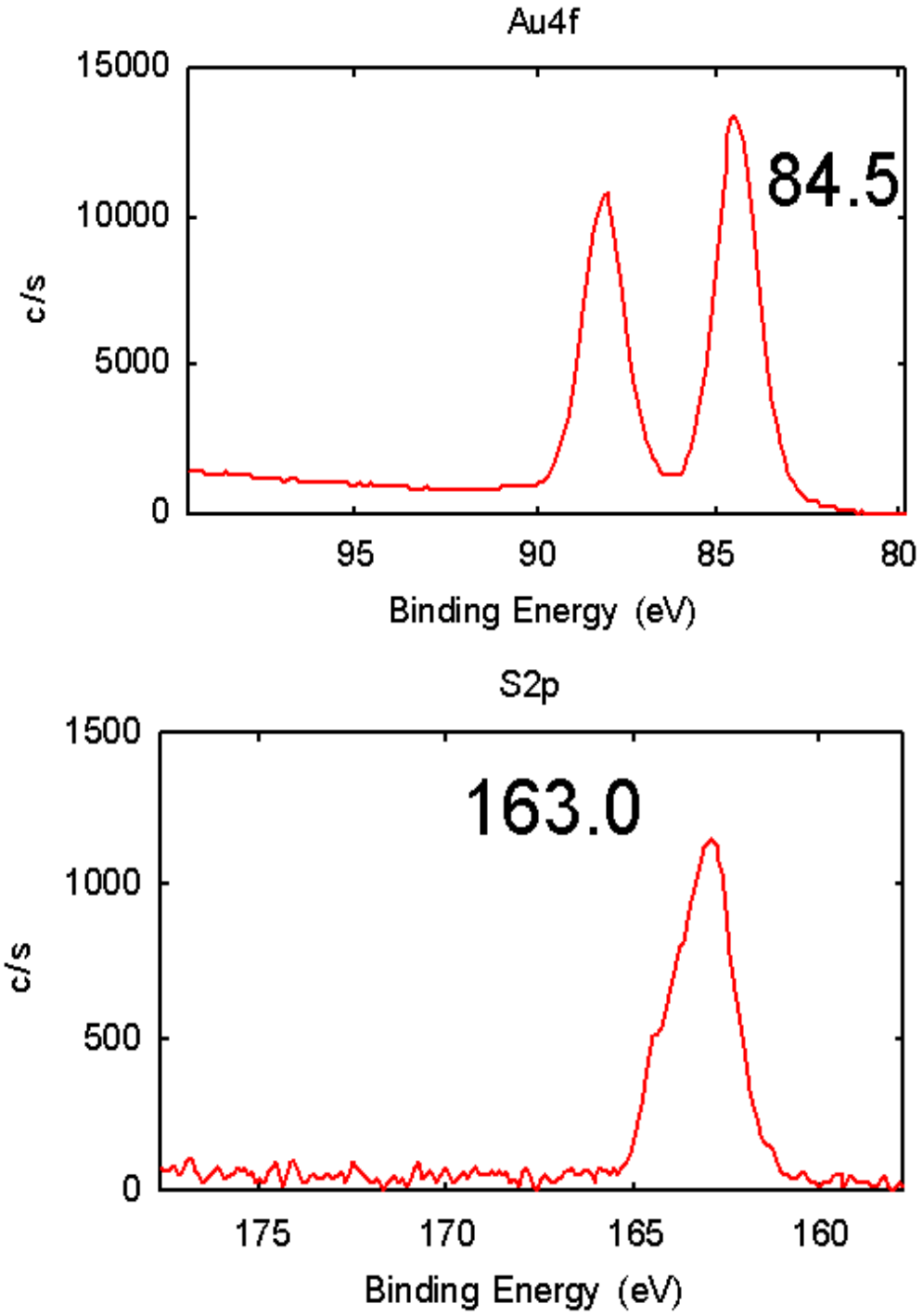

Figure 2.32 XPS spectra of Au and S region of Au@MPP (values for Au $4f_{7/2}$ and S $2p_{3/2}$ highlighted).

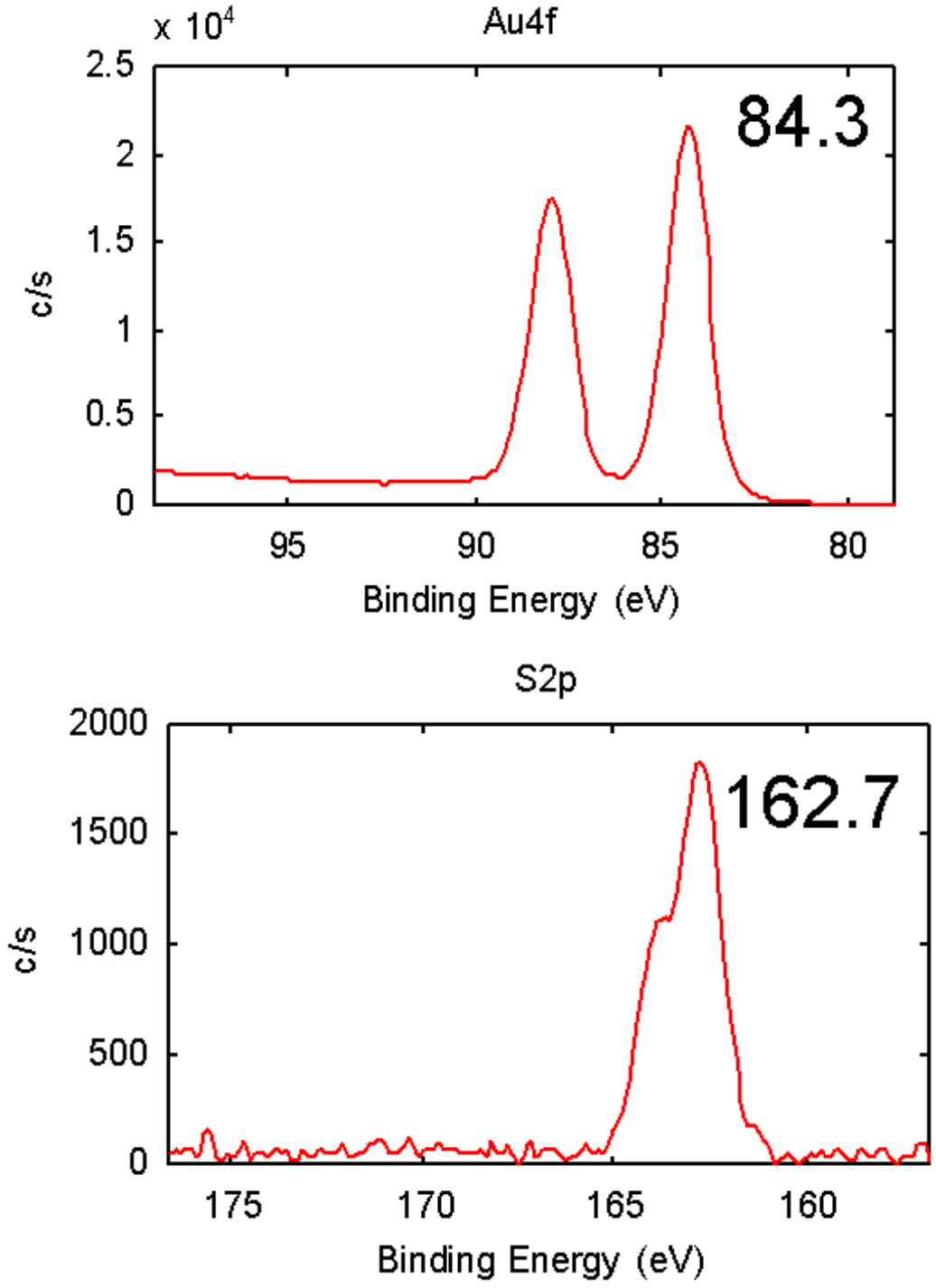

Figure 2.33 XPS spectra of Au and S region of Au@MPL (base-acid-water dialysis.) (values for Au $4f_{7/2}$ and S $2p_{3/2}$ highlighted).

Table 2.3 A summary of Au $4f_{7/2}$ and S $2p_{3/2}$ binding energy for tiopronin-derivative capped gold nanoparticles and the gold to sulphur ratio obtained by XPS.

Derivatives capped gold nanoparticles	Au $4f_{7/2}$ peak position (eV)	S 2p signal peak position (eV)	Au : S
Au@tiopronin	84.6	163.1	1.91
Au@MBG	84.7	163.2	1.60
Au@MPA	84.5	163.0	1.75
Au@MPP	84.5	163.0	1.70
Au@MPL	84.3	162.7	1.85

2.3.9 Luminescence spectroscopy

Figure 2.34 shows the excitation and the emission profiles for individual tiopronin-derivative capped gold nanoparticles. The excitation and emission profiles of Au@tiopronin are included for comparison.

It can be seen that all Au@tiopronin-derivative nanoparticles expressed a broad range near infra-red emission between 700 – 880 nm, with maximum emission appeared mostly at 770 nm upon excited at maximum excitation wavelength (360 – 370 nm). Among the four candidates, Au@MPL showed the most similar emission and excitation profiles, even the maximum excitation and emission wavelength, to the Au@tiopronin. This suggested that the excitation and radiative relaxation pathways employed by both nanoparticles are virtually the same.

The excitation and emission profile of Au@MPA are also similar to the Au@MPL purified with base-acid-water dialysis approach and the Au@tiopronin, except the luminescent intensity is about seven-fold lower than both counterparts. Luminescent intensity is likely to be governed by the quantity of charge carrier and the possible non-radiative relaxation routes available. The emission from non-emissive alkanethiols-capped gold nanoparticles initiated by progressive oxidative charging of the gold core[191] demonstrated that a charge depleted gold core is essential towards gold nanoparticles emission. Since the tiopronin and the derivatives used in this study are polar and possess groups that help disperse the electronic charge, their attachment to the gold nanoparticles may lead to dissipation of charge in the metal core. The higher Au 4f electron binding energy found for tiopronin-derivative capped gold nanoparticles than

most conventional alkanethiol-capped gold nanoparticles further supported the proposed charge depletion in gold core. Such charge dispersing ability may induce luminescence from nanoparticles in a way similar to the deliberate oxidative charging aforementioned and the introduction of more polar ligands.[191] As charging was intensified, a stronger luminescence resulted. This reflected that the luminescence intensity was closely related to the degree of metal core charge depletion. The observed lower luminescence intensity from Au@MPA may be due to the intrinsic lower charge removing ability of the MPA ligand.

The presence of non-radiative pathways can also lead to reduced luminescence from gold nanoparticles.[124] When examined carefully, the emission profile for Au@MPA was not entirely symmetric. A slight bump in the right side of the emission peak indicated that more than one predominating relaxation pathway existed. Therefore, it can be inferred that Au@MPA contains several significant relaxation pathways and some of which may be non-radiative which cause a reduced emission. The lower intensity at maximum emission wavelength and the less symmetric emission profile of Au@MPP and Au@MBG may also be attributed to the presence of other radiative and non-radiative pathways.

The observed emission around 700 – 770 nm (~ 1.7 eV) for all tiopronin-derivative capped gold nanoparticles, also the Au@tiopronin, may mainly be due to the electron transitions across the valence d-band doublet formed by spin-orbital splitting,[187]

(b)

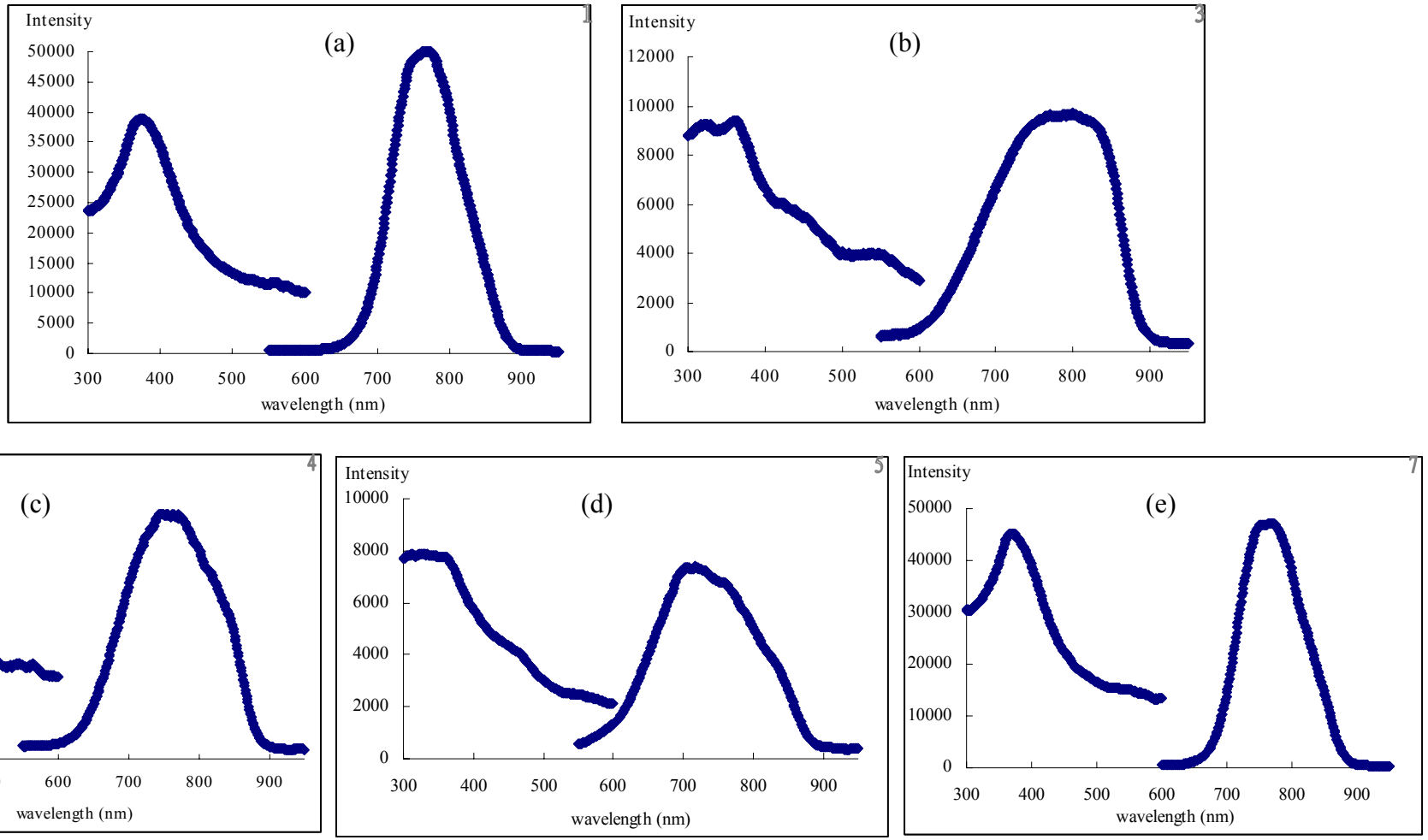

Figure 2.34 Excitation and emission profiles for (a) Au@tiopronin, (b) Au@MBG, (c) Au@MPA, (d) Au@MPP and (e) Au@MPL (Profiles on left from 300 – 600 nm: excitation spectra, profiles on right from 550 – 950 nm : emission spectra)

.

2.4 Concluding remarks:

Tiopronin derivatives produced by modifying amino acid residues and the alkyl substituents of the parent tiopronin backbone have been prepared. The four tiopronin derivative capped gold nanoparticles fabricated were 1.8 – 2.2 nm in diameter. They are all water-soluble and express a high stability towards aggregation in high ionic strength solution.

The infra-red spectra and thermogravimetric analysis revealed that the tiopronin derivatives were held strongly on gold surface and they are hydrogen-bonded extensively. XPS results indicated depletion in the gold core electronic density upon passivation by the tiopronin derivatives. This may account for the observed luminescence from all the tiopronin-derivative capped gold nanoparticles.

The structural effect of ligand is not apparent in terms of nanoparticle stability and water solubility. However, it leads to significant difference in ligand monolayer packing efficiency as reflected by thermogravimetric analysis. An enhanced bulkiness in ligand structure near the gold surface strengthened the ligand interaction in the passivating monolayer on gold surface, which manifested in a higher decomposition temperature in the TGA profile. The presence of cyclic structure in amino acid segment led to a less efficient ligand arrangement, but a flexible bulky iso-butyl side chain in the leucine segment of MPL did not severely reduce the packing efficiency.

The emission of gold nanoclusters capped with all four derivatives occurred over the near-infra red region (700 – 880 nm) upon excitation at 360 – 375 nm. The structure of

the bound tiopronin derivatives does not show a direct correlation with the luminescence profiles of the gold nanoparticles, but it may account for the sublet differences in the maximum emission wavelength and the width of the emission profile.

Chapter 3

Ligand exchange reaction of gold nanoparticles involving tiopronin-derivatives

3.1. Introduction

Ligand exchange is one of the most important phenomena that happen on the surface of gold nanostructures. The dynamic and reversible nature of such process facilitates the self-assembly of protecting ligands into monolayer with the most stable conformation on the nanoparticles, as the ligands can adsorb and desorb freely to adopt different arrangements and monolayer morphologies to achieve the minimum surface energy. On the other hand, ligand exchange enables the introduction of functional groups that are vulnerable to damages during nanostructure synthesis. Moieties like fluorophores,[192] sensor components,[193] and biological molecules[194] are usually anchored to gold nanoparticles or flat gold surface by exchanging their thiol-linker tagged derivatives with the pre-formed surface-bound ligands. The attachment of these motifs makes gold nanoclusters a valuable new generation detection tool.

In this chapter, the ligand exchange reactions between tiopronin and its derivatives on gold nanoparticles were explored. Unlike the exchange reaction of alkanethiols studied in numerous previous reports which involve organic solvent as the reaction medium, the ligand exchange for the present study proceeded entirely under aqueous condition. The terminal carboxyl group of tiopronin and also its derivatives can be deprontonated by adjusting to higher pH. This enables the investigation of ligand exchange between monolayer and free ligands, which are both negatively charged. The exchange kinetics involving electrostatically charged species is seldom explored up to this moment. The results obtained in this chapter provide more insights about the ligand exchange reaction in aqueous system, which is useful for the utilization of gold nanoparticles for

biological and physiological purposes.

The ligand exchange kinetic data are usually analyzed with the initial rate method. Since the change in the quantity of bound thiol is minimal at the early stage of the exchange process, it can be safely assumed that a pseudo first order kinetics is followed. Recently, report by Kassam et al.[84] demonstrated that an exchange reaction between decanethiol-passivated gold nanoparticles and dodecanethiol can be well described with the second-order Langmuir diffusion-limited model. The data obtained in this chapter will also be fitted with such a model to examine its potential use in describing the ligand exchange behavior of gold nanoparticles in aqueous medium.

3.2. Experimental section

3.2.1. Materials and instruments

Tiopronin derivatives (MBG (mercaptobutanoyl glycine), MPA (mercaptopropanoyl alaine), MPP (mercaptopropanoyl proline), and MPL (mercaptopropanoyl leucine)), and their gold nanoparticles (Au@tiopronin, Au@MBG, Au@MPA, Au@MPP, Au@MPL) were synthesized as described in the previous chapter. Tiopronin, deuterium oxide containing 0.05wt% of 3-(trimethylsilyl)propionic-2,2,3,3-d_4 acid, sodium salt (TMSP-Na), deuterated acetonitrile, and potassium dihydrogenphosphate were obtained from Aldrich.

The kinetics of all ligand exchange reactions were monitored by a Varian AS500 nuclear magnetic resonance spectrometer operating at 500 MHz under the array acquisition mode. Spectra for the reaction mixture were obtained every minute. The spectra for the first two minutes after the commencement of the reaction were omitted due to machine shimming. Every kinetic experiment was repeated three times to assure the accuracy and the consistency.

All stock solutions, unless otherwise stated, were prepared by dissolving the corresponding substrate(s) into the desired volume of deuterium oxide containing 0.05 wt% (3.2 mM) sodium salt of 3-(trimethylsilyl)propionic-2,2,3,3-d_4 acid (TMSP-Na). TMSP-Na was employed as the internal standard for quantifying different species in the kinetic study described in this chapter. The total volume of the reaction mixture used in all experiments was always maintained at 500 μL.

3.2.2. Ligand exchange reaction between Au@tiopronin and different tiopronin derivatives at various free thiol loadings.

For each kinetic experiment, 250 μL of Au@tiopronin stock solution (13.4 mg/mL) was used. Different volumes of the tiopronin-derivative stock solution (213 mM) and deuterated water with TMSP-Na were added to achieve the various free thiol loading ratios (free-to-bound thiol ratios). The volumes of various component stock solutions used to compose the reaction mixture are shown in Table 3.1.

Table 3.1 Volume of different stock solutions used to prepare the ligand exchange reaction mixture with various free thiol loading ratios.

Free thiol loading ratio (Equivalent(s))	Volume of Au@tiopronin stock solution (13.4 mg/ml) (μL)	Volume of tiopronin derivatives stock solution (213 mM)* (μL)	Deuterated water* (with 3.2 mM TMSP-Na) (μL)
1	250	25	225
2	250	50	200
5	250	125	125
10	250	250	0

*. Due to the low solubility of MPLin water, a 4 : 1 (v/v) mixture of deuterated acetonitrile-deuterated water with 0.05% TMSP-Na was used in the MPL stock solution.

3.2.3. Ligand exchange reaction between Au@tiopronin-derivatives and tiopronin

In order to make fair comparisons, the stock solution of four tiopronin-derivative capped gold nanoparticles were prepared to contain the same quantity of bound thiols as that in the Au@tiopronin stock solution (quantity of tiopronin in 250 μL Au@tiopronin stock solution = 6.69 μmol). Table 3.2 summarizes the concentration of each Au@tiopronin derivative stock solution prepared. The amounts of bound thiols on each type of tiopronin-derivative capped gold nanoparticles were estimated by the iodine cleavage method as described in section 3.3.5

For each trial, 250 μL of the nanoparticle stock solution was mixed with 250 μL of tiopronin stock solution (21.84 mg/mL) in a NMR tube (tiopronin loading ratio = 5 equivalents). After mixing, the reaction mixture was quickly loaded into the NMR spectrometer for shimming and spectra acquisition.

Table 3.2 Concentration of different Au@tiopronin-derivative stock solutions used.

Au@tiopronin derivatives	Concentration of Au@tiopronin-derivatives stock solution (mg/mL)
Au@MBG	13.52
Au@MPA	13.67
Au@MPP	15.52
Au@MPL	17.63

3.2.4. Ligand exchange reaction between Au@tiopronin and different tiopronin derivatives at pH 6.5

The pKa values for carboxyl group lies between 3 to 4. When medium pH is higher than 4, carboxyl group is deprotonated to give negatively charged carboxylate ion. The most convenient way to obtain electronegatively charged monolayer and free ligand is to adjust the reaction medium pH to above 7 by adding base. However, in some preliminary investigations, the Au@tiopronin nanoparticles degraded quite rapidly when the exchange reaction was allowed to proceeded at pH higher than 7 or, more precisely, in the presence of hydroxide ion. Meanwhile, the mercapto group is well-known for its rapid oxidation to disulfide in alkaline condition. The optimum medium pH for complete deprotonation, stability of gold nanoparticles, and the mercapto group of the free thiol added was determined by measuring the infra-red spectra for different gold nanoparticles + free thiol solution mixture at various pH.

Figure 3.1 shows the solution ATR-IR spectra of the nanoparticles and the nanoparticles + free tiopronin mixture at pH 6.5 buffered by dipotassium hydrogenphosphate. It can be seen that the hydrogen-bonded carboxyl carbonyl group (C=O) stretching (~ 1722 cm^{-1})[195] were absent in both the nanoparticles-only solution and the free tiopronin + nanocluster mixture. Instead, only the C=O stretching for the deprotonated carboxylate ion (COO^-) (~ 1590 cm^{-1}) was found.[182] The spectra suggested that the carboxylic acid groups in the SAM on nanocluster and the free ligands were completely deprotonated in aqueous solution of pH 6.5, despite the increased pKa values[196] of the monolayer ligands, which is one to two unit higher than that of their free state, because of the enhanced electronic repulsion and the hydrogen-bond interaction.

The pKa values for most of the polar thiols, like glutathione and cysteine, range between 8 – 10.[197] The mercapto group in a pH 6.5 environment should be in its protonated form.

On the other hand, it was found that the addition of 1.5 equivalents of dipotassium hydrogenphosphate (with respect to the amount of carboxylic acid of ligand present both on the nanoparticle and in the solution) resulted in the solution pH of ca. 6.5. Based on this result, the exchange reaction medium for each trial was prepared by directly mixing of hydrogenphosphate salt, nanoparticles, and the free ligand under the HPO_4^- to $COOH_{(total)}$ ratio of 1.5.

The amount of tiopronin-derivatives used in each trial was five times more than that of tiopronin on nanoparticle. 250 μL of Au@tiopronin stock solution (13.4 mg/mL) was mixed with 8.70 mg of dipotassium hydrogenphosphate in a NMR tube. The mixture was shaken to the complete dissolution, followed by the quick addition of 125 μL of 213 mM tiopronin-derivative stock solution and 125 μL of TMSP-Na containing deuterated water. After all components were added and mixed, the tube was loaded into the NMR spectrometer for data acquisition. Since MPL is only soluble in water at higher pH ranges, the reaction mixture for MPL experiment was prepared by firstly dissolving the MPL in hydrogenphosphate solution, formed by quick addition nanoparticle stock solution.

The terms ‘buffered’ and ‘unbuffered’ will be used throughout this chapter to represent the reaction medium which its pH was maintaineded at 6.5 and the one with no deliberate control (pH = 3 – 3.5), respectively.

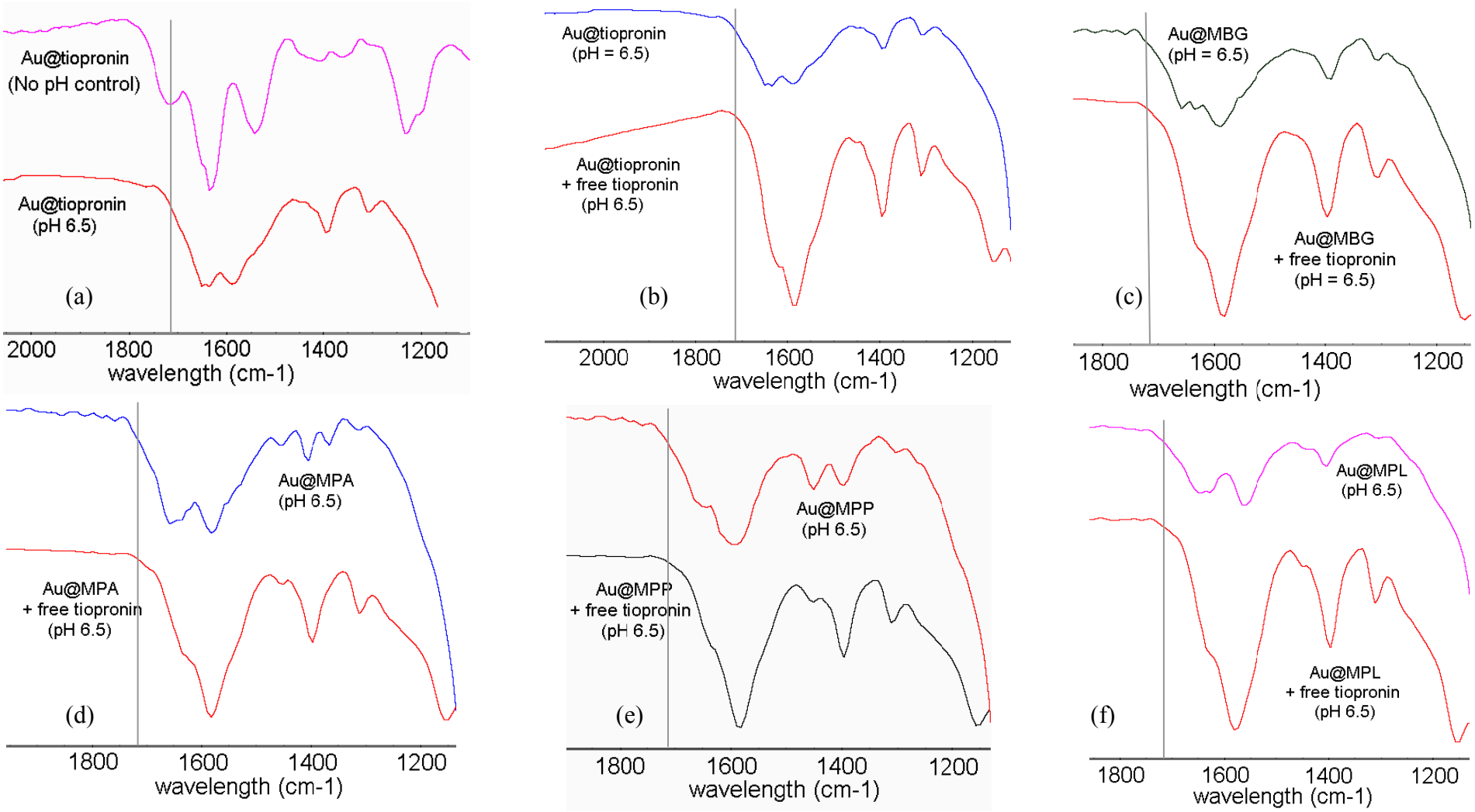

Figure 3.1 ATR-FTIR spectra for tiopronin-derivative capped gold nanoparticles and the mixtures of five equivalents free tiopronin+nanoparticles in pH 6.5 medium. The grey vertical line represents the position for the C=O stretching peak of COOH group.

3.2.5. Ligand exchange reaction between Au@tiopronin and mercarptobutanoyl glycine (MBG) at pH 6.5

The free MBG loading ratios of 1, 2 5 and 10 equivalent(s) were employed. For exchange experiment at each loading, 250 μL of Au@tiopronin stock solution (13.4 mg/mL) was mixed with 1.5 equivalents (relative to the total amount of thiol ligand present in the reaction solution) of dipotassuim hydrogenphosphate in a NMR tube. The volume combinations of the MBG stock solution (213 mM) and deuterated water with TMSP-Na used to achieve the desired free MBG loading ratios were the same as those stated in Table 3.1. After all the components were mixed, the tube was immediately loaded into the spectrometer for shimming and data acquisition.

3.2.6. Kinetic studies

In all the exchange reactions studied, the progress of the exchange kinetics was followed by monitoring the amount of desorbed thiol over the entire reaction period. The quantity of bound-thiol exchanged into the reaction medium was represented as desorbed thiol quantity ratio shown below:

$$\text{Quantity ratio of desorbed thiol} = \frac{\text{Quantity of desorbed thiol vs TMSP} - \text{Na}}{\text{Total amount of originally bound -thiol vs TMSP} - \text{Na}}$$

The quantity of desorbed thiol is the amount of the orginially bound-thiol found in the 500 μL reaction medium at a particular time. This was obtained from the momentary integration of a chosen NMR peak of the desorbed thiol. Since the structural characteristics of tiopronin and its derivatives are quite similar, the peak for the

integration had to be carefully selected for each derivative to avoid peak masking. The selected peaks for individual derivatives are stated in later sections.

The total amount of originally bound thiol was obtained from iodine cleavage method where 500 μL of 1 : 1 mixture of gold nanoparticle stock solution and TMSP-Na contained deuterated water were used. With iodine, all bound thiols were released as disulfides into the solution. The quantity of the disulfide was determined by the integration of the same selected peak used with the momentary desorbed thiols.

All integrations were always relative to that of the trimethyl singlet of the TMSP-Na internal standard, yielding the corresponding integration ratio. This allowed the comparison of the results from different trials.

The exchange reactions involving the tiopronin-derivatives under various reactant loading ratios and solution pH conditions were analysed with both the pseudo first order initial rate approach and the second order Langmuir diffusion-limited model.

The terms ‘initial reaction extent’ and ‘equilibrium final reaction extent’ appeared in the rest of this chapter refer to the extent of ligand exchange reaction at the third minute since the reaction started and when equilibrium state was established, respectively.

The kinetics data were firstly examined with the initial rate method to obtain the pseudo first order rate constant and, in some cases, also the second order rate constant. In addition, they were fitted to the second order Langmuir diffusion-limited model in order to better understand the kinetic of exchange reaction.

3.3. Results and discussion

3.3.1. Extent of ligand exchange reaction between Au@tiopronin nanoparticles and free tiopronin-derivatives

In this section, the seven-day exchange reactions between Au@tiopronin and the four tiopronin derivatives – MBG, MPA, MPP and MPL – were described. Different free thiol loading ratios of: 1, 2, 5 and 10 equivalents were employed in order to investigate the effect of incoming ligand content and to probe the mechanism of the exchange process.

The progress of the exchange reaction was monitored by measuring the momentary integration of the methyl doublet (1.50 ppm) of the detached tiopronin when MBG served as the incoming ligand. On the other hand, the integration of the tiopronin methylene doublet (4.00 ppm) was employed when the incoming ligand were MPA, MPP, and MPL.

3.3.1.1. Reaction progress for the exchange reactions between Au@tiopronin and tiopronin-derivatives

Figure 3.2 shows the time progress plots for the exchange reactions between the four tiopronin derivatives and the Au@tiopronin nanoparticles.

At the earliest stage of the process when the first few NMR spectra of the reaction mixture were acquired, they all indicated that more than 30% of the originally bound tiopronin had undergone exchange with the tiopronin-derivatives added. Among those scarce reports concerning the detailed kinetic study on ligand exchange of nanoparticles in aqueous system, it is common to observe a huge population change in the self-assembled monolayer on the nanoclusters shortly after the commencement of exchange reaction. About 50% of the originally bound-thiol was found to have desorbed from the metal surface a few minutes after the process had started.[198] This is significantly different from most kinetic studies[83,86,199] involving alkanethiols and gold nanoparticles soluble in organic solvents, in which the status of the ligand exchange increase progressively from zero and reach equilibrium after a certain period. This indicates that the dielectric properties of the reaction medium have significant influence on the exchange process. The exchange of polar ligands is highly favored in polar medium like water, leading to the observed high extent of reaction at the very early stage.

In some studies of gold nanoparticles with diameter of 1.8 – 2.2 nm, the equilibrium extent of the ligand exchange ranged from 0.3 to 0.55 when the free thiol-loading ratio was less than two equivalents, regardless of the polarity of the solvent and the ligands

involved.[87] Such behavior was also observed in the present study for ligand exchange reaction involving the tiopronin-derivatives and the gold nanoparticles. The final extent of exchange at equilibrium ranged from 0.39 to 0.48 with one equivalent loadings, while the value increased to 0.53 – 0.65 when the amount of free thiol added was doubled. The similarity in the extent of reaction achieved in various reported exchange experiments, including the present study, with different ligands and media could be explained by the great influence from the surface conditions of the metal core.

Since the metal surface defective sites like vertices and edges on the gold nanoparticles of 1.8 to 2.2 nm in diameter account for 43 – 52 % of the entire metallic core surface,[170] the achieved extent of reaction (0.3 – 0.55) was mainly due to the preferential exchange of ligands bound on these higher energy locations. The low ligand loading ratio (e.g. 1 equivalent) provided insufficient driving force to initiate further ligand exchange at the less or reactive terrace area.

When the free thiol loading ratio was elevated to 5 and 10 equivalents, the extent of the exchange reaction at both the initial and equilibrium final stages also increased. An intriguing interpretation of the initial extent of reaction for these higher loading trials is that all the facile defect sites on the metal core were almost ‘immediately’ colonized, according to the percentage surface defect on nanoparticle mentioned previously, by the incoming ligands soon after the reactants were mixed. This is due to the presence of excessive amount of incoming thiol which generated a strong driving force and flux for the exchange to occur. After all the reactive sites had been exchanged with the incoming ligands, thiols on the less reactive terrace sites were then replaced gradually until equilibrium was reached.

Table 3.3 shows that the variation in the extent of reaction among the four derivatives was about 10 % at the initial stage of the exchange process under different free thiol loadings. Such variation reduced to ~ 7% when the exchange reaction had reached equilibrium. The degree of variation became smaller in trials with higher incoming ligand loading. The smaller difference in the extent of exchange reaction at equilibrium among the tiopronin derivatives demonstrates that the structural characteristics of these derivatives have little effect on determining the equilibrium state of the binary monolayer.

Even though the difference in the extent of reaction is small amid the four derivatives, some observations are still worth noting. It is noted that MPP generally replaces a greater proportion of the bound-tiopronin from the nanoclusters than the other three derivatives in most loading ratios studied. This may be attributed to the bulky proline segment of MPP, which exerts a great steric effect to the original tiopronin monolayer anchored on the gold nanocluster surface. This is similar to the previous report[200] that when structurally hindered ferrocene-tagged thiol was incorporated into the alkanethiol monolayer on gold surface, defects in the ligand monolayer were then produced accompanied by a lower ligand packing efficiency. Together with the higher MPP content in the reaction medium, the tiopronin adsorbed near these monolayer defects are prone to the exchange, leading to the higher extent of reaction obsereved.

The bulky iso-butyl side chain in the leucine segment of MPL is flexible and experiences a higher degree of freedom due to the lower terminal group packing density compared to the Au-S bond on the core surface,[170] so the incorporation of MPL is

expected to place limited steric constrain to the adjacent monolayer. Meanwhile, the hydrophobic intereaction between the isobutyl side chains may counteract the increased steric hindrance. This may account for the similar equilibrium extent of exchange reaction with MPL compared to the less hindered MBG and MPA ligand.

The structural characteristics of MBG, MPA, and the tiopronin ligand are more similar, so the degree of tiopronin displacement in the exchange reaction with these two derivatives was quite close to each other.

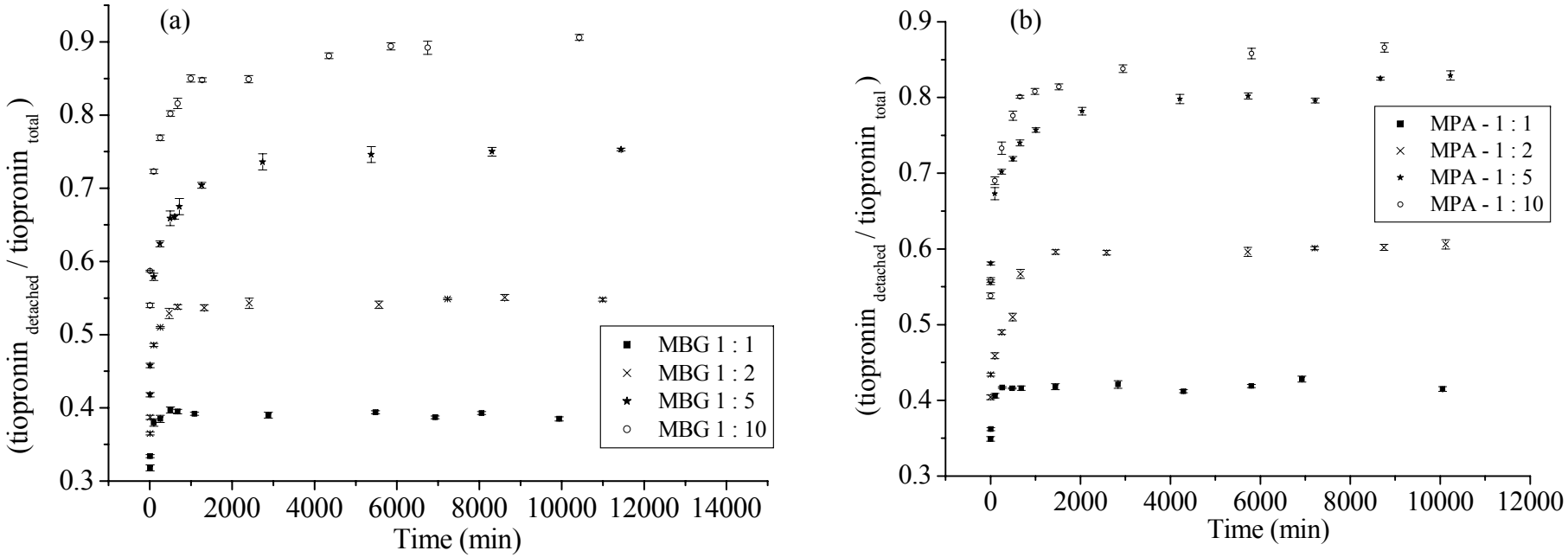

Figure 3.2 Time progress plot for the exchange reaction between Au@tiopronin vs a) MBG and b) MPA at free thiol loading ratio = 1, 2, 5 and 10 equivalent(s) respectively.

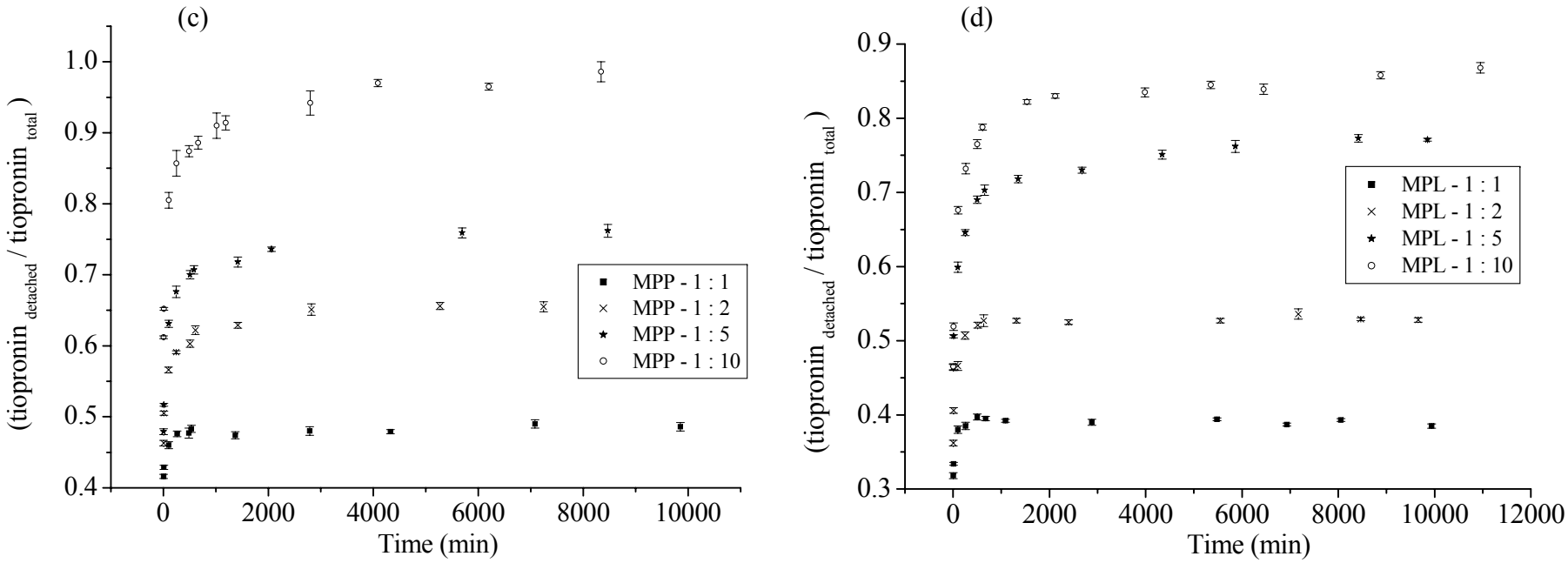

Figure 3.2 (cont'd) Time progress plot for the exchange reaction between Au@tiopronin vs c) MPP and d) MPL at free thiol loading ratio = 1, 2, 5 and 10 equivalent(s) respectively.

Table 3.3 Extent of the exchange reaction at the initial and equilibrium stage between Au@tiopronin and tiopronin derivatives with different free tiopronin-derivatives loading ratios.

Extent of reaction at Initial and Equilibrium stage of the reaction								
Free thiol loading ratio (Equilvalent(s))	MBG		MPA		MPP		MPL	
	Initial	Equil	Initial	Equil.	Initial	Equil.	Initial	Equil.
1	0.31	0.40	0.34	0.45	0.36	0.48	0.31	0.39
2	0.37	0.55	0.41	0.61	0.46	0.65	0.36	0.53
5	0.41	0.74	0.53	0.83	0.48	0.76	0.47	0.77
10	0.53	0.89	0.54	0.86	0.61	0.97	0.46	0.85

3.3.1.2. Pseudo first order initial rate plot for the exchange reaction between Au@tiopronin and tiopronin-derivatives

Figures 3.3 – 3.6 show the pseudo first order initial rate plot for the exchange reaction between the bound-tiopronin and the four tiopronin derivatives under different free thiol loading ratios. The rate constants obtained are tabulated in Table 3.4. From the figures, it can be seen that the exchange between the incoming thiol and the labile nanocluster bound-tiopronin ligands, possibly at the defect sites on the nanoparticle, obey a pseudo first order behavior under different added thiol concentrations.

The first order rate constant unraveled the exchange kinetics between the bound tiopronin and those most early-arrived incoming ligand molecules at the monolayer. The ligand exchange with MBG, MPA, and MPP were conducted in pure deuterated water while a deuterated acetonitrile-deuterium oxide binary solution was used when MPL was used due to its poor solubility in water. The relatively small difference in initial rate constants obtained for the exchange reactions involving MBG and MPP indicate that the kinetics of both processes are quite similar, even though the structure of the two candidates are quite different. When MPA served as the incoming ligand, the increase in rate constant was less rapid than those with MBG and MPP.

A difference in rate constant of a ligand exchange reaction on gold nanoparticles was previously explained in terms of substituent electronic effects, surface electron binding energy, and ligand desolvation energy.[199] However, neither of these considerations can explain the observed kinetics for the three tiopronin derivatives. This is due to the insignificant variation in electronic effect among candidates, as the polar groups present

in all derivatives are virtually the same.

The only major difference among the four tiopronin derivatives is steric factor. Previous study[201] has demonstrated that the steric effect brought by the alkyl side chain could contribute to a sharp variation in the ligand exchange kinetics on very small sized gold nanoparticles (~ 2.6 nm). Branching from the parent carbon skeleton, in most cases, leads to a better monolayer packing and therefore faster exchange kinetics in order to adopt the more stable conformation. This was further substantiated by the higher decomposition temperature recorded in the thermal analysis of the gold nanoparticles passivated with branched thiols.

From the TGA and DSC data in the previous chapter, the profiles for Au@MBG showed a complete destruction of monolayer at a temperature higher than that for Au@tiopronin. Therefore, MBG can give a more stable monolayer than tiopronin which could be the cause for its generally faster exchange rate among the derivatives. The TGA and DSC profile for Au@MPA are very similar to those of Au@tiopronin, especially the sharp transition in DSC profile at about the same temperature for both nanoparticles. This reflects that the packings of MPA and tiopronin in their corresponding monolayers are of high similarity and no prominent preference for the replacement of the bound tiopronin with MPA was anticipated.

Although thermal analysis suggested that the packings of the monolayer in Au@MPP and Au@MPL were less efficient as proved by their the lower destruction temperature, the steric strain in the monolayer [200] can promote the departure of the originally bound tiopronin once MPP or MPL had been introduced. The less tightly packed monolayer,

on the other hand, provides less screening for the defect sites on metal core and makes the more accessible to the approach of subsequent incoming thiols. These factors would lead to the higher exchange rate observed.

When the free ligand loading ratio was ten times to that of the bound-tiopronin, a drop in reaction rate constant was observed with all four derivatives. This is probably due to the spatially hindered environments at the monolayer-bulk solution interface caused by the high concentration of added thiol, which prohibited the penetration of the ligands and therefore led to a lower rate of exchange.[202]

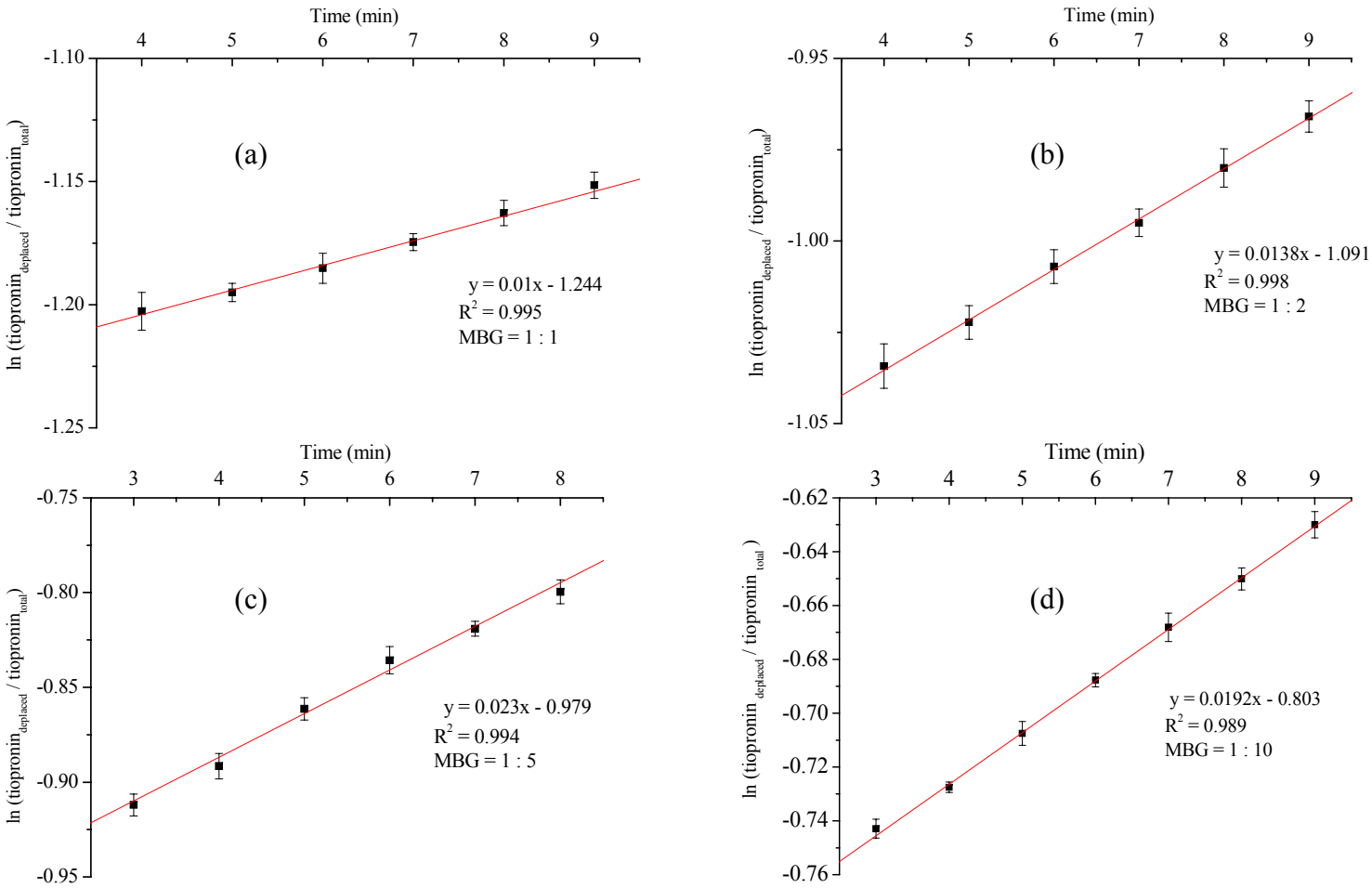

Figure 3.3 Pseudo-first-order rate plot for ligand exchange reaction between Au@tiopronin vs MBG at free MBG loading ratio = (a) 1, (b) 2, (c) 5 and (d) 10 equivalent(s).

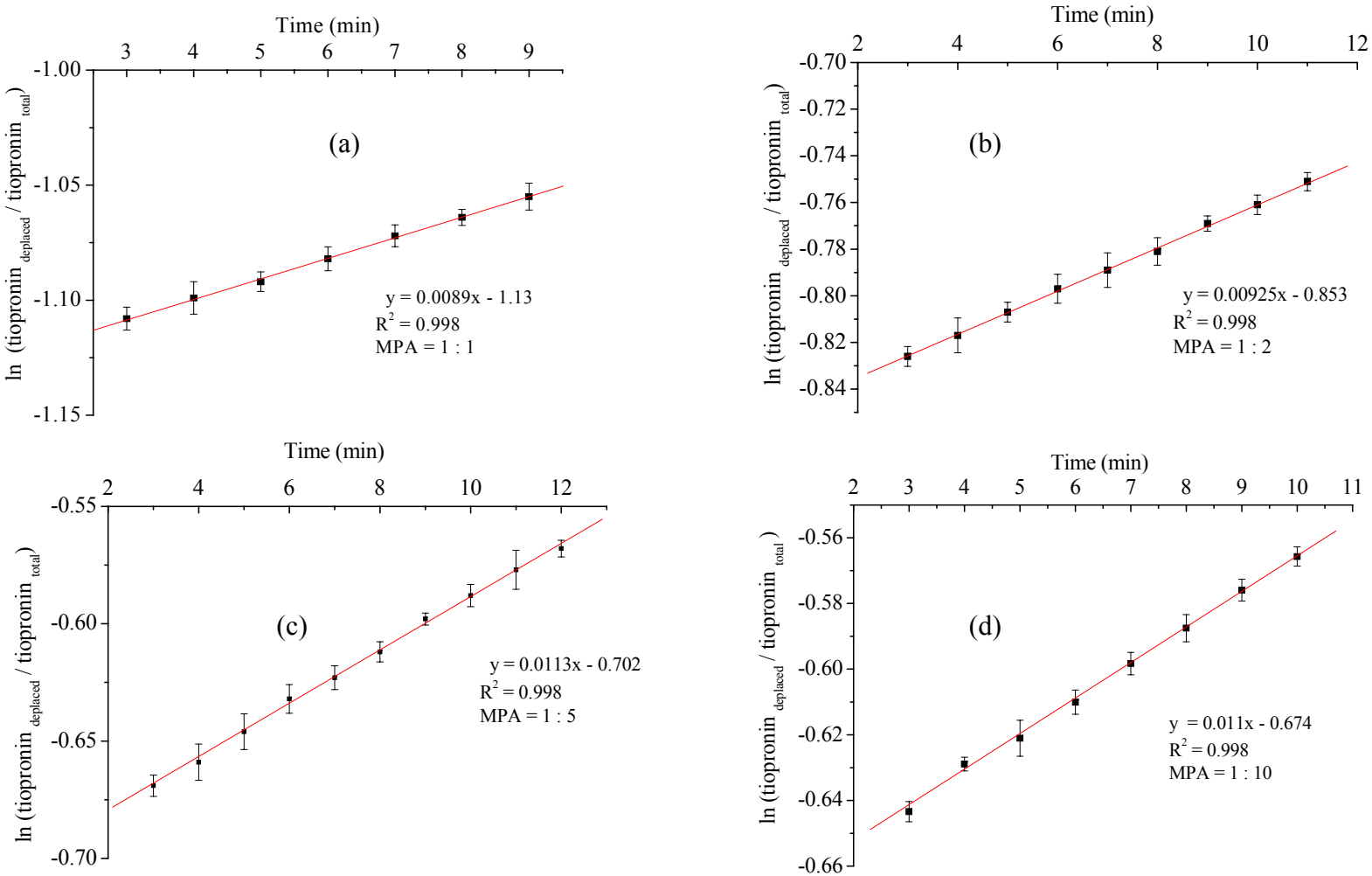

Figure 3.4 Pseudo-first-order rate plot for ligand exchange reaction between Au@tiopronin vs MPA at free MPA loading ratio = (a) 1, (b) 2, (c) 5 and (d) 10 equivalent(s).

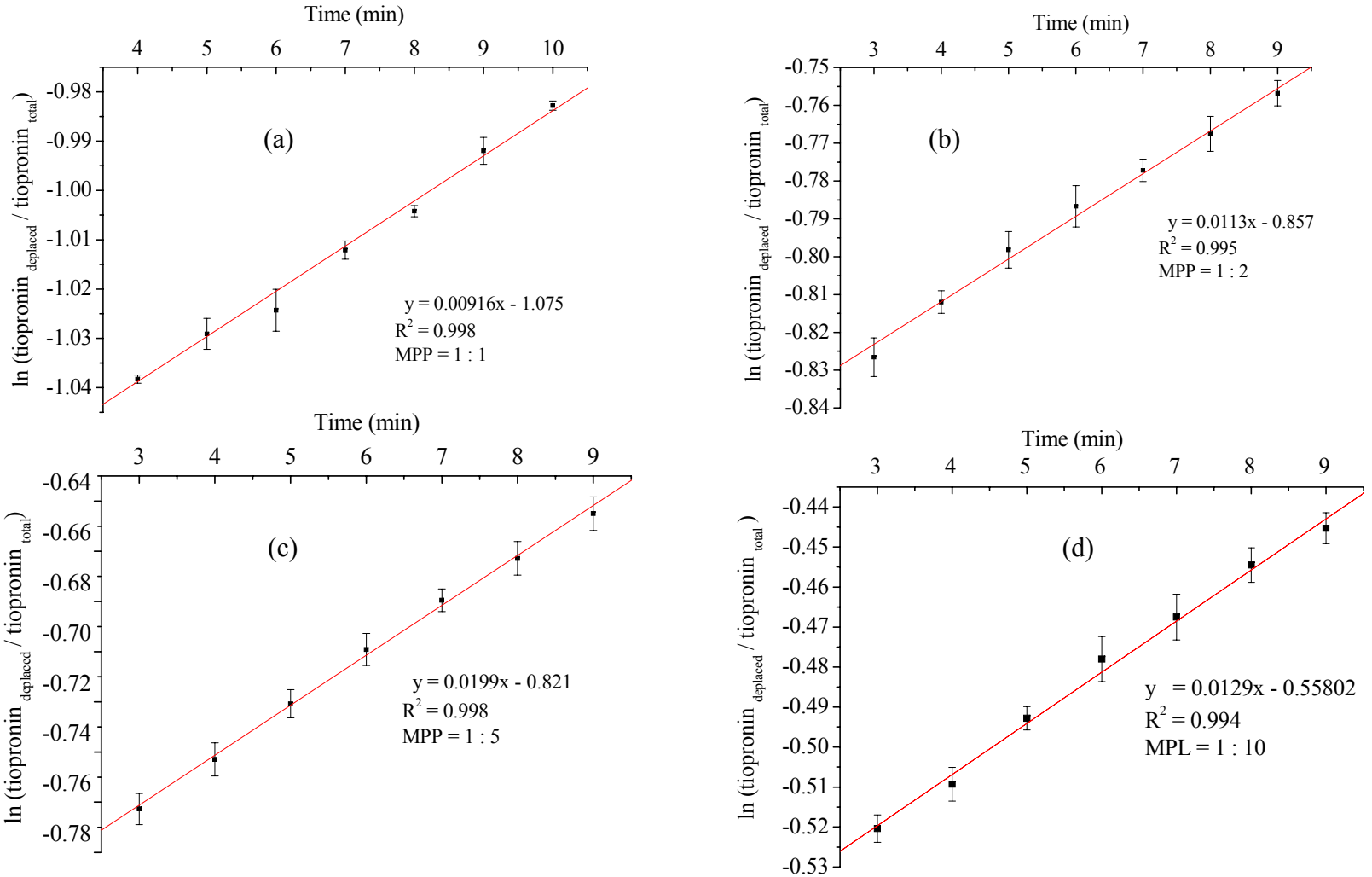

Figure 3.5 Pseudo-first-order rate plot for ligand exchange reaction between Au@tiopronin vs MPP at free MPP loading ratio = (a) 1, (b) 2, (c) 5, and (d) 10 equivalent(s).

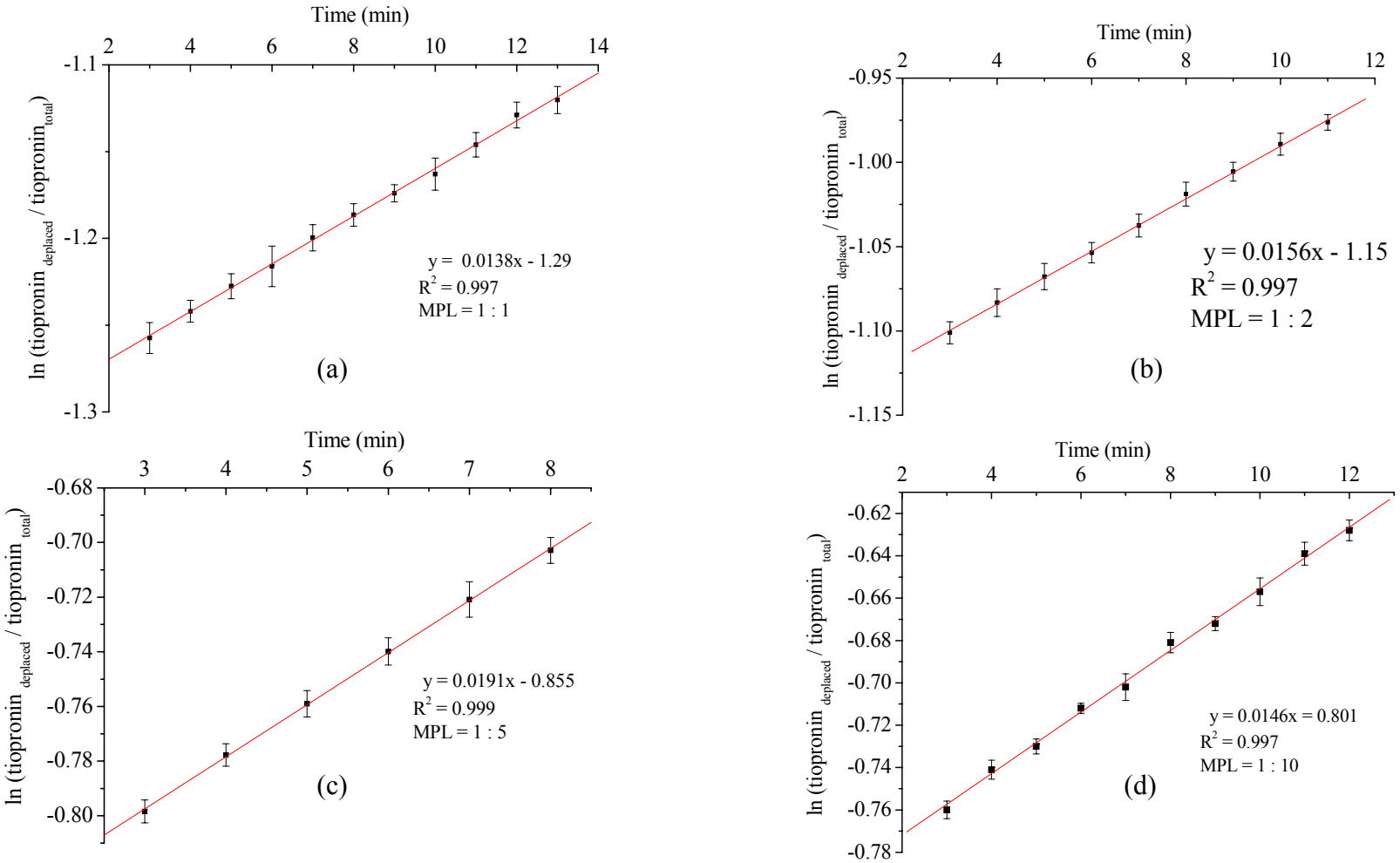

Figure 3.6 Pseudo-first-order rate plot for ligand exchange reaction between Au@tiopronin vs MPL at free MPL loading ratio = (a) 1, (b) 2, (c) 5, and (d) 10 equivalent(s).

Table 3.4 Pseudo first order rate constant (k_{obs}) for exchange reaction between Au@tiopronin and tiopronin-derivatives with free thiol loading ratios of 1, 2, 5 and 10 equivalents.

Pseudo first order rate constant (k_{obs}) , 10^3 s^{-1}				
Free RSH-to -bound RSH	MBG	MPA	MPP	MPL
1 : 1	10.0 ± 0.2	8.9 ± 0.1	9.2 ± 0.1	13.8 ± 0.1
1 : 2	13.8 ± 0.4	9.3 ± 0.1	11.3 ± 0.3	15.6 ± 0.3
1 : 5	23.0 ± 0.1	11.3 ± 0.1	19.9 ± 0.8	19.1 ± 0.1
1 : 10	19.2 ± 0.2	11.0 ± 0.2	12.9 ± 0.1	14.6 ± 0.1

3.3.1.3. Second order plot for exchange reaction between Au@tiopronin and tiopronin-derivatives.

Figures 3.7 – 3.8 and Table 3.5 show the second order plots and the second order rate constant obtained. The second order plots reflect that the pseudo first order rate of the exchange reaction generally shows linear dependence on the concentration of the incoming tiopronin derivatives, except a slight off-linear behavior observed with lower MPA concentration. Such linear dependence strongly indicates that the exchange reaction between the bound tiopronin and the tiopronin derivatives follows an overall second order kinetics:

$$k_{obs} = k_2 \text{ [concentration of tiopronin derivatives]}$$

,where k_2 is the second order rate constant for the exchange process and k_{obs} is the observed pseudo first order rate constant. The linear relationship obtained in the second order plot obviously demonstrates that the ligand exchange between the free tiopronin-derivatives and the tiopronin on a $Au_{180\text{-}201}$ core surface proceeds through an associative pathway, which is consistent with previous reports[83,87] and the well-accepted mechanism for ligand exchange on gold surface.[203]

The second order rate constants obtained follow the order:

$$MPA < MPL < MPP < MBG$$

The largest k_2 obtained for MBG may be due to its ability to form most stable monolayer, which facilitates the departure of tiopronin initially bound on the gold

cluster.

The kinetic data for the ligand exchange reaction with tiopronin derivatives were not completely ideal. Similar to the exchange reaction between p-nitrothiophenol and octanethiol-capped[83] or phenylethanethiol-capped[85,86] gold nanoparticles, the second order plots for all derivatives show a non-zero y-intercept. This may be explained by the co-existence of competing processes like dissociation and oxidation-promoted exchange, which could lead to the observed non-ideal behavior. Previous reports indicated that the non-ideal behavior is insignificant in exchange reaction with ligands without electron-withdrawing substituents and the very small nanoparticles (e.g. Au_{38}).[86] The non-ideal behavior observed in the present study may be attributed to the larger gold nanoparticles core (~ Au_{180} – Au_{245}) and the electron-withdrawing property of the tiopronin derivatives.

Since the first order rate constants obtained from ten equivalents of free thiol loading did not follow the linear up-rising trend due to spatial hindrance effect of excess thiol, the second order plot was only constructed with the first order rate constants from thiol loadings of one to five equivalents.

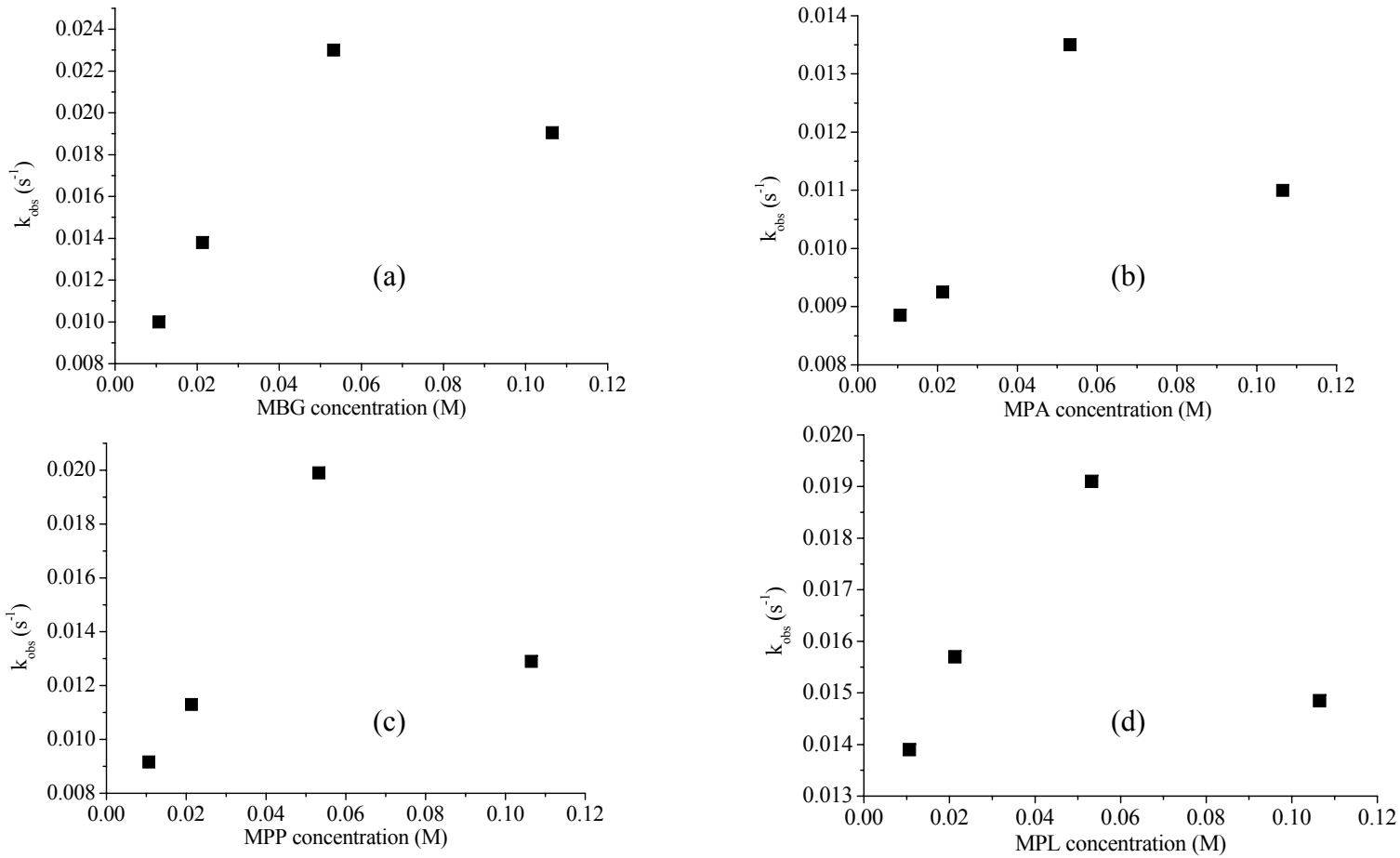

Figure 3.7 Second order rate plot for ligand exchange reaction between Au@tiopronin and (a) MBG, (b) MPA, (c) MPP, and (d) MPL. k_{obs} refers to the pseudo first order rate constant for respective tiopronin-derivative obtained from Figure 3.2 – 3.5.

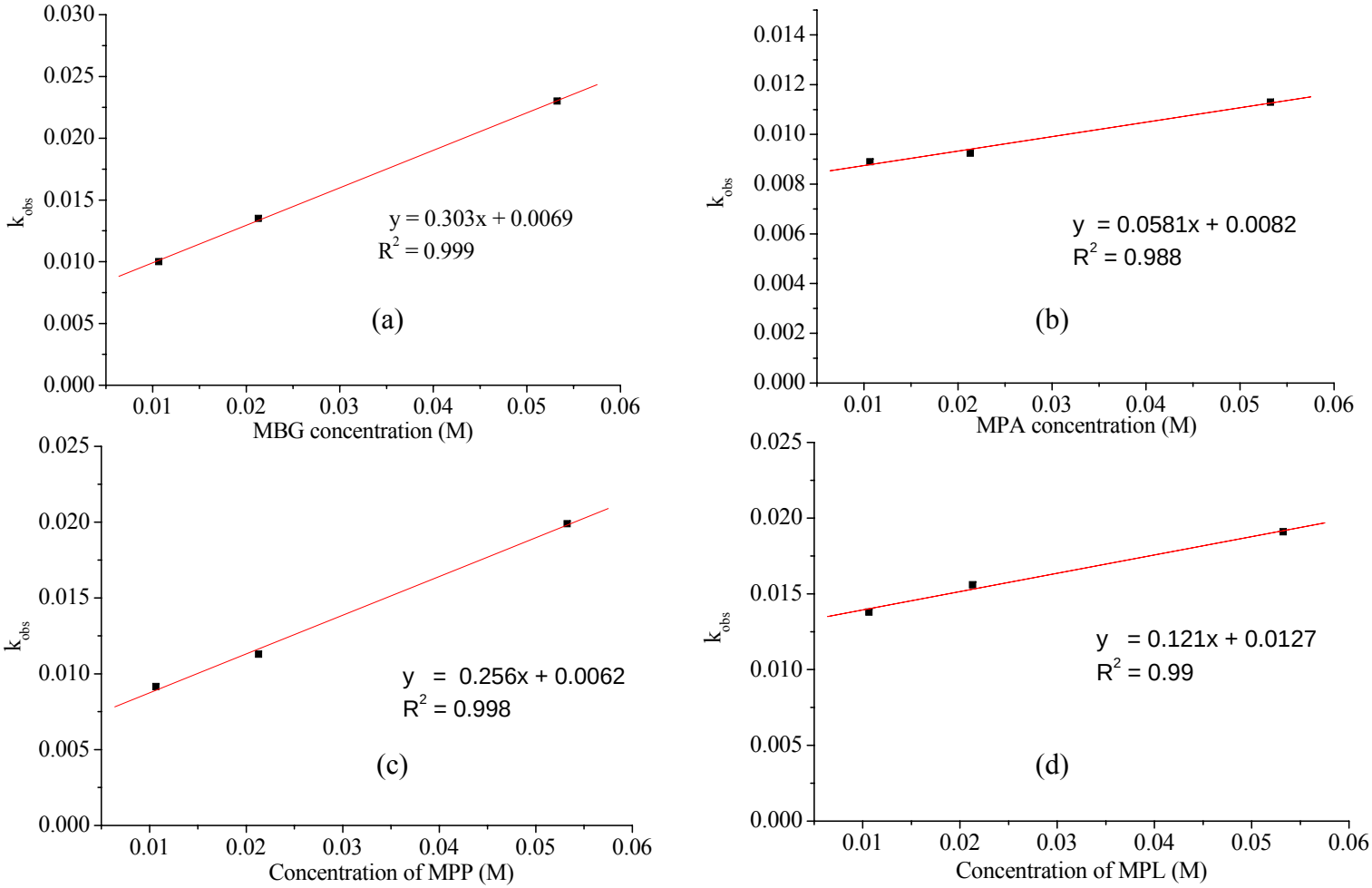

Figure 3.8 Linear fit of the second order rate plot for ligand exchange reaction between Au@tiopronin and (a) MBG, (b) MPA, (c) MPP, and (d) MPL. k_{obs} refers to the pseudo first order rate constant for respective tiopronin-derivative obtained from Figure 3.2 – 3.5.

Table 3.5 Second order rate constant (k_2) for the exchange reaction between Au@tiopronin and MBG, MPA, MPP, MPL.

Incoming thiol	Second order rate constant (M^{-1} s^{-1})
MBG	0.30
MPA	0.06
MPP	0.26
MPL	0.12

3.3.2. Ligand exchange reaction between Au@tiopronin-derivatives and free tiopronin

The reverse of the exchange reaction in the previous section was also examined in order to probe the backward reaction kinetics of free tiopronin replacing different tiopronin-derivative monolayers. The seven-day ligand exchange reaction between the four tiopronin-derivative passivated gold nanoparticles and free tiopronin were performed with a tiopronin loading ratio of 5 equivalents.

To follow the progress of the exchange reactions, the integration of selected peak corresponding to a particular structure of the detsorbed tiopronin derivative was monitored. The peak chosen for individual exchange reaction was as follows:

Au@MBG: triplet for the methine proton for MBG (3.43 ppm)

Au@MPA : quartet for the methine proton of the alanine segment of MPA (4.33 ppm)

Au@MPP multiplet for the methine proton of the proline segment of MPP (4.42 ppm)

Au@MPL : quartet for the methine proton of the 2-mercaptopropanoyl segment of MPL (3.47 ppm)

The integrations of the above selected peaks were made reference to the TMSP-Na internal standard in order to allow mutual comparison between ligands.

3.3.2.1. Extent of ligand exchange reaction between tiopronin-derivative capped gold nanoparticles and free tiopronin

Figure 3.9 and Table 3.6 show the reaction progress plots and the comparison between the extent of the forward and the backward reaction for the ligand exchange between tiopronin and its derivatives on gold nanoparticle surface. While the extent of the ligand exchange reaction between the free derivatives and the bound tiopronin converges into a narrow range at both the initial and the equilibrium stage under the same free thiol loading, it spreads over a wider range when the tiopronin was in exchange for the bound derivative. This may imply that the properties of the derivative monolayer were different from each other which were manifested in the exchange reaction.

The extent of reaction at the initial and equilibrium stage for the exchange reaction between Au@MBG / Au@MPA vs tiopronin and Au@tiopronin vs MBG / MPA are very similar. This suggests that a slight increase in side chain bulkiness at the mercapto group did not significantly alter the exchange kinetics. On the other hand, discrepancy in the extent of reaction was observed when tiopronin was taken to exchange with monolayer of bulky tiopronin derivatives. The less perfectly packed MPP monolayer suffers from a higher strain and replacement with tiopronin would be alleviated at these higher energy locations. Therefore, a greater portion of MPP desorbed from the monolayer at the early stage of the reaction. In the case of MPL monolayer, the hydrophobic iso-butyl leucine side chain might protect the monolayer against the ligand exchange by steric effect and inter-ligand interaction, giving rise to a lower reaction extent compared to its counterparts.

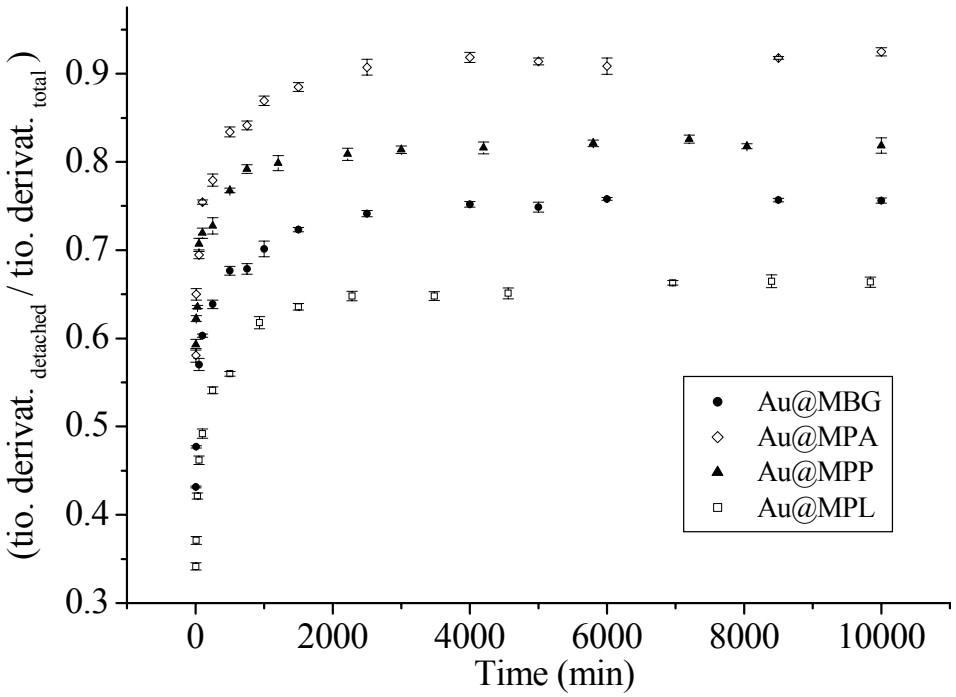

Figure 3.9 Reaction progress plots for ligand exchange between Au@tiopronin-derivatives and free tiopronin. Free ligand loading ratio = 5 equivalents.

Table 3.6 Comparison between the extent of ligand exchange reaction between Au@tiopronin vs tiopronin derivatives (Section 3.4.1.1) and Au@tiopronin derivatives vs free tiopronin. Free ligand loading ratio = 5 equivalents in both cases.

Au@tiopronin vs free tiopronin derivatives (Section 3.4.1.1)								
	MBG		MPA		MPP		MPL	
Tiopronin derivative loading (equivalents)	Initial	Equil.	Initial	Equil.	Initial	Equil.	Initial	Equil.
5	0.41	0.74	0.53	0.83	0.48	0.76	0.47	0.77

Au@Tiopronin derivatives vs free tiopronin								
	Au@MBG		Au@MPA		Au@MPP		Au@MPL	
Tiopronin loading (equivalents)	Initial	Equil.	Initial	Equil.	Initial	Equil.	Initial	Equil.
5	0.43	0.76	0.58	0.93	0.59	0.82	0.34	0.66

3.3.2.2. Pseudo-first order plot for the exchange reaction between Au@tiopronin derivatives and free tiopronin

Figure 3.10 and Table 3.7 show the initial rate plots and the pseudo first order rate constant for exchange reaction of individual Au@tiopronin-derivative nanoparticles. It can be seen that the ligand exchange reaction between the free tiopronin and the four tiopronin-derivative passivated gold nanoparticles obey the pseudo first order behavior with respect to the incoming ligand concentration.

By comparing the pseudo first order rate constant of the reaction obtained in the previous section and the reverse reaction presented in this section, it can be seen that there is in general insignificant difference between the two opposite reactions for the derivatives in aqueous medium. This is contrary to a previous report by Guo *et al*.[86] who studied the exchange reaction between a series of para-substituted thiophenol with phenylethanethiol capped gold nanoparticles of very small size (Au_{38}). The substituents on thiophenol were either electron donating or withdrawing. The author observed a four times faster reaction rate for the forward reaction than the backward reaction.

Both Guo's report and the present study employed the initial first order rate approach to investigate the exchange processes during the rapid exchange period in which the ligands were on high-energy sites like vertexes and edges. In Guo's report, the difference between the forward and the backward reaction rate constant was attributed to the electronic effect of the ligands used. The strongly electron-withdrawing ligands in Guo study, like para-nitrothiolphenol and para-bromothiolphenol, exerted a potent stabilizing effect to the Au-S bond by dissipating the negative charge on the S atom.

This facilitated the entry of the nitro derivative into the phenylethanethiol monolayer already bound on the nanoparticles due to the extra stability acquired. However, the reverse scenario with replacement of the bound nitrothiolphenol monolayer on nanoclusters with the arylalkanethiol was much less favored due to the destruction of the extra stability formed in the monolayer. Therefore, the observed faster forward rate than the reverse one is rational. In the present study, since the difference in electronic effect between tiopronin derivatives was not as prominent as the ligands used in Guo's investigation, the observed similarity of forward and reverse reaction rate constants is reasonable.

On the other hand, the most possible cause for inducing difference in exchange kinetics – steric effect – was very minor in the present reversed ligand exchange study. The anticipated higher steric hindrance in the four tiopronin derivative monolayers on gold nanoparticles, relative to the parent tiopronin monolayer in Au@tiopronin, showed no significant discrimination in the kinetics for the ligand exchange with tiopronin. This may be explained by the highly curved surface of the very small gold nanoparticles used in this study (1.8 – 2.2 nm). The increase in surface curvature of nanoparticles is inversely proportional to the particle size. The molecular footprint of the particle will then be minimized. The molecular footprint can be calculated with the equation[204] -

$$\text{Molecular footprint} = \frac{4\pi r^2}{N}$$

, where N equals to the number of ligands attached to a single nanoparticles and r corresponds to the radius of the nanospheres. For very small size nanoparticles, the molecular footprint of the surface bound thiol will become extremely small. The

average size of the nanoparticles used in this study was ~ 2 nm. Using an average radius of 1 nm for r and N = 114 for the average number of ligand attached onto the four tiopronin derivative capped gold nanoparticles. The generated average molecular footprint of the tiopronin derivatives on gold nanoclusters is 0.11 nm^2, which is about three times less than that for mercapto-tagged PEG adsorbed on nanoparticles of ~ 2.8 nm in diameter.[121] A very small footprint leads to a big deflection angle which implies a wider spatial area around the carboxyl terminal and outweighs the steric effect of ligands. Together with the large amount of defective sites on the ~ 2 nm gold nanoparticles aforementioned, the initial exchange rate constants for both the forward and backward reactions should be similar. This is consistent with the results obtained.

Based on the similar rate constant obtained for the forward and the reverse reactions, the observed rate constant for the exchange reaction may solely be due to the intrinsic kinetic properties of respective tiopronin derivative to anchor onto and to desorb from the gold nanoparticles. Steric factor is only responsible for the minute difference in rate constants between the derivatives.

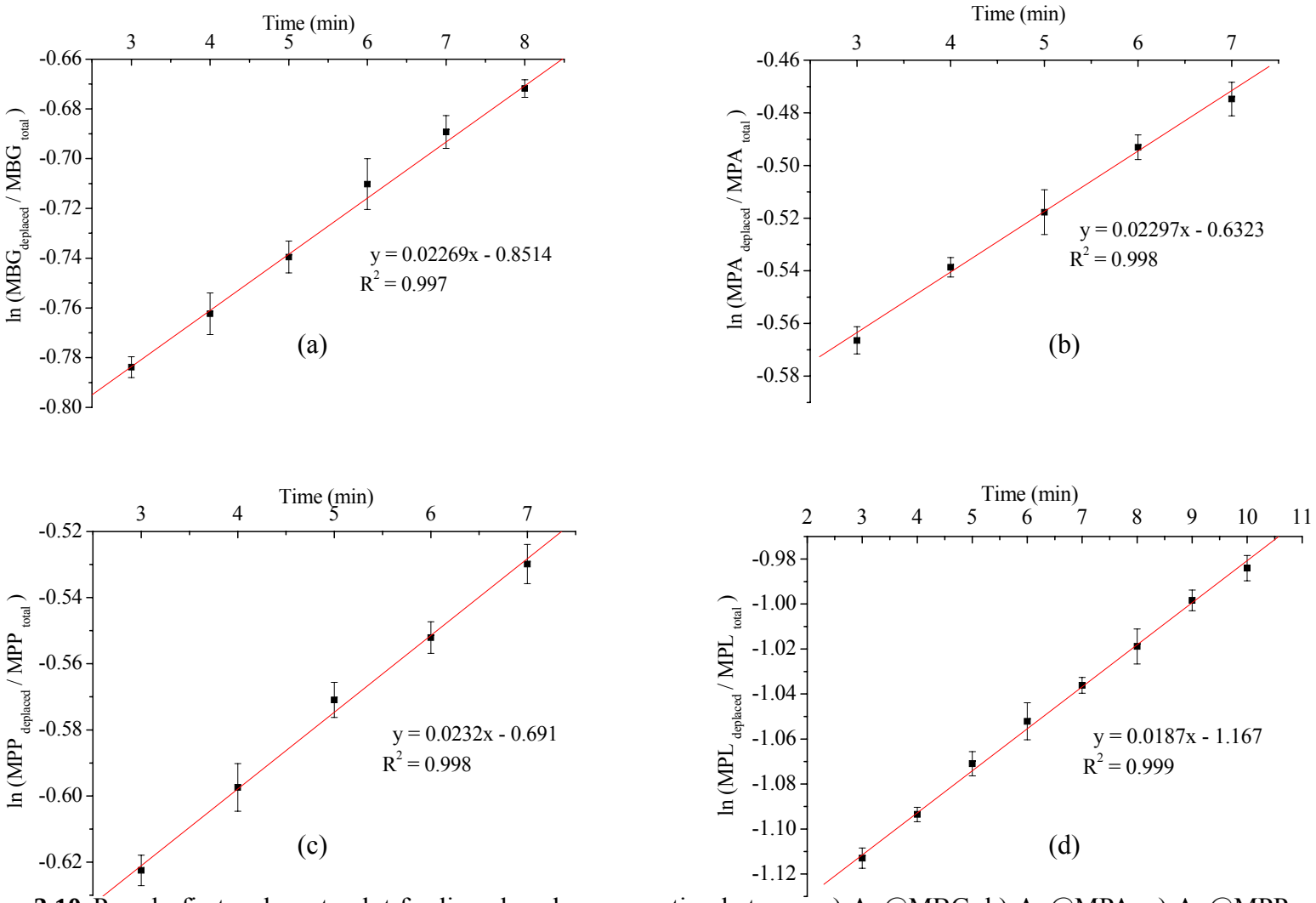

Figure 3.10 Pseudo-first-order rate plot for ligand exchange reaction between a) Au@MBG, b) Au@MPA, c) Au@MPP and d) Au@MPL vs tiopronin at free tiopronin loading ratio = 5 equivalents

Table 3.7 Comparison between the pseudo first order initial rate constant (k_{obs}) for Au@tiopronin vs free tiopronin derivatives (Section 3.4.1.2) and Au@tiopronin-derivatives vs free tiopronin. Free ligand loading ratio = 5 equivalents in both cases.

Pseudo first order initial rate constant (k_{obs}) for Au@tiopronin vs free tiopronin derivatives (Section 3.4.1.2), 10^3 s^{-1}				
Tiopronin derivative loading (equivalents)	MBG	MPA	MPP	MPL
5	23.0 ± 0.1	11.3 ± 0.1	19.9 ± 0.8	19.1 ± 0.1
Pseudo first order initial rate constant (k_{obs}) for Au@tiopronin derivatives vs free tiopronin, 10^3 s^{-1}				
Tiopronin loading (Equivalents)	Au@MBG	Au@MPA	Au@MPP	Au@MPL
5	22.7 ± 0.2	23.0 ± 0.3	23.2 ± 0.3	18.7 ± 0.2

3.3.3. Ligand exchange reaction between Au@tiopronin vs tiopronin derivatives in pH 6.5 aqueous medium

Nearly all reports published on ligand exchange kinetics were conducted in organic solvents or aqueous solution with no deliberate pH adjustment. Carboxyl terminal is sensitive to the change of environment pH and can be deprotonated at higher pH. Removal of proton from ω-carboxyalkanethiol SAM imparts the monolayer a net negative charge. Significant effect imposed on the ligand exchange process thereafter is anticipated.

The ligand exchange reaction between Au@tiopronin and tiopronin derivatives at pH 6.5 were conducted with the same procedures as in previous unbuffered experiments.

In this section, the results of the ligand exchange reactions between Au@tiopronin and the tiopronin derivatives are presented.

3.3.3.1. Ligand exchange reaction between Au@tiopronin versus tiopronin derivatives in pH 6.5 aqueous solution

The free tiopronin derivatives were added to a mixture of Au@tiopronin and dipotassium hydrogenphosphate in deuterated water. After mixing, the resulting solution had a pH value of ~ 6.5. To monitor the reaction progress, the integration of the methyl doublet of tiopronin referenced to the TMSP-Na was used to estimate the quantity of tiopronin detached, which directly reflected the amount of incoming ligand exchanged onto the metal surface. The duration for the ligand exchange reaction of all four tiopronin derivatives was 5000 - 7000 minutes.

3.3.3.1.1. Extent of reaction for ligand exchange reaction - Au@tiopronin and tiopronin derivatives at pH 6.5

Figure 3.11 and Table 3.8 show the reaction progress plots and the extent of reaction for the ligand exchange reaction between Au@tiopronin and tiopronin derivatives at pH 6.5. The data of the extent of reaction indicated that the negatively charged SAM layer caused a great variation among the exchange processes with different derivatives at both the initial and the equilibrium stage.

The initial extent of ligand exchange reaction in pH 6.5 aqueous solution for the four tiopronin-derivatives ranged from 0.27 to 0.50. Compared to the initial stage of the similar reaction in the previous section with no adjustment of medium pH, which spread over a narrower range from 0.41 to 0.53, a significant reduction in tiopronin desorption was observed when the reaction medium was made more alkaline.

Because of electrostatic repulsion, the negatively charged free thiol molecules were much less available to the deprotonated tiopronin monolayer on nanoclusters. Therefore, only a portion of bound-tiopronin on the defective sites of the nanoparticles was replaced by the added derivatives leading to a lower initial extent of reaction. This is in contrast to the complete ligand exchange observed under unbuffered condition.

The small difference in extent of reaction between the bulky side chain amino acid incorporated ligands (MPA, MPP and MPL) may be due to their penetrating abilities into the monolayer carrying a net negative charge, since penetration to the proximity of gold core is the first step for the subsequent exchange event.[83] The initial extent of

reaction increased from MPA to MPL with increasing side chain hindrance. The iso-butyl side chain in MPL might better shield the carboxylate terminal from the surrounding negative charge repulsion and facilitate the penetration of the ligand, leading to a higher initial extent of reaction.

Interestingly, the extent of exchange reaction for MBG was found to be independent of monolayer electrostatic charge status. Since the structural characteristics of MBG is not greatly different from MPA, the difference in the extent of reaction should not be too significant. To substantiate the independent relationship, exchange reactions between Au@tiopronin and different loading ratios of MBG under pH = 6.5 were conducted and the results will be discussed in a later section (section 3.4.3.2).

When the equilibrium stage had been reached, the bulky tiopronin derivatives achieved nearly complete exchange. The final population of tiopronin remained on nanoclusters was < 5 %, which was nearly 18% lowerer than that achieved in exchange reaction under unbuffered condition. This can be explained by the gradual increase in repulsion in terms of steric and electrostatic aspects. As bulky ligands successively anchored on the very small nanoparticles, the original packing of the tiopronin monolayer would be distorted significantly. The strain developed and the extra stability acquired by relieving such stress in the monolayer encouraged the exchange reaction. Therefore, a higher extent of reaction was observed in the cases where MPA, MPP, and MPL were used as the incoming ligand. Meanwhile, the more favorable hydration of the deprotonated glycine than other amino acids with bulky hydrophobic side chain[205] may also a possible reason that led to the nearly complete detachment of tiopronin observed, which also contain a glycine residue.

From the time progress plots for the exchange reaction involving MPA and MPL, it can be seen that the negative charge or the nanoparticle surface strongly affected the exchange process and limited the exchange with bulky ligands at the initial stage. However, a negatively charged monolayer may promote a complete exchange for bulky in-coming ligand at equilibrium.

Table 3.8 The extent of ligand exchange reaction between Au@tiopronin versus tiopronin derivatives at pH 6.5 (a) and unbuffered medium (section 3.4.1.1) (b). The free tiopronin derivative loading ratio was 5 equivalents in both cases.

(a)

Extent of ligand exchange reaction between Au@tiopronin vs tiopronin derivatives at pH 6.5								
Free tiopronin-derivative loading ratio (equivalents)	MBG		MPA		MPP		MPL	
	Initial	Equil.	Initial	Equil.	Initial	Equil.	Initial	Equil.
5	0.49	0.82	0.27	0.94	0.28	0.98	0.35	0.99

(b)

Extent of ligand exchange between Au@tiopronin vs tiopronin derivatives (unbuffered) (Section 3.4.1.1)								
Free tiopronin-derivative loading ratio (equivalents)	MBG		MPA		MPP		MPL	
	Initial	Equil.	Initial	Equil.	Initial	Equil.	Initial	Equil.
5	0.41	0.74	0.53	0.83	0.48	0.76	0.47	0.77

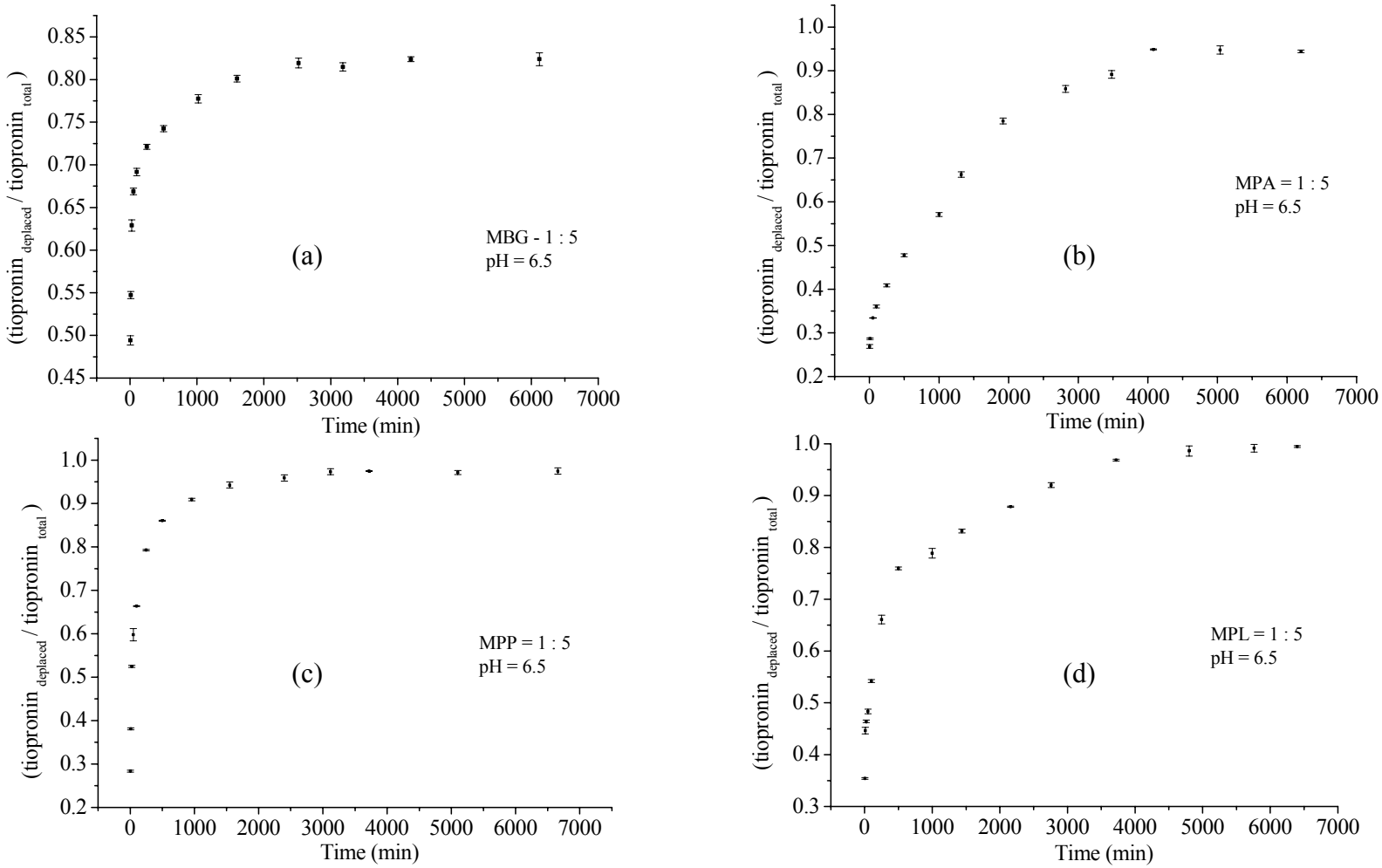

Figure 3.11 Reaction progress for the ligand exchange reaction between Au@tiopronin vs a) MBG, b) MPA, c) MPP and d) MPL vs tiopronin at free tiopronin derivative loading ratio = 5 equivalents. Reaction medium pH = 6.5.

3.3.3.1.2. Pseudo first order reaction rate plot for ligand exchange reaction between Au@tiopronin and tiopronin derivatives at pH 6.5

Figure 3.12 and Table 3.9 show the first order plots and the first order rate constants obtained for exchange reaction in pH 6.5 medium. The net negative charge developed on the monolayer and free thiol yielded larger first order rate constants for ligand exchange reactions compared to those under unbuffered condition. This is particularly true of derivatives constructed by bulky amino acids. The displacement of bound-tiopronin with MBG, on the contrary, always gives a similar rate constant regardless of monolayer electrostatic status.

After a portion of the added thiols had colonized some defect sites on metal surface, the monolayer mismatching between the new and the old ligands was likely to be intensified. The strain developed in the monolayer, enhanced steric hindrance, and electrostatic repulsion widened the inter-ligand distance and the ligand deflection angle. Such changes reduced the packing density and provided easier access for further entry of the in-coming ligands. As previously mentioned, the percentage surface defect for nanoparticles of ~ 2 nm was close to 50%. The observed lower initial extent of reaction (27 – 35 %) suggests that the initial rate plots obtained are actually reflecting the exchange events of the remaining ligands at the defective sites of the nanoparticles. Therefore, a higher rate was anticipated for exchange reaction in less acidic medium.

The larger rate constant for exchange reaction with the more hindered MPL compared to MPA may be explained by the shielding of the leucine iso-butyl side chain around the negatively charged carboxylate ion, which facilitated the penetration of MPL into the

deprotonated tiopronin monolayer.

The proline ring in MPP is bulky, rigid, and located relatively close to the mercapto group. In addition, the carboxyl group on the proline ring is located adjacent to the amide group and structurally points towards the monolayer when bound on gold surface. All these structural properties pose a strong repulsion within the tiopronin monolayer when a deprotonated MPP molecule was exchanged onto the nanocluster surface. Such interaction after MPP implantation is likely to induce a wider passage opening and monolayer distortion, thus further promoting the exchange with MPP molecules. Therefore, a threefold increase in rate constant was observed when MPP was the incoming ligand.

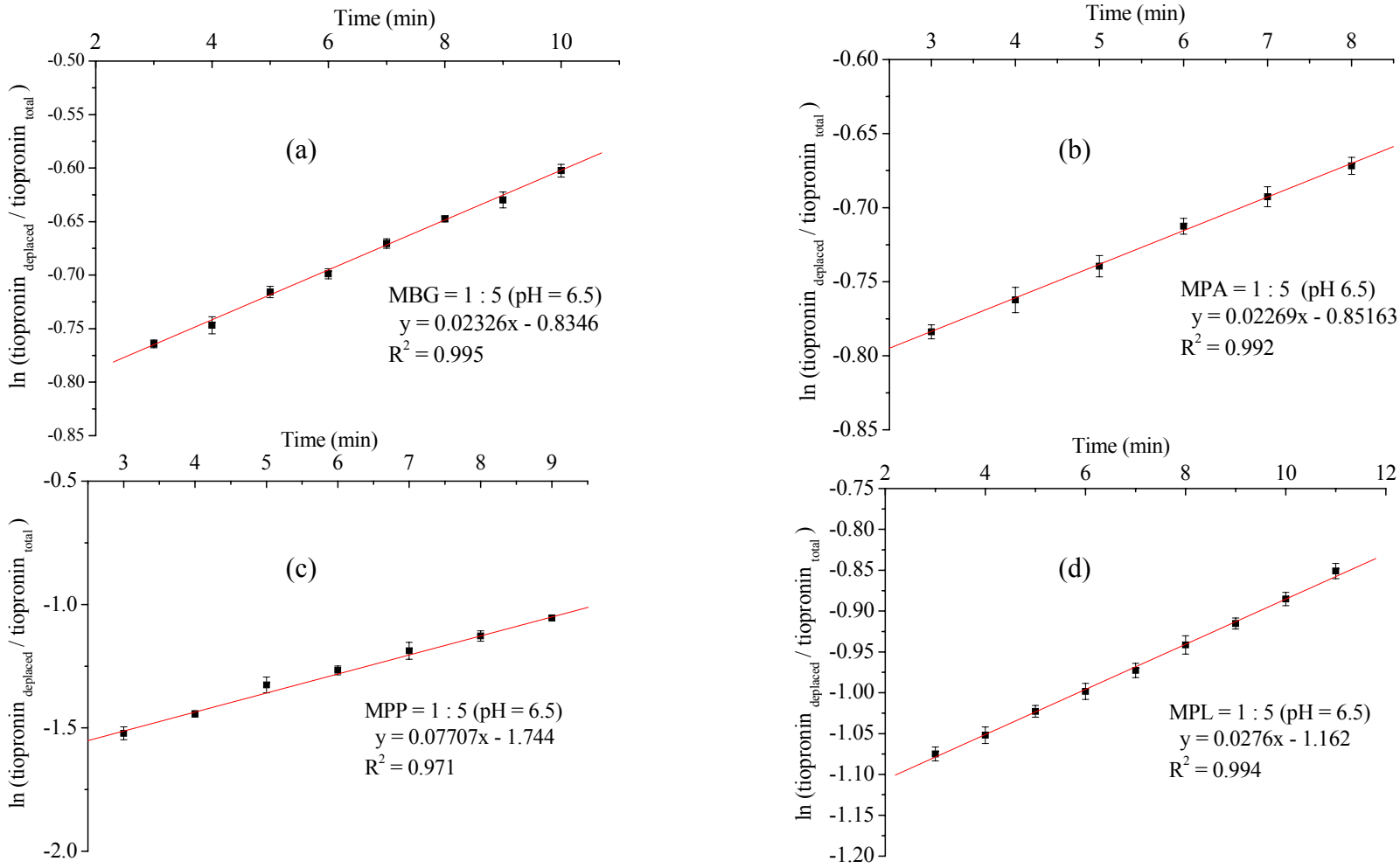

Figure 3.12 Pseudo-first-order rate plot for ligand exchange reaction between Au@tiopronin vs a) MBG, b) MPA, c) MPP, and d) MPL at free tiopronin derivative-to-bound-tiopronin ratio = 5. Reaction medium pH = 6.5.

Table 3.9 Pseudo first order rate constant of ligand exchange reaction between Au@tiopronin versus tiopronin derivatives (a) at pH 6.5 and (b) in unbuffered medium (Section 3.4.1.2). The free tiopronin derivative loading ratio was 5 equivalents in both cases.

(a)

Pseudo first order rate constant of ligand exchange between Au@tiopronin vs tiopronin derivatives at pH 6.5, 10^3 s^{-1}				
Free thiol used / Free thiol loading	MBG	MPA	MPP	MPL
5 equivalents	23.3 ± 0.3	22.7 ± 0.2	77 ± 2	27.6 ± 0.1

(b)

Pseudo first order rate constant of ligand exchange between Au@tiopronin vs tiopronin derivatives without pH adjustment, 10^3 s^{-1} (Section 3.4.1.2)				
Free thiol used / Free thiol loading	MBG	MPA	MPP	MPL
5 equivalents	23.0 ± 0.1	11.3 ± 0.1	19.9 ± 0.8	19.1 ± 0.1

3.3.3.2. Ligand exchange reaction between Au@tiopronin vs MBG at pH 6.5 with different MBG loadings

From the result in section 3.4.3.1, the similar pseudo first order rate constants under buffered and unbuffered conditions seems to suggest that the ligand exchange reaction between Au@tiopronin and MBG is independent of the electrostatic charge. In order to prove such relationship, a set of ligand exchange reactions between Au@tiopronin and MBG at pH 6.5 was performed with different MBG loading ratios. The duration for each exchange process was 5000 – 8000 minutes.

3.3.3.2.1. Extent of ligand exchange between Au@tiopronin vs MBG at pH 6.5 with different MBG loadings

Figure 3.13 and Table 3.10 show the time progress plot and extent of reaction for the ligand exchange between Au@tiopronin and MBG in pH 6.5 medium at different MBG loadings. It can be seen that the initial extent of reaction increased gradually from ~ 25% to 50 % when the MBG content increased successively. The initial extent of reaction leveled off after five equivalents of MBG were added and no further exchange was observed with further increase in the MBG content. Similar trend was also observed in the extent of reaction at equilibrium.

Compared with the experiments in unbuffered media, the extent of reaction achieved at the initial and equilibrium stage were quite similar. A slight difference only appeared at the initial stage when one to two equivalent of MBG was added. This indicates that the extent of reaction is sensitive to thiol loading and a change in electrostatic status did not alter much the thermodynamics of the exchange process involving MBG.

At higher thiol loadings, all the vertexes- or edges-bound tiopronin were ‘instantly’ exchanged similar to the situation in unbuffered medium. The vast quantity of incoming ligands around the monolayer counteracted the repulsion present and led to a prompt replacement.

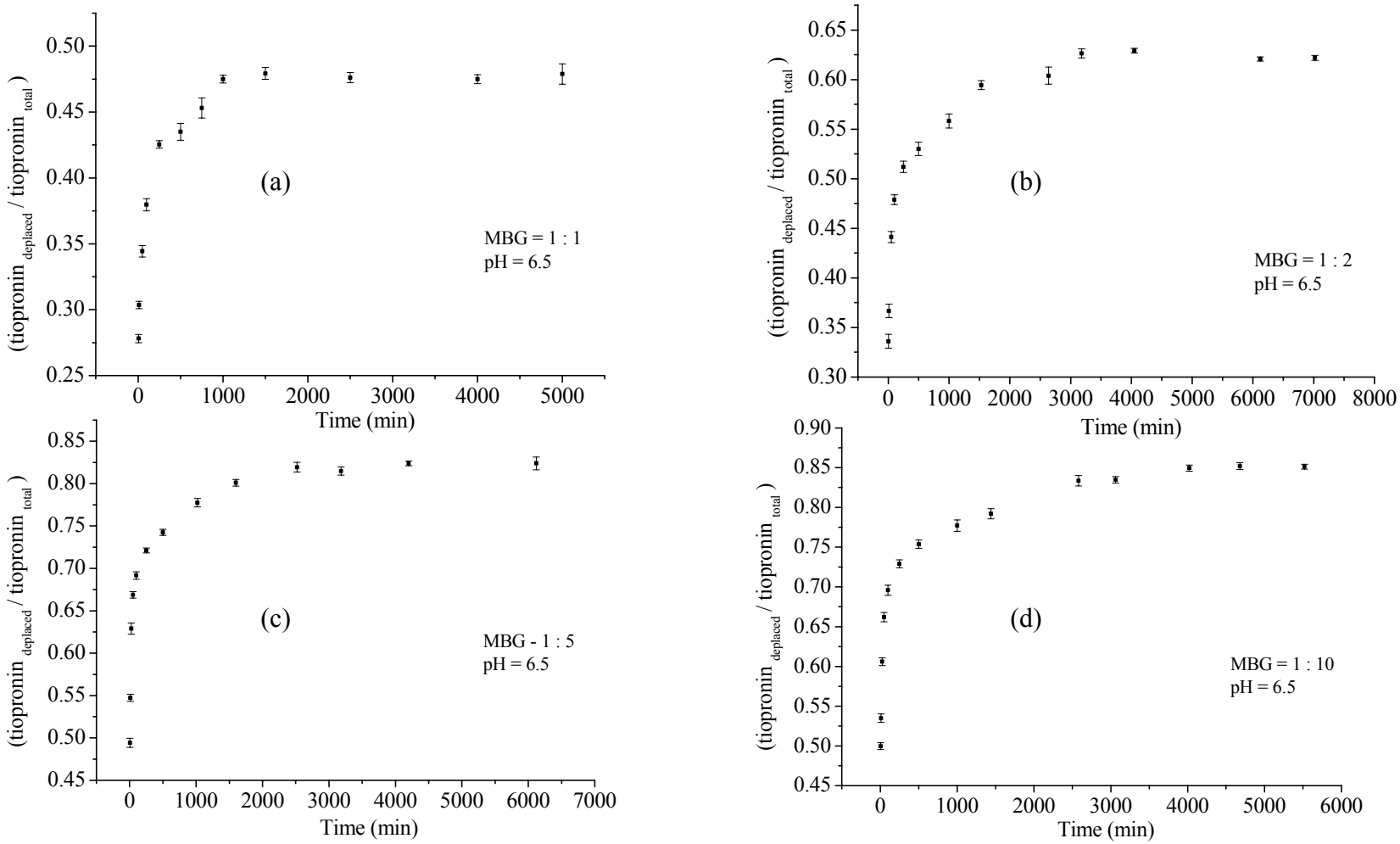

Figure 3.13 Reaction progress plot for the ligand exchange reaction between Au@tiopronin vs MBG with free MBG loading ratio = (a) 1, (b) 2, (c) 5, and (d) 10 equivalents and reaction medium pH = 6.5.

Table 3.10 The extent of ligand exchange reaction between Au@tiopronin versus MBG at (a) pH 6.5 and (b) unbuffered medium (section 3.4.1). The free tiopronin derivative loading ratios are 1, 2, 5, and 10 equivalent(s) in both cases.

(a)

Extent ligand exchange reaction between Au@tiopronin vs MBG at pH 6.5								
Free thiol loading / Free thiol used	1 equivalent		2 equivalents		5 equivalents		10 equivalents	
	Initial	Equil.	Initial	Equil.	Initial	Equil.	Initial	Equil.
MBG	0.25	0.44	0.31	0.55	0.49	0.82	0.50	0.85

(b)

Extent of ligand exchange reaction between Au@tiopronin vs MBG with unbuffered medium (Section 3.4.1.1)								
Free thiol loading / Free thiol used	1 equivalent		2 equivalents		5 equivalents		10 equivalents	
	Initial	Equil.	Initial	Equil.	Initial	Equil.	Initial	Equil.
MBG	0.31	0.40	0.37	0.55	0.41	0.74	0.53	0.89

3.3.3.2.2. Pseudo first order plot for the ligand exchange between Au@tiopronin vs MBG with different MBG loadings at pH 6.5

Figure 3.14 and Table 3.11 show the pseudo first order plots and the first order rate constants obtained for the ligand exchange reaction between Au@tiopronin and MBG under medium pH 6.5 and with different MBG loadings. The rate constant increased steadily from one to five equivalents and dropped significantly when ten equivalents of MBG were added. This is consistent with the results under unbuffered condition reported in previous sections.

When compared with the experiments under unbuffered condition, larger rate constants were obtained at pH 6.5 with lower thiol loadings. Thus the ligand exchange proceeded more quickly at higher pH. It seems rather contradictory that a higher reaction rate was observed when electrostatic repulsion was in effect. However, as previously discussed, about half of the tiopronin on metal core defect sites were not exchanged for MBG when the initial rate of the exchange process was measured, the rate constant obtained for the experiments with one and two equivalents at pH 6.5 actually reflected the exchange events of the labile bound-tiopronin and therefore a higher rate was observed. The combined contributions from the monolayer defects generated by the entry of MBG ligand and the electrostatic repulsion of carboxylate groups may caused the faster departure of the liable tiopronin ligand, which gives rise to the higher exchange rate under buffered condition with low thiol loadings.

With five equivalents MBG loading, the rate constant of the exchange reaction seems to become almost pH independent because of the similar value obtained under buffered

and unbuffered condition. As reflected by the initial extent of reaction, the nanoparticle surface defective sites were fully occupied once the thiol and the nanoparticles were mixed. It is likely that only the exchange at less reactive terrace sites was recorded during the initial rate estimation. Therefore, the effect of the pH on the rate constants under such condition appears minimal.

A sudden drop in reaction rate constant can be observed with ten equivalents MBG loading in both buffered and unbuffered media. Under such condition, the steric and electrostatic repulsion developed near the monolayer blocked the access of free MBG. Therefore, a lower reaction rate is expected.

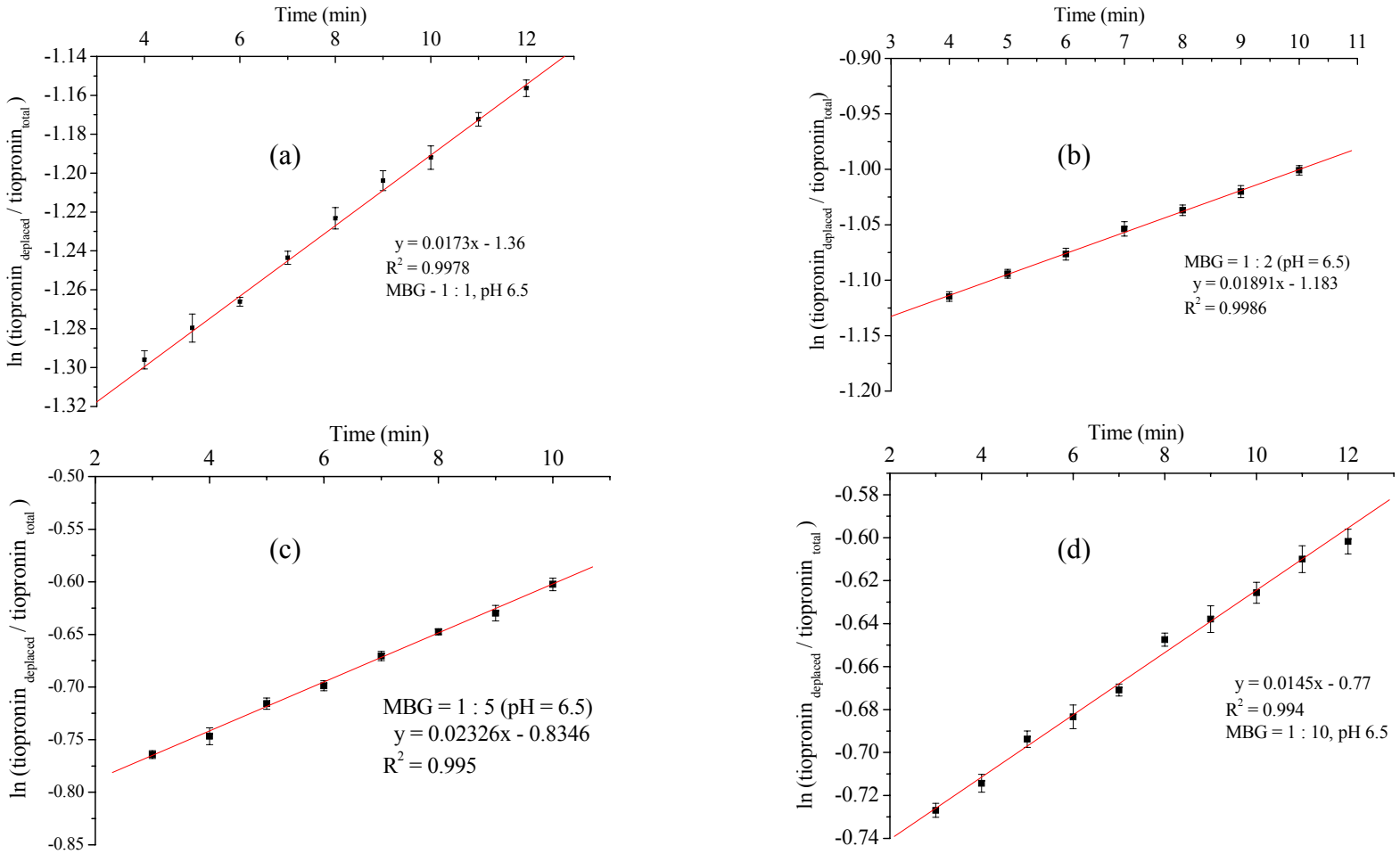

Figure 3.14 Pseudo-first-order rate plot for ligand exchange reaction between Au@tiopronin vs MBG with free MBG loading ratio of (a) 1, (b) 2 (c) 5, and (d) 10 equivalents. Reaction medium pH = 6.5.

Table 3.11 The first order rate constant of ligand exchange reaction between Au@tiopronin versus MBG at (a) pH 6.5 and (b) unbuffered medium (section 3.4.1.2). The free tiopronin derivatives loading ratio used were 1, 2, 5 and 10 equivalent(s).

(a)

First order rate constant (k_{obs}) of ligand exchange between Au@tiopronin vs MBG at pH 6.5 (Section 3.4.1.2) , 10^3 s^{-1}				
Free thiol loading / Free thiol used	1 equivalent	2 equivalents	5 equivalents	10 equivalents
MBG	17.3 ± 0.1	18.8 ± 0.1	23.3 ± 0.3	15.4 ± 0.3

(b)

First order rate constant (k_{obs}) of ligand exchange between Au@tiopronin vs MBG in non-buffered medium, 10^3 s^{-1}				
Free thiol loading / Free thiol used	1 equivalent	2 equivalents	5 equivalents	10 equivalents
MBG	10.0 ± 0.2	13.8 ± 0.4	23.0 ± 0.1	19.2 ± 0.2

3.3.3.2.3. Second order plot for ligand exchange reaction between Au@tiopronin nanoparticles and MBG at pH 6.5

The linear relationship established in the second order plot in Figure 3.15 indicats that the ligand exchange at pH 6.5 also proceeds through an associative mechanism, which is consistent with the reaction mechanism in unbuffered condition and previous studies.

In the previous section, it can be seen that the rate of exchange reaction still depends on the amount of free thiol added to the reaction medium when both the monolayer and incoming thiol were negatively charged under buffered condition. To illustrate the strength of such dependence, the second order plot of the first order rate constant against the concentration of free thiol was constructed.

The second order rate constant for the Au@tiopronin vs MBG exchange reaction at pH 6.5 is 0.148 $M^{-1}s^{-1}$, which is only half of that under the more acidic unbuffered condition (0.303 $M^{-1}s^{-1}$). As the second order rate constant is the slope of the plot, a steeper slope (larger second order rate constant) suggests that the change in the pseudo first order rate constant, i.e. the rate of the exchange reaction, shows a stronger dependence on the free thiol loading. Therefore, the smaller second order rate constant obtained in buffered condition indicates that exchange kinetics becomes less dependent on the quantity of thiol added when both the monolayer and incoming thiol carry the same charge.

Based on the results obtained, it can be seen that the electrostatic charging of the monolayer and the free thiol significantly affect the kinetics and the thermodynamics of

the exchange reaction. However, the effect of the negative charging is ligand sensitive. The dependence of the exchange kinetics on the quantity of free thiol added and the extent of the reaction at different stages vary between thiols.

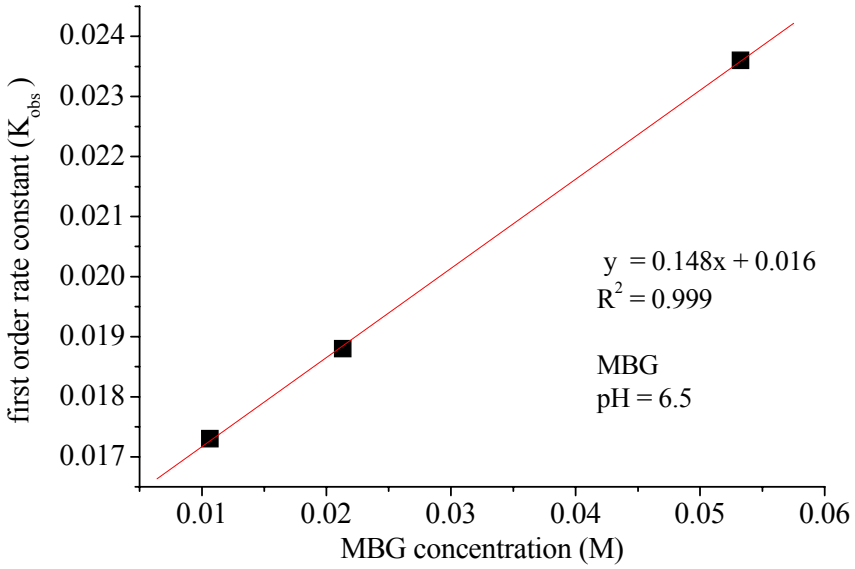

Figure 3.15 Second order rate plot for ligand exchange reaction between Au@tiopronin and MBG at reaction medium pH = 6.5. k_{obs} refers to the pseudo first order rate constant for respective tiopronin-derivative obtained from Figure 12 and 14.

3.3.4. Second order Langmuir diffusion-limited fitting of the ligand exchange reaction profile

Apart from the most popular initial rate method for examining ligand exchange kinetics occurring on gold nanoparticles surface, the second-order Langmuir diffusion-limited model was recently found useful in describing the entire progress of the exchange reaction. The equation for the model is as follows:

$$\Theta(t) = \frac{Ak\sqrt{t}}{1 + k\sqrt{t}}$$

,where Θ(t), A, and K are the instantaneous reaction extent, maximum fractional surface coverage of in-coming ligand, and rate constant, respectively. While Kassam *et al.* obtained a good fitting of the model to his kinetic data for the exchange reaction involving alkanethiols in organic solvent, the potential use of this model in depicting the kinetics of the ligand exchange reaction in aqueous medium with polar thiols deserves detailed investigation.

The reaction progress data of the ligand exchange reactions between the tiopronin and its derivatives on gold nanoparticles in buffered and unbuffered conditons were examined if they could be described by the second order Langmuir diffusion-limited model.

3.3.4.1. Fitting of the reaction profile of exchange reaction between Au@tiopronin and tiopronin-derivatives

Figures 3.16 – 3.19 show the time progress plots for ligand exchange reaction between Au@tiopronin and the free tiopronin-derivatives fitted with the second order Langmuir diffusion-limited model. The time progress plots at one equivalent loading for all derivatives were generally well described by the model. However, the plots of higher free-thiol loadings show derivation from the model, especially when approaching equilibrium stage. This may indicate that other exchange modes were in effect at this slow exchanging period.

The lower thiol loadings reaction progress plots of all derivatives are generally in better agreement with the second-order diffusion-limited model. This suggests that diffusion process plays an active role in the exchange process under polar medium with limited supply of free thiol and the exchange is associative in nature.

A study on surfactant micelle assisted alkanethiol self-assemble monolayer (SAM) formation on gold surface by Yan *et al*.[206] suggested that the reaction progress is well-described by the second order Langmuir diffusion-limited model. The good agreement between their experimental data and the model suggested that the SAM formation followed a reaction scheme involving the activated diffusion of thiol into the admicelles followed by the associative interaction between the physisorbed alkanethiol and the adsorbed surfactant molecule. Based on the similar fitting result, the exchange reaction of the tiopronin derivatives at lower thiol loading should be in similar fashion as the thiol/surfactant displacement proposed by Yan.

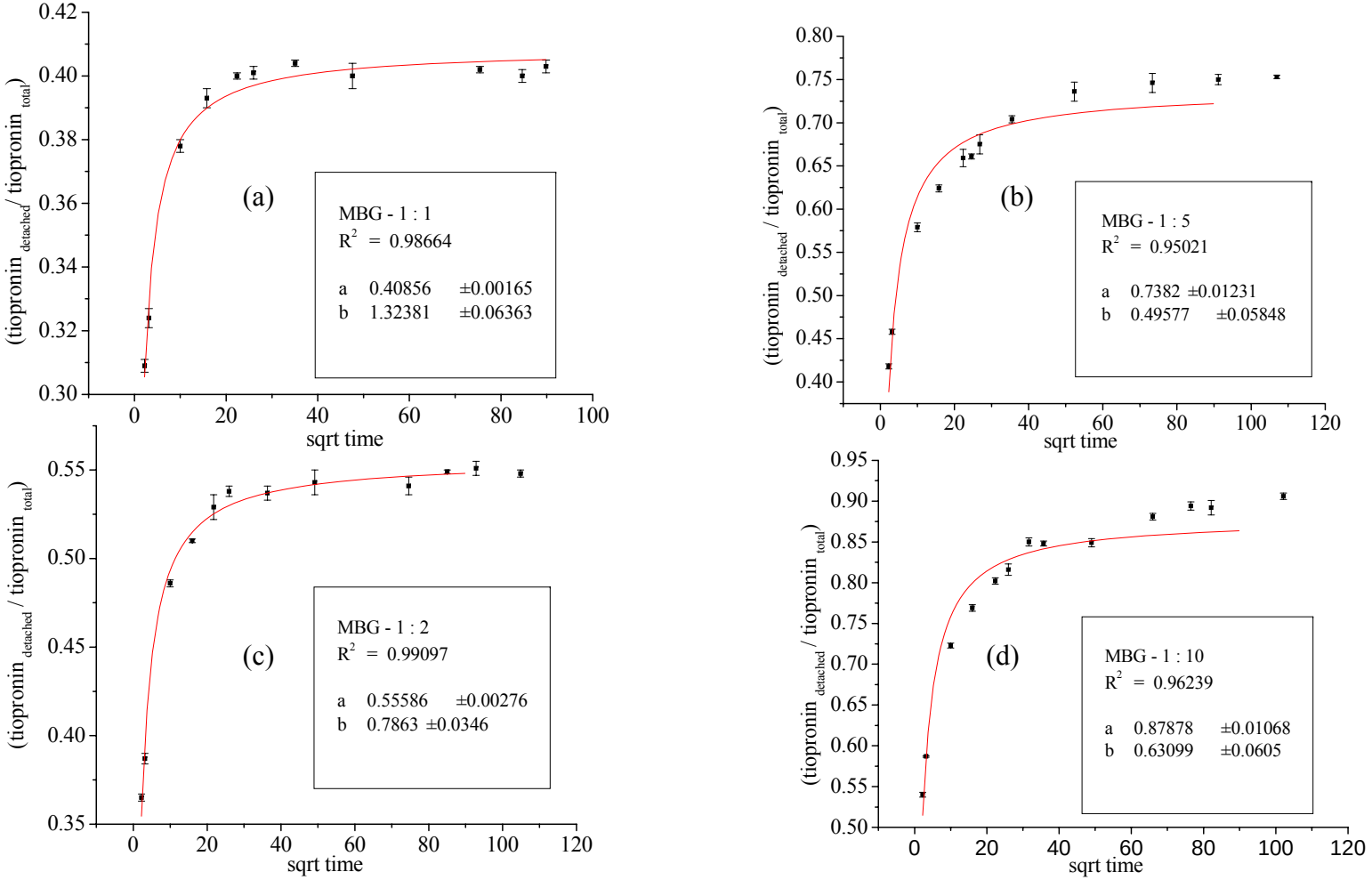

Figure 3.16 Second order Langmuir diffusion-limited fitting for the ligand exchange reaction progress between Au@tiopronin vs MBG at free MBG loading ratios of (a) 1, (b) 2, (c) 5, and (d) 10 equivalent(s).

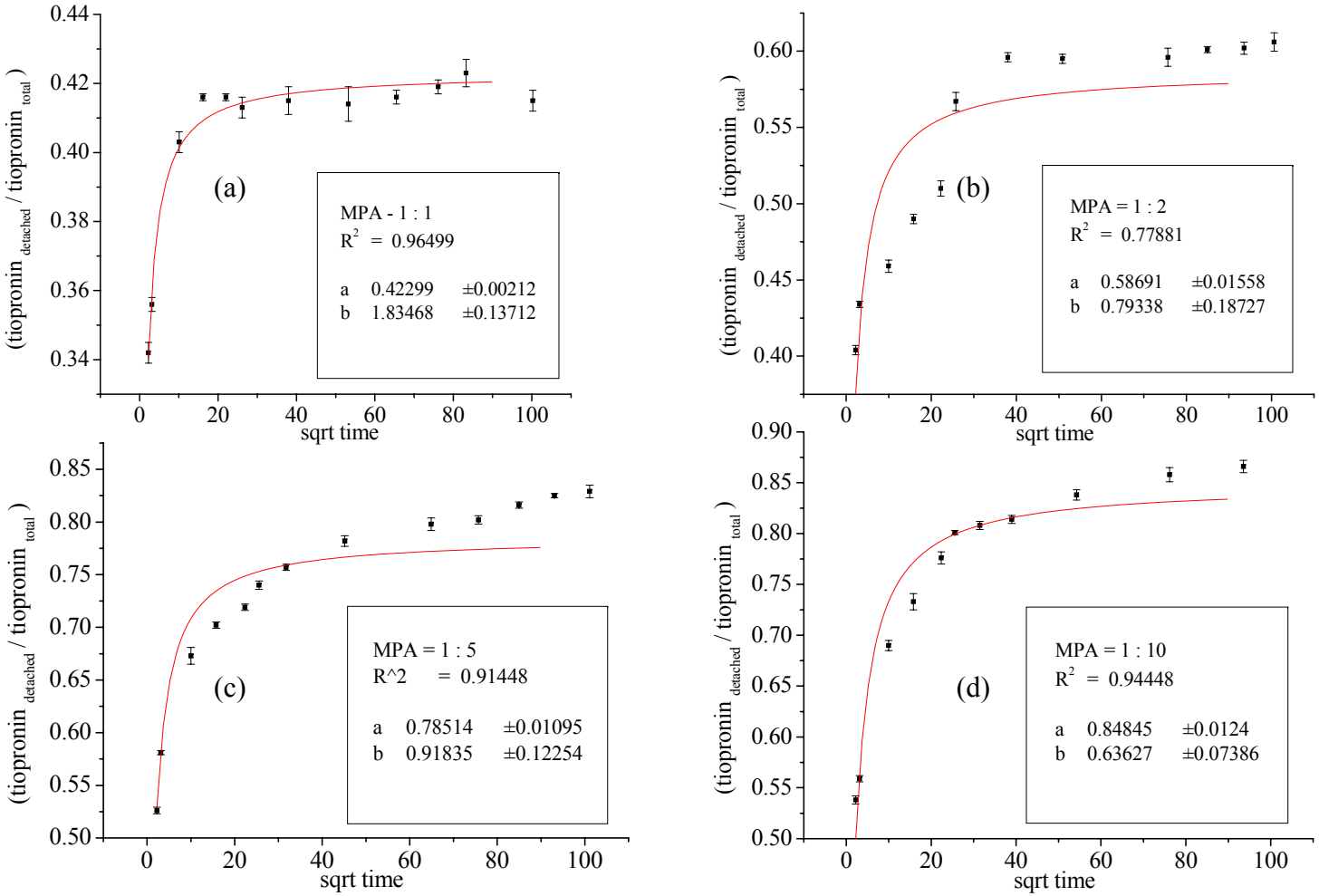

Figure 3.17 Second order Langmuir diffusion-limited fitting for the ligand exchange reaction progress between Au@tiopronin vs MPA at free MPA loading ratios of (a) 1, (b) 2, (c) 5, and (d) 10 equivalent(s).

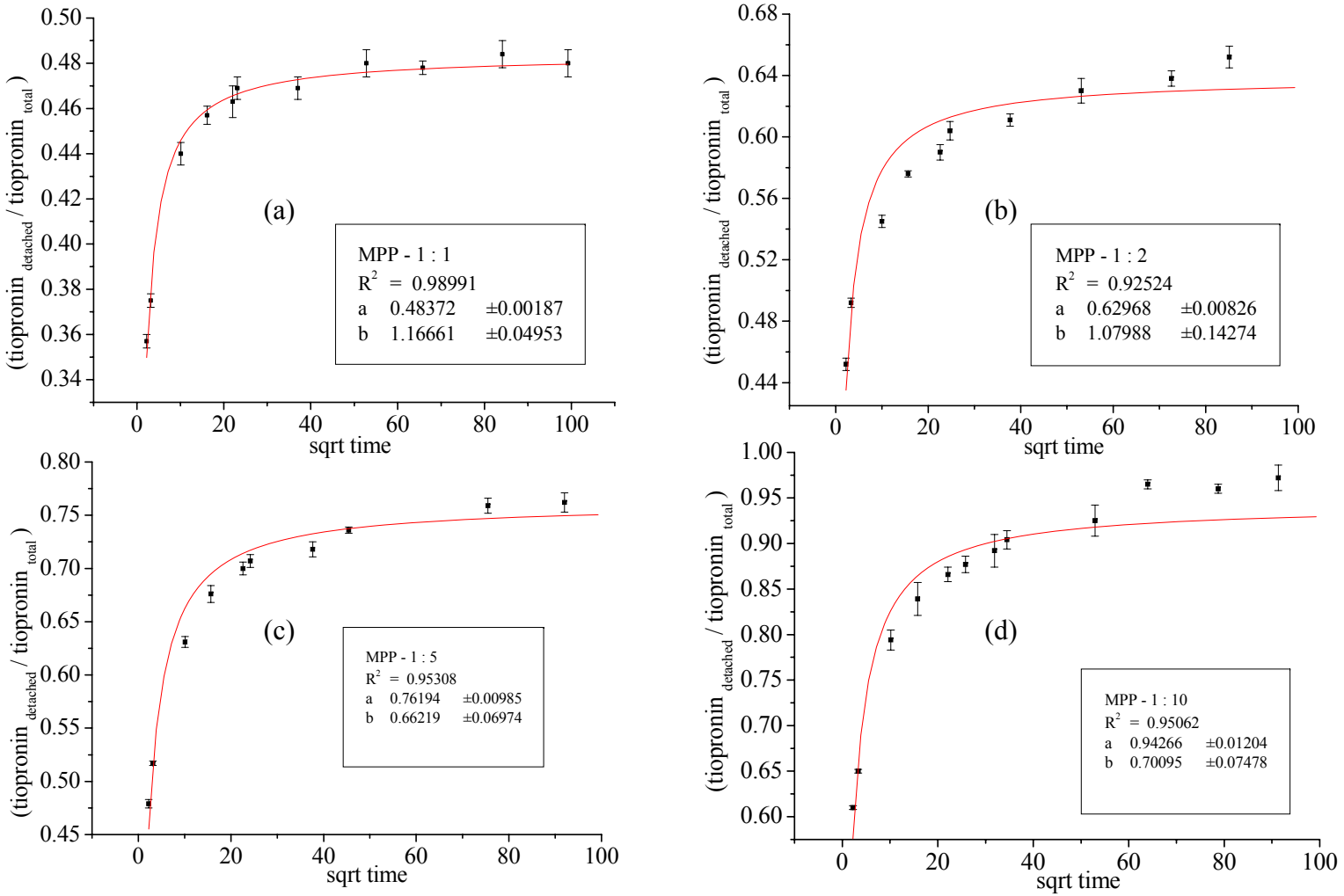

Figure 3.18 Second order Langmuir diffusion-limited fitting for the ligand exchange reaction progress between Au@tiopronin vs MPP at free MPP loading ratios of (a) 1, (b) 2, (c) 5, and (d) 10.equivalent(s).

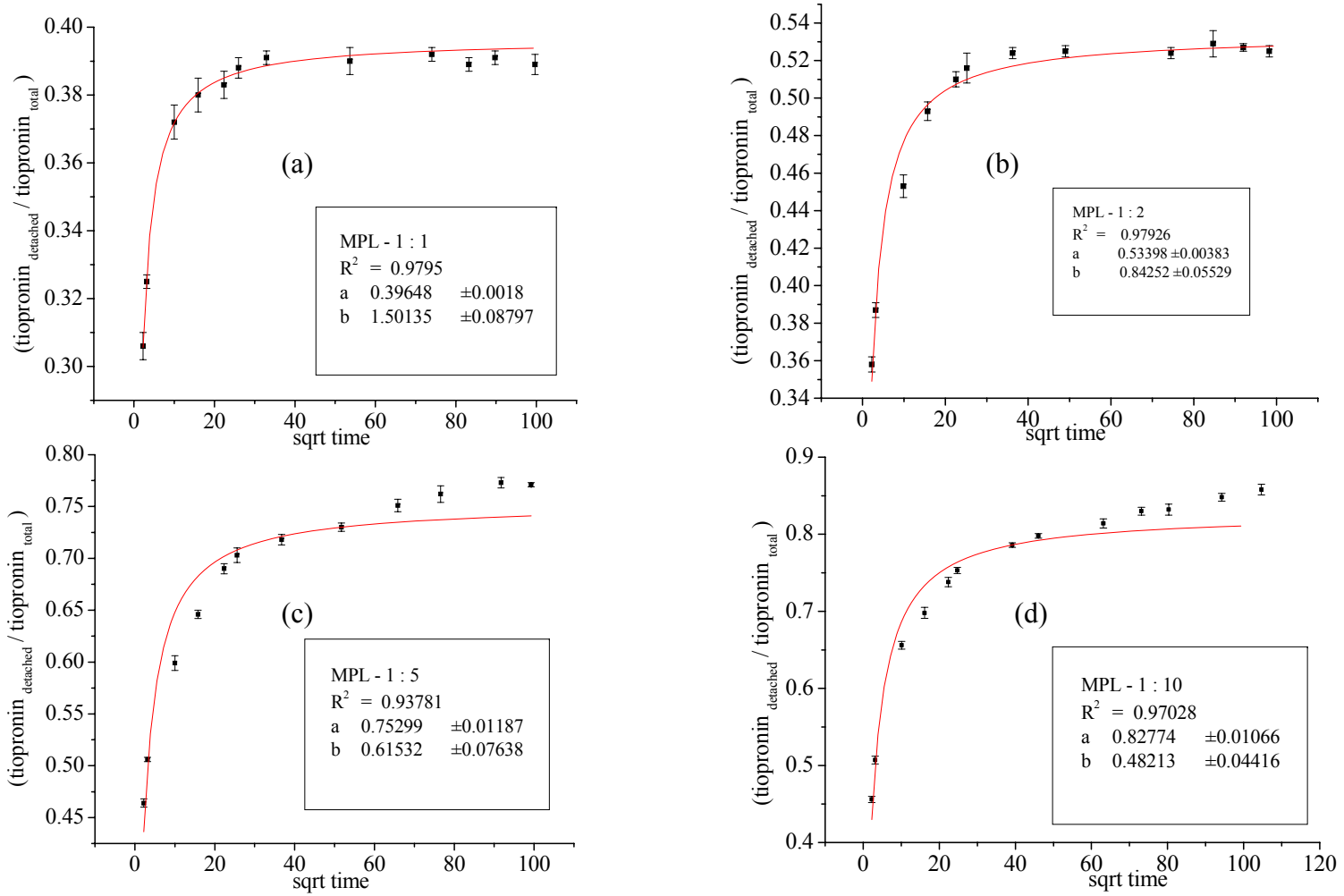

Figure 3.19 Second order Langmuir diffusion-limited fitting for the ligand exchange reaction progress between Au@tiopronin vs MPL at free MPL loading ratios of (a) 1, (b) 2, (c) 5, and (d) 10 equivalent(s).

3.3.4.2. Second order Langmuir diffusion –limited fit of the reaction profile for ligand exchange reaction between Au@tiopronin-derivatives nanoparticles and free tiopronin

Figure 3.20 shows the fitting of the time progress plots of the ligand exchange reactions between the four tiopronin derivative-capped gold nanoparticles and free tiopronin ligand to the second order Langmuir diffusion-limited model. It can be seen that the data were perfectly described by the model at the early time course. Deviation occurred at the transition period when the exchange reaction approached equilibrium. After the equilibrium had been established, the extent of reaction predicted by the model was always slightly below the actual experimental values.

Despite the experimental data do not perfectly described by the model, deviation between the experimental and the values predicted by the model is generally small.

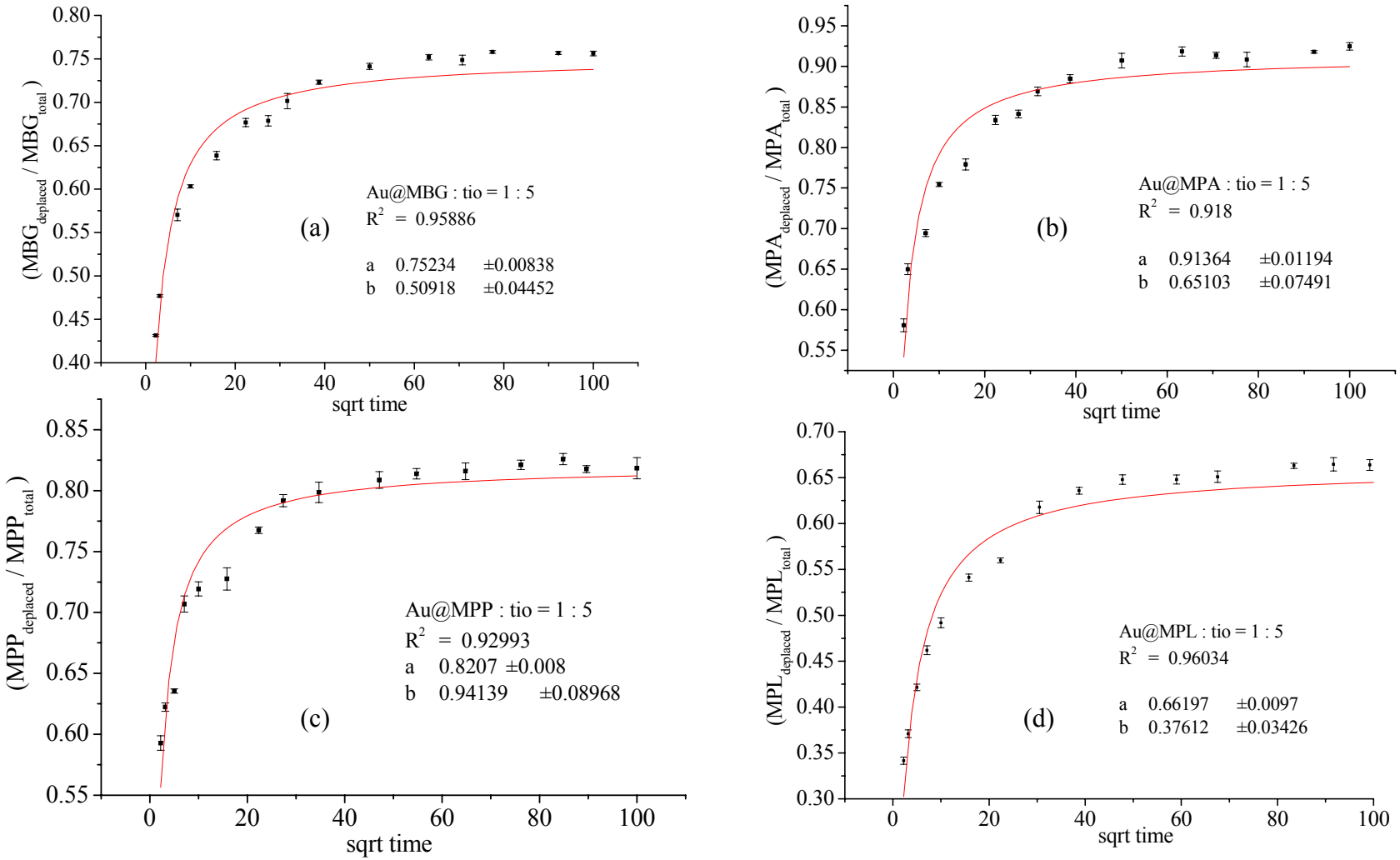

Figure 3.20 Second order Langmuir diffusion-limited fitting for the ligand exchange reaction progress between a) Au@MBG, b) Au@MPA, c) Au@MPP, and d) Au@MPL vs tiopronin at free tiopronin-to-bound-tiopronin-derivative ratios of 5.

3.3.4.3. Fitting of the data for the exchange reaction between Au@tiopronin and tiopronin derivatives at pH 6.5.

Figures 3.21 and 3.22 show the reaction progress plots for the ligand exchange reaction between Au@tiopronin and tiopronin derivatives in medium with pH 6.5 as fitted by the second order Langmuir diffusion-limited model. The fitting to the exchange progress with MPA and MPL by the model are generally poor. It is because the time progresses obtained for the two ligands are less commonly encountered. Better fitting with the model was achieved for time progress plots when MBG and MPP served as the incoming ligand under buffered condition, although small deviations can be observed. This indicates that the ligand exchange reactions involving MBG and MPP are more likely to follow the associative mechanism and diffusion-limited approach in the presence of electrostatic charge.

The second order Langmuir diffusion-limited model seemed to describe the reaction data at pH 6.5 better when compared with the unbuffered condition. The entire reaction progress at low free thiol loadings and the early period of the exchange reactions for all the derivatives were generally well-predicted by the model. In some cases, perfect fitting extended into the equilibrium stage even when the free thiol loading was high. Since the electrostatic repulsion between the ligand and monolayer on gold nanoclusters greatly limited the approach of in-coming thiol to the gold surface, the observed ligand exchange may largely be attributed to the diffusion of free thiol. The stronger dependence on diffusion for ligand exchange occurred in buffered solution may accounts for the generally better description by the diffusion-limited model.

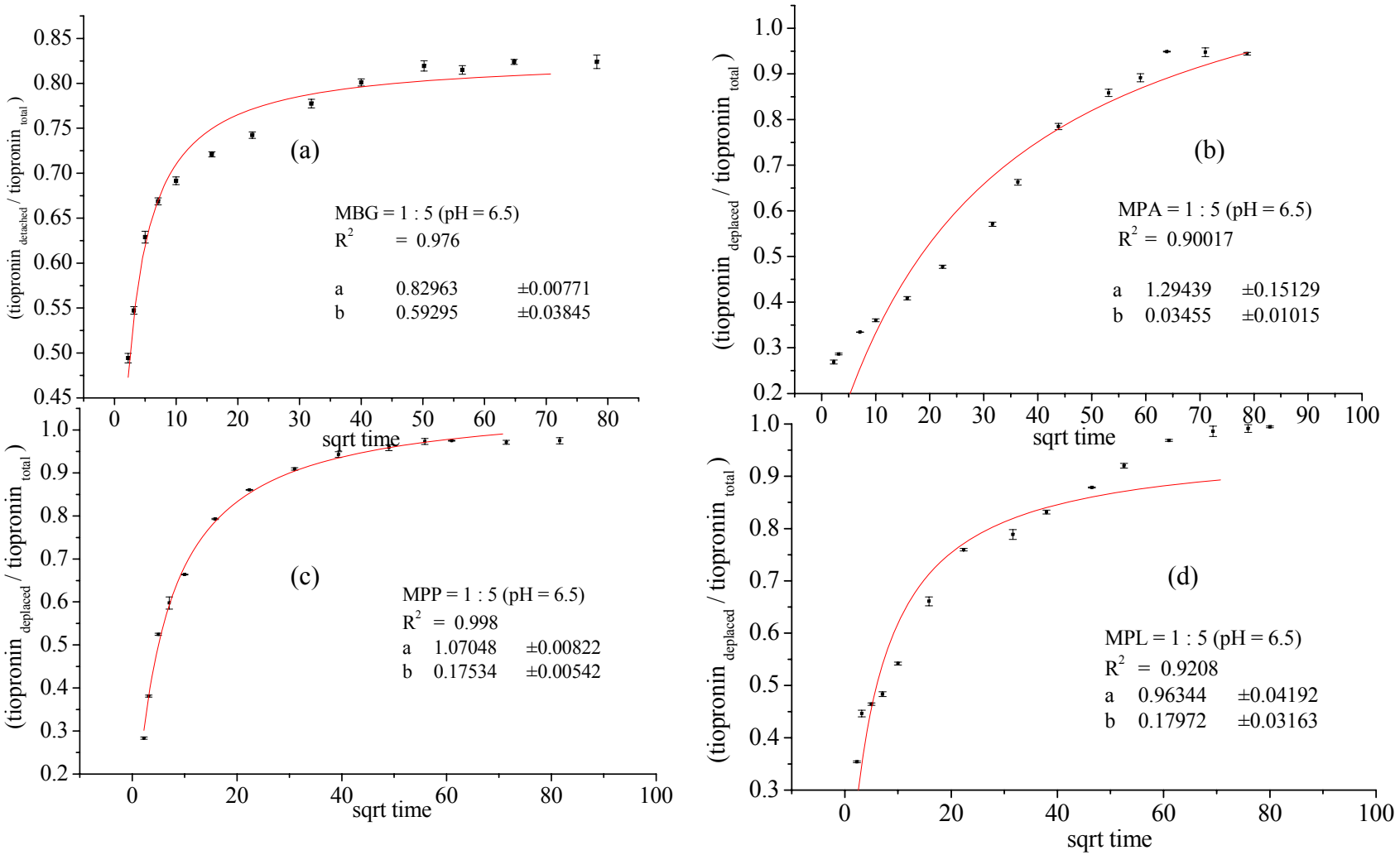

Figure 3.21 Second order Langmuir diffusion-limited fitting for the ligand exchange reaction progress between Au@tiopronin vs a) MBG, b) MPA, c) MPP, and d) MPL vs tiopronin at a free tiopronin derivative loading ratio of 5 equivalents. Reaction medium pH = 6.5.

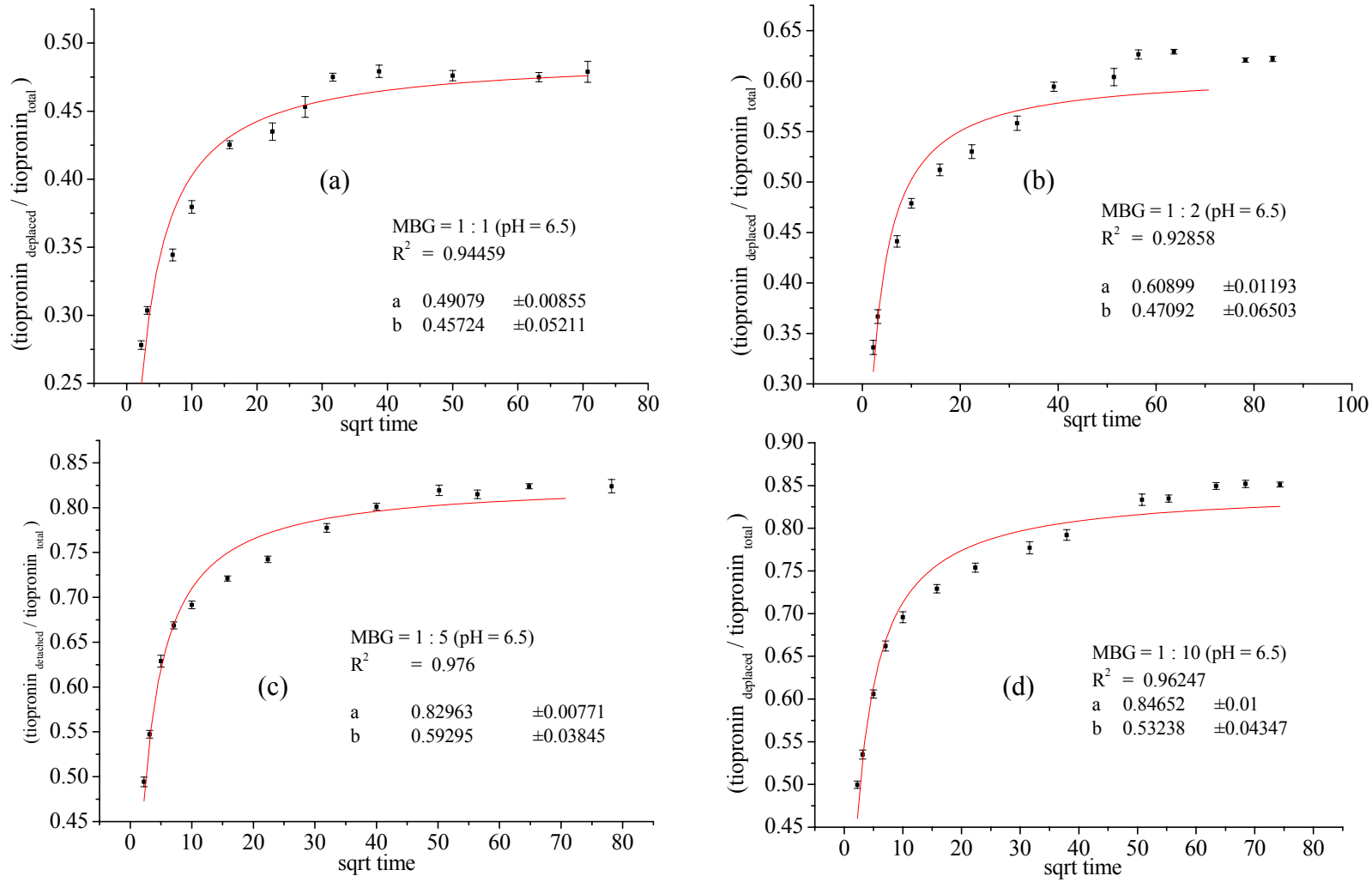

Figure 3.22 Second order Langmuir diffusion-limited fitting for the ligand exchange reaction progress between Au@tiopronin vs MBG at a free MBG loading ratios of a) 1, b) 2 and c) 5 and d) 10 equivalent(s). Reaction medium pH = 6.5

3.4. Concluding remarks

The exchange reactions between tiopronin and tiopronin derivatives on gold nanoparticle surface under various free ligand loadings and medium pH have been investigated.

In unbuffered medium, the extents of exchange reactions among various tiopronin-derivatives are generally similar and solely depend on the free ligand loading. Ligand exchange is primarily limited to metal surface defective site-bound ligands with free thiol loading smaller than two equivalents. As the ligand loading increases, the ligands at the core defects are 'instantly' exchanged and those less reactive terrace-bound ligands become involved. The rate constants obtained for the exchange between bound tiopronin and the derivatives and the reverse reaction, are similar in magnitude.

Under the pH 6.5 buffered condition, the extent of exchange is greatly reduced compared to unbuffered condition due to electrostatic repulsion. Further reduction in initial exchange extent is observed when ligands composed of hindered amino acid residue were used. From the experimental data, however, a bulky amino acid residue in ligand skeleton is advantageous to achieve complete exchange. The exchange kinetics at low thiol loading is faster in buffered medium than in the more acidic unbuffered condition, although the difference becomes insignificant at higher loading. The exchange kinetics becomes less dependent on free ligand loading at pH 6.5.

The ligand exchange with tiopronin derivatives proceeded in an associative pathway

under both acidic and nearly neutral pH, as proven by the linear relationship between the pseudo first order rate constant and the quantity of thiol loaded. The reaction progresses of lower thiol loadings are generally in better agreement with the second order Langmuir diffusion-limited model. Deviation becomes significant under higher loadings and near equilibrium stage. The time progress plots for buffered exchange reactions are generally better described by the diffusion-limited model.

Chapter 4

Preparation and characterization of gold nanoparticles capped with pyrrolidinium-based ionic liquid

4.1 Introduction

Gold nanoparticles are usually prepared in aqueous or organic solvent medium with common reducing agents like sodium borohydride, citrate, etc. in the presence of passivating ligands or polymers. Particles of different dimensions and morphologies can be prepared. Due to the strong desire for a greener and environmentally friendly reaction medium, much effort has been devoted to the use of room temperature ionic liquids as a new generation of solvent in the last decade.[141] However, many of the reported synthetic approaches involved the use of water and/or other organic solvents.[3] The nanoparticles formed were only 'dispersed' into the ionic liquid by removing the solvent under reduced pressure. Genuine protocol for preparing nanoparticles directly in ionic liquid remains to be explored, though there is one report on the preparation of gold nanoparticles with ionic liquid capping agents by sputter deposition.[155]

Inspired by reports on the preparation of gold nano-colloids with borohydride as the reducing agents in the presence of surfactants, tetraalkylammonium salts of these reductive anions were used to facilitate their entry into the hydrophobic medium to achieve the preparation in pure ionic liquid. In this chapter, the preparation of gold nanoparticles with tetrabutylammonium borohydride under different experimental conditions in ionic liquids is presented. The N-alkyl-N-methylpyrrolidinium bis(trifluoromethanesulfonyl)imide ($PyC_n[Tf_2N]$) family of ionic liquids was selected as the medium in this study. The fully saturated nature of the pyrrolidinium cation prevents the reductive decomposition of ionic liquid, which might occur with the widely used imidazolium-base ionic liquids when they were mixed with strong reducing agent

directly without the dilution with other solvents.

To demonstrate the passviating ability of pyrrolidinium salts and the possible single phase preparation of gold nanoparticles in ionic liquid, several experiments were performed and their results will be discussed in this chapter. Firstly, the preparation of gold nanoclusters with pyrrolidinium salts and gold salts in chloroform was conducted. Then, the modified Brust two-phase-synthesis of gold nanoparticles, with the pyrrolidinium-based ionic liquids replaced for the organic solvent, was studied in order to examine the stability of nanoclusters produced in the ionic liquids. Finally, the single ionic liquid phase preparation of gold nanoparticles by direct addition of tetrabutylammoninm borohydride was investigated.

For the single phase preparation in ionic liquids, the effect of the cation alkyl chain length, the concentration of gold precursor in the reaction medium, the presence of halides, and the reaction temperature toawrds the gold nanoparticles synthesized was examined in detail.

4.2 Experimental section

4.2.1 Materials

1-Bromohexane, 1-bromooctane, 1-bromodecane, 1-bromotetradecane, 1-chlorohexene, 1-chlorooctane, 1-chlorodecane, 1-chlorotetradecane, *N*-methylpyrrolidine, lithium bis(trifluoromethanesulfonyl)imide, gold(III) bromide, gold(III) chloride, hydrogen tetrachloroaurate (III) hydrate, sodium borohydride, tetrabutylammonium borohydride, and activated charcoal were obtained from Aldrich. ACS grade dichloromethane, diethyl ether, ethyl acetate, methanol and petroleum ether were obtained from Tedia. Basic form alumina was purchased from Merck.

4.2.2 Preparation of N-alkyl-N-methylpyrrolidinium bromides (PyC_nBr), chlorides (PyC_nCl) and bis(trifluoromethanesulfonyl)imides ($PyC_n[Tf_2N]$)

4.2.2.1 Preparation of N-hexyl-N-methylpyrrolidinium bromide (PyC_6Br) (16)

To a chilled solution of 1-bromohexane (14 mL, 100 mmol) in ethyl acetate (500 mL) was added N-methylpyrrolidine (13.5 mL, 130 mmol) under stirring. The reaction mixture was then warmed at 50℃ for 24 hours under nitrogen. The crude bromide salt precipitated out slowly as a fine white solid. After the reaction had completed, diethyl ether (1 L) was poured into the stirring reaction mixture. Greater quantity of white solid ermerged and the reaction mixture was allowed to settle for one hour. Since the bromide salt obtained is highly hygroscopic, the solid product was washed in the reaction flask firstly with diethyl ether followed by n-hexane using a cannula. The bromide salt was washed until no unreacted substrates were found in the effluent by TLC, and the retaining solvent was removed completely under vacuum. The dried bromide was obtained as a white solid and stored under vacuum. Yield: 90 %. ^{1}H NMR($CDCl_3$) : δ3.83 (4H, m), δ3.64 (2H, m) , δ3.29 (3H, s) , δ2.28 (4H, m) , δ1.75 (2H, q) , δ1.38 (2H, m) , δ1.30 (4H, m) , δ0.86 (3H, t).

4.2.2.2 Preparation of N-octyl-N-methylpyrrolidinium, N-decyl-N-methylpyrrolidinium and N-tetradecyl-N-methylpyrrolidinium bromides

The N-octyl, N-decyl, and N-tetradecyl-N-methylpyrrolidinium bromide were prepared by similar procedures by using the corresponding alkyl bromides.

N-octyl-N-methylpyrrolidinium bromide (PyC_8Br) (17)

White hygroscopic solid. Yield : 85 %, ^1H NMR($CDCl_3$) : δ3.84 (4H, m), δ3.65 (2H, m) , δ3.31 (3H, s) , δ2.30 (4H, m) , δ1.76 (2H, q) , δ1.36 (2H, m) , δ1.26 (8H, m) , δ0.87 (3H, t)

N-decyl-N-methylpyrrolidinium bromide ($PyC_{10}Br$) (18)

White hygroscopic solid. Yield : 85 %. ^1H NMR($CDCl_3$) : δ3.84 (4H, m), δ3.65 (2H, m) , δ3.30 (3H, s) , δ2.28 (4H, m) , δ1.75 (2H, q) , δ1.37 (2H, m) , δ1.25 (12H, m) , δ0.86 (3H, t)

N-tetradecyl-N-methylpyrrolidinium bromide ($PyC_{14}Br$) (19)

White hygroscopic solid. Yield : 85 %. ^1H NMR($CDCl_3$) : δ3.84 (4H, m), δ3.64 (2H, m) , δ3.31 (3H, s) , δ2.30 (4H, m) , δ1.75 (2H, q) , δ1.37 (2H, m) , δ1.24 (22H, m) , δ0.87 (3H, t)

4.2.2.3 Preparation of N-hexyl-N-methylpyrrolidinium chloride (PyC_6Cl) (20)

The preparation of **5** follows similar synthetic approach as its bromide salt. Briefly, N-methylpyrrolidine (13.5 mL, 130 mmol was added to chilled 1-chlorohexane (13.7 mL, 100 mmol) in methanol (500 ml). The reaction mixture was refluxed for 24 hours under nitrogen. The crude pale yellow methanolic solution was cooled to room temperature and diethyl ether was poured to precipitate the chloride salt formed. A plentiful amount of whitish fine solid was obtained and the yellowish supernatant was drained with a cannula, because of the hygroscopic nature of the chloride salt. Afterwards, the solid product was washed firstly with diethyl ether and then petroleum ether under nitrogen atmosphere until no more impurities were found in the wash by TLC. The off-white solid was dried and stored under vacuum. Yield : 75 %. ^{1}H NMR($CDCl_3$) : δ3.89 (4H, m), δ3.78 (2H, m) , δ3.63 (3H, m) , δ3.32 (4H, s) , δ2.28 (2H, m) , δ1.75 (2H, q) , δ1.39 (2H, m) , δ1.31 (4H, m), δ0.87 (3H, t)

4.2.2.4 Preparation of N-octyl-N-methylpyrrolidinium, N-decyl-N-methylpyrrolidinium and N-tetradecyl-N-methylpyrrolidinium chlorides

The N-octyl, N-decyl, and N-tetradecyl-N-methylpyrrolidinium chloride were prepared by similar procedures as the N-hexyl counterpart using the corresponding alkyl chlorides.

N-octyl-N-methylpyrrolidinium chloride (PyC_8Cl) (21)

White hygroscopic solid. Yield : 85 %. ^1H NMR($CDCl_3$) : δ3.89 (4H, m), δ3.79 (2H, m) , δ3.63 (3H, m) , δ3.32 (4H, s) , δ2.29 (2H, m) , δ1.75 (2H, q) , δ1.35 (2H, m) , δ1.25 (8H, m), δ0.86 (3H, t)

N-decyl-N-methylpyrrolidinium chloride ($PyC_{10}Cl$) (22)

White hygroscopic solid. Yield : 85 %. ^1H NMR($CDCl_3$) : δ3.89 (4H, m), δ3.77 (2H, m) , δ3.63 (3H, m) , δ3.32 (4H, s) , δ2.29 (2H, m) , δ1.74 (2H, q) , δ1.35 (2H, m) , δ1.24 (12H, m), δ0.87 (3H, t)

N-tetradecyl-N-methylpyrrolidinium chloride ($PyC_{14}Cl$) (23)

White hygroscopic solid. Yield : 85 %. ^1H NMR($CDCl_3$) : δ3.85 (4H, m), δ3.75 (2H, m) , δ3.58 (3H, m) , δ3.29 (4H, s) , δ2.26 (2H, m) , δ1.72 (2H, q) , δ1.32 (2H, m) , δ1.21 (12H, m), δ0.84 (3H, t)

4.2.2.5 Preparation of N-alkyl-N-methyl-pyrrolidinium bis(trifluoromethanesulfonyl)imides

The bis(trifluoromethanesulfonyl)imide salts of the N-alkyl-N-methylpyrrolidinium derivatives were prepared by anion exchange between the commercially available lithium bis(trifluoromethanesulfonyl)imide and the chloride or bromide salts described above. In this study, the N-hexyl, N-octyl, and N-decyl derivatives were prepared. The detailed synthetic procedures for the candidates are illustrated by the preparation of the

hexyl derivatives described as follows:

Preparation of N-hexyl-N-methylpyrrolidinium bis(trifluoromethanesulfonyl)imide ($PyC_6[Tf_2N]$) (24)

N-hexyl-N-methylpyrrolidinium bromide (12.5 g, 50 mmol) was dissolved in 100 mL of deionized water. Meanwhile, lithium bis(trifluoromethanesulfonyl)imide (15.8 g, 55 mmol) was dissolved in another 100 mL of deionized water. Both solutions obtained are colourless and clear. N-alkyl-Nmethylpyrrolidinium bis(trifluoromethanesulfonyl)imide was formed by simply mixing the two clear solutions, giving an opaque mixture. Upon standing, the pyrrolidinium imide salt separated as a milky liquid phase at the bottom of the mixture. The milky mixture was poured into a separatory funnel containing dichloromethane (70 mL) and the ionic liquid formed was extracted into the organic phase. The aqueous phase was extracted several times with aliquots of fresh dichloromethane (70 mL). The organic extracts were collected, combined, dried over anhydrous magnesium sulfate, and rotary-evaporated to give an oily pale yellowish clear liquid. This liquid was then washed with several aliquots of hot water (30 mL) in order to remove as much halide ions as possible. After the wash, the ionic liquid was dissolved in dichloromethane (50 mL), dried, and rotary evaporated. Activated charcoal was then added to the liquid and the mixture was stirred overnight to remove the coloured impurities. The ionic liquid was further purified by passing through an alumina column with dichloromethane as the eluent. The effluent was collected and rotary evaporated to give a clear and colourless oily liquid.

Yield : 90%. ^{1}H NMR ($CDCl_3$) : δ3.53 (4H, m), δ3.31 (2H, m), δ3.06 (3H, m), δ2.28 (4H, m), δ1.75 (2H, q), δ1.38 (2H, m), δ1.34 (4H, m), δ0.89 (3H, t)

4.2.2.6 Preparation of N-octyl-N-methylpyrrolidinium, and N-decyl-N-methylpyrrolidinium bis(trifluoromethanesulfonyl)imide

The N-octyl and N-decyl-N-methylpyrrolidinium bis(trifluoromethanesulfonyl)imide were prepared by similar procedures as the N-hexyl counterpart using the corresponding N-alkyl-N-methylpyrrolidinium bromides.

N-octyl-N-methylpyrrolidinium bis(trifluoromethanesulfonyl)imide (PyC_8Tf_2N) (25)

Colourless clear liquid. Yield : 97 %. ^{1}H NMR ($CDCl_3$) : δ3.56 (4H, m), δ3.33 (2H, m), δ3.09 (3H, m), δ2.30 (4H, m), δ1.77 (2H, q), δ1.37 (2H, m), δ1.28 (8H, m), δ0.89 (3H, t)

N-decyl-N-methylpyrrolidinium bis(trifluoromethanesulfonyl)imide ($PyC_{10}[Tf_2N]$) (26)

Colourless clear liquid. Yield : 96 %. ^{1}H NMR ($CDCl_3$) : δ3.55 (4H, m), δ3.32 (2H, m), δ3.07 (3H, m), δ2.29 (4H, m), δ1.76 (2H, q), δ1.36 (2H, m), δ1.27 (12H, m), δ0.88 (3H, t)

4.2.3 Preparation of gold nanoparticles in pyrrolidinium-based ionic liquids

4.2.3.1 Preparation of pyrrolidinium-capped gold nanoparticles in chloroform

In this section, the preparation of gold nanoparticles in chloroform containing the bromide or chloride salt of pyrrolidinum and gold was studied. The reducing agent used was an aqueous solution of sodium borohydride.

Table 4.1 shows the different combination of concentrations of gold salt and N-tetradecyl-N-methylpyrrolidinium bromide in the preparation of gold nanoparticles used in this study. The volume of the chloroform phase for every experiment was kept at 3 mL and the concentration of borohydride aqueous solution was maintained at 0.15 M. The colloids were formed by dropwise addition of the borohydride solution to a rapidly stirred gold-containing chloroform solution. After the addition had completed, the reaction mixture was vigorously stirred at ambient conditions for 30 minutes. The UV-visible spectra and the TEM images for all entries were recorded.

Table 4.1 Concentration of gold(III) bromide, N-tetradecyl-N-methylpyrrolidinium bromide and gold(III) to borohydride ratio used in the aqueous-chloroform two-phase preparation of gold nanoparticles.

Entry	$[AuBr_3]$ (mM)	$[PyC_{14}Br]$ (mM)	Vol. of 0.15M borohydride solution added (mL)
1	10	500	2
2	5	500	1
3	10	10	2
4	5	5	1

For each experiment, volume of chloroform used = 3 mL and Au^{+3} : BH_4^- = 1 : 10.

4.2.3.2 Ionic liquid-aqueous biphasic preparation of gold nanoparticles

In this section, the ionic liquid-aqueous biphasic preparation of gold nanoparticles, which is a modified Brust protocol of two-phase syntheis, was demonstrated. To examine the effect of halide towards the nanoparticles produced by the biphasic approach, the chloride and the bromide of gold and pyrrolidinium salts were used in different experiments. A schematic diagram illustrating the experimental setup for the ionic liquid-aqueous biphasic preparation was shown in Figure 4.1.

Table 4.2 summarized the quantity of pyrrolidinium and gold salt used in each trial of experiment. Gold nanoparticles were synthesized by adding an aqueous sodium borohydride solution to the slowly stirred (~ 100 rpm) ionic liquid phase containing the gold salt. Stirring was maintained at a slow speed so that the aqueous-ionic liquid interface was not disturbed. The biphasic reaction proceeded at ambient condition for three hours. UV-visible spectra and TEM images of the gold nanoparticles were recorded after the reaction had completed.

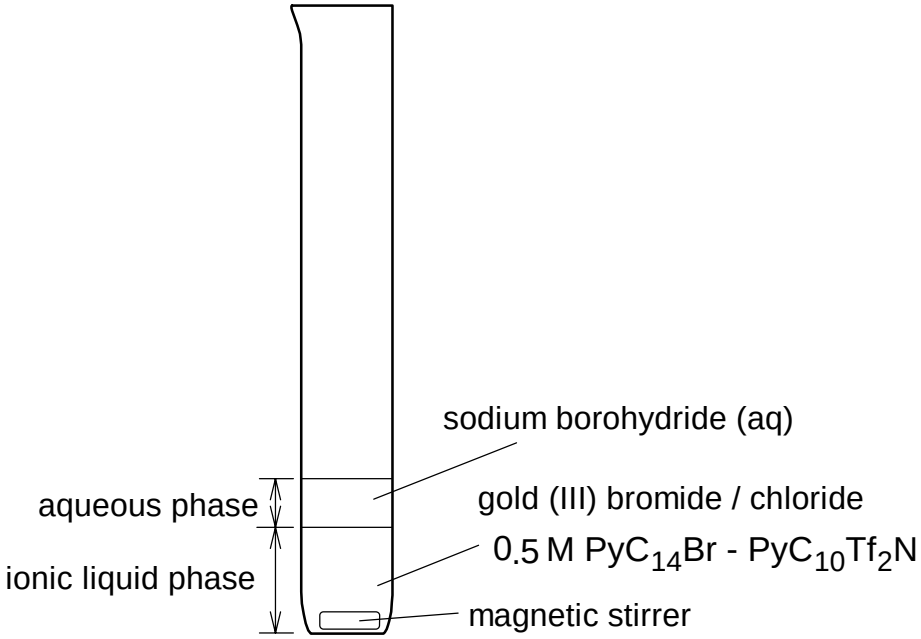

Figure 4.1 Schematic diagram illustrating the ionic liquid-aqueous biphasic preparation of gold nanoparticles.

Table 4.2 Concentration of gold(III) salts, N-methyl-N-tetradecylpyrrolidinium salts, and and borohydride used in the aqueous-ionic liquid two-phase preparation of gold nanoparticles

X = Br					
Entry	$[AuX_3]$ (mM)	Au : BH_4^- ratio	Vol. of 2M $NaBH_4$ (mL)	Vol. of 1M $NaBH_4$ (mL)	Stir speed (rpm)
5	10	1 : 100	1	0	100
6	5	1 : 200	1	0	100
7	5	1 : 100	0	1	100
8	0.5	1 : 2000	1	0	100
9	5	1 : 100	0	1	1250
X = Cl					
10	10	1 : 100	1	0	100
11	5	1 : 200	1	0	100
12	5	1 : 100	0	1	100
13	0.5	1 : 2000	1	0	100
14	5	1 : 100	0	1	1250

Experimental conditions: All experiments were carried out under ambient conditions with 2 mL ionic liquid containing 0.5M *N*-methyl-N-tetradecylpyrrolidinium halide.

4.2.3.3 Single ionic liquid phase preparation of gold nanoparticles

The direct one-phase preparation of gold nanoparticles in pyrrolidinium ionic liquids of four different chain lengths, hexyl-, octyl-, decyl- and tetradecyl, was studied.

For each chain length of ionic liquid, ionic liquid solutions with different concentrations of N-alkyl-N-methylpyrrolidinium tetrabromoaurate(III) ($PyC_n[AuBr_4]$, the gold precursor) were prepared by dissolving equal amount of PyC_nBr and $AuBr_3$ into the imide ionic liquid, $PyC_n[Tf_2N]$, with gentle heating and stirring. In each experiment, the pyrrolidinium cation of the gold precursor and the imide ionic liquid were the same (alkyl chain length) except in the trials with N-tetradecyl derivative, where N-tetradecyl imide was replaced by N-decyl imide because of its lower melting point (this reaction mixture was abbreviated as 'C_{14}/C_{10}' in the later text). On the other hand, in order to examine the effect of halide on nanoparticles preparation, the above solutions with chloride anion were also prepared. The components and their quantity used to compose the ionic liquid solutions are summarized in Table 4.3 and 4.4

The reducing agent was prepared by dissolving tetrabutylammonium borohydride in a pyrrolidinium-based ionic liquid of appropriate alkyl chain length under gentle warming and stirring. When all the solid tetrabutylammonium borohydride had been dissolved, it was added dropwise to the stirring gold precursor solution in ionic liquid under either room temperature or at two degree Celsius. The reaction mixture was stirred for two hours before it was sampled for TEM and UV-visible spectroscopic analysis.

Direct acquisition of the UV-visible spectra for the gold nanoparticles prepared from 10

and 50 mM gold salt in ionic liquid was hindered by the high concentration of colloidal nanoparticles. To overcome this, the spectra of diluted nano-colloids in dichloromethane were acquired instead. However, the nanospheres fabricated in C_6 and C_8 ionic liquids could not yield a stable dispersion in organic solvent. All nanoparticles were precipitated, leaving a transparent and clear supernatant. Therefore, no UV-visible spectra for nanoparticles from C_6 and C_8 ionic liquid at high gold precursor concentration were obtained. Since the UV-visible spectra for 50 mM experiments are representative enough to reflect the spectroscopic properties of gold nanoparticles prepared under a higher gold content, the spectra for all 10 mM experiments were therefore omitted. Details of all the experimental conditions are given in Table 4.4 – 4.7.

Table 4.3 The components employed for preparation of ionic liquid solutions for single ionic liquid phase nanoparticle synthesis.

Ionic liquid Solution	Bromides + gold salt + ionic liquid	Chlorides + gold salt + ionic liquid
C_6 ionic liquid	$PyC_6Br + AuBr_3 + PyC_6[Tf_2N]$	$PyC_6Cl + AuCl_3 + PyC_6[Tf_2N]$
C_8 ionic liquid	$PyC_8Br + AuBr_3 + PyC_8[Tf_2N]$	$PyC_8Cl + AuCl_3 + PyC_8[Tf_2N]$
C_{10} ionic liquid	$PyC_{10}Br + AuBr_3 + PyC_{10}[Tf_2N]$	$PyC_{10}Cl + AuCl_3 + PyC_{10}[Tf_2N]$
C_{14}/C_{10} ionic liquid mixture	$PyC_{14}Br + AuBr_3 + PyC_{10}[Tf_2N]$	$PyC_{14}Cl + AuCl_3 + PyC_{10}[Tf_2N]$

Four different gold precursor ($PyC_n[AuX_4]$, X = Cl / Br, n = 6, 8, 10, 14) concentrations used for each ionic liquid of particular chain length are: 0.5, 5, 10, 50 mM.

Table 4.4 Concentrations of *N*-alkyl-*N*-methylpyrrolidinium tetrahaloaurate(III) and volume of 500 mM tetrabutylammonium borohydride ($TBABH_4$) ionic liquid solution used in each entry of experiments under room temperature and at 2 ˚C

(X = Br)						
Entry				$\{PyC_n[AuX_4]\}$ (mM)	Vol. of 500 mM $TBABH_4$ in $PyC_n[Tf_2N]$ added (μL)	Temperature
X = Br n = 6	X = Br n = 8	X = Br n = 10	X = Br n = 14*			
15	31	47	63	0.5	5	Room Temperature
16	32	48	64	5	50	
17	33	49	65	10	100	
18	34	50	66	50	500	
19	35	51	67	0.5	5	2℃
20	36	52	68	5	50	
21	37	53	69	10	100	
2	38	54	70	50	500	
(X = Cl)						
Entry				$\{PyC_n[AuX_4]\}$ (mM)	Vol. of 500 mM $TBABH_4$ in $PyC_n[Tf_2N]$ added (μL)	Temperature
X = Cl n = 6	X = Cl n = 8	X = Cl n = 10	X = Cl n = 14*			
23	39	55	71	0.5	5	Room Temperature
24	40	56	72	5	50	
25	41	57	73	10	100	
26	42	58	74	50	500	
27	43	59	75	0.5	5	2℃
28	44	60	76	5	50	
29	45	61	77	10	100	
30	46	62	78	50	500	

Experimental conditions : Au^{3+} : BH_4^- ratio = 1: 5, stirring speed : 150 rpm and 500 rpm for low and room temperature experiments respectively. Total ionic liquid phase volume : 1 ml, Reaction time: 2 hrs.

* The ionic liquid used for trials with n = 14 is $PyC_{10}[Tf_2N]$. For n = 6, 8, and 10, the chain length of the pyrrodinium cation composing the ionic liquid and the gold precursor are consistent.

4.2.4 UV-visible spectroscopy

The UV-visible spectra of gold nanoparticles in ionic liquid or organic solvent were obtained with a HP 8453 spectrophotomer. The spectral range examined for each sample was 300 – 1000 nm.

4.2.5 Transmission electron microscopy (TEM)

The TEM samples of gold nanoparticles dispersed in organic solvent were prepared by putting a drop of the nanoparticles solution to a carbon-coated copper grid. The excess solution was removed from the grid with the tip of a piece of filter paper. The grid was then dried under ambient condition before measurement. For gold nanoparticles dispersed in ionic liquid, a drop of the colloids contained ionic liquid was added directly to a holely-carbon film coated copper grid. The excess ionic liquid was removed by soaking with a filter paper. The TEM measurement were performed with a JEOL model JEM 2010 operating at 200 kV, equipped with a GATAN MSC 794 CCD camera. The average size and the size distribution of each type of nanoparticles were obtained by counting 100 – 200 particles in several randomly selected areas of the grid.

4.3 Results and discussion

4.3.1 Preparation of N-alkyl-N-methylpyrrolidnium bromide, chloride and bis-(trifluoromethanesulfonyl)imide

The hexyl- octyl-, decyl-, and tetradecyl- derivatives of N-alkyl-N-methylpyrrolidinium bromide were conveniently prepared with high purity and yield under mild conditions. The synthesis of their chloride counterparts were, however, more difficult that prolonged reflux was required. The reaction mixture, from which the chloride salt was formed, turned to yellowish upon continuous heating. Copious washing with diethyl ether was necessary to achieve a high purity product. The imide salts of N-alkyl-N-methyl pyrrolidinium, with an alkyl chain shorter than twelve carbons, are clear and colourless oily liquids at room temperature. The crude ionic liquid obtained from the metathesis of the corresponding pyrrolidinium bromide and commercially available lithium bis(trifluoromethanesulfonyl)imide showed a yellowish colour. The colour can be completely removed by activated charcoal. Purification with charcoal and alumina caused nearly no loss in the ionic liquid obtained. The ionic liquids were always heated at 70℃ under vacuum overnight, before they were used for nanoparticles synthesis. No significant change in the ionic liquids was observed upon prolonged heating at reduced pressure. All the imide ionic liquids are immiscible with water, but show high solubilities towards pyrrolidinium bromide and chloride salts. Besides, the imide ionic liquids show a higher solubility towards auric chloride than the auric bromide in the presence of the pyrrolidinium halide.

4.3.2 Preparation of pyrrolidinium-capped gold nanoparticles in chloroform

Similar to the observations reported in studies in the synthesis of tetraalkylammonium halide passivated gold nanoparticles[207-209] a wine red colour was formed immediately once borohydride solution was added to the chloroform solution containing the pyrrolidinium ionic liquid and gold salt. The colloids remained stable during the entire reaction period without significant precipitation.

Figure 4.2 – 4.5 show the UV-visible spectra and the TEM images of the gold nanoparticles prepared as in entry 1 – 4. The SPR peaks for the gold colloids gave a maximum absorption at ~ 530 nm and no broadening at longer wavelength, suggesting a weak interaction between the particles and the absence of coagulation. The average size of the nanospheres formed ranged between 9 – 11 nm. From the size distribution analysis on the TEM images, it can be seen that the average size of the gold nanoparticles prepared under a higher pyrrolidinium salt concentration (entry 1 and 2) was slightly smaller than those (entry 3 and 4) prepared under a lower pyrrolidinium concentration. Meanwhile, a strong correlation between surfactant content and the size dispersity of the nanoparticles formed was observed. Under a higher surfactant concentration, the distribution of colloid size was less than 2 nm. Reducing the amount of ammonium salt in the organic phase, however, resulted in broadening the size variation of the nanospheres formed. Based on the results obtained, it can be concluded that pyrrolidinium salt could function as a good passivating ligand to preserve gold nanoparticles and to stabilize them in organic solvent. On the other hand, the results also suggested that a higher pyrrolidinium salt concentration environment promotes the formation of smaller, spherical nanoparticles with a narrower size distribution.

Therefore, the use of neat ionic liquid, which provide a vast quantity of the quaternary ammonium cation in small volume, may be advanteageous to the formation of stable gold nanoparticles and serves as a promising new strategy for uniform nanoclusters preparation.

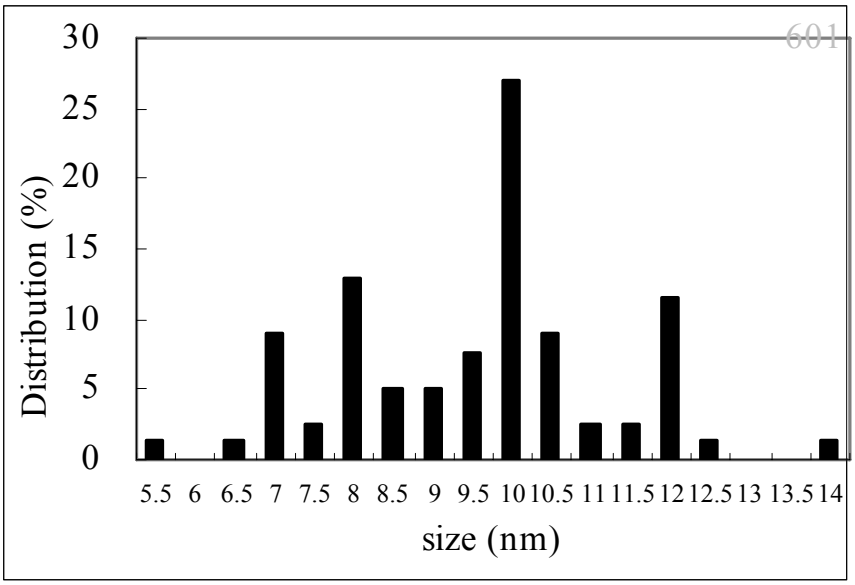

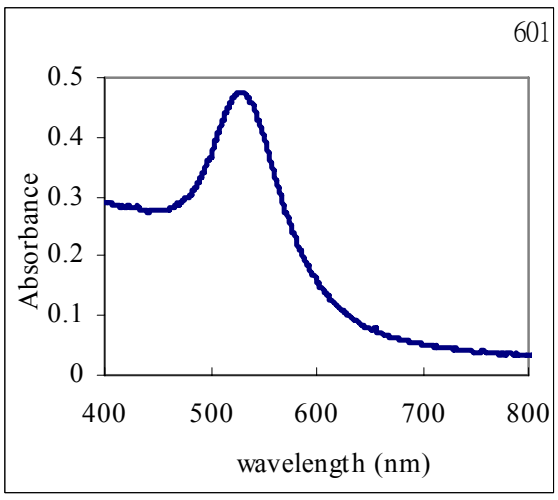

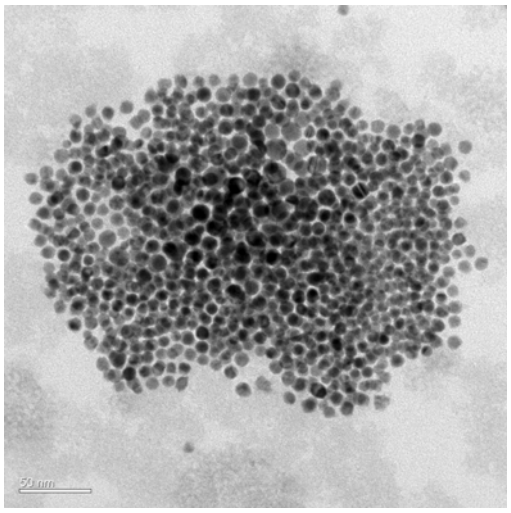

Figure 4.2 TEM image, size distribution statistics, and the UV-visible profile for gold nanoparticles synthesized with 10 mM $HAuCl_4$ in 500 mM $PyC_{14}Br$ chloroform solution. (entry 1)

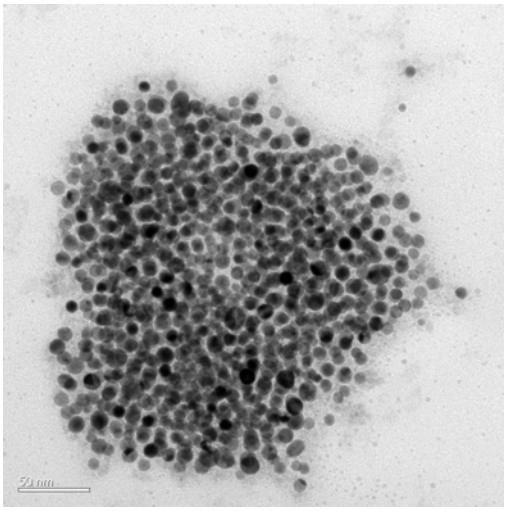

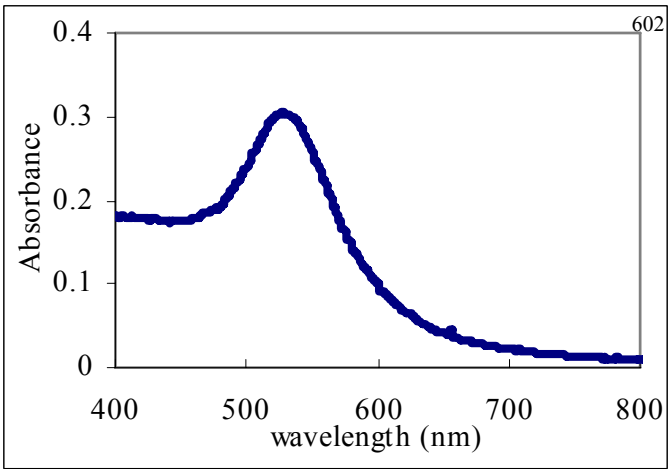

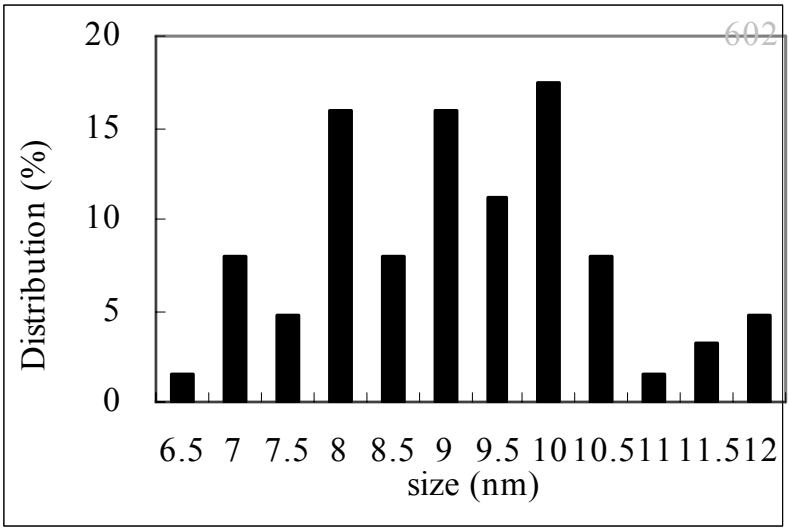

Figure 4.3 TEM image, size distribution statistics, and the UV-visible profile for gold nanoparticles synthesized with 5 mM $HAuCl_4$ in 500 mM $PyC_{14}Br$ chloroform solution. (entry 2)

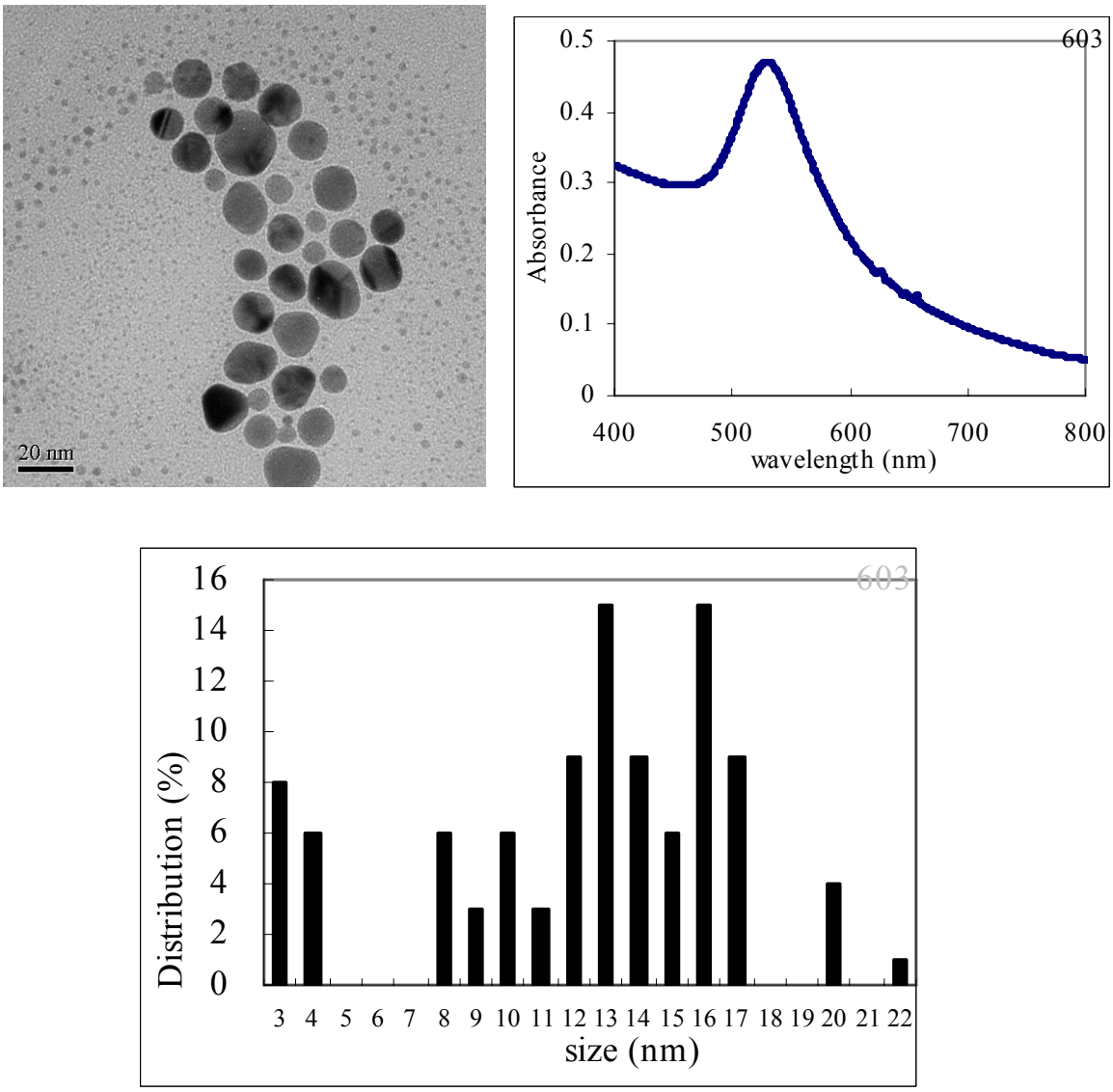

Figure 4.4. TEM image, size distribution statistics, and the UV-visible profile for gold nanoparticles synthesized with 10 mM $HAuCl_4$ in 10 mM $PyC_{14}Br$ chloroform solution. (entry 3)

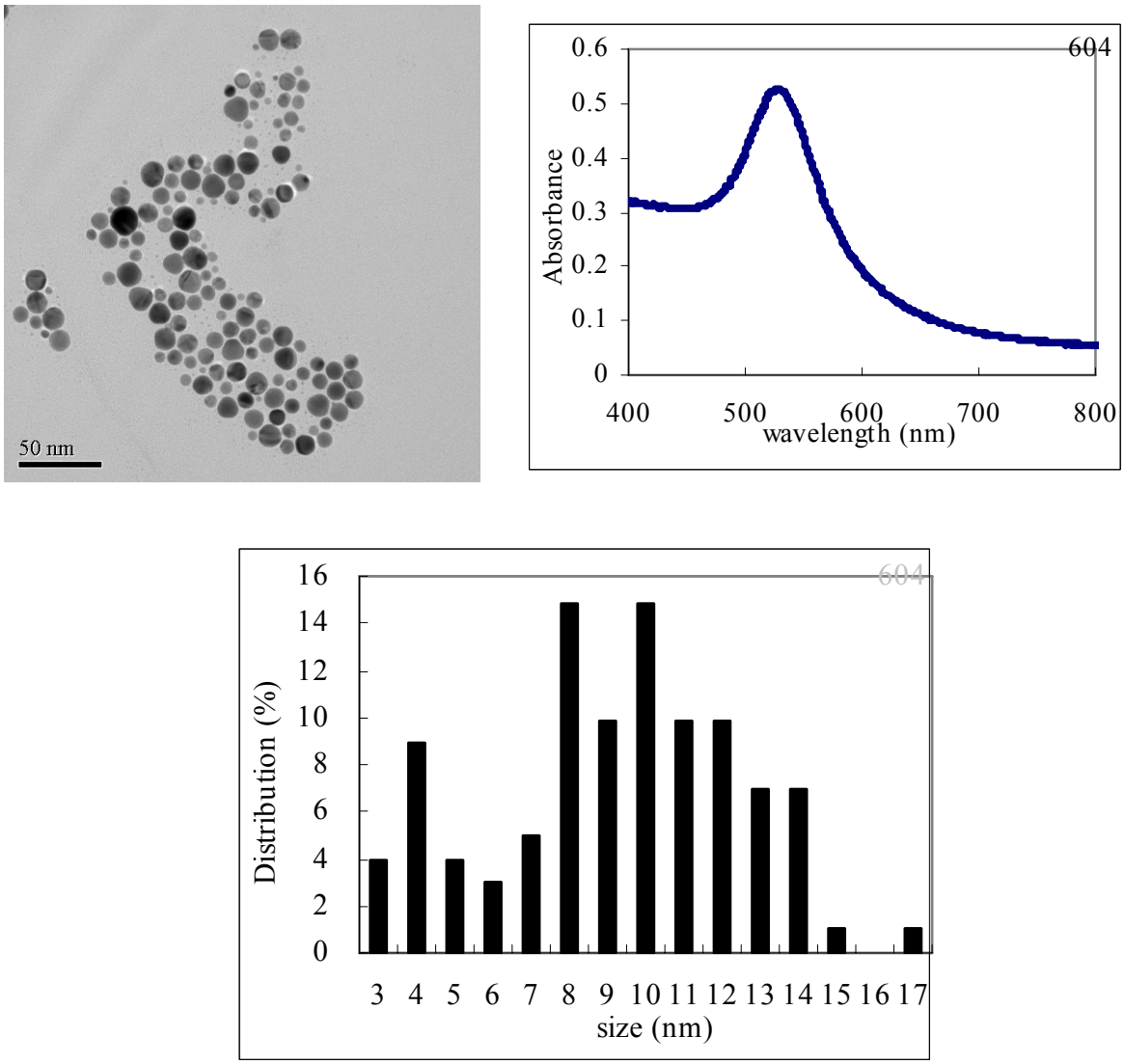

Figure 4.5 TEM image, size distribution statistics, and the UV-visible profile for gold nanoparticles synthesized with 5 mM $HAuCl_4$ in 5 mM $PyC_{14}Br$ chloroform solution. (entry 4)

4.3.3 Ionic liquid-aqueous biphasic preparation of gold nanoparticles

Table 4.5 summarizes the results of the gold nanoparticle synthesis under the ionic liquid-aqueous biphasic condition. When an aqueous solution of borohydride was added on top of the ionic liquid layer, gas bubbles evolved from the aqueous phase and the liquid-liquid interface. Reddish colour developed gradually at the interface and propagated to the entire ionic liquid phase with the aid of stirring. Finally, a wine red coloured ionic liquid phase was obtained.

Figure 4.6 – 4.11 show the TEM images and the UV-visible spectra of the gold nanospecies prepared under ionic liquid-aqueous biphasic condition. It can be seen that stable gold nano-species were generally obtained in the chloride system over a wide range of reactant ratio and gold precursor concentration. On the contrary, gold nano-clusters formed with bromide tend to precipitate and are relatively unstable, especially when high reactant or gold concentration was applied.

When the ionic liquid-aqueous biphasic system was stirred vigorously similar to the traditional Brust's synthesis(entry 9 and 14), no stable gold nanoparticles could be obtained from both halide systems. Only some black solids were found and the ionic liquid phase turned into a complete colourless and clear solution eventually. This may indicated that the formation of stable nanoparticles requires slow reduction by the gradual transfer of borohydride from aqueous phase to the ionic liquid phase.

Under a higher gold salt concentration in the ionic liquid phase, nano-threads of various lengths and morphologies were obtained (entry 6, 10 and 11). TEM image for entry 13

suggested that an extraordinarily high borohydride to gold ratio (2000 : 1) also lead to the formation of irregular and discontinuous threads.

A lower gold content facilitated the formation of spherical nanoparticles. This may be due to the slower reduction rate of the metal ions to the corresponding nuclei, allowing more time to adopting better passivation configuration. Although a drastic increase in spherical nanoparticles population were found in both halide systems when the concentration of the gold precursor was loweren to 5 mM at a reduced Au^{3+} to BH_4^- ratio of 1 : 100, a sharp difference in average size between the nanospheres prepared with chloride and bromide was observed. The nanospheres from chloride were less spherical and had an average size of 3.6 ± 0.5 nm, while those from bromide were more spherical with an average diameter of 6.8 ± 0.9 nm.

Table 4.5 A summary of the gold nanoparticles formed under ionic liquid-aqueous biphasic condition.

Bromide system					
Entry	$[AuBr_3]$ (mM)	Au : BH_4^- ratio	Stable gold colloids solution ?	Morphology of nano-species formed	Observations
5	10	1 : 100	No	-	Black precipitate formed
6	5	1 : 200	Yes	Nano-threads	Reddish colour
7	5	1 : 100	Yes	Nanospheres 6.8 ± 0.9 nm	Reddish colour
8	0.5	1 : 2000	No	-	Black precipitate formed
9	5	1 : 100	No	-	Black precipitate formed

Chloride system					
Entry	$[AuCl_3]$ (M)	Au : BH_4^- ratio	Stable gold colloids solution ?	Morphology of nano-species formed	Observations
10	10	1 : 100	Yes	Irregular shape nano-threads	Reddish colour
11	5	1 : 200	Yes	Nano-threads with some spherical nanoparticles	Reddish colour
12	5	1 : 100	Yes	Nanospheres of 3.6 ± 0.5 nm with small short nano-threads	Reddish colour
13	0.5	1 : 2000	Yes	Mixture of irregular threads and nanoparticles	Reddish colour
14	5	1 : 100	No	-	Black precipitate formed

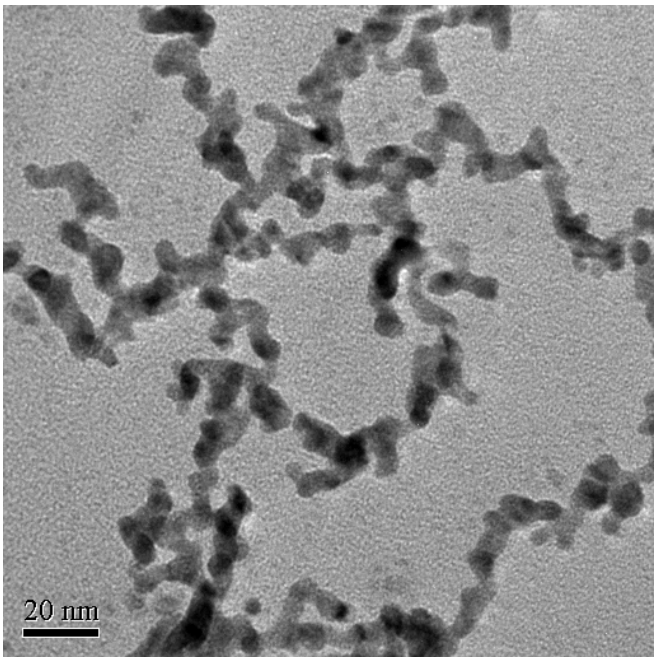

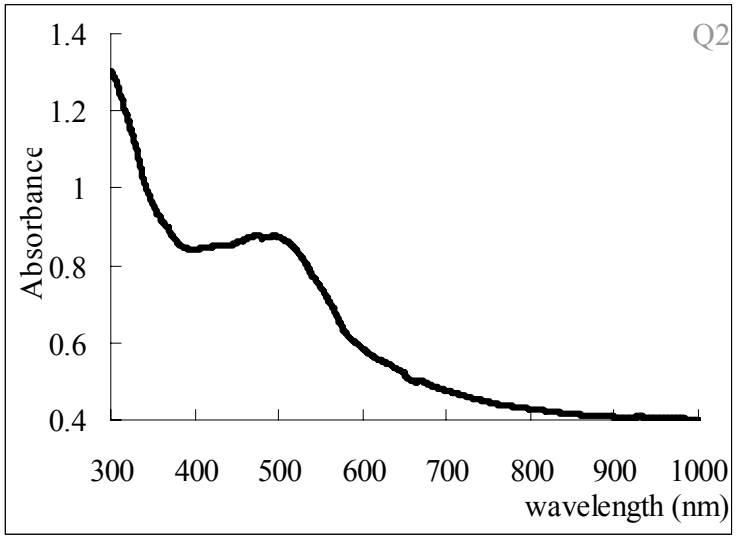

Figure 4.6 TEM image and the UV-visible profile for the biphasic preparation of gold nanoparticles in entry 6.

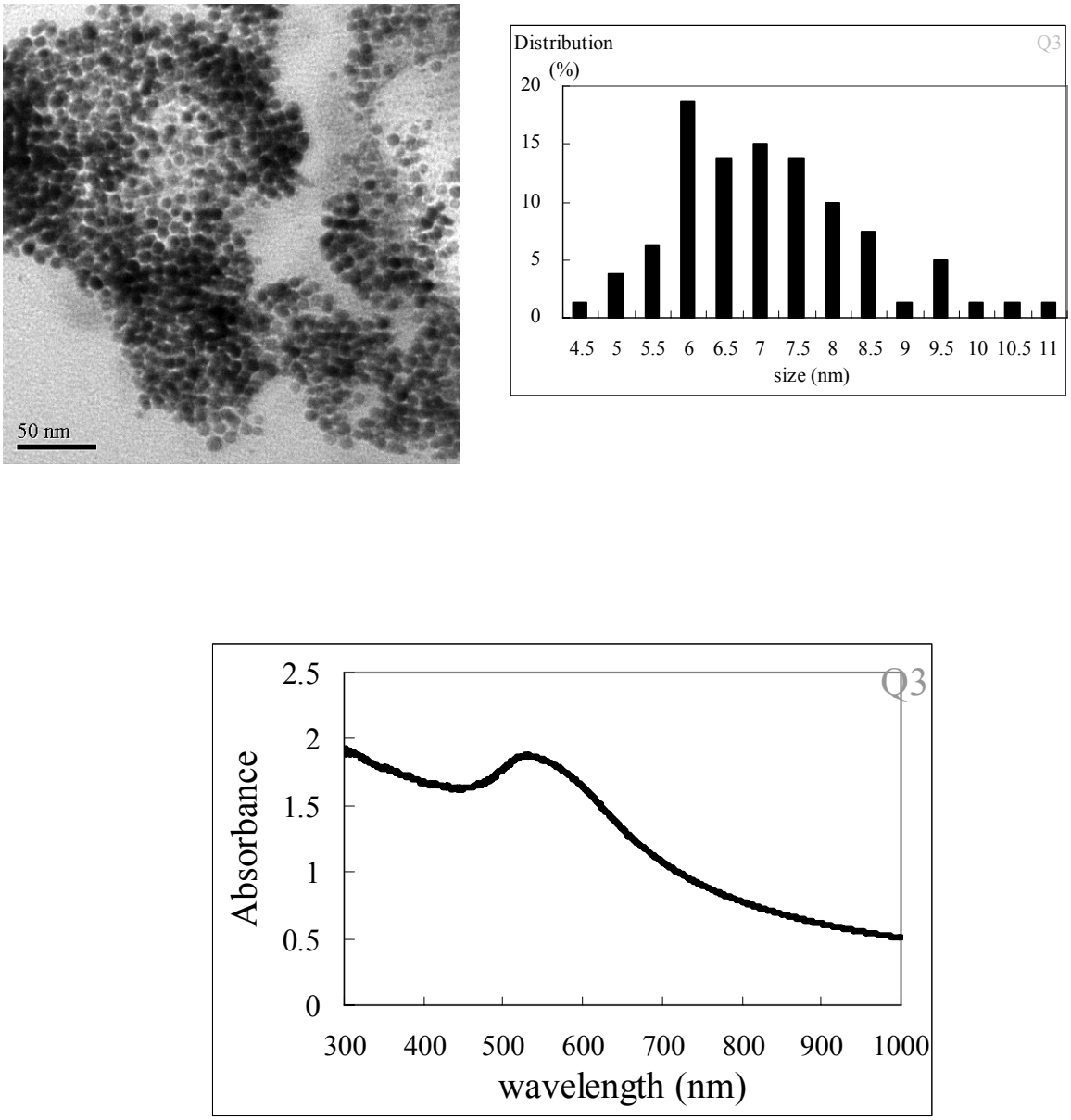

Figure 4.7 TEM image, size distribution statistics, and the UV-visible profile for the biphasic preparation of gold nanoparticles in entry 7.

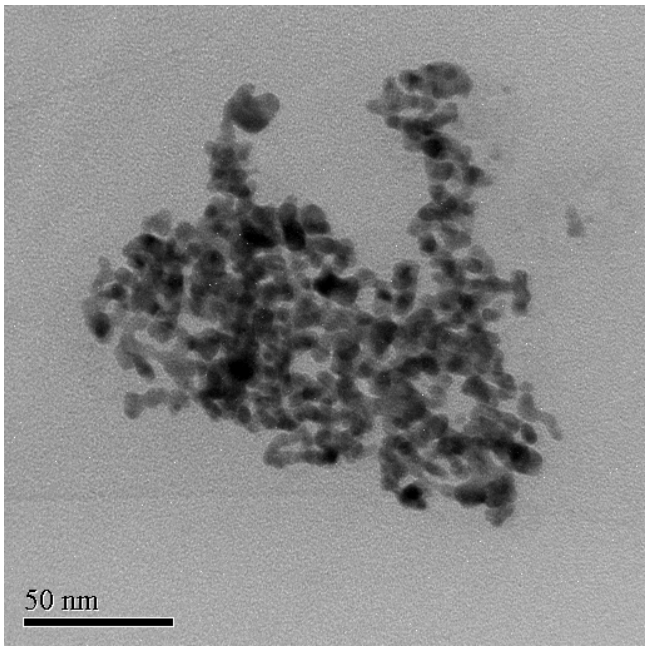

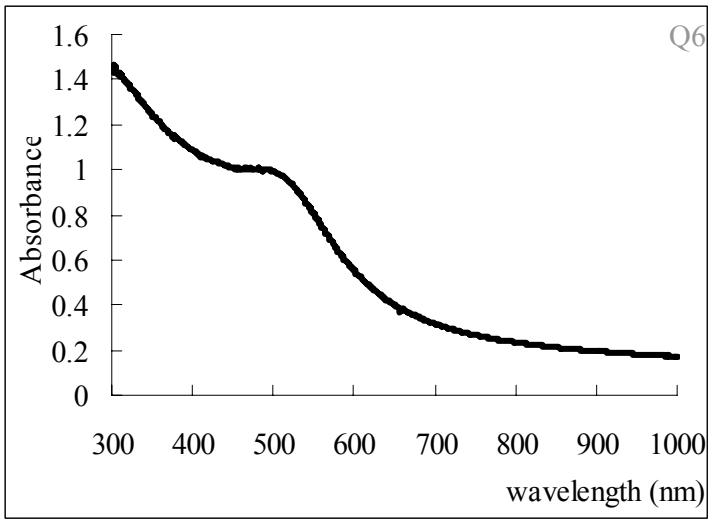

Figure 4.8 TEM image and UV-visible profile for the biphasic preparation of gold nanoparticles in entry 10.

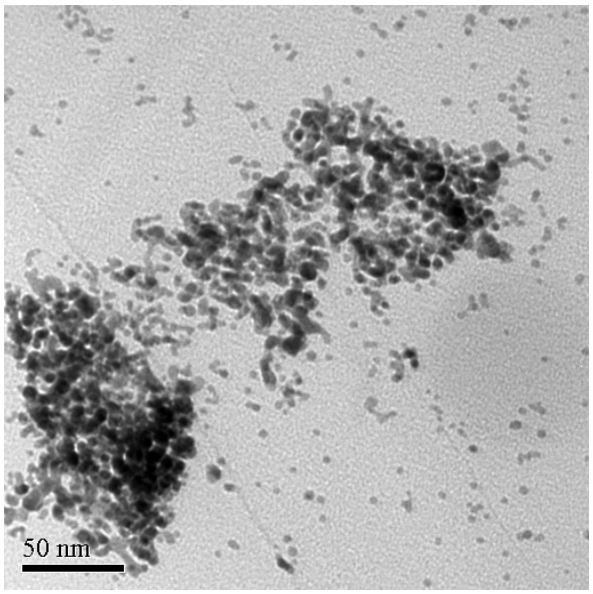

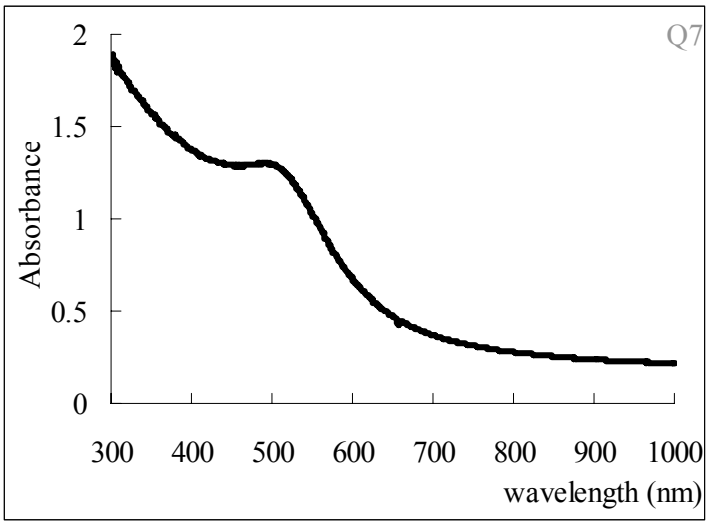

Figure 4.9 TEM image and UV-visible profile for the biphasic preparation of gold nanoparticles in entry 11.

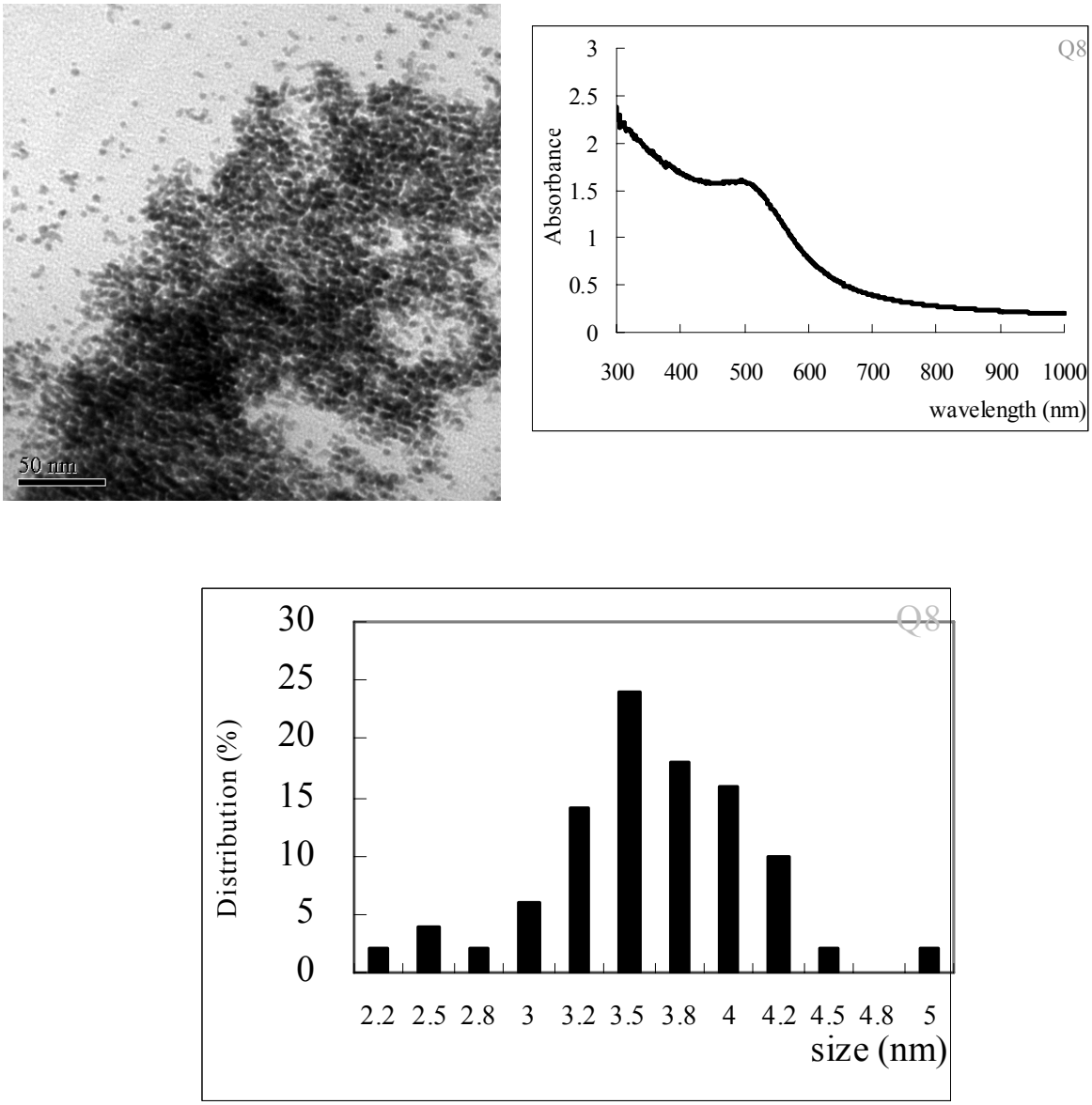

Figure 4.10 TEM image, size distribution statistics, and the UV-visible profile for the biphasic preparation of gold nanoparticles in entry 12.

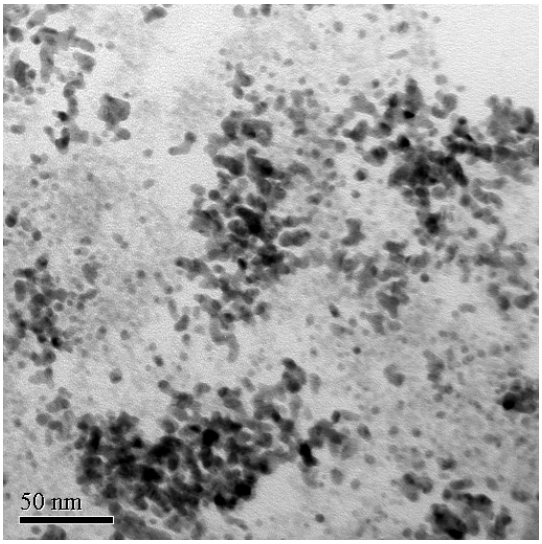

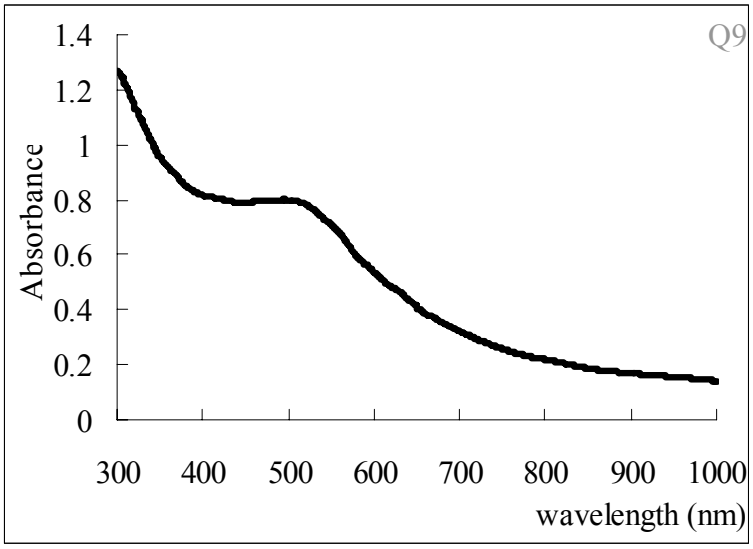

Figure 4.11 TEM image and the UV-visible profile for the biphasic preparation of gold nanoparticles in entry 13.

4.3.4 Single ionic liquid phase preparation of gold nanoparticles

4.3.4.1 Preparation of gold nanoparticles with ionic liquid solvated tetrabutylammonium borohydride – general observations

In order to understand the effects of different parameters on the morphology of the gold nanoparticles produced, the preparation were conducted under various conditions. The parameters investigated include – i) chain length of the pyrrolidinium cation, ii) temperature, iii) concentration of gold salt, and iv) types or kinds of halide.

When an ionic liquid solution of tetrabutylammonium borohydride was mixed with the ionic liquid containing the gold salt, an immediate colour change occurred. At the very beginning of the reaction, a wine red colour was developed in experiments with gold content of 5 to 50 mM. In experiments with lower gold content (~0.5 mM), a pinky red colour was formed. When the reaction proceeded, the wine red colour was generally preserved in experiments performed under low temperature and with a longer alkyl chain ionic liquids regardless of gold salt content. In contrast, a change from red to blue was commonly observed in experiments performed under room temperature and with shorter alkyl chain ionic liquids (e.g. C_6 and C_8). This was attributed to an enhanced near-field coupling as a result of particle aggregation coupling.[210] Black granules were produced in all experiments with a gold content of 50 mM. These granules formed in longer chain ionic liquid (C_{10} and C_{14}/C_{10}) could be dissolved in dichloromethane to give a clear wine red solution, while those from short chain ionic liquids gave a blue solution followed by gradual precipitation. The clear wine red coloured dichloromethane solution of the granules prepared from longer chain ionic liquid at

lower temperature was more stable than those prepared at room temperature. Therefore, a reduced temperature and longer-chain passivating ligands are favorable to the formation of more stable nanoparticles.

4.3.4.2 Effect of pyrrolidinium cation alkyl chain length on gold nanoparticles prepared with low concentration of pyrrolidinium tetrabromoaurate(III) (0.5 – 5 mM) at room temperature.

The average size of the gold nanoparticles formed with different pyrrolidinium alkyl chain length at low gold salt content were 4 – 6 nm. The average particle size (4.1 - 6.3 nm) (entries 15, 16, 31 and 32) changed with the gold concentration in the synthesis with the two shorter alkyl chain ionic liquids (C_6 and C_8). The distribution of particle diameter for nanospheres synthesized in the shortest chain C_6 ionic liquid was wider than that of their C_8 counterparts.

However, such variation in the size and dispersity was greatly reduced when longer alkyl chain ionic liquids were used. The C_{10} ionic liquid yielded gold nanospheres with average size of 5 and 5.6 nm (entries 47 and 48), while the difference in size was even limited to 0.2 nm in the presence of N-tetradecyl-pyrrolidinium cation (5.1 and 5.3 nm for entries 63 and 64). The particle size distribution demonstrates that the two longer chain pyrrolidinium cations could effectively limit the size dispersity down to less than one nanometer.

The morphologies of the gold nanoparticles in ionic liquids are shown in the TEM images (Figure 4.12 – 4.15). It can be seen that the clusters produced with all ionic liquids were mostly spherical. Some bigger sized or fused nanoparticles were found when the C_6 and C_8 ionic liquids were used in the synthesis. The small nanospheres prepared with C_{10} and C_{14}/C_{10} ionic liquids formed localized 2D monolayer with a repeating hexagonal arrangement, indicating that they are virtually monodispersed.

The UV-visible spectra (Figure 4.17) for the perfectly spherical nanoparticles in C_{10} and C_{14}/C_{10} ionic liquids showed a maximum absorption at 525 – 539 nm, corresponding to the surface plasmon resonance absorption of the gold nanospheres. The absorption profile nanoparticles in (entry 48) where a strong broad absorption was extended into the longer wavelength region may be due to the agglomeration of nanoparticles in the ionic liquid medium.

The maximum absorption wavelength (525 – 601 nm) in the UV-visible profiles for nanoparticles prepared in C_6 and C_8 ionic liquids (Figure 4.16 and 4.17) were in general inconsistent with the actual nanoparticle average dimension found (4 – 7 nm). Since the bathochromic shift of the UV-visible absorption can result from either particle size enlargement or reduced inter-particle distance,[210] the observed optical spectra for the nanoparticles in C_6 and C_8 were therefore likely due to reduced distance between particles.

a)

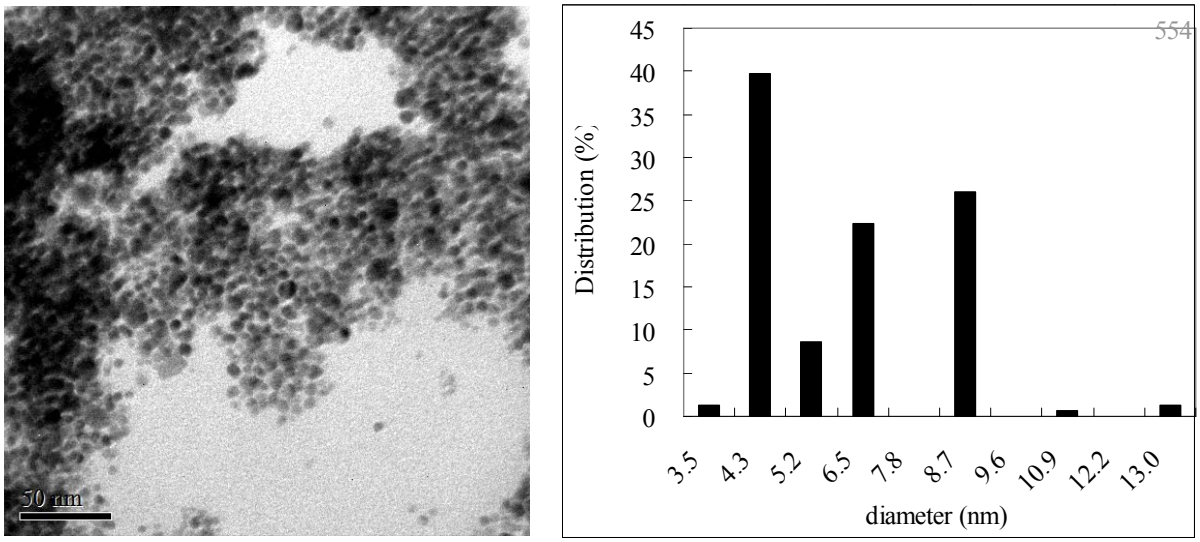

b)

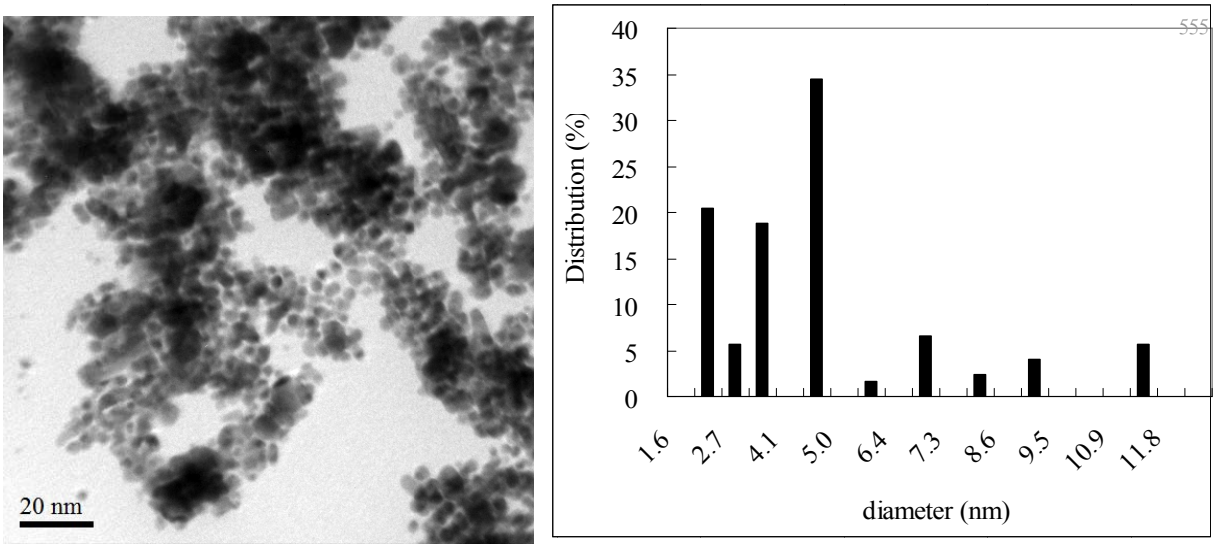

Figure 4.12 TEM images and size distributions of gold nanoparticles in ionic liquid synthesized at room temperature with 1 mL $PyC_6[Tf_2N]$ containing a) 0.5 mM $PyC_6[AuBr_4]$ (entry 15) and b) 5 mM $PyC_6[AuBr_4]$ (entry 16)

a)

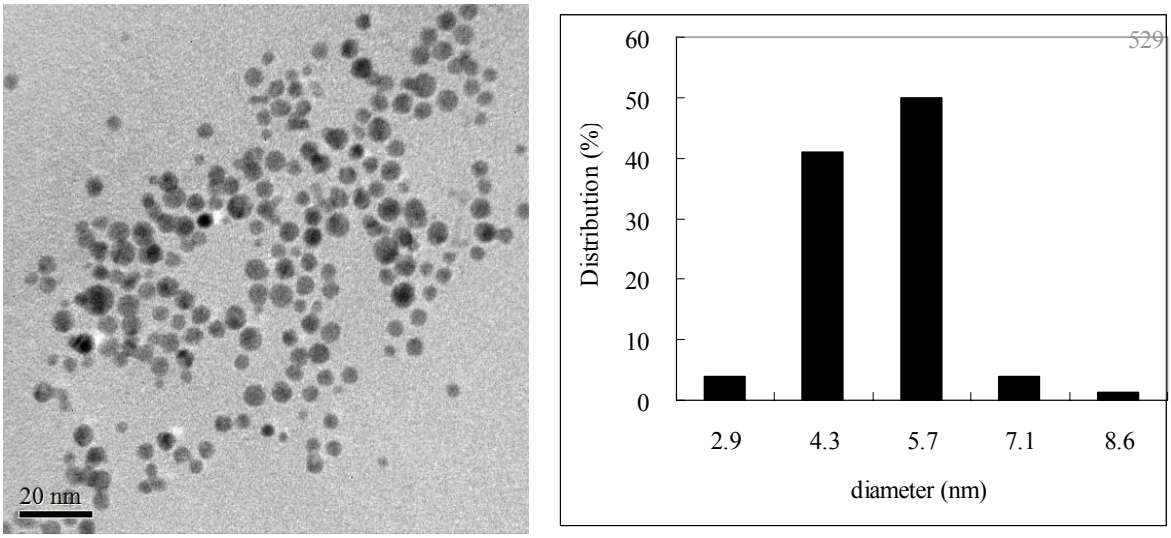

(b)

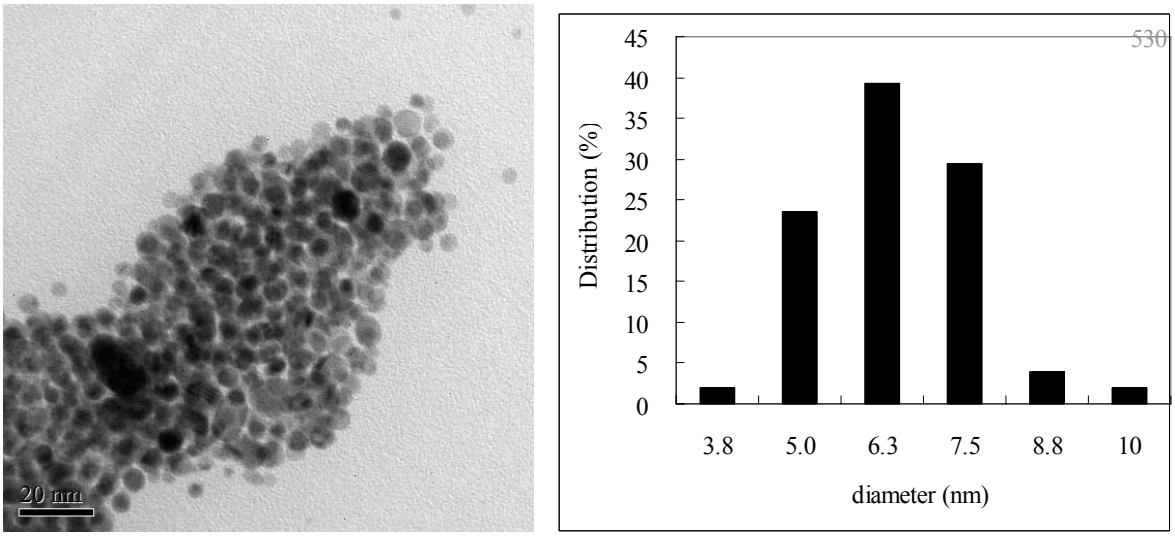

Figure 4.13 TEM images and size distributions of gold nanoparticles in ionic liquid synthesized at room temperature with 1 mL $PyC_{8}[Tf_2N]$ containing a) 0.5 mM $PyC_{8}[AuBr_4]$ (entry 31) and b)5 m M $PyC_{8}[AuBr_4]$. (entry 32)

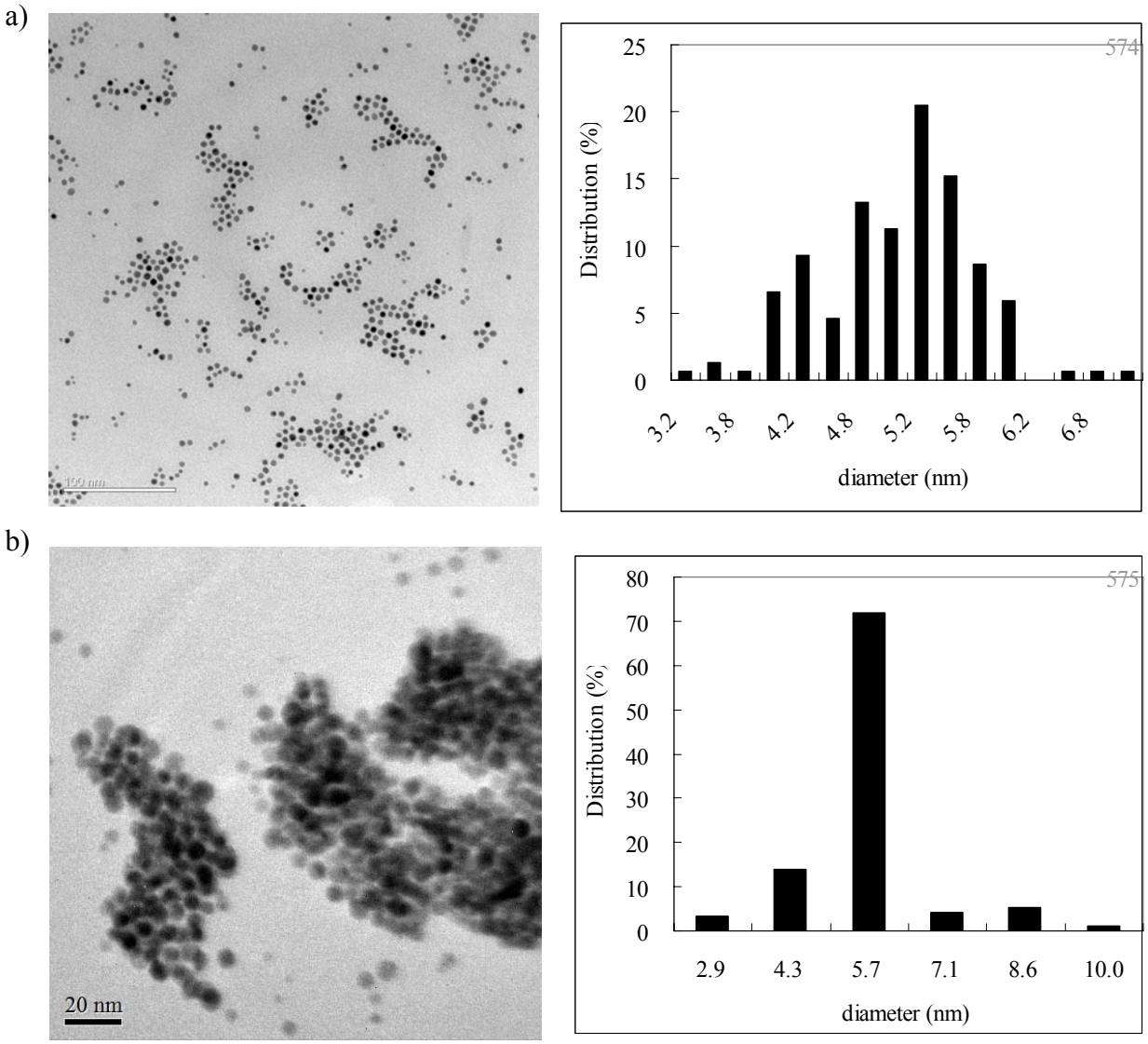

Figure 4.14 TEM images and size distributions of gold nanoparticles in ionic liquid synthesized at room temperature with 1 mL $PyC_{10}[Tf_2N]$ containing a) 0.5 mM $PyC_{10}[AuBr_4]$ (entry 47) and b) 5 mM $PyC_{10}[AuBr_4]$ (entry 48).

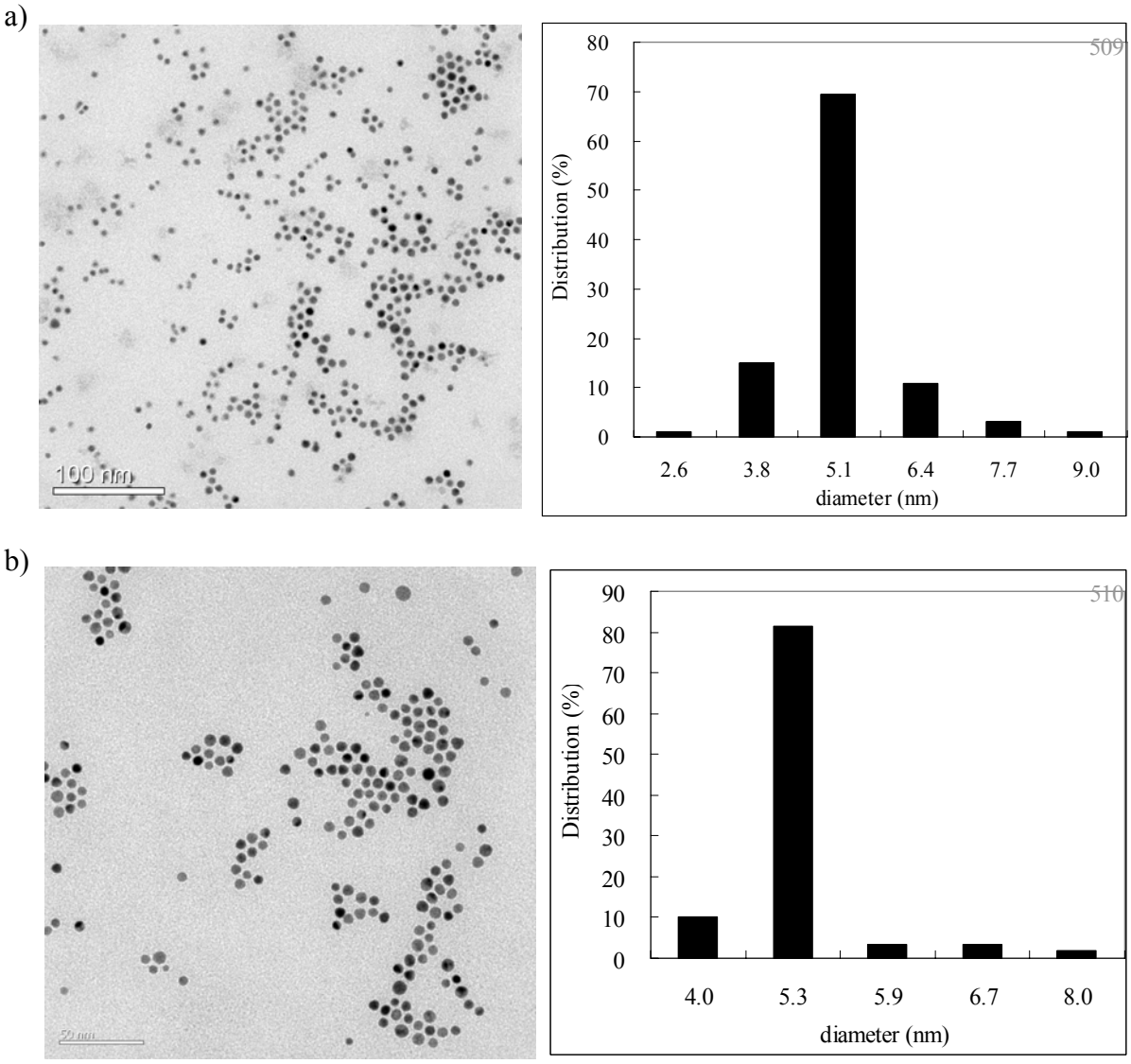

Figure 4.15 TEM images and size distributions of gold nanoparticles in ionic liquid synthesized at room temperature with 1 mL $PyC_{10}[Tf_2N]$ containing a) 0.5 mM $PyC_{14}[AuBr_4]$ (entry 63) and b) 5 mM $PyC_{14}[AuBr_4]$. (entry 64).

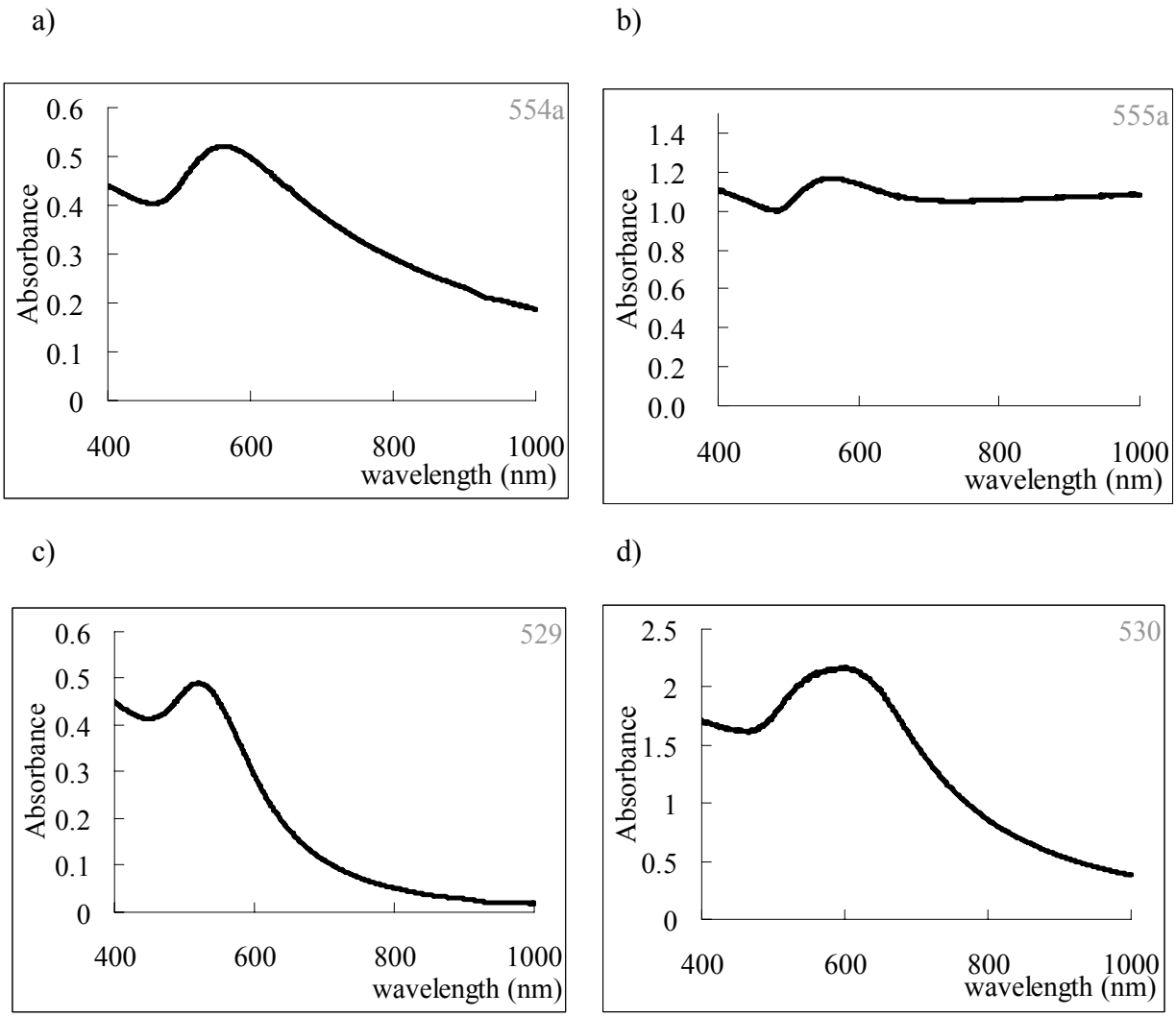

Figure 4.16 UV-visible spectra for gold nanoparticles in ionic liquid synthesized at room temperature in 1 ml $C_6[Tf_2N]$ with a) 0.5 mM $PyC_6[AuBr_4]$ (entry 15), b) 5 mM $PyC_6[AuBr_4]$ (entry 16) and in 1 mL $PyC_8[Tf_2N]$ with c) 0.5 mM $PyC_8[AuBr_4]$ (entry 31), d) 5 mM $PyC_8[AuBr_4]$ (entry 32).

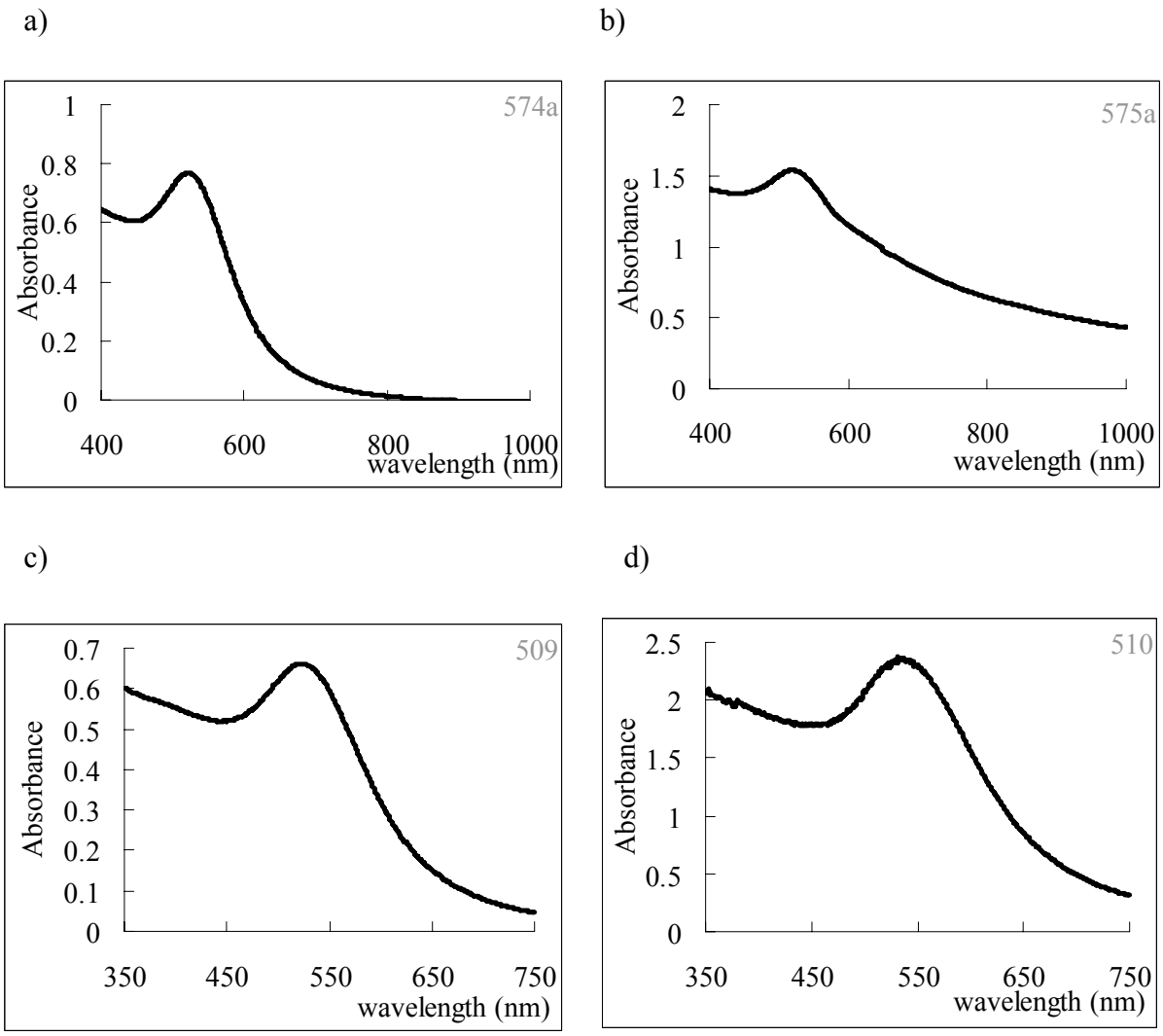

Figure 4.17 UV-visible spectra for gold nanoparticles in ionic liquid synthesized at room temperature in 1 ml $C_{10}[Tf_2N]$ with a) 0.5 mM PyC_{10} $[AuBr_4]$ (entry 47), b) 5 mM $PyC_{10}[AuBr_4]$ (entry 48) and in 1 mL $PyC_{10}[Tf_2N]$ with c) 0.5 mM PyC_{14} $[AuBr_4]$ (entry 63), d) 5 mM PyC_{14} $[AuBr_4]$ (entry 64)

4.3.4.3 Effect of pyrrolidinium cation alkyl chain length on gold nanoparticles prepared with higher concentration of pyrrolidinium tetrabromoaurate(III) (10 and 50 mM) at room temperature.

Once the concentration of the gold salt was raised to 10 – 50 mM, the average size of the nanoparticles formed with shorter chain ionic liquids (C_6 and C_8) was significantly larger than their longer chain counterparts (Figure 4.18 and 4.19). The average particle size obtained was within the range of 5.2 – 7.5 nm with minimal size variation at high gold salt concentration in the four ionic liquids of different chain lengths.

With longer alkyl chain ionic liquids (C_{10}, C_{14}/C_{10}), the dimensional and morphological control of the nanoparticles formed at high gold salt content remained excellent. TEM images (Figure 4.20 and 4.21) show that the average diameter and the dispersity of the nanospheres were close to 5 nm and generally within 1 nm respectively. Except the 2D monolayer hexagonal arrangement mentioned previously, the seemingly monodispersed gold nanoparticles synthesized with C_{14}/C_{10} ionic liquid were aligned in a chain-like arrangement which is highly similar to that observed in the quaternary ammonium bromide passivated gold nanoparticles by Fink *et al*.[209] Such an arrangement is observed when the second layer particles are placed on the 2-fold saddle site between two particles of this first layer underneath. Actually, the occupancy of the 2-fold saddle site rather than the energetically more favorable 3-fold hollow position is strongly related to the strong short-range electrostatic dipolar repulsion by the surface attached quaternary ammonium monolayer.

The nanospheres from C_{10} and C_{14}/C_{10} ionic liquids were dispersed completely in

dichloromethane and the UV-visible spectra for these two colloids organic solutions showed a sharp SPR peak at ~ 530 nm (Figure 4.22), which is consistent with the morphology of the well-separated spherical nanoparticles revealed by TEM.

a)

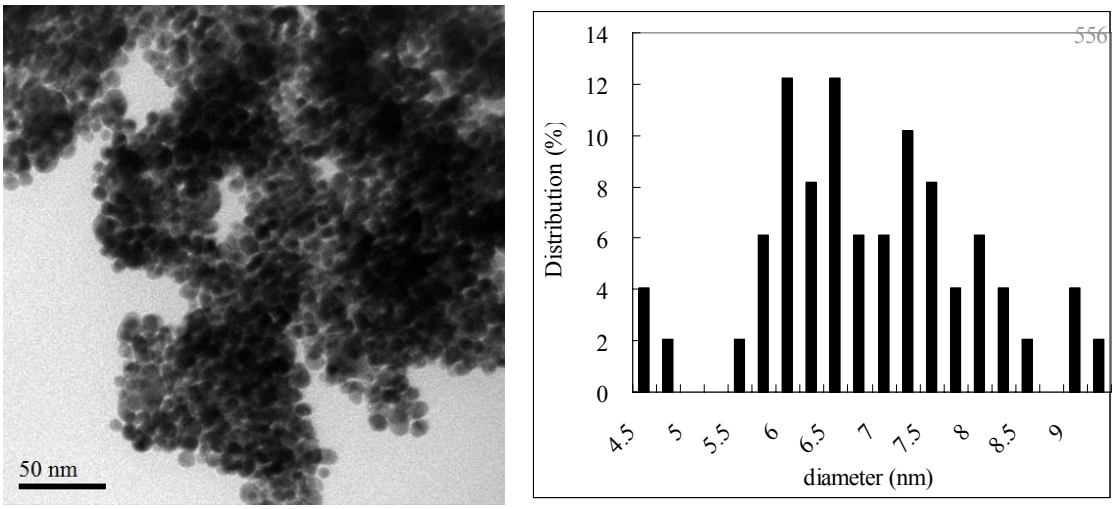

b)

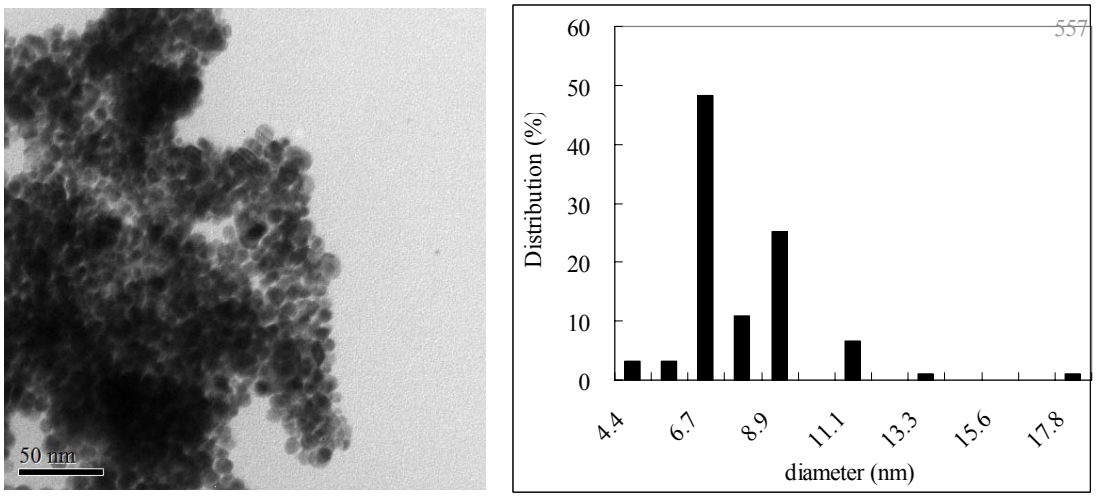

Figure 4.18 TEM images and size distributions of gold nanoparticles in ionic liquid synthesized at room temperature with 1 mL $PyC_{6}[Tf_2N]$ containing: a) 10 mM $PyC_{6}[AuBr_4]$ (entry 17) and b) 50 mM $PyC_{6}[AuBr_4]$ (entry 18).

a)

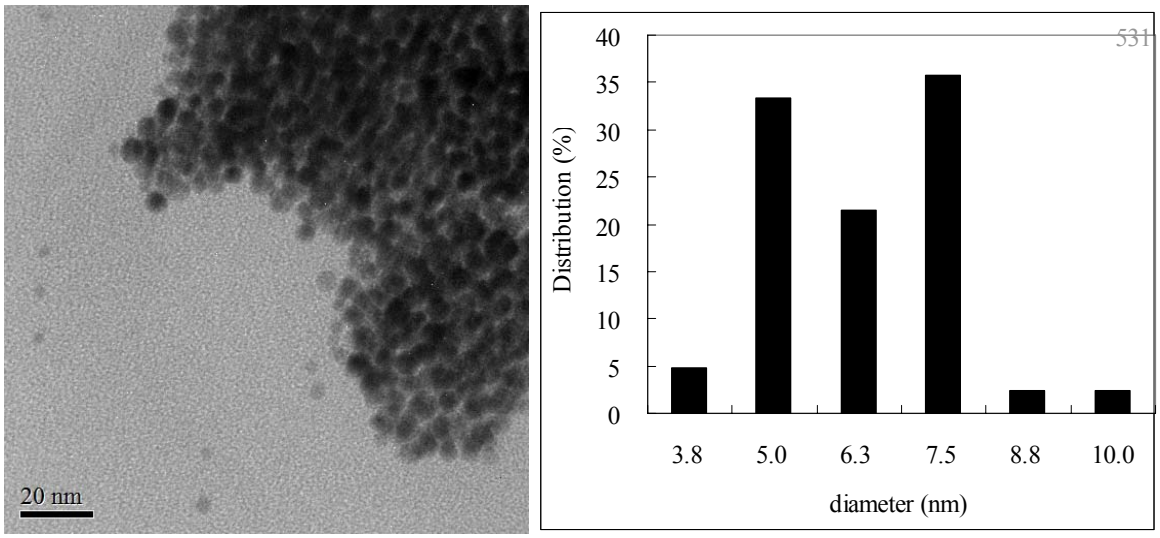

b)

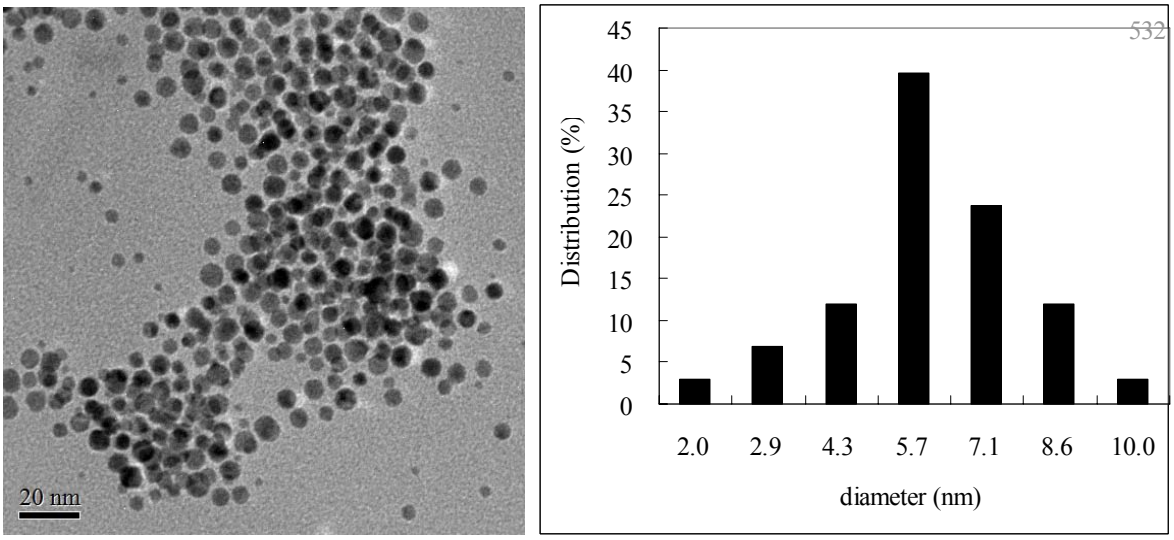

Figure 4.19 TEM images and size distributions of gold nanoparticles in ionic liquid synthesized at room temperature with 1 mL $PyC_{8}[Tf_2N]$ containing: a) 10 mM $PyC_{8}[AuBr_4]$ (entry 33) and b) 50 mM $PyC_{8}[AuBr_4]$ (entry 34).

a)

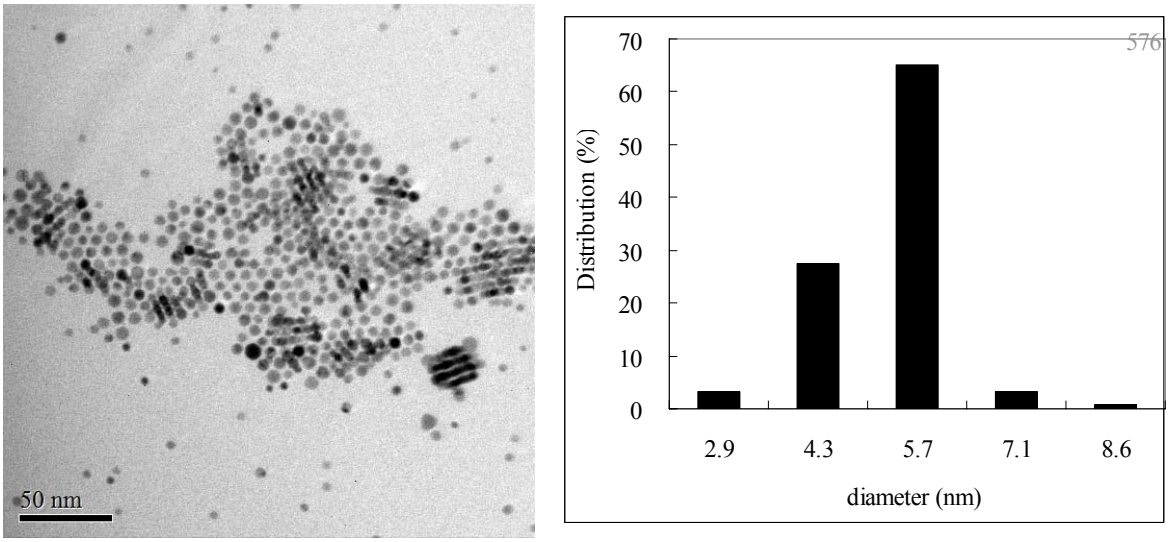

b)

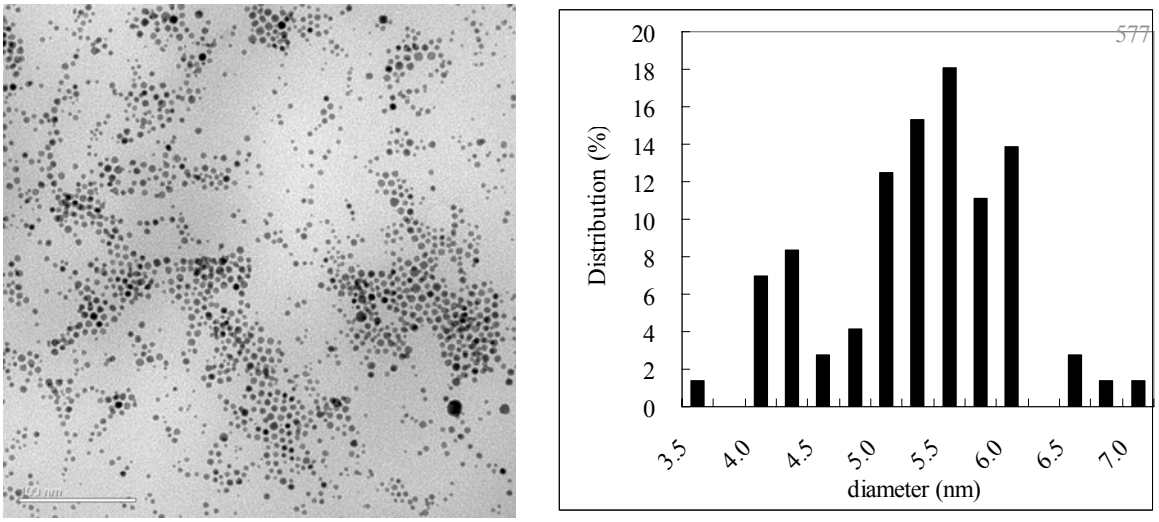

Figure 4.20 TEM images and size distributions of gold nanoparticles in ionic liquid synthesized at room temperature with 1 mL $PyC_{10}[Tf_2N]$ containing: a) 10 mM $PyC_{10}[AuBr_4]$ (entry 49), and b) 50 mM $PyC_{10}[AuBr_4]$ (entry 50).

a)

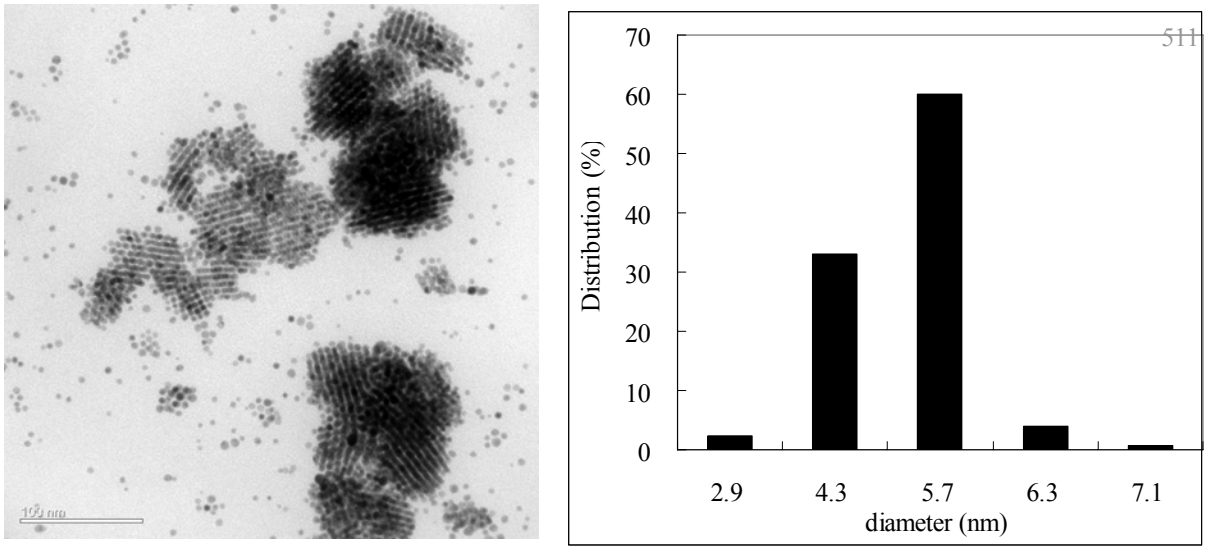

b)

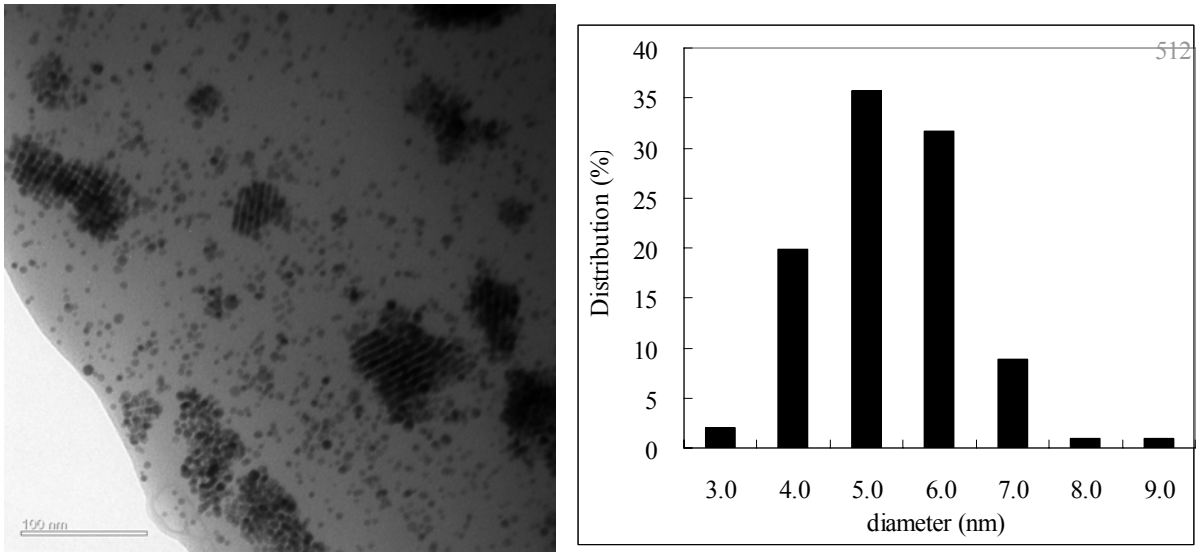

Figure 4.21 TEM images and size distributions of gold nanoparticles in ionic liquid synthesized at room temperature with 1 mL $PyC_{10}[Tf_2N]$ containing: a) 10 mM $PyC_{14}[AuBr_4]$ (entry 65), and b) 50 mM $PyC_{14}[AuBr_4]$ (entry 66).

a)

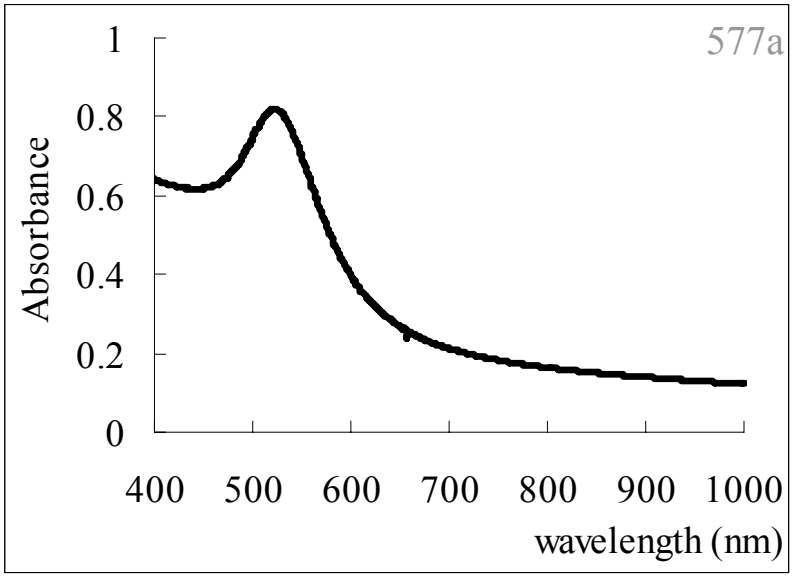

b)

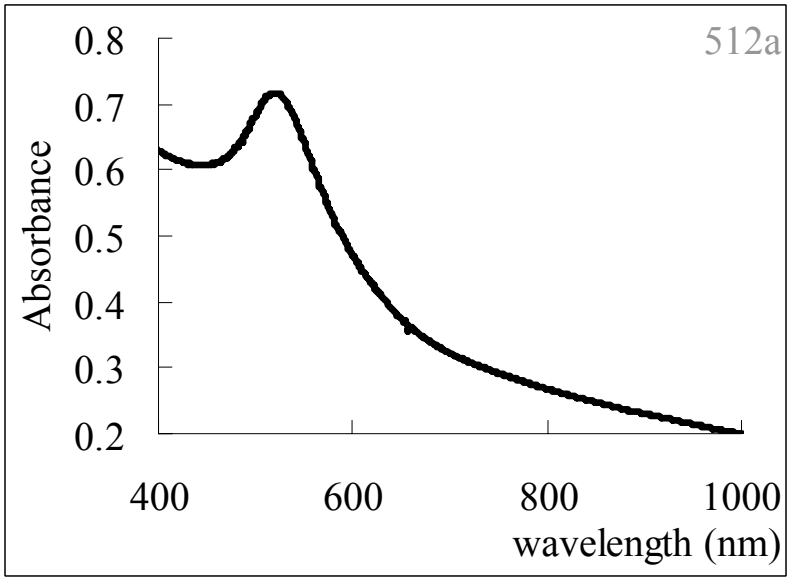

Figure 4.22 UV-visible spectra (in dichloromethane) for gold nanoparticles synthesized at room temperature with 1 mL $PyC_{10}[Tf_2N]$ containing: a) 50 mM $PyC_{10}[AuBr_4]$ (entry 50) and b) 50 mM $PyC_{14}[AuBr_4]$ (entry 66).

4.3.4.4 Effect of pyrrolidinium cation alkyl chain length on gold nanoparticles prepared with low pyrrolidinium tetrachloroaurate(III) (0.5 and 5 mM) content at room temperature.

With a change from bromide to chloride, the average size of the nanoparticles obtained among experiments was highly similar and around a narrow range (4.6 – 5.0 nm), regardless of the chain length of the ionic liquid used (Figure 4.23 – 4.26). Contrary to the bromide system, particle size dispersity was less than 1 nm even when shorter chain ionic liquidswere used. Most UV-visible spectra of the gold nanoparticles in ionic liquids prepared from 0.5 mM gold precursor with chlorides gave a SPR maximum absorption around 520 nm (Figure 4.27 and 4.28), while those prepared with 10 times more concentrated gold solution showed SPR band at 575 or near 600 nm due to enhanced nanoparticle interaction within the viscous ionic liquid medium. The reduced particle separation was also proven by the enhanced absorption at longer wavelength and the less flattened and short SPR peak.

4.3.4.5 Effect of pyrrolidinium cation alkyl chain length on gold nanoparticles prepared with higher pyrrolidinium tetrachloroaurate(III) (0.5 and 5 mM) content at room temperature.

Gradual decrease in average particle diameter from 8.2 to 4.4 nm was observed from C_6 to C_{14}/C_{10} ionic liquid when a higher concentration of gold precursor was employed. This suggests that chloride can help to produce smaller nanoparticles in the presence of longer chain ionic liquids. On the other hand, a greater dependence of the particle size on gold precursor concentration was observed when the nanoparticles were synthesized in the C_6 ionic liquid, while such relationship became much less pronounced when the alkyl chain in the ionic liquid increased. The difference in the average size of the nanoparticles dropped from 3 nm for C_6 (entry 25 and 26, 5.1 nm to 8.2 nm) to 0.4 nm for C_{14}/C_{10} (entry 73 and 74, 4.0 nm to 4.4 nm) when the concentration of the gold precursor was increased from 10 M to 50 mM.

The UV-visible spectra for nanoparticles prepared with C_{10} and C_{14}/C_{10} ionic liquids in the presence of high concentration auric-chloride precursor are shown in Figure 4.33. The sharp SPR peak, showing maximum at 525 nm and limited broadening at longer wavelength, shows that the spherical nanoparticles formed were well-dispersed in the C_{14}/C_{10} ionic liquid, as shown in the Figure 4.32a. The spectrum for colloids in C_{10} showed a red-shifting of the SPR band (~ 565 nm) with apparent broadening extended to wavelengths longer than the plasmon peak. This was due to the nanoparticles aggregation mentioned previously. A sudden change in solvent may induce the coagulation of nanoparticles.

a)

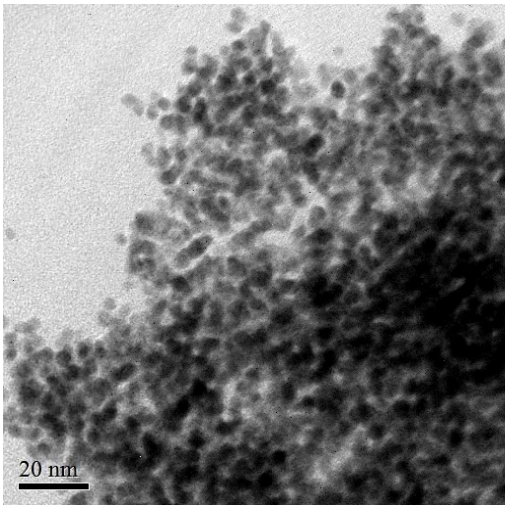

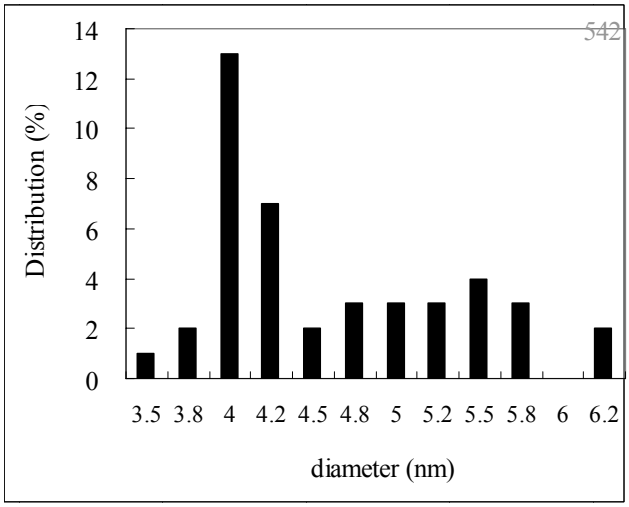

b)

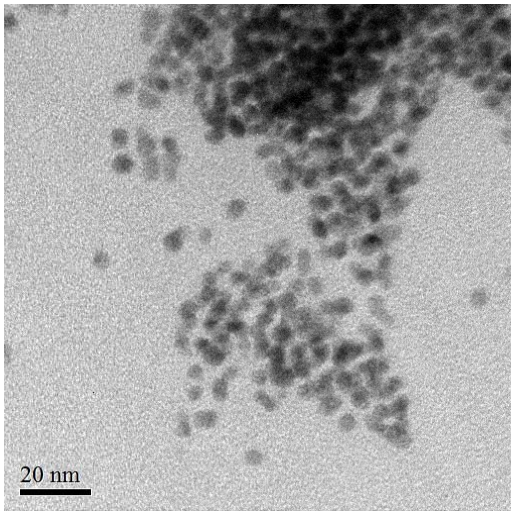

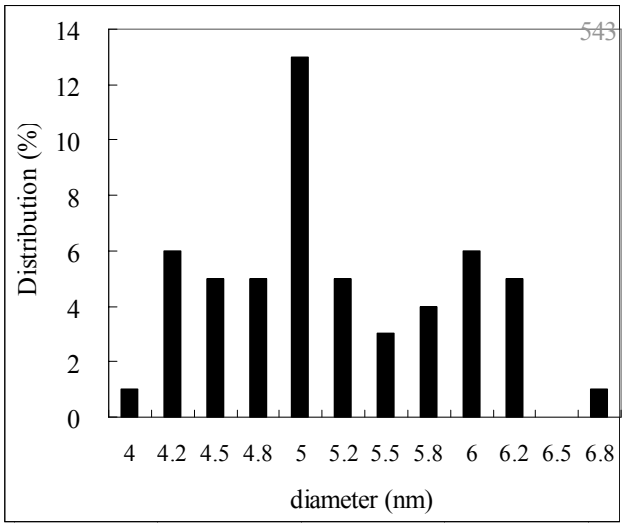

Figure 4.23 TEM images and size distributions of gold nanoparticles in ionic liquid synthesized at room temperature with 1 mL $PyC_{\mathbf{8}}[Tf_2N]$ containing: a) 0.5 mM $PyC_{\mathbf{6}}[AuCl_4]$ (entry 23) and b) 5 mM $PyC_{\mathbf{6}}[AuCl_4]$ (entry 24).

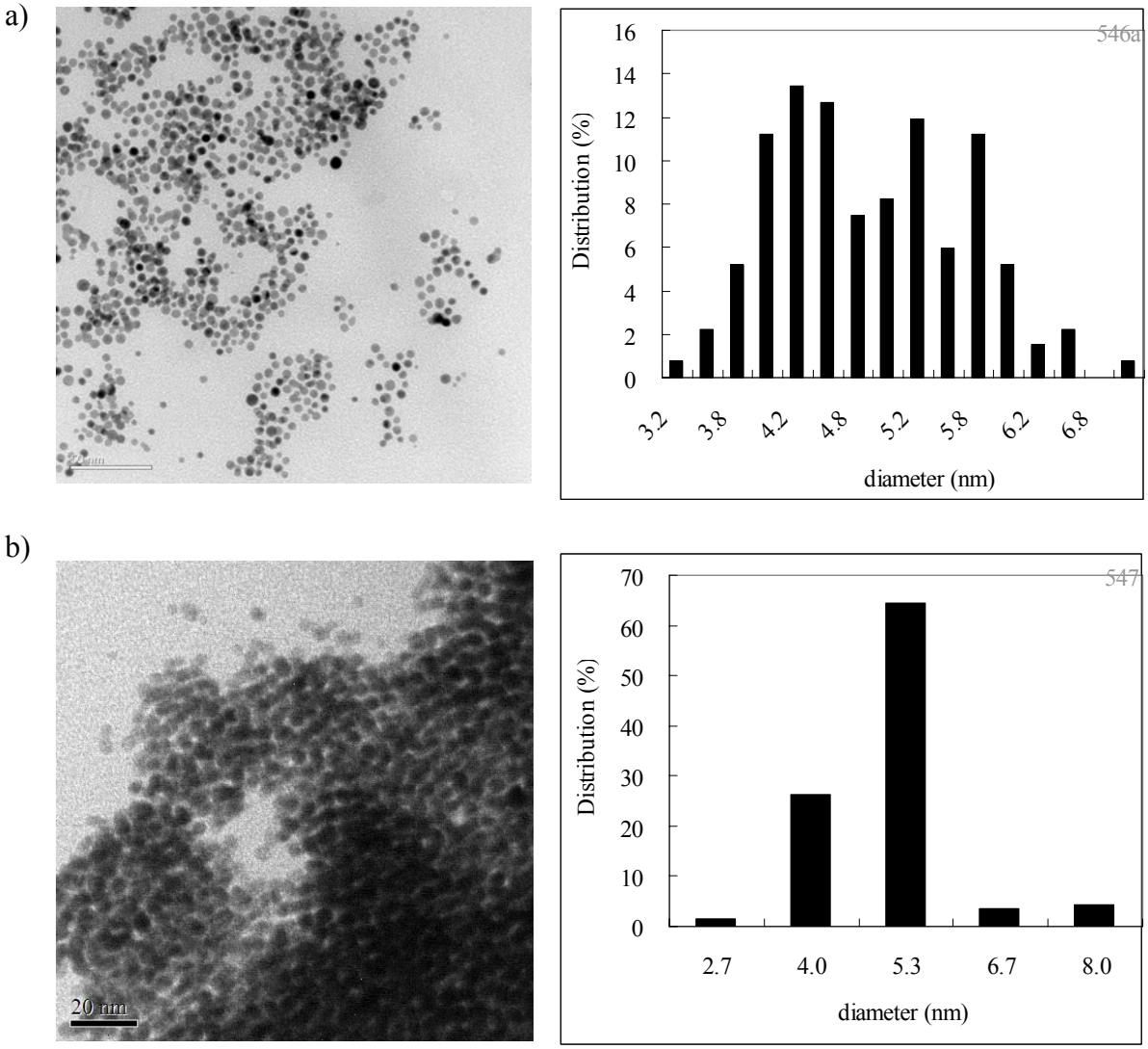

Figure 4.24 TEM images and size distributions of gold nanoparticles in ionic liquid synthesized at room temperature with 1 mL $PyC_8[Tf_2N]$ containing: a) 0.5 mM $PyC_8[AuCl_4]$ (entry 39) and b) 5 mM $PyC_8[AuCl_4]$ (entry 40).

a)

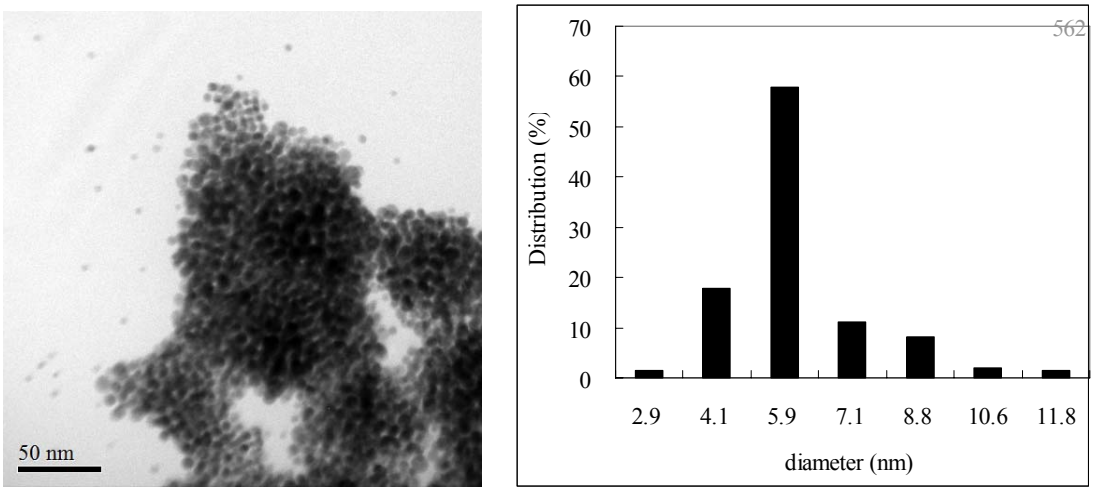

b)

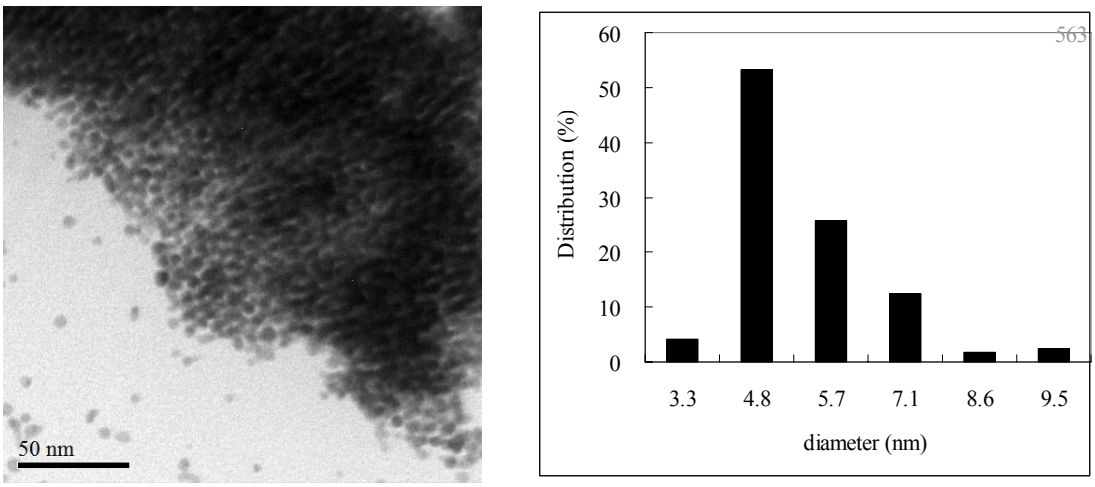

Figure 4.25 TEM images and size distributions of gold nanoparticles in ionic liquid synthesized at room temperature with 1 mL $PyC_{10}[Tf_2N]$ containing: a) 0.5 mM PyC_{10} $[AuCl_4]$ (entry 55) and b) 0.5 mM PyC_{10} $[AuCl_4]$ (entry 56)

a)

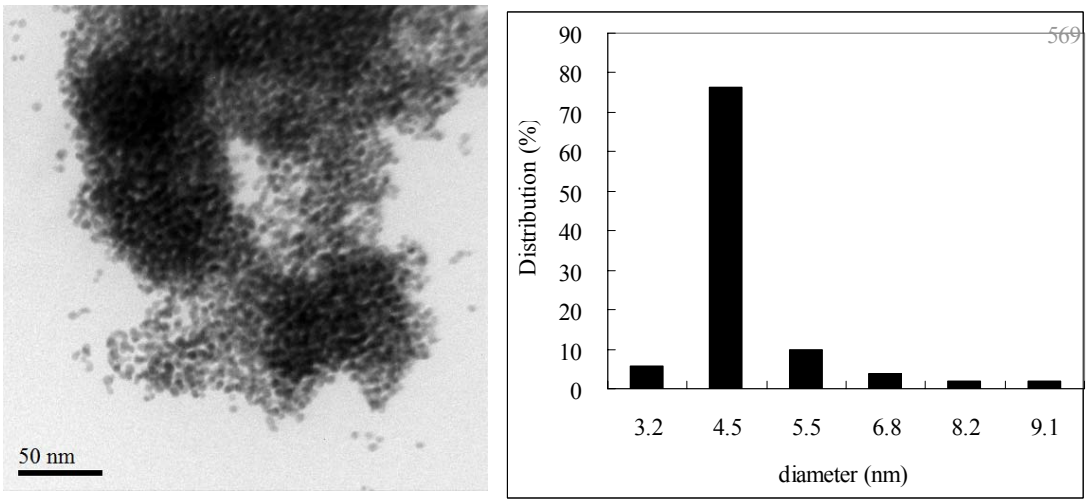

b)

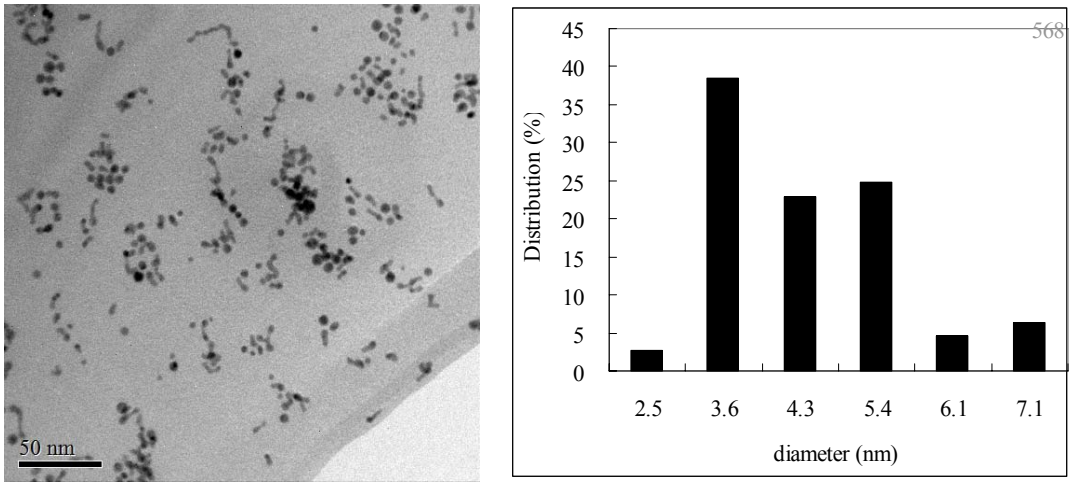

Figure 4.26 TEM images and size distributions of gold nanoparticles in ionic liquid synthesized at room temperature with 1 mL $PyC_{10}[Tf_2N]$ containing a) 0.5 mM $PyC_{14}[AuCl_4]$ (entry 71) and b) 5 mM $PyC_{14}[AuCl_4]$. (entry 72).

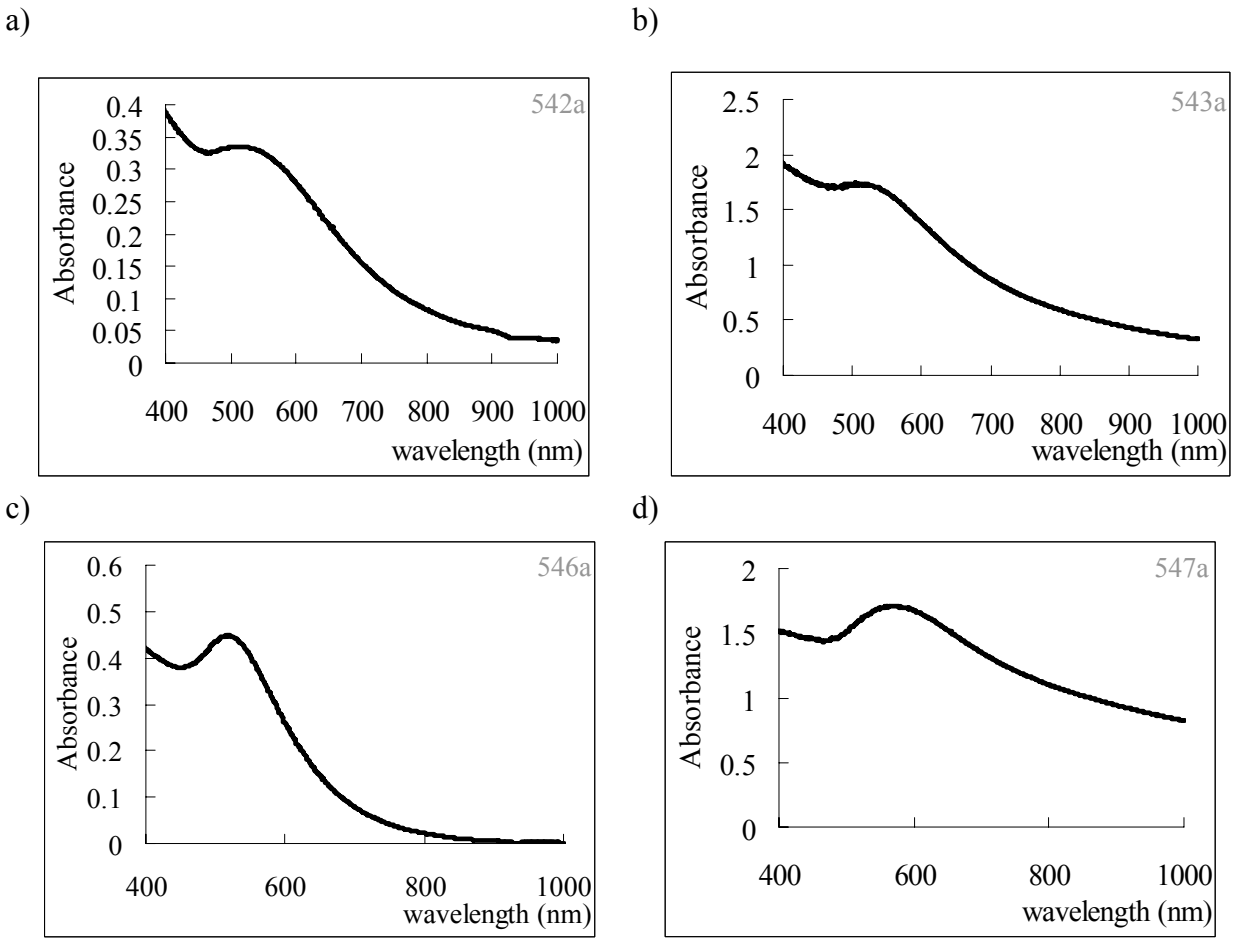

Figure 4.27 UV-visible spectra for gold nanoparticles in ionic liquid synthesized at room temperature with 1 ml $PyC_{\mathbf{6}}[Tf_2N]$ containing: a) 0.5 mM $PyC_{\mathbf{6}}[AuCl_4]$ (entry 23), b) 5 mM $PyC_{\mathbf{6}}[AuCl_4]$ (entry 24) and with 1 ml $PyC_{\mathbf{8}}[Tf_2N]$ containing c) 0.5 mM $PyC_8[AuCl_4]$ (entry 39) and d) 5 mM $PyC_{\mathbf{8}}[AuCl_4]$ (entry 40).

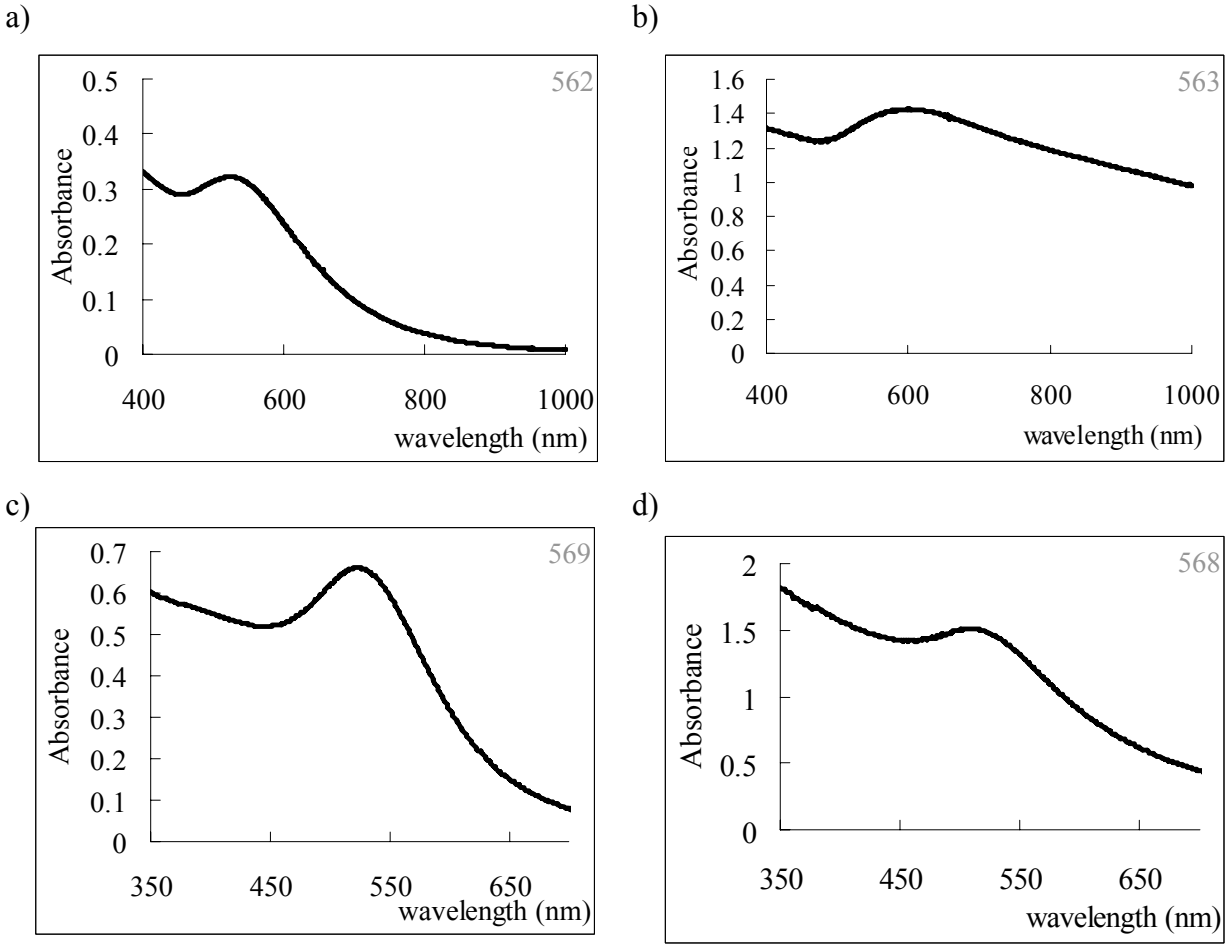

Figure 4.28 UV-visible spectra for gold nanoparticles in ionic liquid synthesized at room temperature with 1 ml $PyC_{\mathbf{10}}[Tf_2N]$ containing a) 0.5 mM $PyC_{\mathbf{10}}[AuBr_4]$ (entry 55), b) 5 mM $PyC_{\mathbf{10}}[AuBr_4]$ (entry 56) and with 1 ml $PyC_{\mathbf{10}}[Tf_2N]$ containing c) 0.5 mM $PyC_{14}[AuBr_4]$ (entry 71), d) 5 mM $PyC_{\mathbf{14}}[AuBr_4]$ (entry 72).

a)

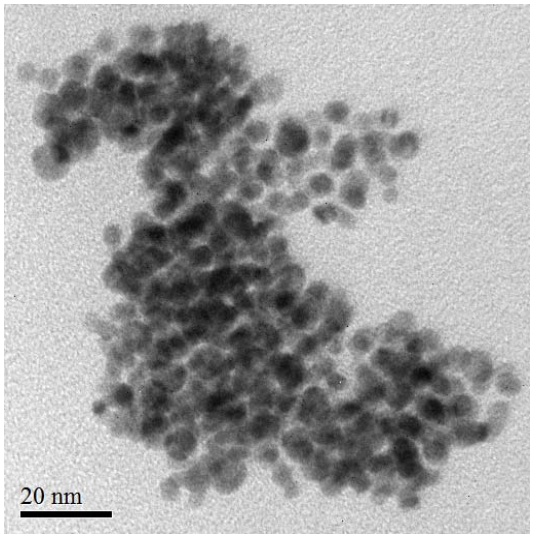

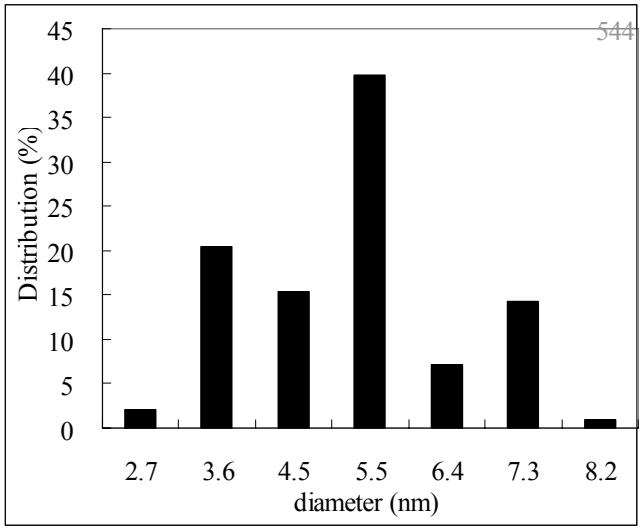

b)

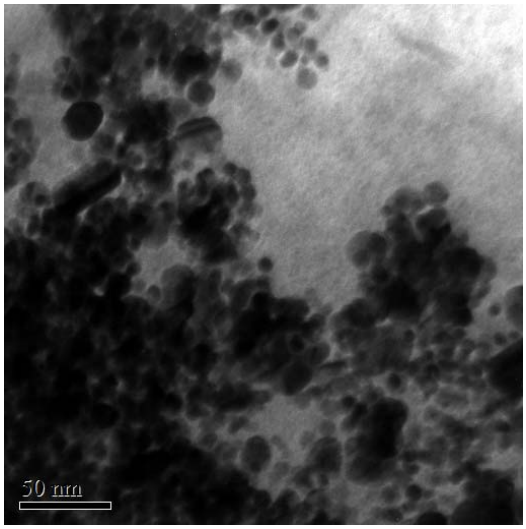

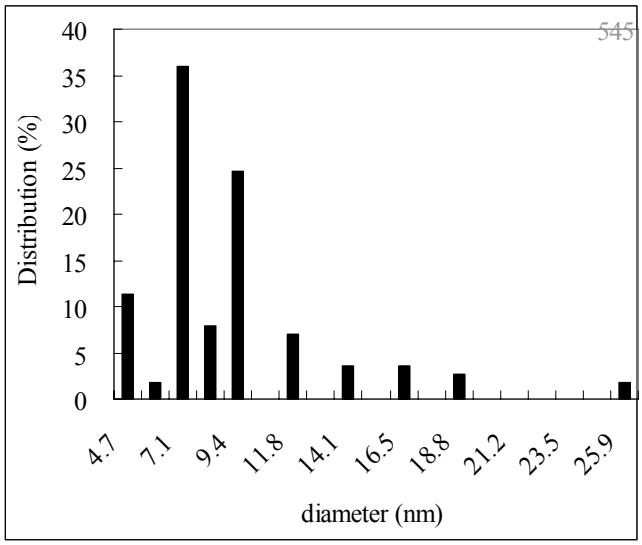

Figure 4.29 TEM images and size distributions of gold nanoparticles in ionic liquid synthesized at room temperature with 1 mL $PyC_{6}[Tf_2N]$ containing a) 10 mM $PyC_{6}[AuCl_4]$ (entry 25) and b) 50 mM $PyC_{6}[AuCl_4]$. (entry 26).

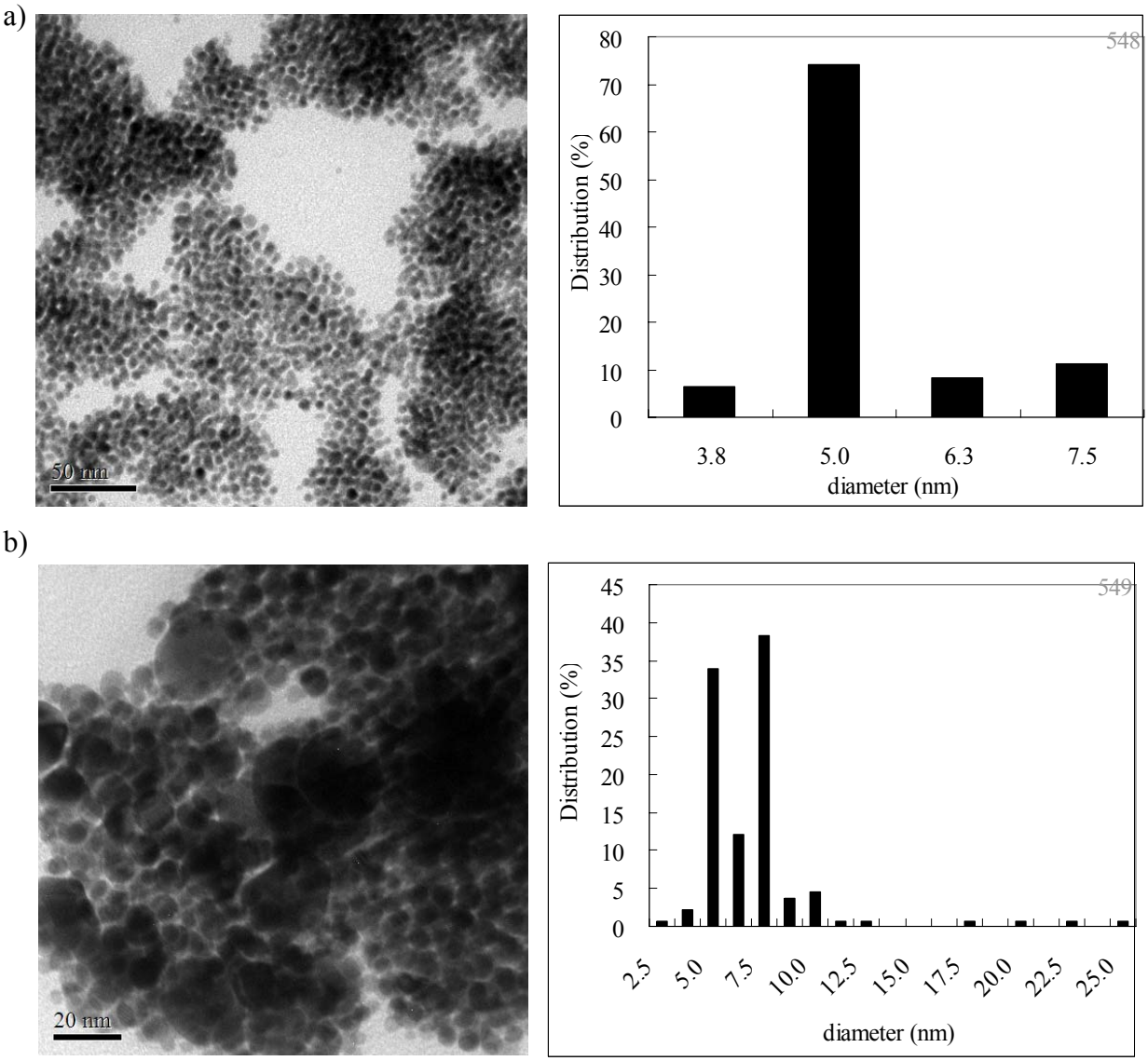

Figure 4.30 TEM images and size distributions of gold nanoparticles in ionic liquid synthesized at room temperature with 1 mL $PyC_8[Tf_2N]$ containing: a) 10 mM $PyC_8[AuCl_4]$ (entry 41) and b) 50 mM $PyC_8[AuCl_4]$ (entry 42).

a)

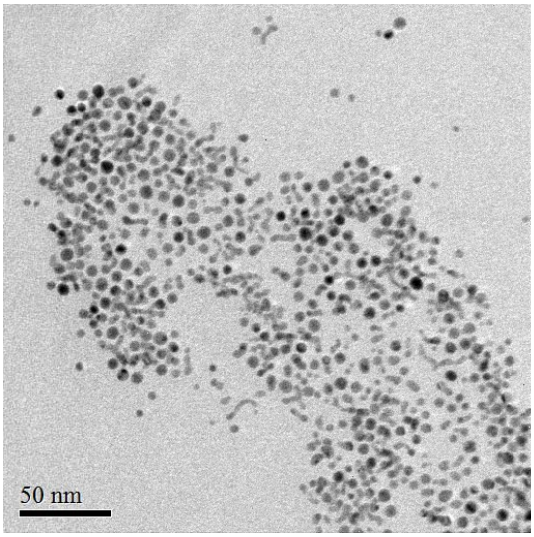

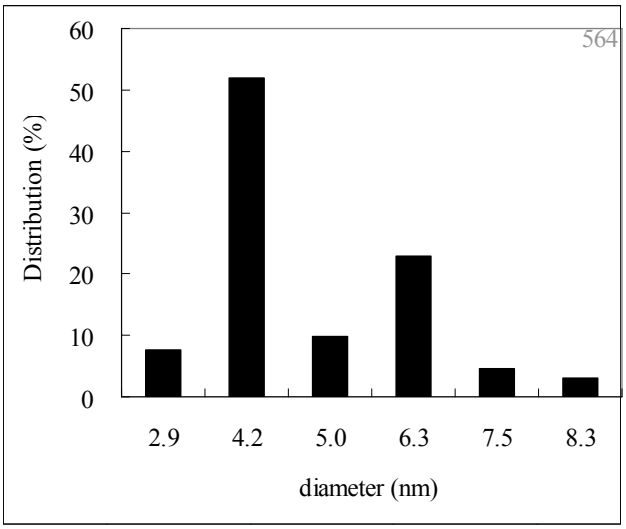

b)

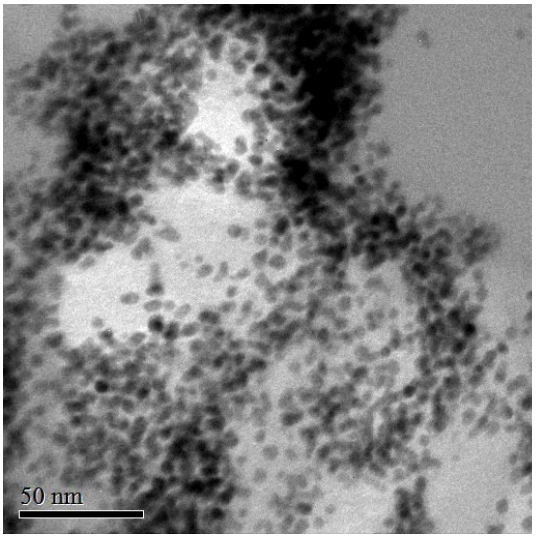

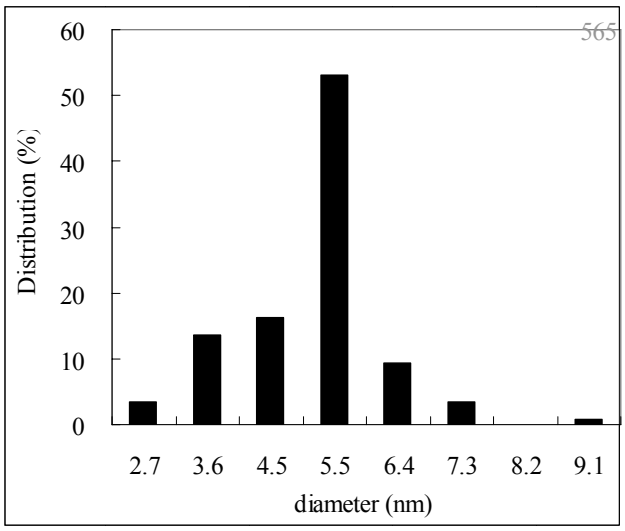

Figure 4.31 TEM images and size distributions of gold nanoparticles in ionic liquid synthesized at room temperature with 1 mL $PyC_{10}[Tf_2N]$ containing: a) 10 mM $PyC_{10}[AuCl_4]$ (entry 57) and b) 50 mM $PyC_{10}[AuCl_4]$ (entry 58).

a)

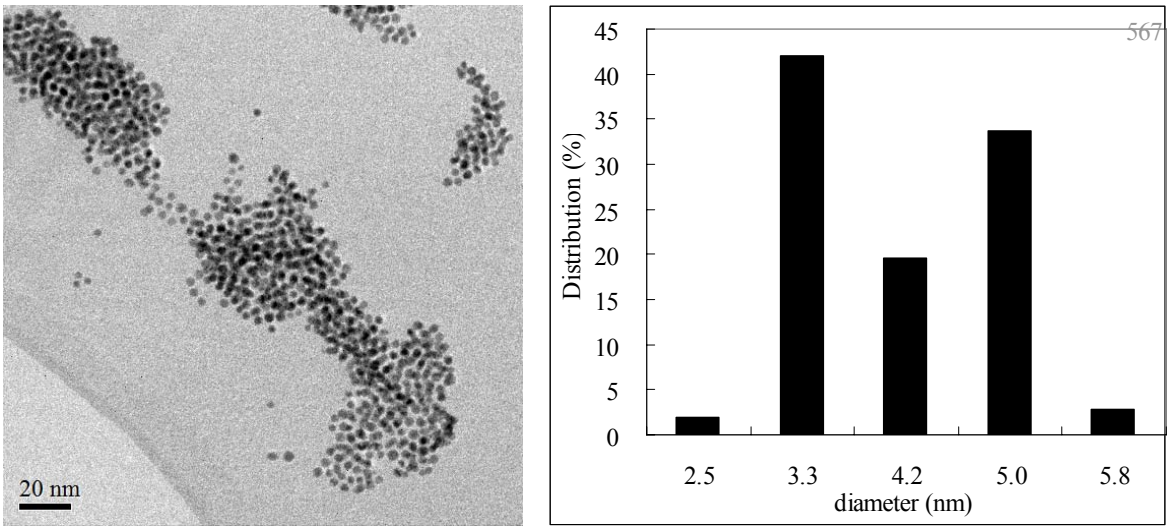

b)

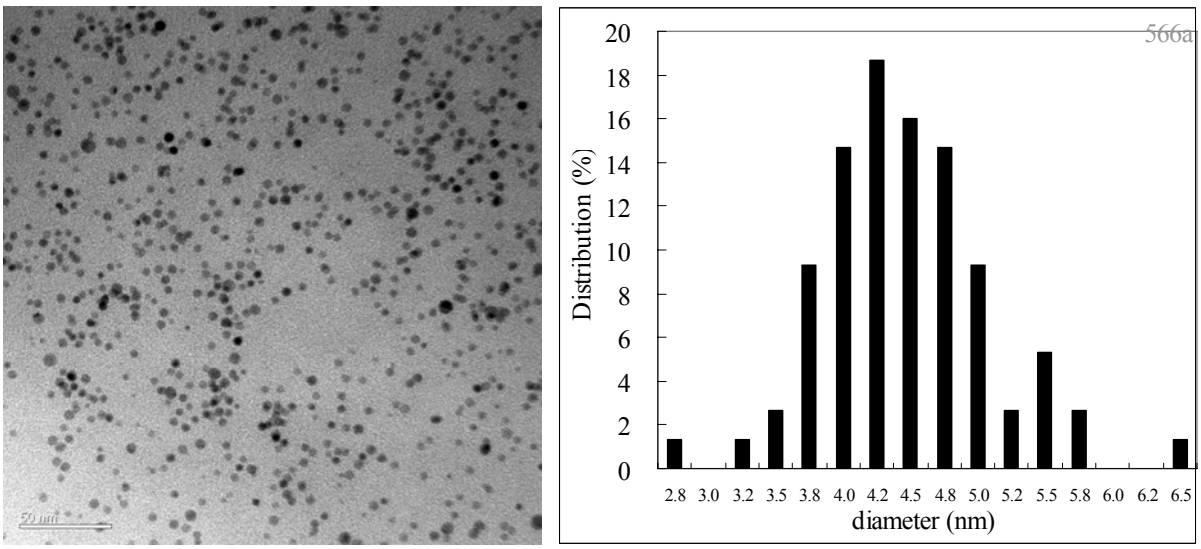

Figure 4.32 TEM images and size distributions of gold nanoparticles in ionic liquid synthesized at room temperature with 1 mL $PyC_{10}[Tf_2N]$ containing a) 10 mM $PyC_{14}[AuCl_4]$ (entry 73) and b) 50 mM $PyC_{14}[AuCl_4]$ (entry 74).

a)

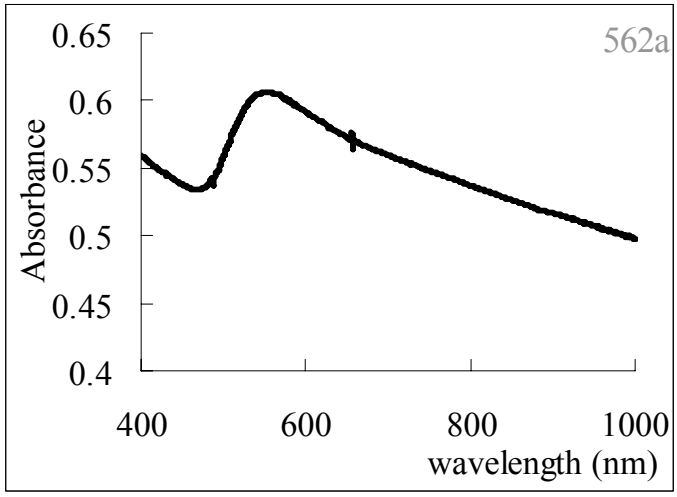

b)

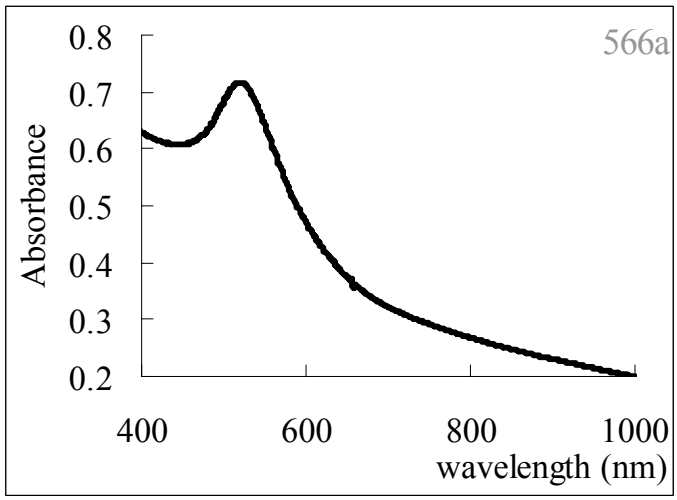

Figure 4.33 UV-visible spectra (in dichloromethane) for gold nanoparticles synthesized at room temperature in 1 mL $PyC_{\mathbf{10}}[Tf_2N]$ containing a) 50 mM $PyC_{\mathbf{10}}[AuCl_4]$ in (entry 58) and in 1 ml $PyC_{\mathbf{10}}[Tf_2N]$ containing b) 50 mM $PyC_{\mathbf{14}}[AuCl_4]$ in (entry 74).

4.3.4.6 Effect of pyrrolidinium cation alkyl chain length on gold nanoparticles prepared with low pyrrolidinium tetrabromoaurate(III) concentration (0.5 and 5 mM) at low temperature (~ 2℃).

In figure 4.34, it can be seen that a drop in the reaction temperature caused a sharp increase in the average diameter and polydispersity of the nanoparticles synthesized in C_6 ionic liquid. The average dimension increased four times (~ 5 nm, entry 19 to ~20 nm, entry 20) when the gold content was increased from 0.5 to 5 mM. In Figure 4.35 – 4.37, the distribution of the gold nanoparticles diameter varied from +/- 0.6 nm to +/- 4.9 nm. However, when longer chain pyrrolidinium ionic liquids (C_{10} and C_{14}/C_{10}) were used (entry 51, 52, 67 and 68), only minor difference in size (0.2 nm) and dispersity towards the variation in gold precursor concentration was observed. The average size of the nanoparticles prepared at both gold concentrations and with the three ionic liquids - C_8, C_{10} and C_{14}/C_{10} ranged between 5.1 to 5.7 nm while the dispersity was kept to about 1 nm. This indicates that a lower temperature led to a high uniformity of particle size with narrow size distribution when longer chain ionic liquids and lower gold content were used.

The UV-visible spectra (Figure 4.38a,c – 4.39a,c) for the nanoparticles synthesized at 0.5 mM of $[AuBr_4]^-$ in all four ionic liquids gave a sharp SPR peak at 525 nm – 537 nm. The absorption at longer wavelength region (> 700 nm) in all cases was negligible. These spectral characteristics reflected that the nanospheres remained stable and aggregation was insignificant at lower temperature. The spectra for the entries with 5 mM (4.38b,d and 4.39b,d) gold-bromide precursor showed maximum plasmon absorption over a wider spectral range (524 – 551 nm). Absorption at longer wavelength

was apparent for shorter chain ionic liquids, but a strong and plateau-like longer wavelength absorption profile was found for colloids in C_{10} ionic liquid. Such observation suggested that particle coagulation might happen extensively in this ionic liquid.

a)

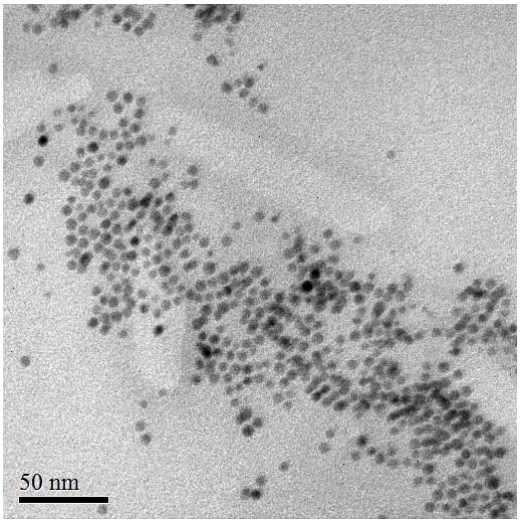

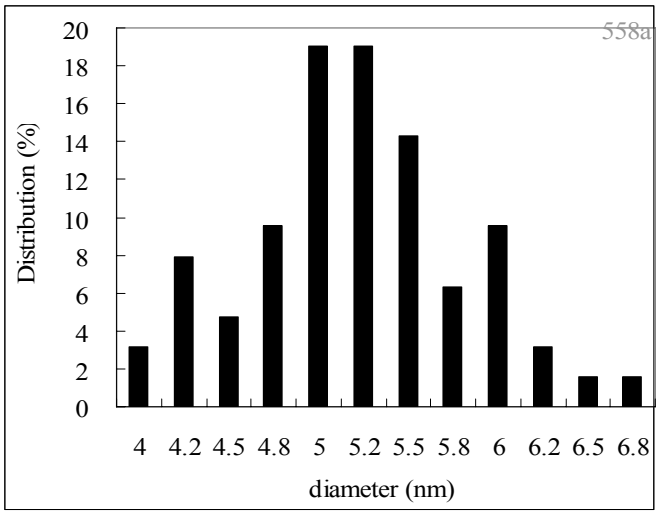

b)

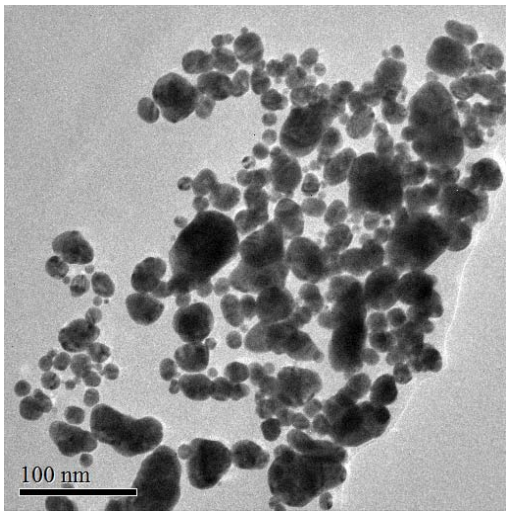

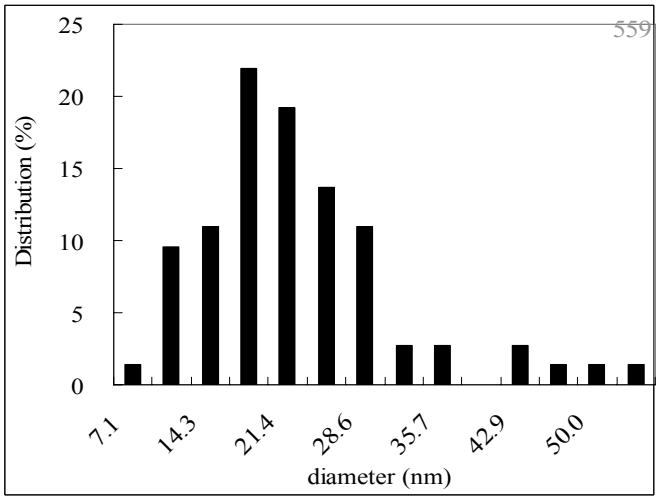

Figure 4.34 TEM images and size distributions of gold nanoparticles in ionic liquid synthesized at ~2℃ with 1 mL $PyC_6[Tf_2N]$ containing: a) 0.5 mM $PyC_6[AuBr_4]$ (entry 19) and b) 5 mM $PyC_6[AuBr_4]$ (entry 20).

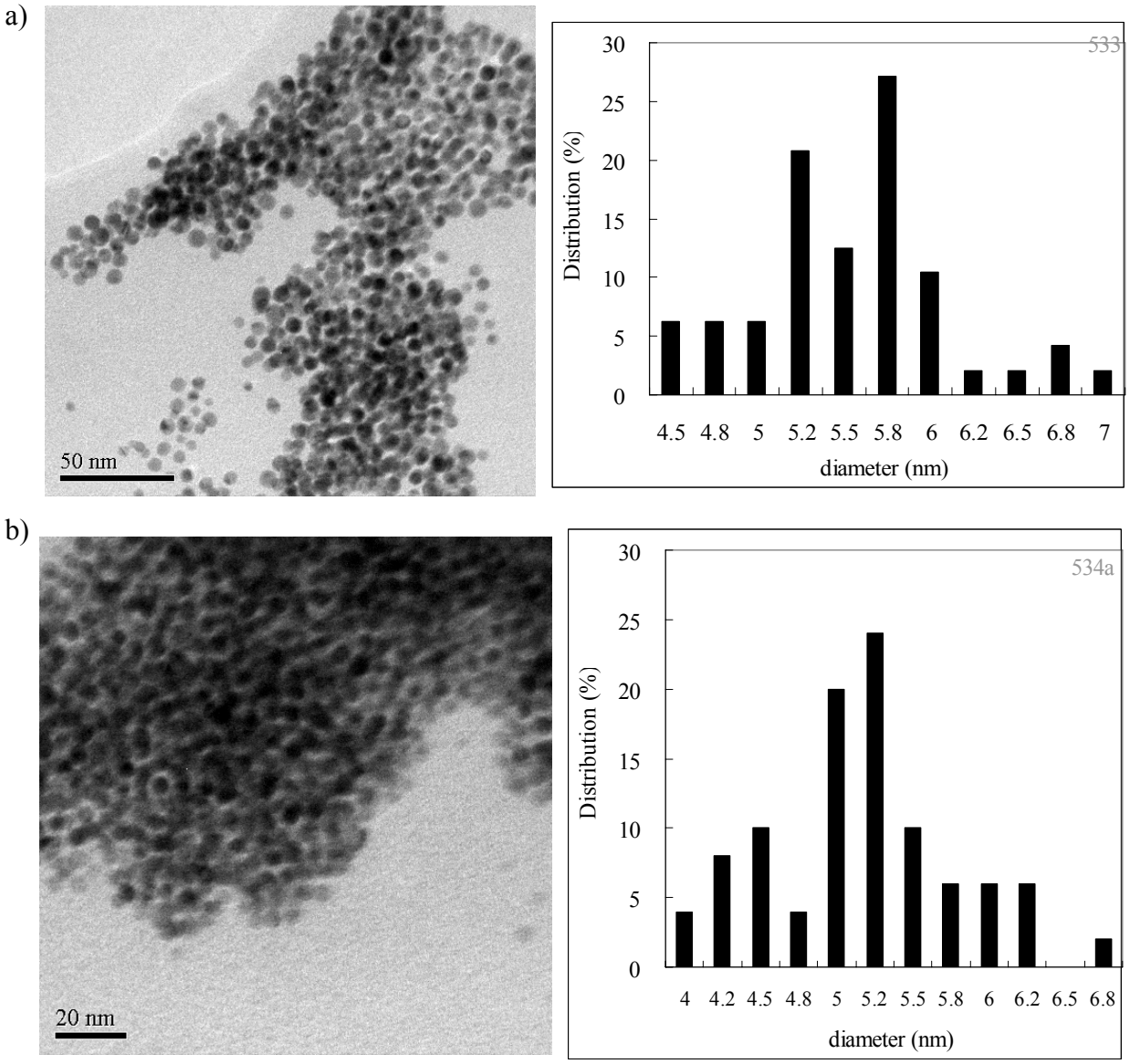

Figure 4.35 TEM images and size distributions of gold nanoparticles in ionic liquid synthesized at 2℃ with 1 mL $PyC_8[Tf_2N]$ containing: a) 0.5 mM $PyC_8[AuBr_4]$ (entry 35) and b) 5 mM $PyC_8[AuBr_4]$ (entry 36).

a)

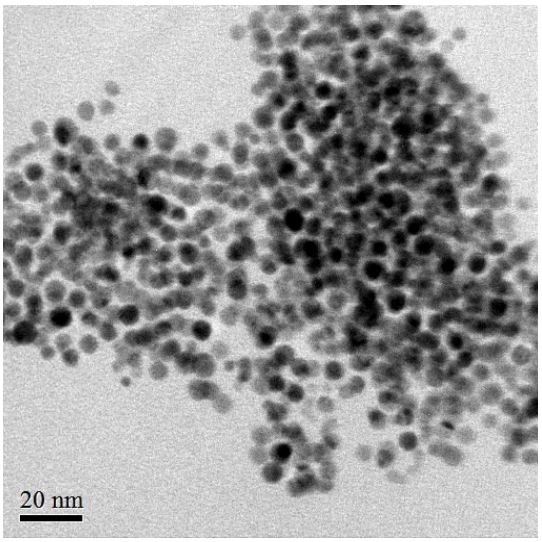

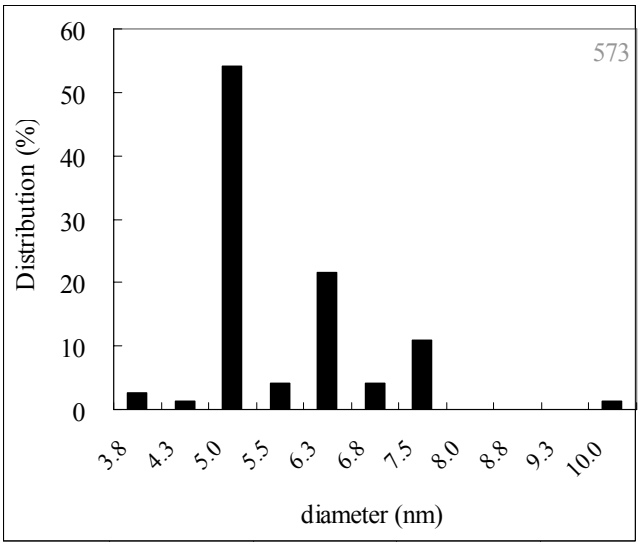

b)

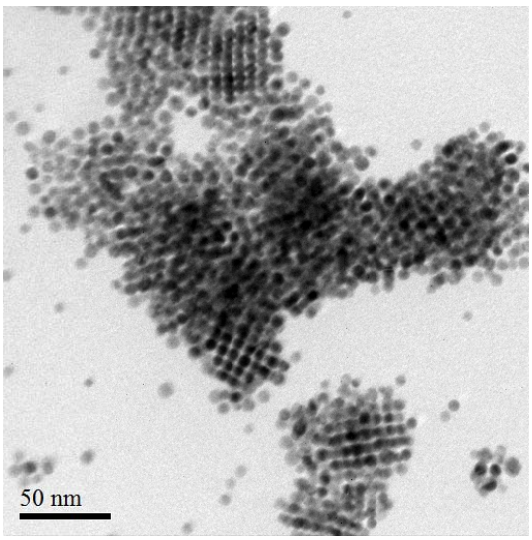

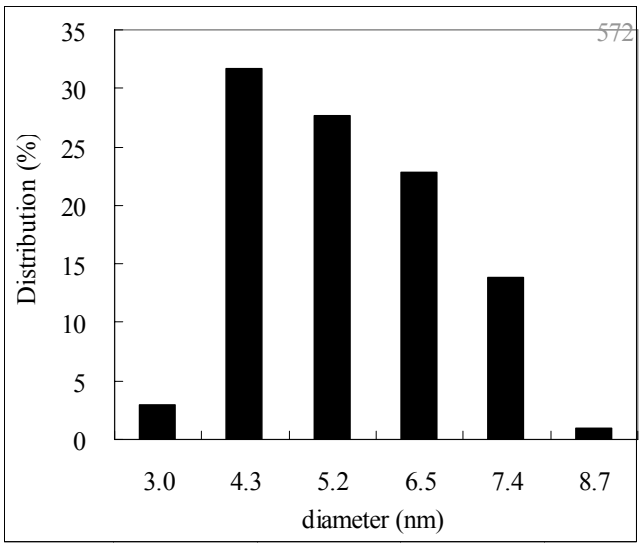

Figure 4.36 TEM images and size distributions of gold nanoparticles in ionic liquid synthesized at 2℃ with 1 mL $PyC_{10}[Tf_2N]$ containing a) 0.5 mM $PyC_{10}[AuBr_4]$ (entry 51) and b) 5 mM $PyC_{10}[AuBr_4]$ (entry 52).

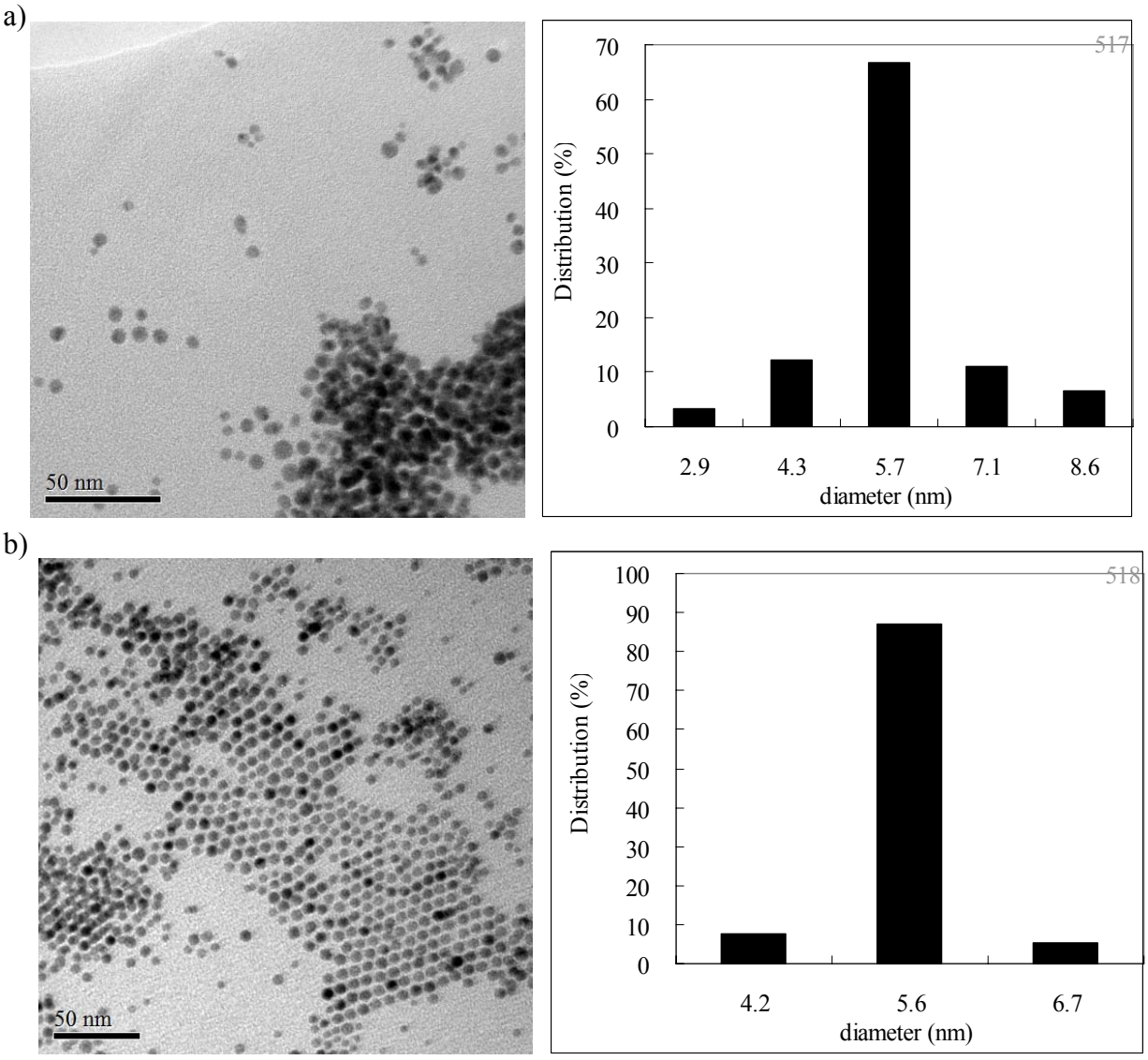

Figure 4.37 TEM images and size distributions of gold nanoparticles in ionic liquid synthesized at ~ 2℃ with 1 mL $PyC_{10}[Tf_2N]$ containing a) 0.5 mM $PyC_{14}[AuBr_4]$ (entry 67) and b) 5 mM $PyC_{14}[AuBr_4]$ (entry 68).

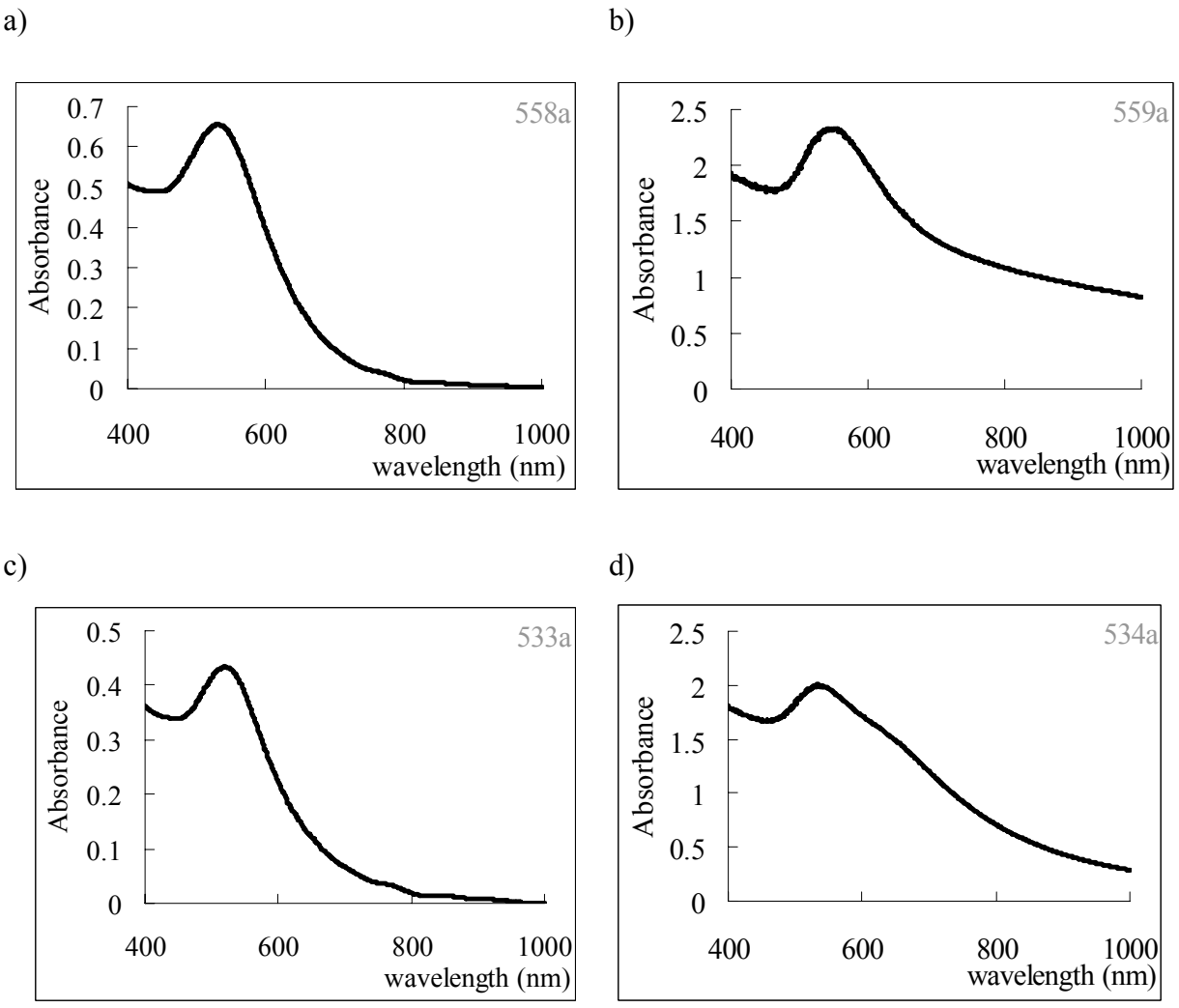

Figure 4.38 UV-visible spectra for gold nanoparticles in ionic liquid synthesized at 2℃ with 1 ml $PyC_{6}[Tf_2N]$ containing: a) 0.5 mM $PyC_{6}[AuBr_4]$ (entry 19), b) 5 mM $PyC_{6}[AuBr_4]$ (entry 20) and with 1 mL $PyC_{8}[Tf_2N]$ containing c) 0.5 mM $PyC_{8}[AuBr_4]$ (entry 35), d) 5 mM $PyC_{8}[AuBr_4]$ (entry 36)

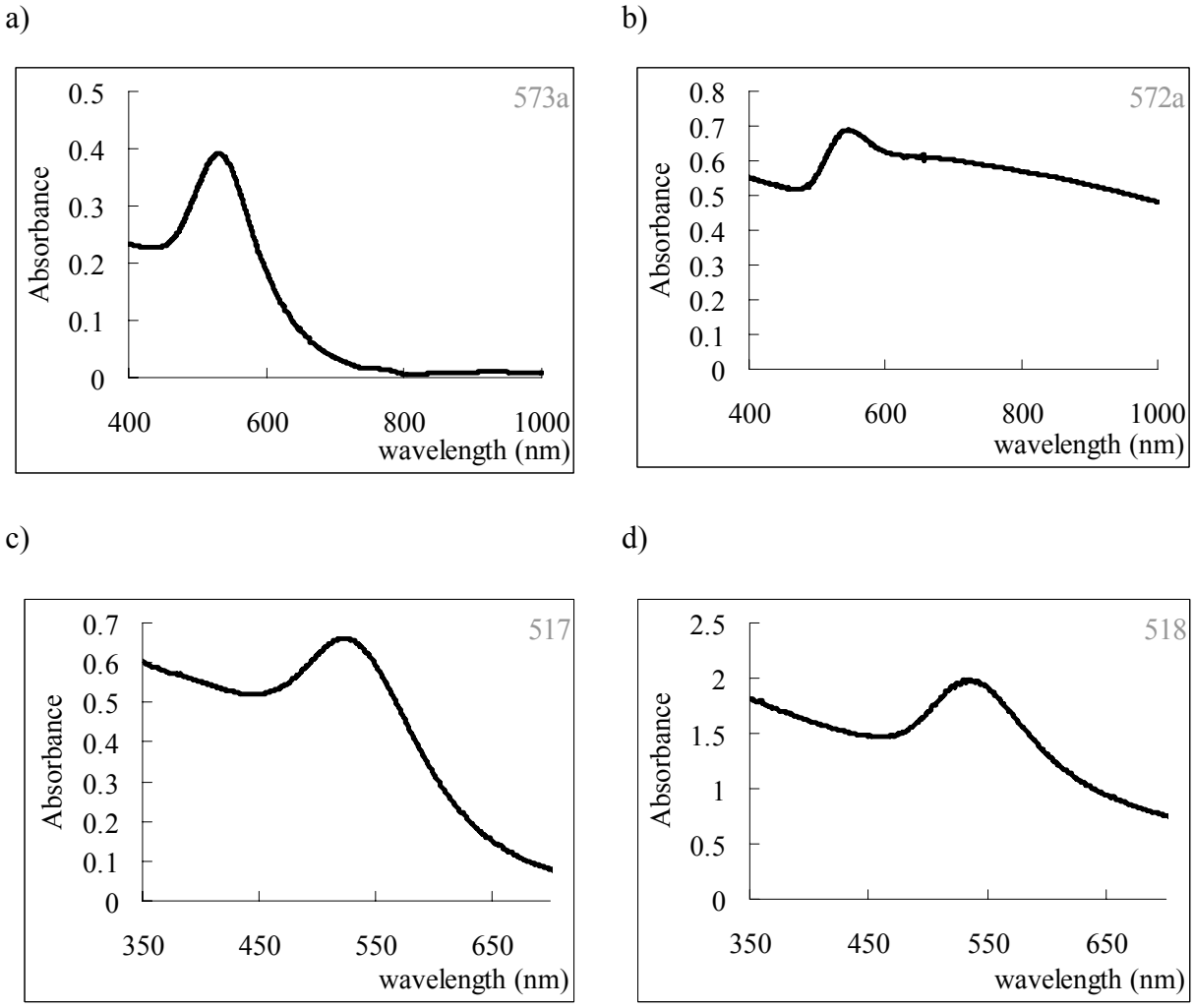

Figure 4.39 UV-visible spectra for gold nanoparticles in ionic liquid synthesized at 2℃ with 1 ml $PyC_{10}[Tf_2N]$ containing: a) 0.5 mM $PyC_{10}[AuBr_4]$ (entry 51), b) 5 mM $PyC_{10}[AuBr_4]$ (entry 52) and with 1 mL $PyC_{10}[Tf_2N]$ containing c) 0.5 mM $PyC_{14}[AuBr_4]$ (entry 67), d) 5 mM $PyC_{14}[AuBr_4]$ (entry 68).

4.3.4.7 Effect of pyrrolidinium cation alkyl chain length on gold nanoparticles prepared with higher pyrrolidinium tetrabromoaurate(III) concentration (10 and 50 mM) at low temperature (~ 2℃).

From Figure 4.40 – 4.43, the chain length effect on the variation of particle dimension at a higher gold content appeared very much similar to the lower concentration series in the previous section, except that the average size of the nanospheres was stabilized to around 24 nm for the C_6 ionic liquid. However, the size dispersity of the nanoparticles in C_6 became more non-uniform when the gold precursor content in the ionic liquid was increased. From the TEM images (Figure 4.40), it can be seen that the nanoparticles prepared in C_6 ionic liquid was a mixture of big and small nanospheres.

The average diameter of the nanoparticles formed in C_8, C_{10} and C_{14}/C_{10} ionic liquids were 4.8 to 5.8 nm, which is virtually the same as those synthesized with less gold salt in the reaction mixture under the same lower temperature conditions. From the TEM images (Figure 4.42 to 4.43), the perfectly spherical nanoparticles, especially found in longer chain ionic liquids, were aligned and partially stacked to give a regular 2D monolayer. This indicated that the particles prepared in C_{10} and C_{14}/C_{10} media were of low size dispersity. The UV-visible absorption spectrum of the dichloromethane solution of gold nanospheres produced in C_{10} and C_{14}/C_{10} ionic liquids (Figure 4.44a, b) gave a sharp SPR peak at 525 nm, but the absorbance dropped to nearly zero at longer wavelength, suggesting a particle aggregation is absent.

With the results from this and the previous section, it can be concluded that that the size and dispersity of the nanoparticles formed with ionic liquid with octyl- or longer alkyl

chain can yield nice nanospheres of about 5 nm in diameter with narrow size dispersity ($< \pm 1$ nm).

a)

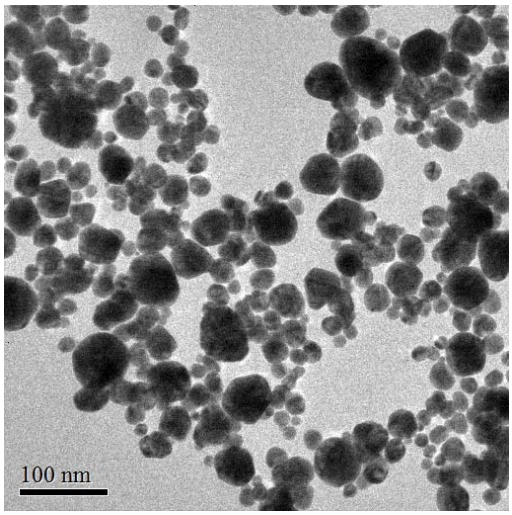

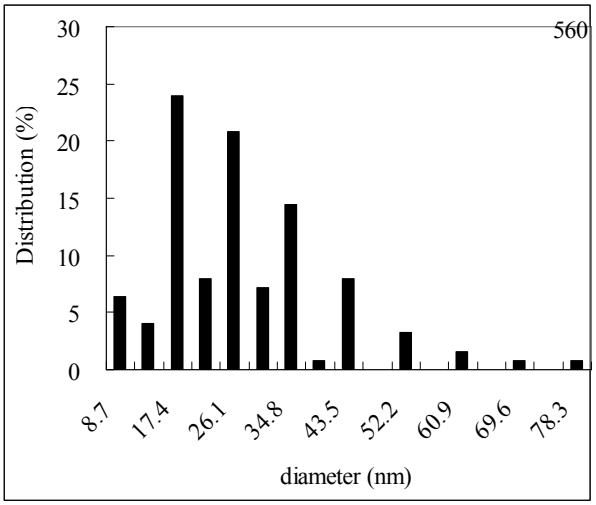

b)

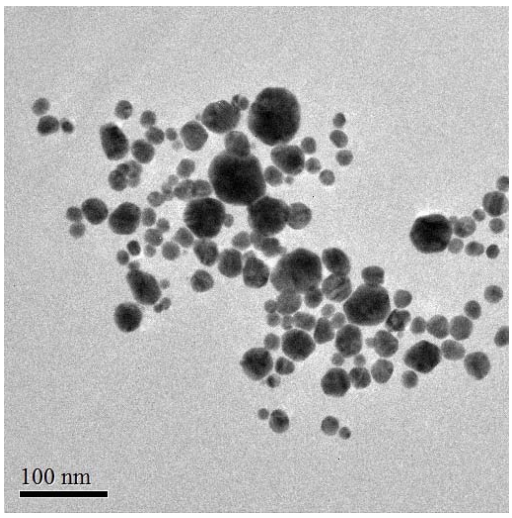

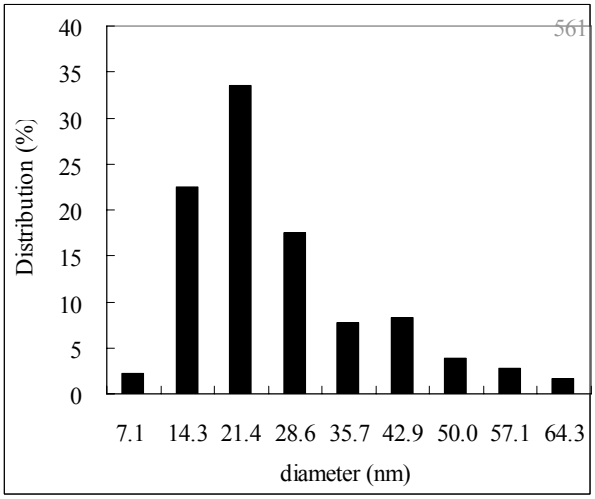

Figure 4.40 TEM images and size distributions of gold nanoparticles in ionic liquid synthesized at ~ 2℃ with 1 mL $PyC_6[Tf_2N]$ containing a) 10 mM $PyC_6[AuBr_4]$ (entry 21) and b) 50 mM $PyC_6[AuBr_4]$ (entry 22).

a)

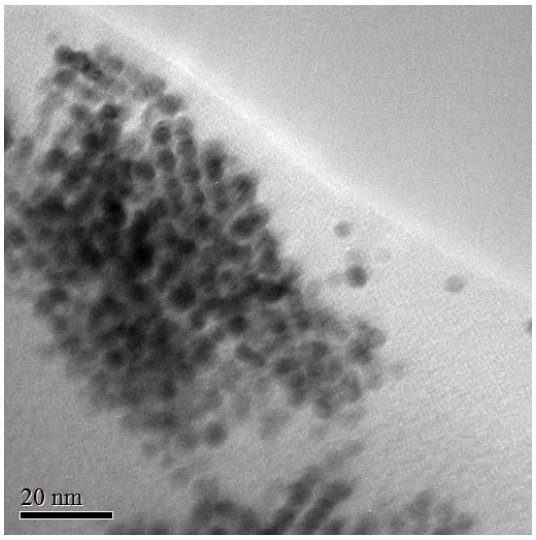

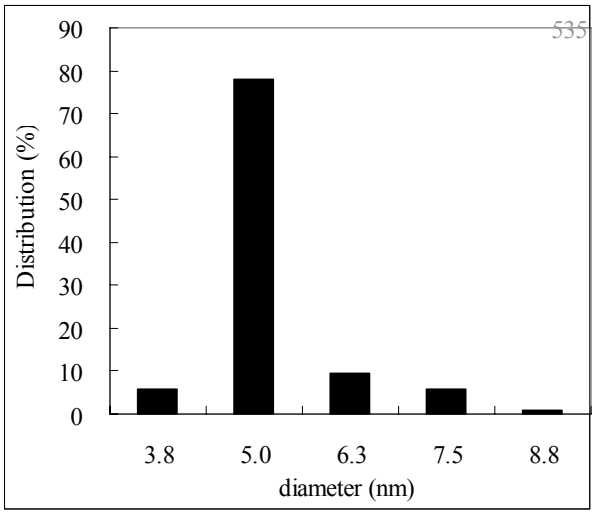

b)

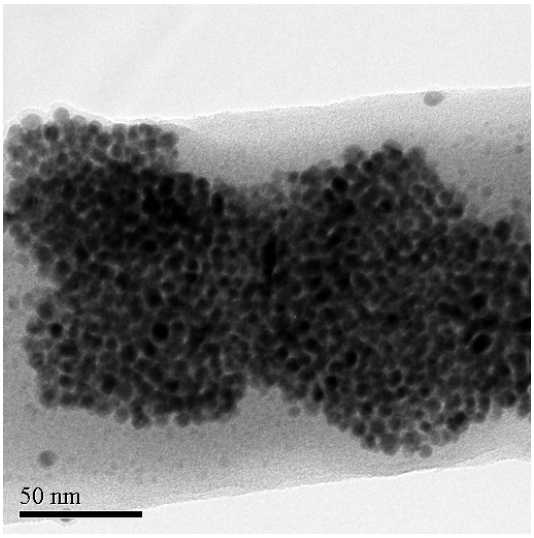

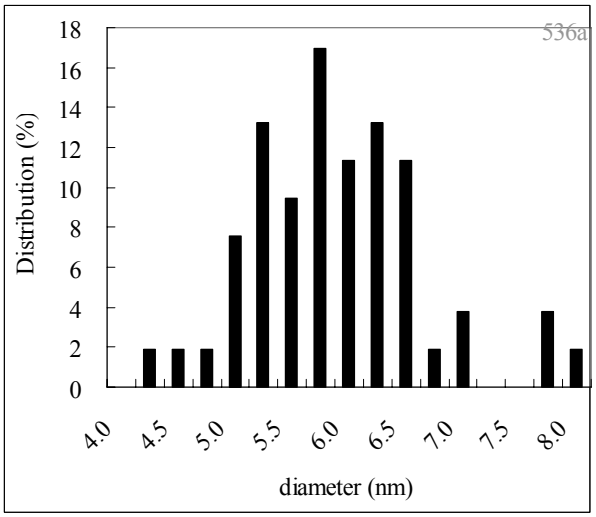

Figure 4.41 TEM images and size distributions of gold nanoparticles in ionic liquid synthesized at ~ 2℃ with 1 mL $PyC_8[Tf_2N]$: a) 10 mM $PyC_8[AuBr_4]$ (entry 37) and b) 50 mM $PyC_8[AuBr_4]$ (entry 38).

a)

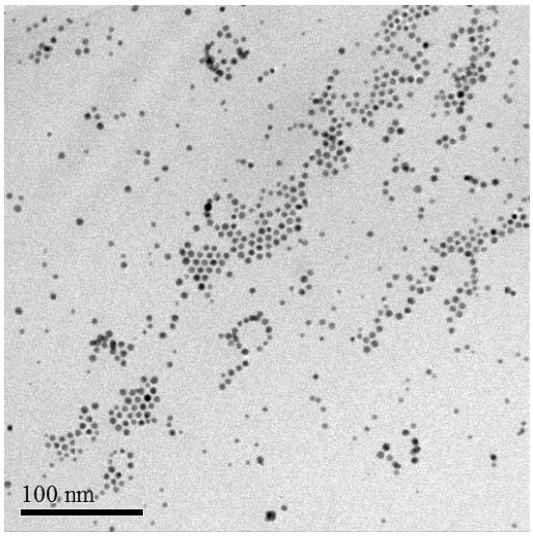

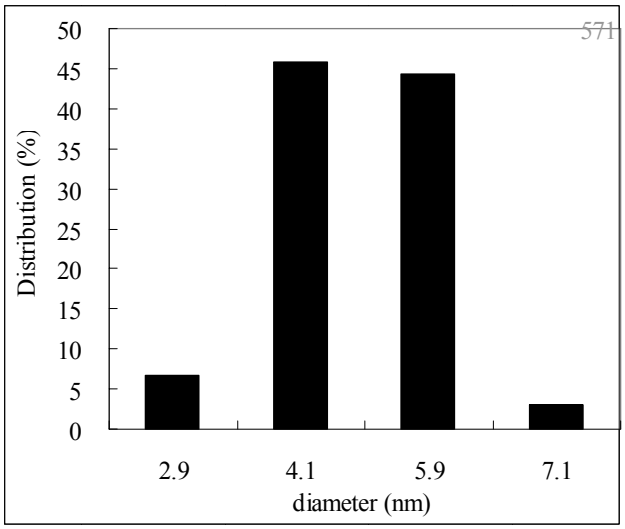

b)

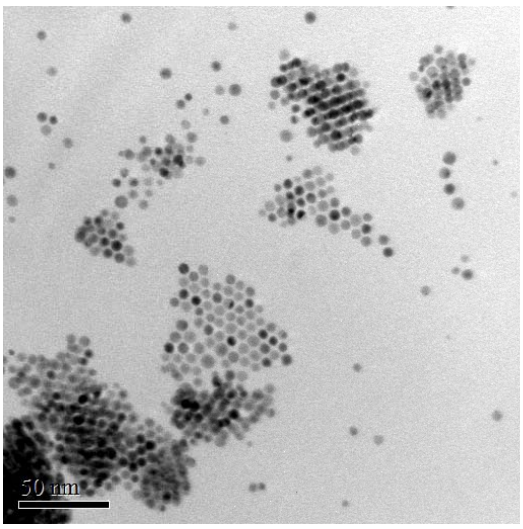

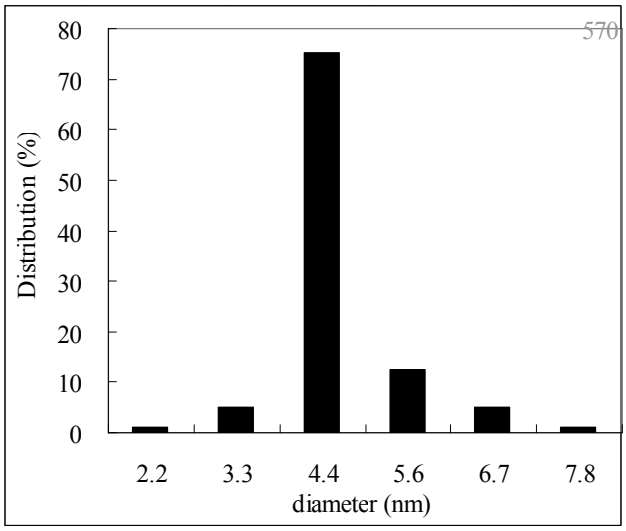

Figure 4.42 TEM images and size distributions of gold nanoparticles in ionic liquid synthesized at ~ 2℃ with 1 mL $PyC_{10}[Tf_2N]$: a) 10 mM $PyC_{10}[AuBr_4]$ (entry 53), and b) 50 mM $PyC_{10}[AuBr_4]$ (entry 54).

a)

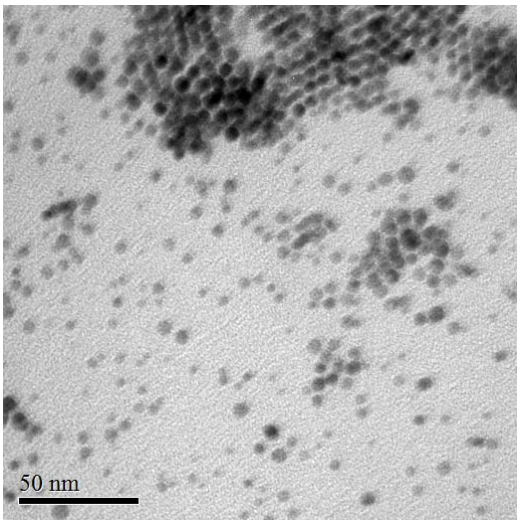

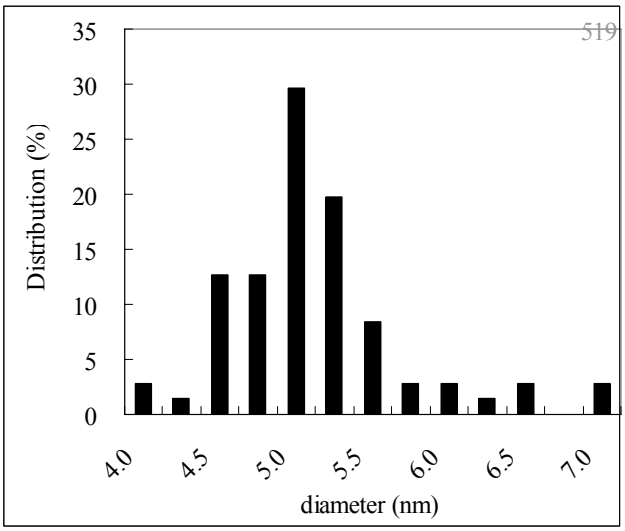

b)

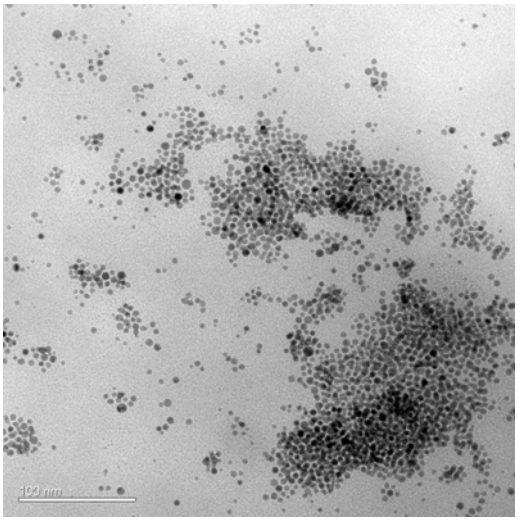

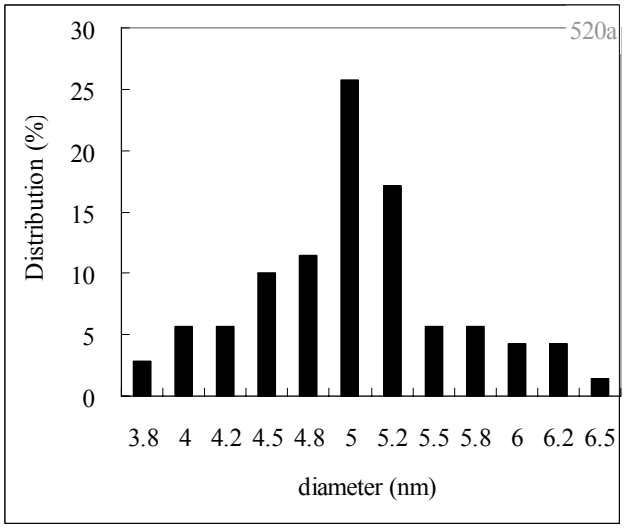

Figure 4.43 TEM images and size distributions of gold nanoparticles in ionic liquid synthesized at 2℃ with 1 mL $PyC_{10}[Tf_2N]$ containing: a) 10 mM $PyC_{14}[AuBr_4]$ (entry 69) and b) 50 mM $PyC_{14}[AuBr_4]$. (entry 70).

a)

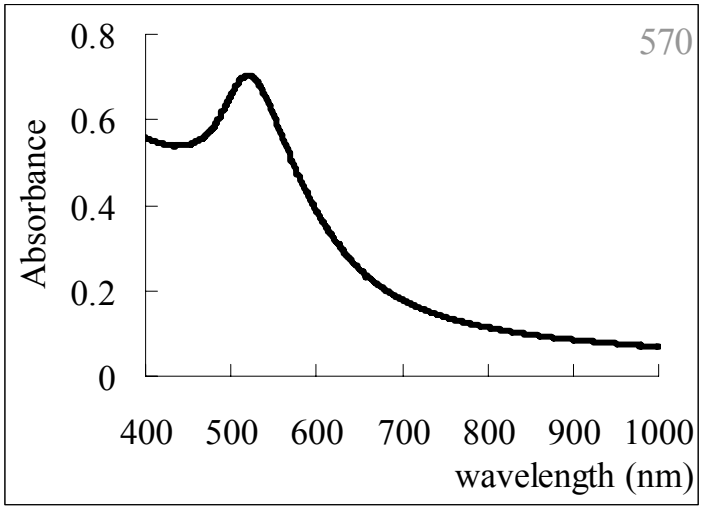

b)

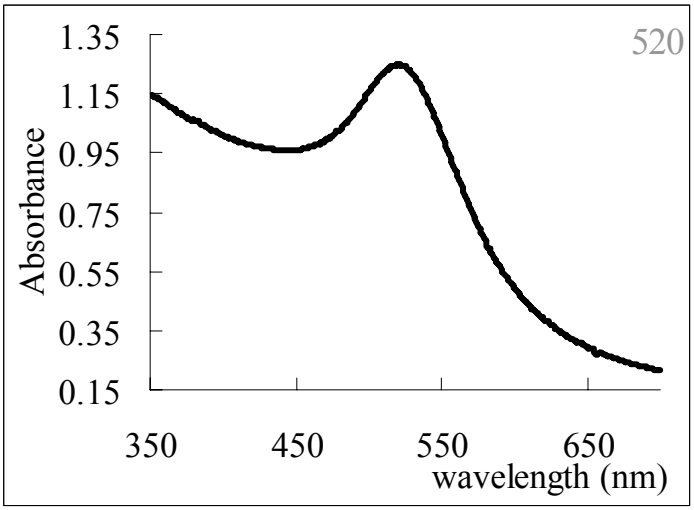

Figure 4.44 UV-visible spectra (in dichloromethane) for gold nanoparticles synthesized at ~ 2 ℃ with 1 mL $PyC_{10}[Tf_2N]$ containing a) 50 mM $PyC_{10}[AuBr_4]$ (entry 54) and b) 50 mM $PyC_{14}[AuBr_4]$ (entry 70).

4.3.4.8 Effect of pyrrolidinium cation alkyl chain length on gold nanoparticles prepared with lower pyrrolidinium tetrachloroaurate(III) concentration (0.5 and 5 mM) at low temperature (~ 2℃).

Figures 4.45 – 4.48 show the TEM images of gold nanoparticles formed at low gold content and low temperature in the presence of chloride. The average size of the gold nanoparticles prepared in these conditionswas within the range of 4 – 8.6 nm. The larger size of ~ 8 nm was found when the shortest chain ionic liquid (C_6) in this study were used at the lowest gold content (Figure 45). In addition, a big difference in average size of about 4 nm appeared upon a 10-fold increase in gold precursor concentrations. It can be seen that a great variation in particle size with different gold precursor concentrations always appear with the use of C_6 ionic liquid at lower temperature, regardless of whether chloride or bromide was present.

The chain length effect on size and dispersity became less prominent for ionic liquids with an octyl or longer chain in the presence of chloride, which is similar to the case with bromide. The nanoparticles formed with the three ionic liquids were 4 – 5 nm in diameter on average and their size dispersity was generally small (around ± 1 nm) (Figure 4.46 to 4.48). The TEM images revealed that different degree of nanosphere fusion were observed in samples prepared with C_6 to C_{10} ionic liquids, but individual nano-spheres were found to be overwhelming majority in the sample.

The SPR peak in absorption profiles for sample prepared using a low auric chloride content and temperature mainly is located at the spectral range of 515 to 540 nm, which is consistent with the small size of the gold nanoclusters observed. However, the

absorption was extended to the longer wavelength region and the SPR peaks were flattened and broadened. The observed spectral characteristic for the chloride containing experiments indicated that interaction between nanoparticles was present in ionic liquid.

Formation of short nano-threads was noted in samples prepared under 0.5 mM gold chloride condition with C_{10} and C_{14}/C_{10} ionic liquids. Such unique character may imply that a combination of chloride and longer chain ionic liquid at the said low gold salt concentration range was favorable to short nano-thread formation. The finding here was somehow consistent to the nano-thread formation in the biphasic ionic liquid-aqueous synthesis of gold nanoparticles in section 4.4.3. That means gold nano-threads can be prepared by conventional biphasic approach or the single ionic liquid phase method.

At more concentrated gold condition (5 mM), particles with spherical and slightly fused morphology were found in the C_6 and C_8 media (Figure 4.45 and 4.46). However, in C_{10} and C_{14}/C_{10} ionic liquids, the amount of nano-threads were greatly reduced (Figure 4.47 and 4.48) and the colloids had a slightly smaller average size than those from bromide at lower temperature. The nanoparticles formed in C_{14}/C_{10} were perfectly spherical and could spread as a regular 2D monolayer.

a)

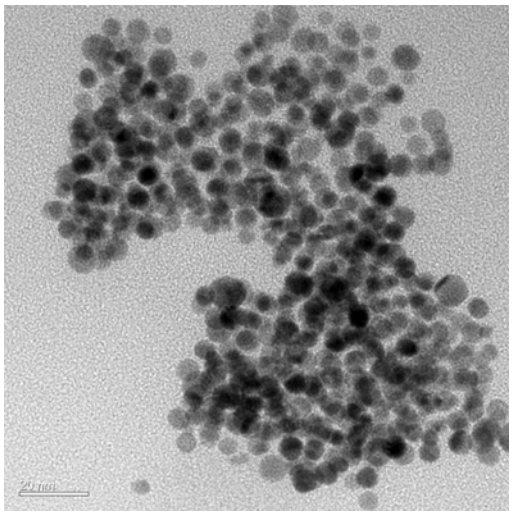

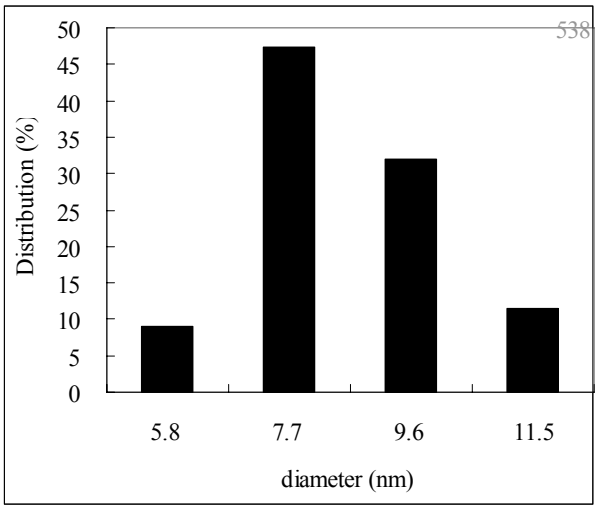

b)

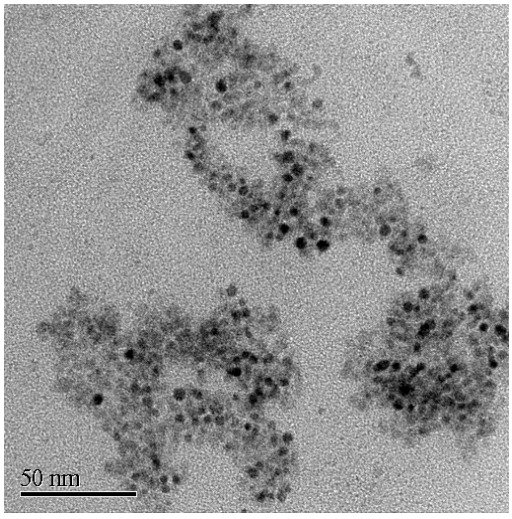

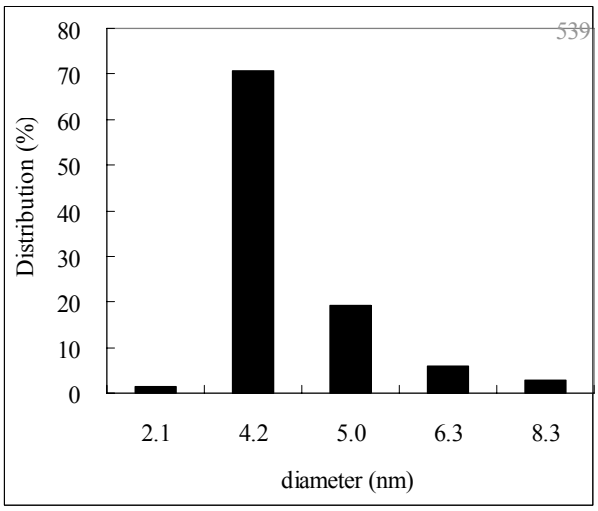

Figure 4.45 TEM images and size distributions of gold nanoparticles in ionic liquid synthesized at ~ 2℃ with 1 mL $PyC_{6}[Tf_2N]$ containing a) 0.5 mM $PyC_{6}[AuCl_4]$ (entry 27) and b) 5 mM $PyC_{6}[AuCl_4]$ (entry 28).

a)

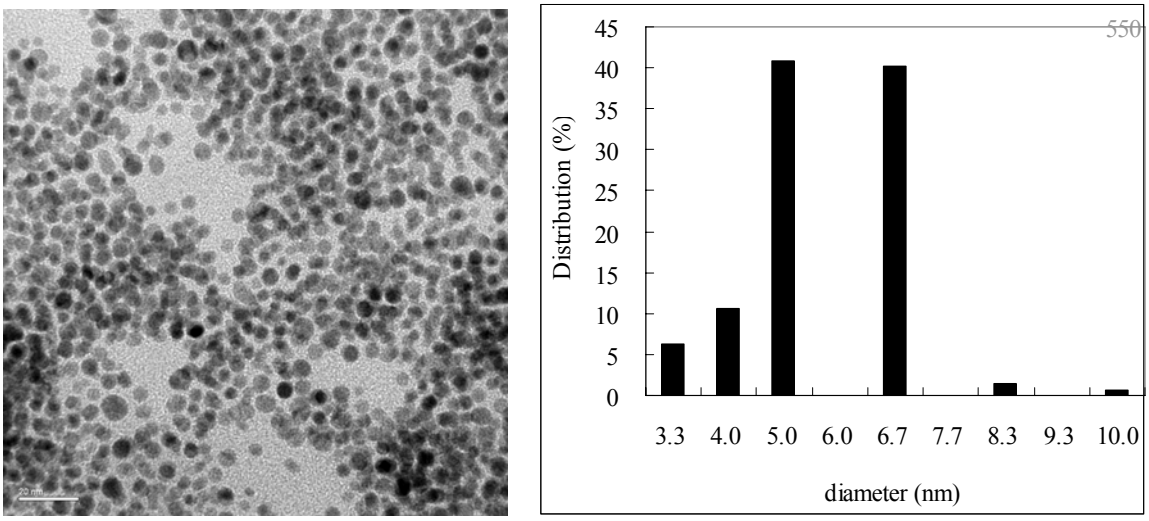

b)

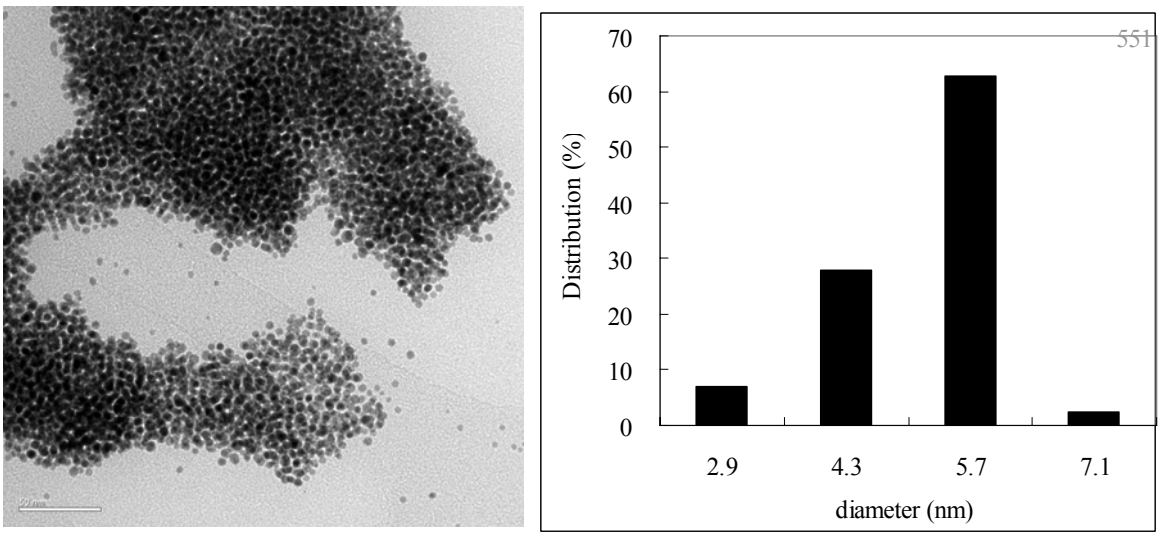

Figure 4.46 TEM images and size distributions of gold nanoparticles in ionic liquid synthesized at ~ 2℃ with 1 mL $PyC_8[Tf_2N]$ containing a) 0.5 mM $PyC_8[AuCl_4]$ (entry 43) and b) 5 mM $PyC_8[AuCl_4]$. (entry 44).

a)

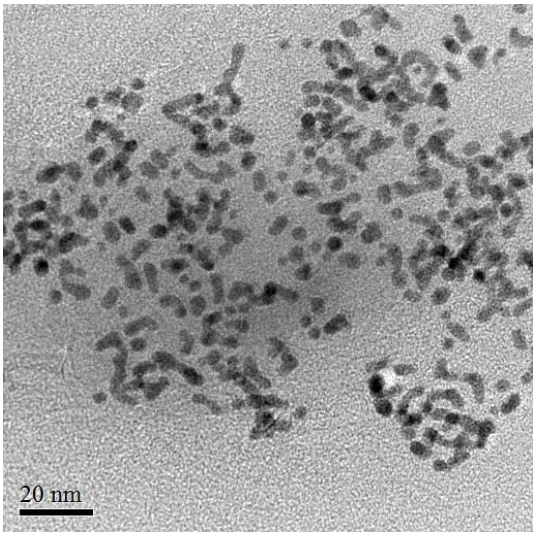

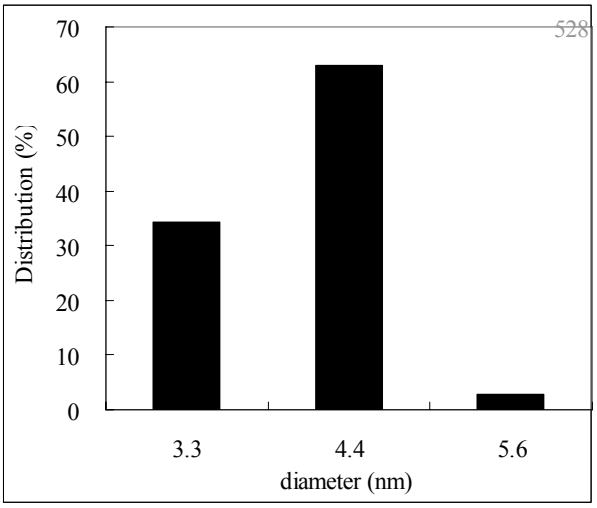

b)

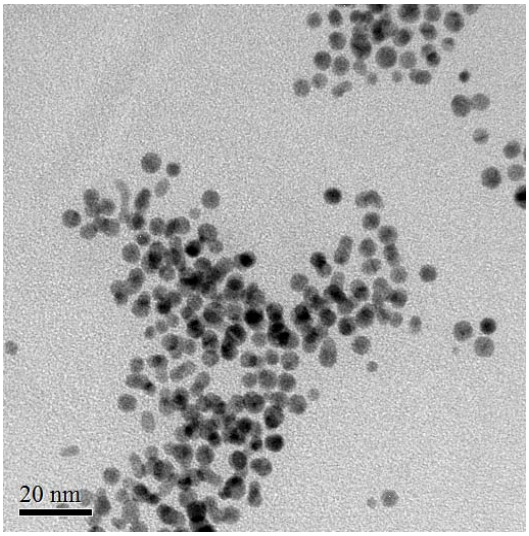

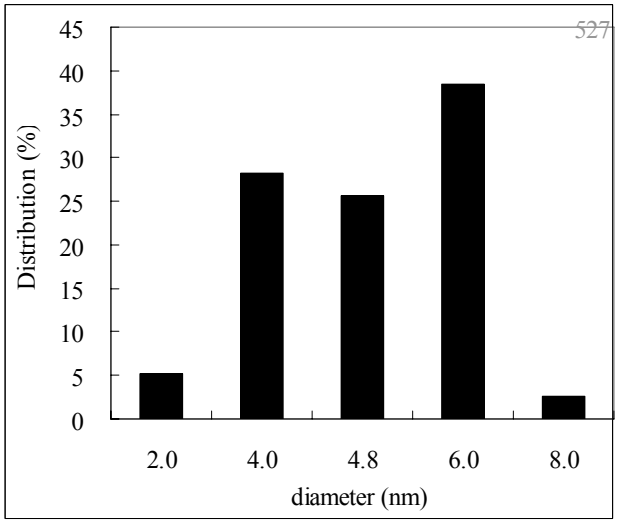

Figure 4.47 TEM images and size distributions of gold nanoparticles in ionic liquid synthesized at ~ 2℃ with 1 mL $PyC_{10}[Tf_2N]$ containing a) 0.5 mM $PyC_{10}[AuCl_4]$ (entry 59) and b) 5 mM $PyC_{10}[AuCl_4]$ (entry 60)

a)

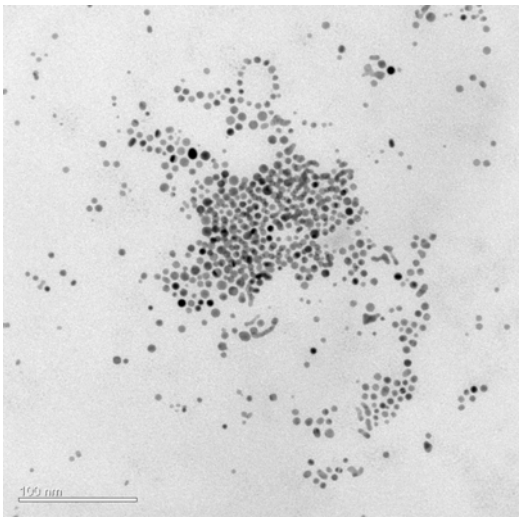

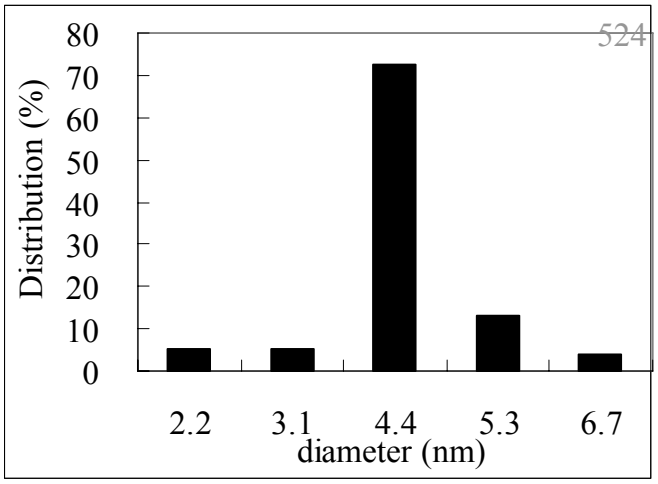

b)

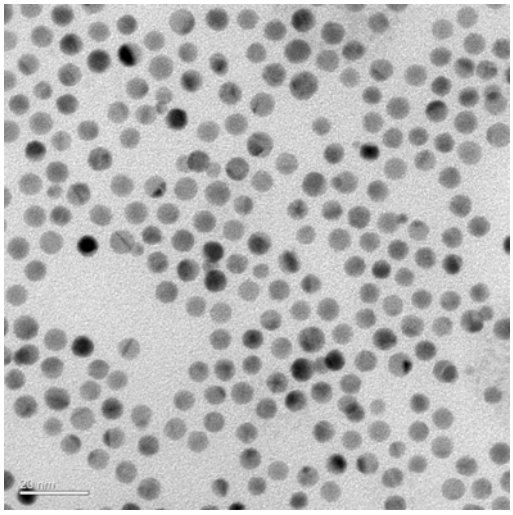

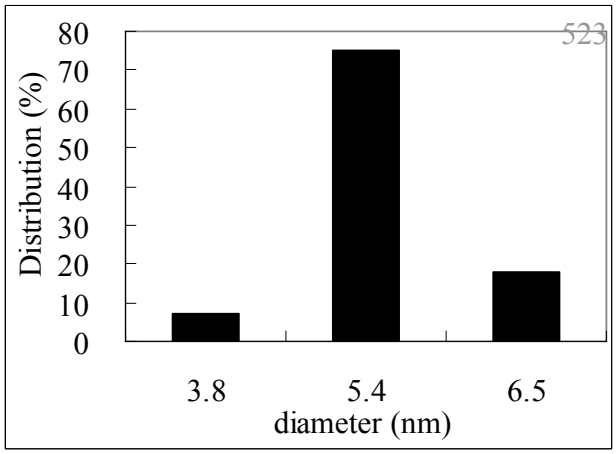

Figure 4.48. TEM images and size distributions of gold nanoparticles in ionic liquid synthesized at ~ 2℃ with 1 mL $PyC_{10}[Tf_2N]$ containing a) 0.5 mM $PyC_{14}[AuCl_4]$ (entry 75) and b) 5 mM $PyC_{14}[AuCl_4]$ (entry 76).

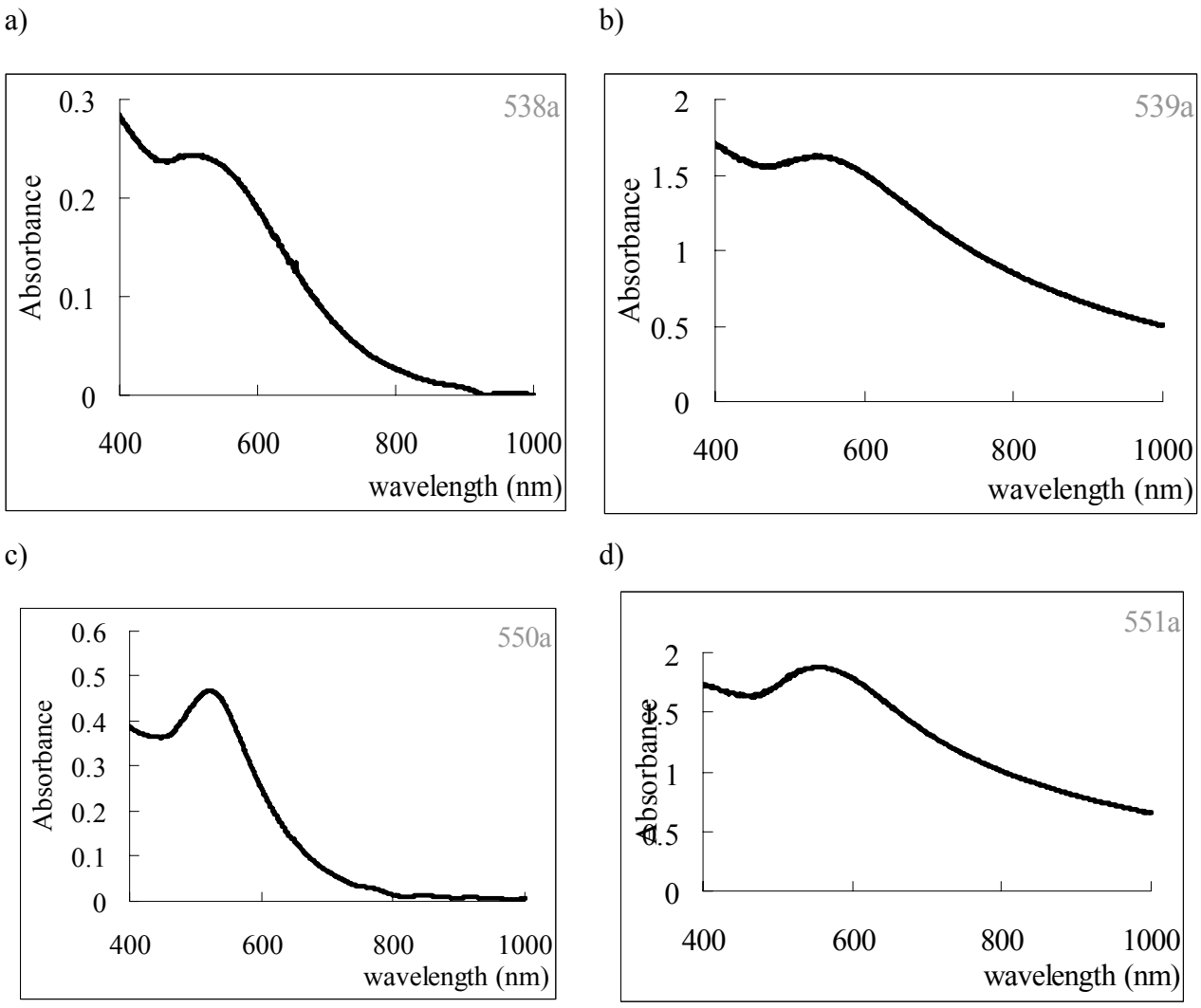

Figure 4.49 UV-visible spectra for gold nanoparticles in ionic liquid synthesized at 2℃ with 1 mL $PyC_{6}[Tf_2N]$ containing a) 0.5 mM $PyC_{6}[AuCl_4]$ (entry 27), b) 5 mM $PyC_{6}[AuCl_4]$ (entry 28) and with 1 mL $PyC_{8}[Tf_2N]$ containing c) 0.5 mM $PyC_8[AuCl_4]$ (entry 43), d) 5 mM $PyC_{8}[AuCl_4]$ (entry 44).

a)

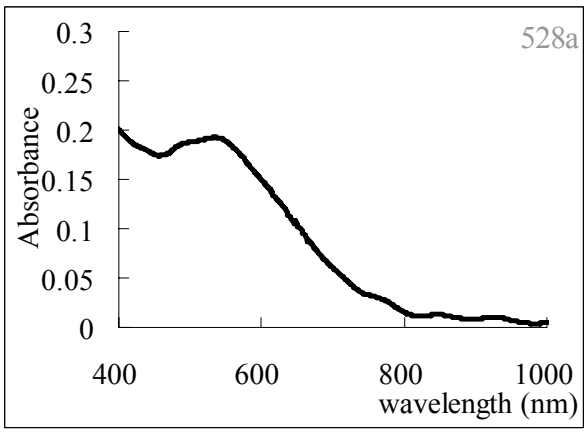

b)

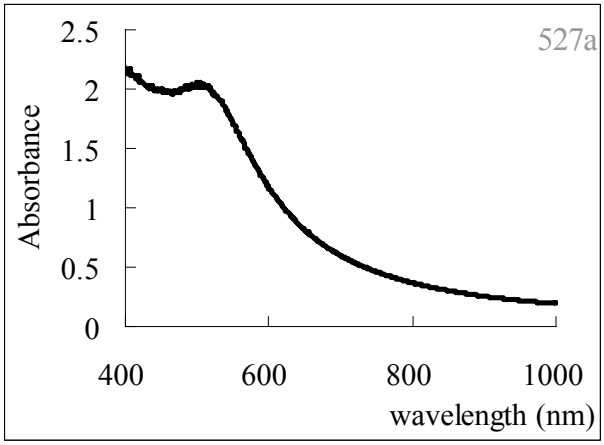

c)

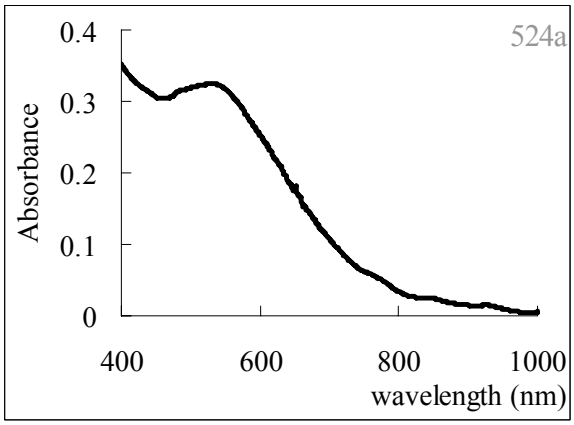

d)

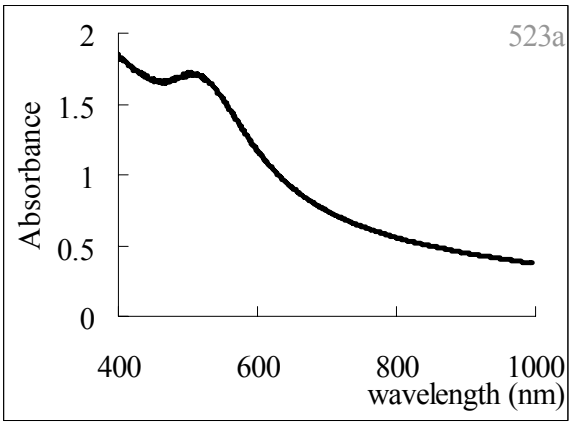

Figure 4.50 UV-visible spectra for gold nanoparticles in ionic liquid synthesized at ~ 2℃ with 1 mL $PyC_{\mathbf{10}}[Tf_2N]$ containing a) 0.5 mM $PyC_{\mathbf{6}}[AuCl_4]$ (entry 59), b) 5 mM $PyC_{\mathbf{6}}[AuCl_4]$ (entry 60) and with 1 mL $PyC_{\mathbf{10}}[Tf_2N]$ containing c) 0.5 mM $PyC_8[AuCl_4]$ (entry 75), d) 5 mM $PyC_{\mathbf{14}}[AuCl_4]$ (entry 76)

4.3.4.9 Effect of pyrrolidinium cation alkyl chain length on gold nanoparticles prepared with higher pyrrolidinium tetrachloroaurate(III) concentration (10 and 50 mM) at low temperature (~ 2℃).

When higher gold precursor concentrations were used in the preparation, an increase in the particle dimension was observed for nanoparticles prepared in short chain pyrrolidinium ionic liquids. The average particle size ranged from 5.4 - 8.6 nm with wider dispersity (±0.9 to ±3 nm). Again, longer chain ionic liquids gave a narrower size distribution (± 0.7 - ± 0.9) and smaller average size (4 – 5.6 nm). The TEM images (Figure 4.51 to 4.54) show that the nanoparticles formed in C_6 and C_8 ionic liquids were more polydispersed and less spherical. Fusion of particles could easily be recognized in C_6 to C_{10} ionic liquid. Sintering of particles was far less common for the nanospheres fabricated C_{14}/C_{10} ionic liquids, in contrast to the lower gold content experiments discussed previously. Variation of average size was more obvious in C_{10} ionic liquid (4 to 5.4 nm) when the gold concentration was raised from 10 to 50 mM, whereas that for C_{14}/C_{10} was just infinitesimal (5.6 to 5.5 nm).

The UV-visible profiles for the dichloromethane solution of the gold nano-clusters from C_{10} and C_{14}/C_{10} ionic liquids showed a maximum absorption at 525 nm. However, both spectra showed extended absorption starting from the apex of the SPR peak to the longer wavelength region. Such profiles strongly suggest that particle coagulation had emerged when the as-prepared ionic liquid gold nanoparticles were dispersed in dichloromethane.

To compare the nature of the nanoparticles formed at low temperature in ionic liquid

medium with bromide or chloride, the use of short chain pyrrolidinium ionic liquid , like the hexyl derivative, was generally less satisfactory if small, uniform and narrowly dispersed particles were required. A lower temperature could still lead to large nanoparticles formation in short chain ionic liquid in the presence of bromide and high concentration of gold salt.

When longer chain ionic liquids were used, the size and dispersity of the nanoparticles formed were generally insensitive towards halide and gold content. The size of nanoparticles produced were about 5 nm with narrow dispersity (< 1 nm).

a)

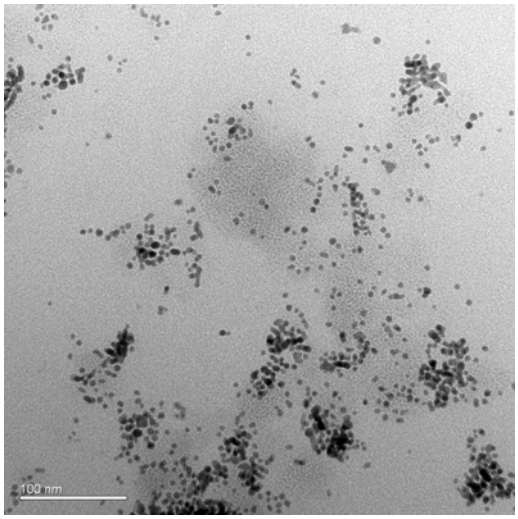

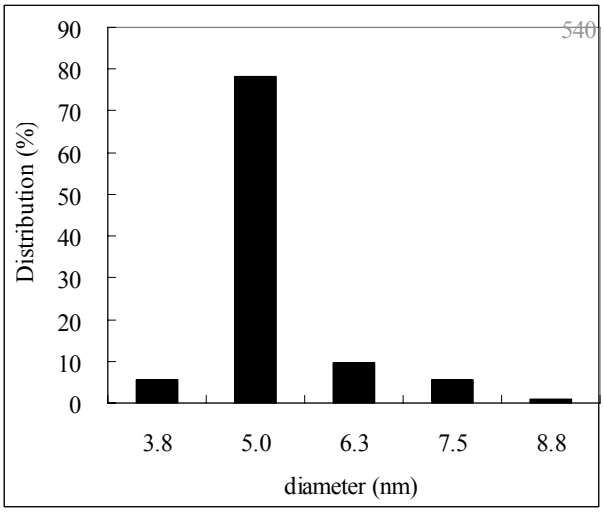

b)

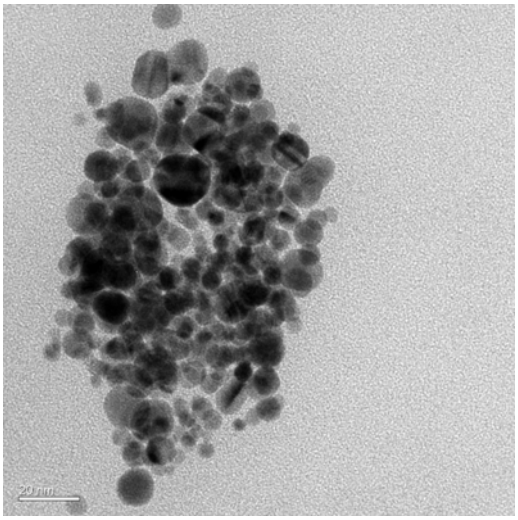

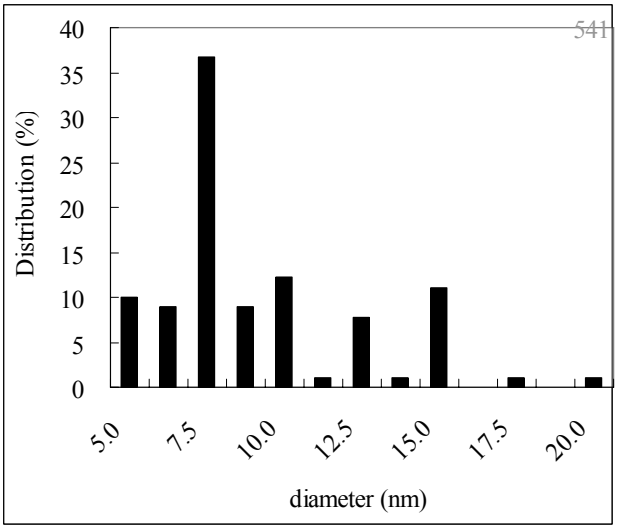

Figure 4.51 TEM images and size distributions of gold nanoparticles in ionic liquid synthesized at ~ 2℃ with 1 mL $PyC_6[Tf_2N]$: a) 10 mM $PyC_6[AuCl_4]$ (entry 29) and b) 50 mM $PyC_6[AuCl_4]$ (entry 30).

a)

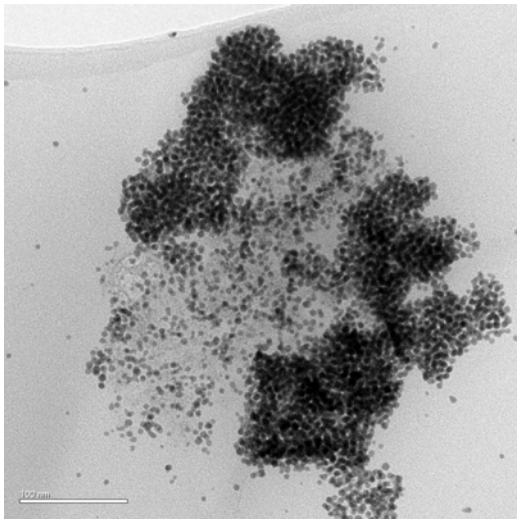

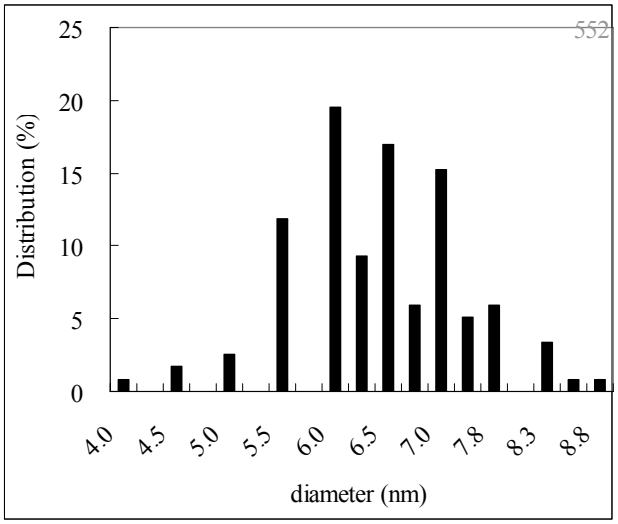

b)

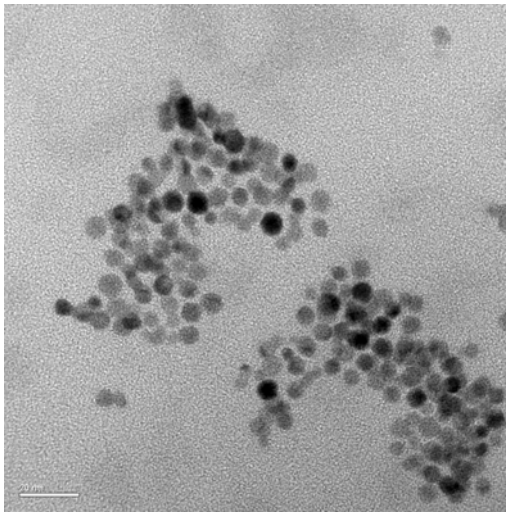

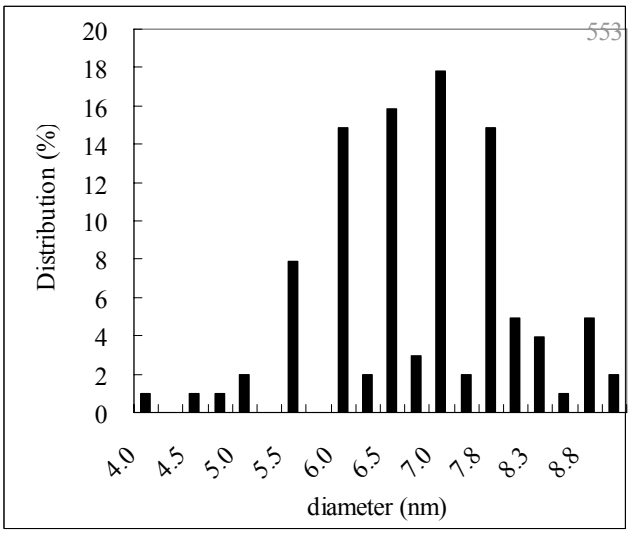

Figure 4.52 TEM images and size distributions of gold nanoparticles in ionic liquid synthesized at ~ 2℃ with 1 mL $PyC_{8}[Tf_2N]$: a) 10 mM $PyC_{8}[AuCl_4]$ (entry 45) and b) 50 mM $PyC_{8}[AuCl_4]$ (entry 46).

a)

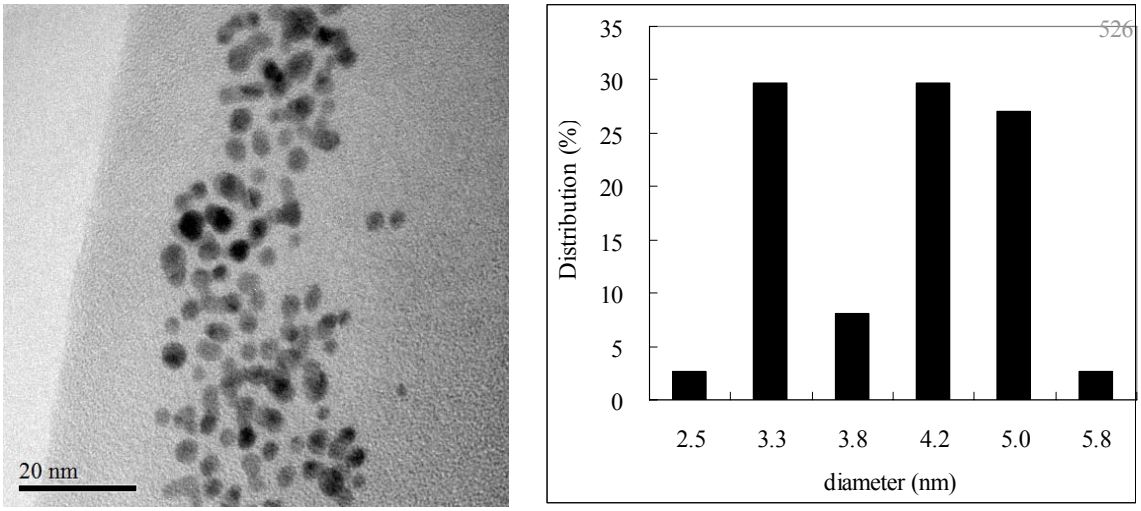

b)

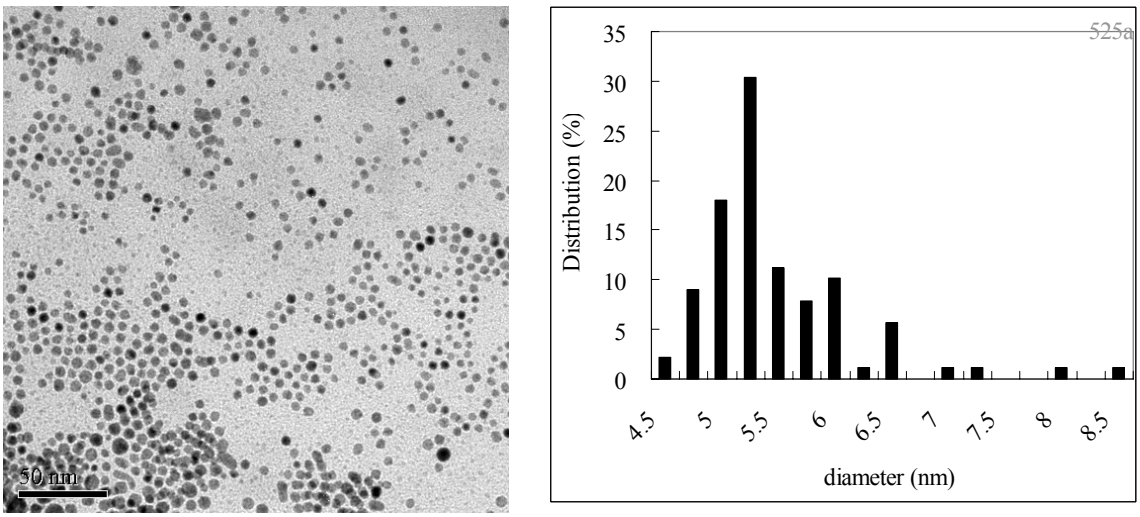

Figure 4.53 TEM images and size distributions of gold nanoparticles in ionic liquid synthesized at ~ 2℃ with 1 mL $PyC_{10}[Tf_2N]$: a) 10 mM $PyC_{10}[AuCl_4]$ (entry 61) and b) 50 mM $PyC_{10}[AuCl_4]$ (entry 62).

a)

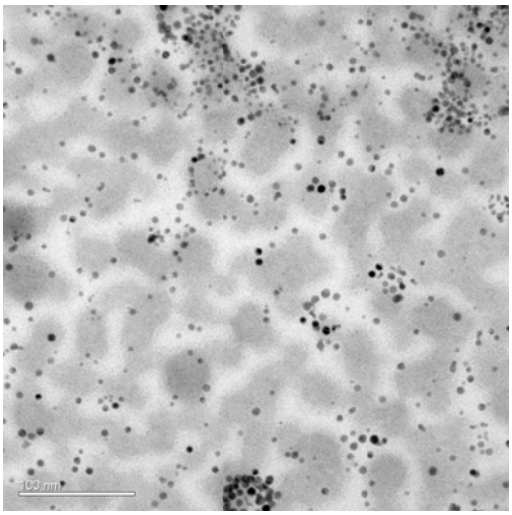

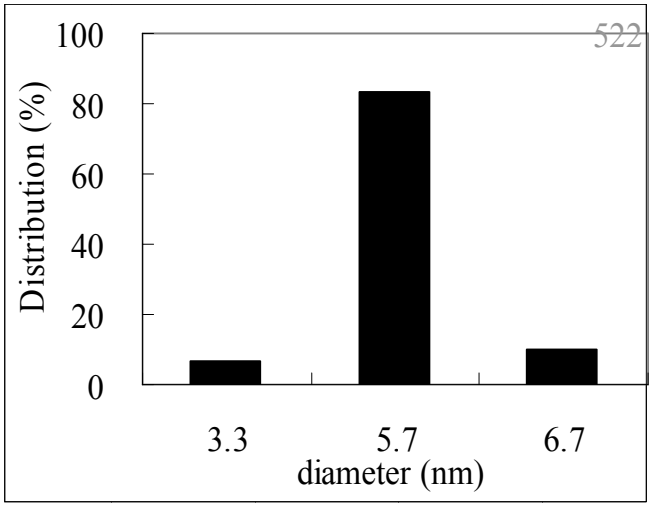

b)

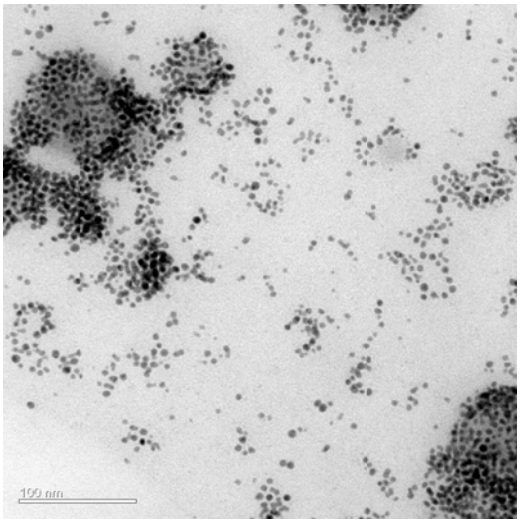

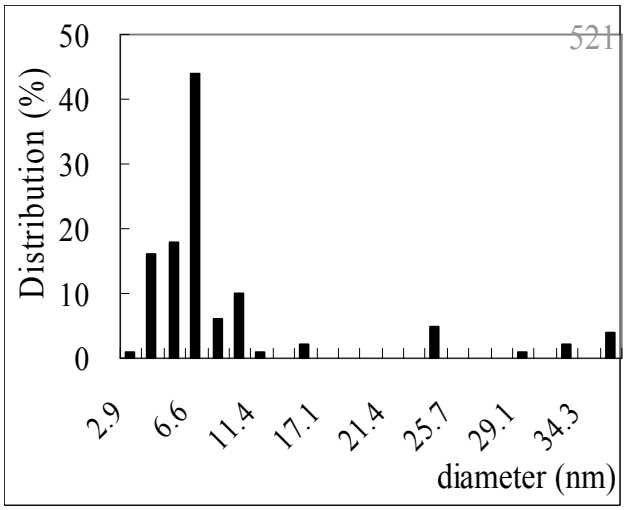

Figure 4.54 TEM images and size distributions of gold nanoparticles in ionic liquid synthesized at ~ 2℃ with 1 mL $PyC_{10}[Tf_2N]$: a) 10 mM $PyC_{14}[AuCl_4]$ (entry 77) and b) 50 mM $PyC_{14}[AuCl_4]$ (entry 78).

4.3.5 Summary of findings in single ionic liquid phase preparation of gold nanoparticles and the possible mechanism for their formation

Table 4.6 and 4.7 summarized the average sizes, dispersities, and the morphologies of the gold nanoparticles formed with single ionic liquid phase preparation under different experimental conditions. It can be seen that nanoparticles formed in longer chain ionic liquids are generally spherical and 4 – 5 nm in diameter with limited size dispersity. Meanwhile, when synthesized with the longer chain ionic liquids, the particle size of the nanospheres formed is insensitive to the gold precursor concentration and the reaction temperature employed. This is contrast to what was observed with shorter chain ionic liquids preparation in which the size and morphology were affected by the gold concentration of the reaction mixture.

The effect of halide to the morphology of the nanoparticles formed in single phase preparation is intriguing. In the presence of bromide, only spherical particles can be obtained. Aligments of monodisperse nanoparticles into regular pattern were observed in the TEM images for nanoparticles synthesized in longer chain ionic liquids containing bromide. For chloride, formation of thread-like structure can be observed, especially when synthesized with longer chain ionic liquids.

The effect of temerpature was not significant on the particle size and morphology, but it shows some influences on the stability of the nanoparticles in organic solvent.

As observed from the reaction, colour change appeared instantly once the borohydride in ionic liquid was added to the gold precursor containing medium. Such a direct

formation of nano-clusters in the absence of water may involve the formation of unstable noble metal hydride by the stepwise reaction between the metal salt (ML_n) and the borohydride ion (BH_4^-),[211] which is proposed to be the mechanism in the chemical vapor generation technique[212,213] to produce volatile metal compounds for analysis. The process involved in the reaction can be briefly described with the schematic diagram below, where M represents the metal of interest and L is the ligand in coordination with the metal. n stands for the stoichiometry of the ligand bonding to the metal centre.[214]:

$$ML_n + [L_3BH]^m \rightarrow \text{intermediates} \rightarrow \underset{\text{(metal atom)}}{M^0} \rightarrow \underset{\text{(nanoparticles)}}{M_n} \quad \textbf{(1)}$$

L can be H^- or other ligands and m represents the charge carried by the borohydride complex.

The first step may involve the formation of the following intermediate complex **(A)** between the borohydride and the metal compound:

$$[L_3BH]^m + ML_n \rightarrow \text{(A)} \rightarrow L_{n-1}M\text{-}H + [L_3BL]^m \quad \textbf{(2)}$$

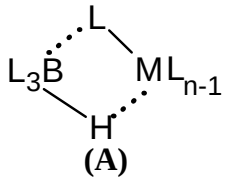

Then the intermediate **(A)** above may further react with other borohydride species for several times to give the multi-hydride metal intermediates, like **(B)** and **(C)** below, and the resultant metal poly-hydride as follows:

$$L_{n-1}M\text{-}H + [L_3BH]^m \rightarrow \underset{\textbf{(B)}}{L_{n-2}MH_2} + L_3B\text{-}L \quad \textbf{(3)}$$

$$LMH_{n-1} + [L_3BH]^m \rightarrow MH_n + L_3B\text{-}L \quad \textbf{(4)}$$

(C) (metal poly-hydride)

Some elements can form the final metal poly-hydride complex becasue their multi-hydride metal intermediates are quite stable. Gold hydrides are proposed to exist as various forms like $(H_2)_nAuH_x$ (n = 0, 1 and x = 1 – 3), L_nAuH_x (L = Cl^- etc)[214] and AuH[215] in several studies. These species were suggested to be less stable [214] than their ethyl-gold-hydride complex counterpart prepared by Xu *et al*.[216] The low stability was believed to facilitate its decomposition to gold atoms and the subsequent formation of the final gold nanoparticles by aggregation of the nascent metal atoms. Recently, Zhang *et al*.[217] confirmed the possible existence of gold-hydride species after the reaction between gold(III) compound and BH_4^- in medium containing room temperature ionic liquid. Therefore, it can be inferred that similar gold-hydride species may also be present in the pyrrolidinium ionic liquid in this study.

The evolution of gas bubbles was observed from the ionic liquid during colloids

preparation. Same phenomenon was also reported in the synthesis of cobalt,[218] copper and nickel nanoparticles[219] with sodium borohydride in dry diglyme. Dihydrogen was formed during the transformation from cobalt-borohydride complex to nascent cobalt(0) atoms. Based on the similar experimental observation and the metallic species production, the effervescence observed may indicate that gold colloids were formed through similar reaction route and intermediates in ionic liquids.

Table 4.6. A summary of the size distributions and the morphologies of the gold nanoparticles produced under different experimental conditions at 2 ℃.

Lower Temperature (2 ℃)

Bromide system					Chloride system				
PyC_6Br- $AuBr_3$-$PyC_6[Tf_2N]$	Conc (mM)	Size (nm)	Morphology	Entry	PyC_6Cl-$AuCl_3$-$PyC_6[Tf_2N]$	Conc.(mM)	Size (nm)	Morphology	Entry
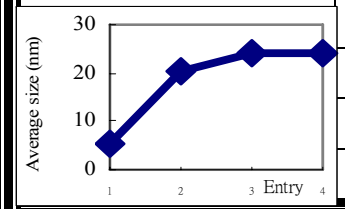	0.5	5.2 +/- 0.6	S, M	19	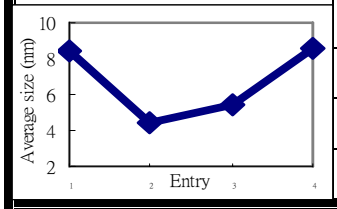	0.5	8.4 +/- 1.6	S	27
	5	20.4 +/- 4.9	S, M, L	20		5	4.5 +/- 0.9	S	28
	10	24.1 +/- 6.6	S, L	21		10	5.4 +/- 1.3	S	29
	50	23.9 +/- 12.3	S, L	22		50	8.6 +/- 3.0	S, L	30
PyC_8Br- $AuBr_3$-$PyC_8[Tf_2N]$					PyC_8Cl-$AuCl_3$-$PyC_8[Tf_2N]$				
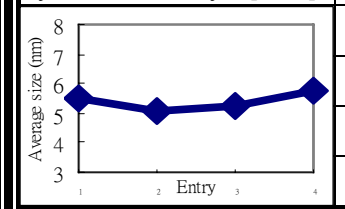	0.5	5.5 +/- 0.6	S	35	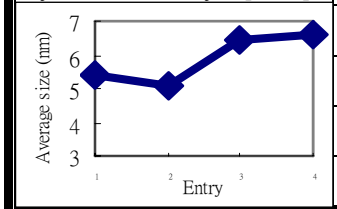	0.5	5.4 +/- 1.2	S	43
	5	5.1 +/- 0.6	S	36		5	5.1 +/- 0.9	S	44
	10	5.2 +/- 0.8	S_P	37		10	6.4 +/- 0.8	S	45
	50	5.8 +/- 0.8	S	38		50	6.6 +/- 1.0	S	46
$PyC_{10}Br$- $AuBr_3$-$PyC_{10}[Tf_2N]$					$PyC_{10}Cl$- $AuCl_3$-$PyC_{10}[Tf_2N]$				
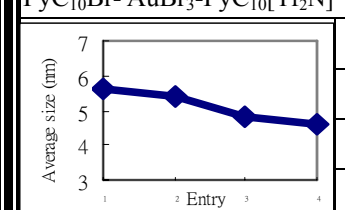	0.5	5.6 +/- 0.9	S	51	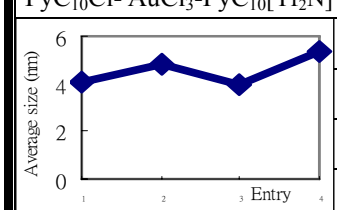	0.5	4.1 +/- 0.6	S, T_S	59
	5	5.4 +/- 1.1	S_{NP}	52		5	4.8 +/- 1.2	S	60
	10	4.8 +/- 0.9	S_{NP}	53		10	4.0 +/- 0.7	S, T_S	61
	50	4.6 +/- 0.7	S_{NP}	54		50	5.4 +/- 0.7	S	62
$PyC_{14}Br$- $AuBr_3$-$PyC_{10}[Tf_2N]$					$PyC_{14}Cl$- $AuCl_3$-$PyC_{10}[Tf_2N]$				
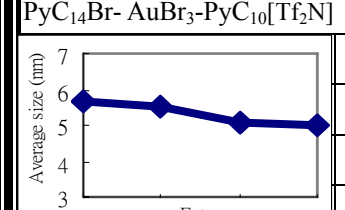	0.5	5.7 +/- 1.1	S	67	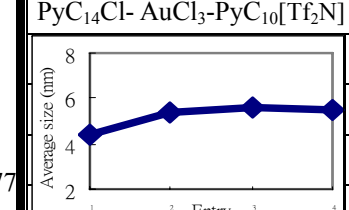	0.5	4.4 +/- 0.8	S, T_S	75
	5	5.5 +/- 0.5	S_{NP}	68		5	5.4 +/- 0.6	S_{NP}	76
	10	5.1 +/- 0.6	S_{NP}	69		10	5.6 +/- 0.7	S	77
	50	5.0 +/- 0.6	S	70		50	5.5 +/- 0.9	S	78

Notations for different morphologies: S = Small spherical nanoparticles (1 – 10 nm), S_N = Nicely spherical small nanoparticles
S_{NP} = Nicely spherical small nanoparticles arranged with pattern, M = Middle size nanoparticles (11 – 20 nm)
L = Large size nanoparticles (> 20 nm), T_s = Short nano-thread

Table 4.7 A summary of the size distributions and morphologies of the gold nanoparticles formed under different experimental conditions at room temperature.

Room Temperature

Bromide system					Chloride system				
PyC_6Br- $AuBr_3$-$PyC_6[Tf_2N]$	Conc(mM)	Size (nm)	Morphology	Entry	PyC_6Cl-$AuCl_3$-$PyC_6[Tf_2N]$	Conc(mM)	Size (nm)	Morphology	Entry
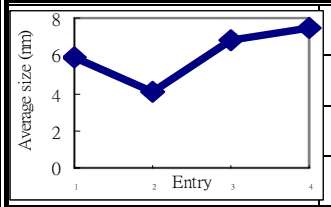	0.5	5.9 +/- 1.8	S, M	15	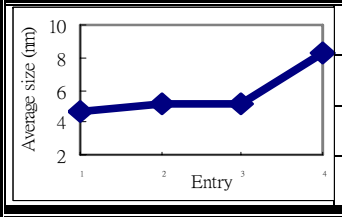	0.5	4.6 +/- 0.8	S	23
	5	4.1 +/- 1.7	S, M, L	16		5	5.1 +/- 0.7	S	24
	10	6.8 +/- 1.1	S, L	17		10	5.1 +/- 1.2	S	25
	50	7.5 +/- 1.0	S, L	18		50	8.2 +/- 2.2	S, L	26
PyC_8Br- $AuBr_3$-$PyC_8[Tf_2N]$					PyC_8Cl-$AuCl_3$-$PyC_8[Tf_2N]$				
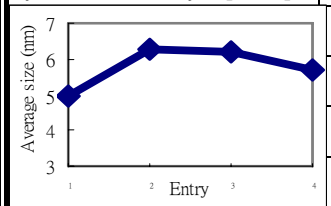	0.5	4.0 +/- 1.0	S	31	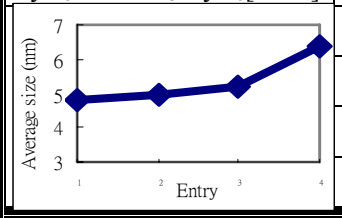	0.5	4.8 +/- 0.8	S_N, T_S	39
	5	6.3 +/- 1.2	S, M	32		5	5.0 +/- 0.9	S	40
	10	6.2 +/- 1.4	S	33		10	5.2 +/- 0.9	S	41
	50	5.7 +/- 1.8	S	34		50	6.4 +/- 1.7	S, M, L	42
$PyC_{10}Br$- $AuBr_3$-$PyC_{10}[Tf_2N]$					$PyC_{10}Cl$- $AuCl_3$-$PyC_{10}[Tf_2N]$				
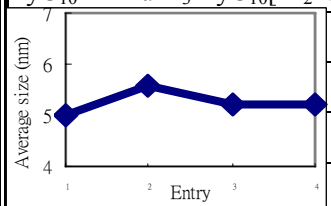	0.5	5.0 +/- 0.7	S_N	47	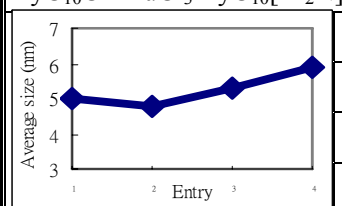	0.5	5.0 +/-1.0	S	55
	5	5.6 +/- 0.9	S	48		5	4.8 +/- 0.9	S	56
	10	5.2 +/- 0.8	S_{NP}	49		10	5.3 +/- 0.8	S, T_S	57
	50	5.2 +/- 0.7	S_{NP}	50		50	5.9 +/- 0.9	S, T_S	58
$PyC_{14}Br$- $AuBr_3$-$PyC_{10}[Tf_2N]$					$PyC_{14}Cl$- $AuCl_3$-$PyC_{10}[Tf_2N]$				
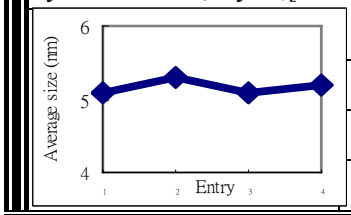	0.5	5.1 +/- 0.9	S_N	63	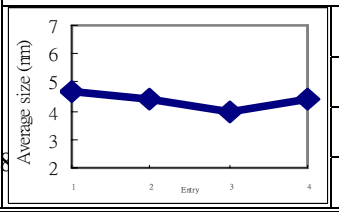	0.5	4.7 +/- 0.7	S, T_S	71
	5	5.3 +/- 0.6	S_N	64		5	4.4 +/- 0.8	S, T_S	72
	10	5.1 +/- 0.7	S_{NP}	65		10	4.0 +/- 0.8	S, T_S	73
	50	5.2 +/- 1.0	S_{NP}	66		50	4.4 +/- 0.6	S	74

Notations for different morphologies: S = Small spherical nanoparticles (1 – 10 nm), S_N = Nicely spherical small nanoparticles
S_{NP} = Nicely spherical small nanoparticles arranged with pattern, M = Middle size nanoparticles (11 – 20 nm)
L = Large size nanoparticles (> 20 nm), T_s = Short nano-thread

4.4 Concluding remarks

In this study, the direct use of tetrabutylammonium borohydride to yield gold nanoparticles in neat ionic liquid was investigated. The size of the nanoparticles formed was within a narrow size range (4 – 7 nm) when a family of N-alkylpyrrolidinium ionic liquid with different alkyl chain lengths was used as the medium. Smaller average particle size and reduced dispersity was achieved with ionic liquids of longer alkyl chain.

Furthermore, especially in experiments with longer chain ionic liquids as medium, perfectly spherical and nearly monodisperse small nanoparticles could be produced in large quantity. The high uniformity in particle size and morphology were manifested as the readily formed 2D monolayer with hexagonal arrangement on the TEM grid. Anisotropic structures were absent in almost all experiments with longer chain ionic liquids, which is expected to be shape-directing in nature.

The length of the alkyl chain was found to be important in maintaining the spherical shape and narrow size-dispersity of the nanoparticles formed over a wide gold concentration range. The gold colloids formed in short chain ionic liquid (C_6 and C_8) are generally bigger in dimension and less uniform in morphology.

The halide present in the ionic liquid medium seems to exert a subtle effect to the resulting nano-species formed. Short nano-threads were formed in longer chain ionic liquid when chloride was present, which was suppressed when the gold content in reaction mixture was increased. However, no such structure was found when bromide

was used. Different degree of particle fusion to give bigger size and less spherical colloids was observed in chloride containing ionic liquids of all chain lengths at room temperature and only in shorter chain ionic liquids at 2˚C. On the other hand, the presence of bromide led to spherical nanoparticles only under various synthetic conditions. With bromide, the longer chain ionic liquids (C_{10} and C_{14}/C_{10}) always produced vast quantity of monodisperse and small nanospheres. However, the concentration of gold salt used should be limited to 10 mM or below, as increased amount of less spherical species were observed under higher gold content.

Based on the information from the optical profiles and TEM images above, it can be concluded that: i) lower gold precursor concentration, ii) mixture of longer chain ionic liquids, iii) lower reaction temperature, and iv) the presence of bromide ion are key factors for producing spherical, well-dispersed, and stable gold nanoparticles in pyrrolidinium-based ionic liquid.

Chapter 5

Conclusions

There are increasing demands for new novel functionalized nanomaterials. In this study, the preparation of some water-soluble gold nanoparticles under various experimental conditions was demonstrated.

Four tiopronin derivatives with different structure have been prepared. The ethyl- (MBG), alanine- (MPA), proline- (MPP), and leucine- (MPL) derivative of tiopronin gave stable and water-soluble gold nanoparticles of 1.8 to 2.0 nm. All tiopronin derivative-capped gold nanoparticles showed a higher tolerance towards a wide range of solution pH and ionic strength. Extensive hydrogen bonding existed in all tiopronin-derivative capped gold nanoparticles, leading to the formation of tightly packed monolayer. Broad range near infra-red luminescence centred at 720 to 780 nm was observed from all tiopronin derivative capped gold nanoclusters when excited at around 360 nm, which was attributed to the depletion of negative charge in the metal core upon the ligation of the polar tiopronin derivatives.

Kinetics studies on the ligand exchange reaction between tiopronin-capped gold nanoparticles and tiopronin derivavtievs indicated that displacement of ligands located at the higher energy metal surface defects was highly favorable. The tiopronin derivatives showed similar kinetics and extent of exchange under unbuffered condition. When the medium for exchange was raised to pH 6.5, the extent of exchange reaction was greatly hampered at the beginning due to the negatively charged ligand monolayer but achieved an even higher equilibrium level compared to that obtained in more acidic unbuffered medium. The reaction progress at lower thiol loadings are generally in better agreement with the second order Langmuir diffusion-limited model compare to higher loading trials under unbuffered condition. Reduced deviation from the model is

observed in experiments with buffered medium.

Gold nanoparticles can be obtained easily by direct reduction of gold salt in neat pyrrolidinium-based ionic bis(trifluoromethanesulfonyl)imide ionic liquids with tetrabutylammonium borohydride. The nanoclusters obtained were generally 4 to 8 nm in size when synthesized with a gold salt content of 0.5 – 50 mM in ionic liquids composed of longer alkyl chain pyrroldinium. The presence of halide and the reaction temperature did not significantly affect the average size of the nanoparticles formed, but they affect the distribution of the average particles size of the nanoparticles produced. On the other hand, chloride could promote the formation of thread-like structure, whereas only spherical nanoparticles were obtained with bromide. A binary mixture of N-tetradecyl-N-methylpyrrolidinium halide and N-decyl-N-methylpyrrolidnium ionic liquid reduced significantly the dependence of the average size of the gold nanoparticles on gold content, especially in the presence of bromide and under room temperature.

As shown in chapter 2, the solubility of Au@MPL is unexpected as MPL is insoluble in water. Such observation is inspiring for the synthesis of gold nanoparticles capped with molecules of low water-solubility but of high bio-activity. Further preparation of a wider family of ligand derivatives in order to obtain a more thorough understanding between ligand structure and the properties of the nanoparticles prepared is therefore highly desirable. Derivatization with amino acid like tryptophan may produce a fluorescence-active tiopronin derivative and also their gold nanoparticles.

A binary mixture of N-alkyl-N-methylpyrrolidinium ionic liquids with unequal alkyl chains led to an apparent suppression in particle size variation at different gold salt

concentrations, which may facilitate the formation of gold nanoparticles with lower size dispersity. Indeed, mixture of ionic liquids at the eutectic composition can offer the further advantage of lower melting points. Therefore, gold nanoparticle preparation in binary ionic liquid mixture of different combinations and compositions deserves further investigations.

References

(1) Hashmi, A. S. K. Gold-catalyzed organic reactions. *Chemical Reviews (Washington, DC, United States)*, 2007, **107**, 3180-3211.

(2) Link, S.; El-Sayed, M. A. Shape and size dependence of radiative, non-radiative and photothermal properties of gold nanocrystals. *International Reviews in Physical Chemistry*, 2000, **19**, 409-453.

(3) Daniel, M.-C.; Astruc, D. Gold Nanoparticles: Assembly, Supramolecular Chemistry, Quantum-Size-Related Properties, and Applications toward Biology, Catalysis, and Nanotechnology. *Chemical Reviews (Washington, DC, United States)*, 2004, **104**, 293-346.

(4) Alivisatos, A. P. Perspectives on the physical chemistry of semiconductor nanocrystals. *Journal of Physical Chemistry*, 1996, **100**, 13226-13239.

(5) Mohamed, M. B.; Ismail, K. Z.; Link, S.; El-Sayed, M. A. Thermal Reshaping of Gold Nanorods in Micelles. *Journal of Physical Chemistry B*, 1998, **102**, 9370-9374.

(6) Mulvaney, P. Surface Plasmon Spectroscopy of Nanosized Metal Particles. *Langmuir*, 1996, **12**, 788-800.

(7) Zhu, M.; Aikens, C. M.; Hollander, F. J.; Schatz, G. C.; Jin, R. Correlating the Crystal Structure of A Thiol-Protected Au25 Cluster and Optical Properties. *Journal of the American Chemical Society*, 2008, **130**, 5883-5885.

(8) Kelly, K. L.; Coronado, E.; Zhao, L. L.; Schatz, G. C. The Optical Properties of Metal Nanoparticles: The Influence of Size, Shape, and Dielectric Environment. *Journal of Physical Chemistry B*, 2003, **107**, 668-677.

(9) Chen, S.; Ingrma, R. S.; Hostetler, M. J.; Pietron, J. J.; Murray, R. W.; Schaaff, T.

G.; Khoury, J. T.; Alvarez, M. M.; Whetten, R. L. Gold nanoelectrodes of varied size: transition to molecule-like charging. *Science (Washington, D. C.)*, 1998, **280**, 2098-2101.

(10) Hofstetter, W.; Zwerger, W. Single-electron box and the helicity modulus of an inverse square XY model. *Physical Review Letters*, 1997, **78**, 3737-3740.

(11) Miles, D. T.; Murray, R. W. Temperature-Dependent Quantized Double Layer Charging of Monolayer-Protected Gold Clusters. *Analytical Chemistry*, 2003, **75**, 1251-1257.

(12) Quinn, B. M.; Liljeroth, P.; Ruiz, V.; Laaksonen, T.; Kontturi, K. Electrochemical Resolution of 15 Oxidation States for Monolayer Protected Gold Nanoparticles. *Journal of the American Chemical Society*, 2003, **125**, 6644-6645.

(13) Guczi, L.; Horvath, D.; Paszti, Z.; Toth, L.; Horvath, Z. E.; Karacs, A.; Peto, G. Modeling Gold Nanoparticles: Morphology, Electron Structure, and Catalytic Activity in CO Oxidation. *Journal of Physical Chemistry B*, 2000, **104**, 3183-3193.

(14) Claus, P.; Brueckner, A.; Mohr, C.; Hofmeister, H. Supported Gold Nanoparticles from Quantum Dot to Mesoscopic Size Scale: Effect of Electronic and Structural Properties on Catalytic Hydrogenation of Conjugated Functional Groups. *Journal of the American Chemical Society*, 2000, **122**, 11430-11439.

(15) Kapoor, M. P.; Sinha, A. K.; Seelan, S.; Inagaki, S.; Tsubota, S.; Yoshida, H.; Haruta, M. Hydrophobicity induced vapor-phase oxidation of propene over gold supported on titanium incorporated hybrid mesoporous silsesquioxane. *Chemical Communications (Cambridge, United Kingdom)*, 2002, 2902-2903.

(16) Meheux, P. A.; Ibbotson, A.; Wells, P. B. Enantioselective hydrogenation. II. Variation of activity and optical yield with experimental variables in methyl pyruvate hydrogenation catalyzed by cinchona-modified platinum/silica (EUROPT-1).

Journal of Catalysis, 1991, **128**, 387-96.

(17) Bond, G. C.; Thompson, D. T. Catalysis by gold. *Catalysis Reviews - Science and Engineering*, 1999, **41**, 319-388.

(18) Haruta, M. Size- and support-dependency in the catalysis of gold. *Catalysis Today*, 1997, **36**, 153-166.

(19) Graham, G. W.; Jen, H. W.; Chun, W.; McCabe, R. W. High-Temperature-Aging-Induced Encapsulation of Metal Particles by Support Materials: Comparative Results for Pt, Pd, and Rh on Cerium-Zirconium Mixed Oxides. *Journal of Catalysis*, 1999, **182**, 228-233.

(20) Uphade, B. S.; Akita, T.; Nakamura, T.; Haruta, M. Vapor-Phase Epoxidation of Propene Using H2 and O2 over Au/Ti-MCM-48. *Journal of Catalysis*, 2002, **209**, 331-340.

(21) Taylor, B.; Lauterbach, J.; Delgass, W. N. Gas-phase epoxidation of propylene over small gold ensembles on TS-1. *Applied Catalysis, A: General*, 2005, **291**, 188-198.

(22) Han, Y. F.; Kumar, D.; Goodman, D. W. Particle size effects in vinyl acetate synthesis over Pd/SiO2. *Journal of Catalysis*, 2005, **230**, 353-358.

(23) Chen, M.; Kumar, D.; Yi, C.-W.; Goodman, D. W. The Promotional Effect of Gold in Catalysis by Palladium-Gold. *Science (Washington, DC, United States)*, 2005, **310**, 291-293.

(24) Hughes, M. D.; Xu, Y.-J.; Jenkins, P.; McMorn, P.; Landon, P.; Enache, D. I.; Carley, A. F.; Attard, G. A.; Hutchings, G. J.; King, F.; Stitt, E. H.; Johnston, P.; Griffin, K.; Kiely, C. J. Tunable gold catalysts for selective hydrocarbon oxidation under mild conditions. *Nature (London, United Kingdom)*, 2005, **437**, 1132-1135.

(25) Xu, Y.-J.; Landon, P.; Enache, D.; Carley, A. F.; Roberts, M. W.; Hutchings, G. J.

Selective conversion of cyclohexane to cyclohexanol and cyclohexanone using a gold catalyst under mild conditions. *Catalysis Letters*, 2005, **101**, 175-179.

(26) Yin, D.; Qin, L.; Liu, J.; Li, C.; Jin, Y. Gold nanoparticles deposited on mesoporous alumina for epoxidation of styrene: effects of the surface basicity of the supports. *Journal of Molecular Catalysis A: Chemical*, 2005, **240**, 40-48.

(27) Patil, N. S.; Uphade, B. S.; Jana, P.; Sonawane, R. S.; Bhargava, S. K.; Choudhary, V. R. Epoxidation of styrene by anhydrous t-butyl hydroperoxide over Au/TiO2 catalysts. *Catalysis Letters*, 2004, **94**, 89-93.

(28) Lignier, P.; Morfin, F.; Mangematin, S.; Massin, L.; Rousset, J.-L.; Caps, V. Stereoselective stilbene epoxidation over supported gold-based catalysts. *Chemical communications (Cambridge, England)*, 2007, 186-8.

(29) Lignier, P.; Morfin, F.; Piccolo, L.; Rousset, J.-L.; Caps, V. Insight into the free-radical chain mechanism of gold-catalyzed hydrocarbon oxidation reactions in the liquid phase. *Catalysis Today*, 2007, **122**, 284-291.

(30) Zhu, K.; Hu, J.; Richards, R. Aerobic oxidation of cyclohexane by gold nanoparticles immobilized upon mesoporous silica. *Catalysis Letters*, 2005, **100**, 195-199.

(31) Eskendirov, I.; Coville, N. J.; Sokolovskii, V. D. Methane oxidative coupling on the Au/La2O3/CaO catalysts in the presence of hydrogen peroxide. *Catalysis Letters*, 1995, **35**, 33-7.

(32) Xu, L.-X.; He, C.-H.; Zhu, M.-Q.; Wu, K.-J.; Lai, Y.-L. Silica-Supported Gold Catalyst Modified by Doping with Titania for Cyclohexane Oxidation. *Catalysis Letters*, 2007, **118**, 248-253.

(33) Blick, K.; Mitrelias, T. D.; Hargreaves, J. S. J.; Hutchings, G. J.; Joyner, R. W.; Kiely, C. J.; Wagner, F. E. Methane oxidation using Au/MgO catalysts. *Catalysis*

Letters, 1998, **50**, 211-218.

(34) Enache, D. I.; Knight, D. W.; Hutchings, G. J. Solvent-free Oxidation of Primary Alcohols to Aldehydes using Supported Gold Catalysts. *Catalysis Letters*, 2005, **103**, 43-52.

(35) Mertens, P. G. N.; Bulut, M.; Gevers, L. E. M.; Vankelecom, I. F. J.; Jacobs, P. A.; De Vos, D. E. Catalytic oxidation of 1,2-diols to Î±-hydroxy-carboxylates with stabilized gold nanocolloids combined with a membrane-based catalyst separation. *Catalysis Letters*, 2005, **102**, 57-61.

(36) Kanaoka, S.; Yagi, N.; Fukuyama, Y.; Aoshima, S.; Tsunoyama, H.; Tsukuda, T.; Sakurai, H. Thermosensitive gold nanoclusters stabilized by well-defined vinyl ether star polymers: reusable and durable catalysts for aerobic alcohol oxidation. *Journal of the American Chemical Society*, 2007, **129**, 12060-1.

(37) Biella, S.; Prati, L.; Rossi, M. Gold catalyzed oxidation of aldehydes in the liquid phase. *Journal of Molecular Catalysis A: Chemical*, 2003, **197**, 207-212.

(38) Biella, S.; Castiglioni, G. L.; Fumagalli, C.; Prati, L.; Rossi, M. Application of gold catalysts to selective liquid phase oxidation. *Catalysis Today*, 2002, **72**, 43-49.

(39) Biella, S.; Prati, L.; Rossi, M. Selective Oxidation of D-Glucose on Gold Catalyst. *Journal of Catalysis*, 2002, **206**, 242-247.

(40) Alivisatos, A. P.; Johnsson, K. P.; Peng, X.; Wilson, T. E.; Loweth, C. J.; Bruchez, M. P., Jr.; Schultz, P. G. Organization of 'nanocrystal molecules' using DNA. *Nature (London)*, 1996, **382**, 609-611.

(41) Faulk, W. P.; Taylor, G. M. Immunocolloid method for the electron microscope. *Immunochemistry*, 1971, **8**, 1081-3.

(42) Park, S.-J.; Taton, T. A.; Mirkint, C. A. Array-based electrical detection of DNA

with nanoparticle probes. *Science (Washington, DC, United States)*, 2002, **295**, 1503-1506.

(43) Xiao, Y.; Patolsky, F.; Katz, E.; Hainfeld, J. F.; Willner, I. "Plugging into Enzymes": Nanowiring of Redox Enzymes by a Gold Nanoparticle. *Science (Washington, DC, United States)*, 2003, **299**, 1877-1881.

(44) Connor, E. E.; Mwamuka, J.; Gole, A.; Murphy, C. J.; Wyatt, M. D. Gold nanoparticles are taken up by human cells but do not cause acute cytotoxicity. *Small*, 2005, **1**, 325-327.

(45) Chithrani, B. D.; Ghazani, A. A.; Chan, W. C. W. Determining the Size and Shape Dependence of Gold Nanoparticle Uptake into Mammalian Cells. *Nano Letters*, 2006, **6**, 662-668.

(46) Cho, E. C.; Xie, J.; Wurm, P. A.; Xia, Y. Understanding the Role of Surface Charges in Cellular Adsorption versus Internalization by Selectively Removing Gold Nanoparticles on the Cell Surface with a I2/KI Etchant. *Nano Letters*, 2009, **9**, 1080-1084.

(47) Rosi, N. L.; Giljohann, D. A.; Thaxton, C. S.; Lytton-Jean, A. K. R.; Han, M. S.; Mirkin, C. A. Oligonucleotide-Modified Gold Nanoparticles for Intracellular Gene Regulation. *Science (Washington, DC, United States)*, 2006, **312**, 1027-1030.

(48) Chithrani, B. D.; Chan, W. C. W. Elucidating the Mechanism of Cellular Uptake and Removal of Protein-Coated Gold Nanoparticles of Different Sizes and Shapes. *Nano Letters*, 2007, **7**, 1542-1550.

(49) Penn, S. G.; He, L.; Natan, M. J. Nanoparticles for bioanalysis. *Current Opinion in Chemical Biology*, 2003, **7**, 609-615.

(50) Seferos, D. S.; Giljohann, D. A.; Hill, H. D.; Prigodich, A. E.; Mirkin, C. A. Nano-Flares: Probes for Transfection and mRNA Detection in Living Cells. *Journal*

of the American Chemical Society, 2007, **129**, 15477-15479.

(51) Tkachenko, A. G.; Xie, H.; Liu, Y.; Coleman, D.; Ryan, J.; Glomm, W. R.; Shipton, M. K.; Franzen, S.; Feldheim, D. L. Cellular trajectories of peptide-modified gold particle complexes: comparison of nuclear localization signals and peptide transduction domains. *Bioconjugate Chemistry*, 2004, **15**, 482-490.

(52) Nitin, N.; Javier, D. J.; Richards-Kortum, R. Oligonucleotide-Coated Metallic Nanoparticles as a Flexible Platform for Molecular Imaging Agents. *Bioconjugate Chemistry*, 2007, **18**, 2090-2096.

(53) Thaxton, C. S.; Daniel, W. L.; Giljohann, D. A.; Thomas, A. D.; Mirkin, C. A. Templated Spherical High Density Lipoprotein Nanoparticles. *Journal of the American Chemical Society*, 2009, **131**, 1384-1385.

(54) Eck, D.; Helm, C. A.; Wagner, N. J.; Vaynberg, K. A. Plasmon Resonance Measurements of the Adsorption and Adsorption Kinetics of a Biopolymer onto Gold Nanocolloids. *Langmuir*, 2001, **17**, 957-960.

(55) Nath, N.; Chilkoti, A. Label-Free Biosensing by Surface Plasmon Resonance of Nanoparticles on Glass: Optimization of Nanoparticle Size. *Analytical Chemistry*, 2004, **76**, 5370-5378.

(56) Marinakos, S. M.; Chen, S.; Chilkoti, A. Plasmonic Detection of a Model Analyte in Serum by a Gold Nanorod Sensor. *Analytical Chemistry (Washington, DC, United States)*, 2007, **79**, 5278-5283.

(57) Lin, T.-J.; Huang, K.-T.; Liu, C.-Y. Determination of organophosphorous pesticides by a novel biosensor based on localized surface plasmon resonance. *Biosensors & Bioelectronics*, 2006, **22**, 513-518.

(58) He, L.; Musick, M. D.; Nicewarner, S. R.; Salinas, F. G.; Benkovic, S. J.; Natan, M. J.; Keating, C. D. Colloidal Au-enhanced surface plasmon resonance for

ultrasensitive detection of DNA hybridization. *Journal of the American Chemical Society*, 2000, **122**, 9071-9077.

(59) Li, Y.; Wark, A. W.; Lee, H. J.; Corn, R. M. Single-nucleotide polymorphism genotyping by nanoparticle-enhanced surface plasmon resonance imaging measurements of surface ligation reactions. *Analytical Chemistry*, 2006, **78**, 3158-3164.

(60) Matsui, J.; Akamatsu, K.; Hara, N.; Miyoshi, D.; Nawafune, H.; Tamaki, K.; Sugimoto, N. SPR Sensor Chip for Detection of Small Molecules Using Molecularly Imprinted Polymer with Embedded Gold Nanoparticles. *Analytical Chemistry*, 2005, **77**, 4282-4285.

(61) Zayats, M.; Kharitonov, A. B.; Pogorelova, S. P.; Lioubashevski, O.; Katz, E.; Willner, I. Probing Photoelectrochemical Processes in Au-CdS Nanoparticle Arrays by Surface Plasmon Resonance: Application for the Detection of Acetylcholine Esterase Inhibitors. *Journal of the American Chemical Society*, 2003, **125**, 16006-16014.

(62) Li, Y.; Schluesener, H. J.; Xu, S. Gold nanoparticle-based biosensors. *Gold Bulletin (London, United Kingdom)*, 2010, **43**, 29-41.

(63) Brown, K. R.; Fox, A. P.; Natan, M. J. Morphology-dependent electrochemistry of cytochrome c at Au colloid-modified SnO2 electrodes. *Journal of the American Chemical Society*, 1996, **118**, 1154-7.

(64) Lin, J.; Qu, W.; Zhang, S. Disposable biosensor based on enzyme immobilized on Au-chitosan-modified indium tin oxide electrode with flow injection amperometric analysis. *Analytical Biochemistry*, 2007, **360**, 288-293.

(65) Liu, S.; Peng, L.; Yang, X.; Wu, Y.; He, L. Electrochemistry of cytochrome P450 enzyme on nanoparticle-containing membrane-coated electrode and its applications for drug sensing. *Analytical Biochemistry*, 2008, **375**, 209-216.

(66) Luo, X.-L.; Xu, J.-J.; Du, Y.; Chen, H.-Y. A glucose biosensor based on chitosan-glucose oxidase-gold nanoparticles biocomposite formed by one-step electrodeposition. *Analytical Biochemistry*, 2004, **334**, 284-289.

(67) Andreescu, S.; Luck, L. A. Studies of the binding and signaling of surface-immobilized periplasmic glucose receptors on gold nanoparticles: A glucose biosensor application. *Analytical Biochemistry*, 2008, **375**, 282-290.

(68) Luo, X.-L.; Xu, J.-J.; Zhang, Q.; Yang, G.-J.; Chen, H.-Y. Electrochemically deposited chitosan hydrogel for horseradish peroxidase immobilization through gold nanoparticles self-assembly. *Biosensors & Bioelectronics*, 2005, **21**, 190-196.

(69) Patolsky, F.; Gabriel, T.; Willner, I. Controlled electrocatalysis by microperoxidase-11 and Au-nanoparticle superstructures on conductive supports. *Journal of Electroanalytical Chemistry*, 1999, **479**, 69-73.

(70) Liu, Z.-M.; Wang, H.; Yang, Y.; Yang, H.-F.; Hu, S.-Q.; Shen, G.-L.; Yu, R.-Q. Amperometric Tyrosinase Biosensor Using Enzyme-Labeled Au Colloids Immobilized on Cystamine/Chitosan Modified Gold Surface. *Analytical Letters*, 2004, **37**, 1079-1091.

(71) Faraday, M. *Philos. Trans. R. Soc. London*, 1857, **147**, 145.

(72) J. Turkevich, P. C. S., J. Hillier, A study of the nucleation and growth processes in the synthesis of colloidal gold. *Discuss. Faraday. Soc.*, 1951, **11**, 55-75.

(73) Frens, G. Controlled nucleation for the regulation of the particle size in monodisperse gold suspensions. *Nature (London), Physical Science*, 1973, **241**, 20-2.

(74) McPartlin, M.; Malatesta, L.; Mason, R. Cluster complexes of gold(0)-gold(I). *Journal of the Chemical Society [Section] D: Chemical Communications*, 1969, 334.

(75) Schmid, G.; Pfeil, R.; Boese, R.; Brandermann, F.; Meyer, S.; Calis, G. H. M.;

Van der Velden, J. W. A. Au55[P(C6H5)3]12Cl6 - a gold cluster of unusual size. *Chemische Berichte*, 1981, **114**, 3634-42.

(76) Schmid, G.; Klein, N.; Korste, L.; Kreibig, U.; Schoenauer, D. Large transition metal clusters-VI. Ligand exchange reactions on the gold triphenylphosphine chloro cluster, Au55(PPh3)12Cl6 - the formation of a water soluble gold (Au55) cluster. *Polyhedron*, 1988, **7**, 605-8.

(77) Brust, M.; Walker, M.; Bethell, D.; Schiffrin, D. J.; Whyman, R. Synthesis of thiol-derivatized gold nanoparticles in a two-phase liquid-liquid system. *Journal of the Chemical Society, Chemical Communications*, 1994, 801-2.

(78) Lover, T.; Henderson, W.; Bowmaker, G. A.; Seakins, J. M.; Cooney, R. P. Functionalization and Capping of a CdS Nanocluster: A Study of Ligand Exchange by Electrospray Mass Spectrometry. *Chemistry of Materials*, 1997, **9**, 1878-1886.

(79) C.H. Langford and H. B. Gray *Ligand Substitution Processes*; W. A. Benjamin: New York, 1966.

(80) Tirado, J. D.; Abruna, H. D. Exchange Dynamics of Redox-Active Self-Assembling Mixed Monolayers. *Journal of Physical Chemistry*, 1996, **100**, 4556-63.

(81) Schlenoff, J. B.; Li, M.; Ly, H. Stability and Self-Exchange in Alkanethiol Monolayers. *Journal of the American Chemical Society*, 1995, **117**, 12528-36.

(82) Hickman, J. J.; Ofer, D.; Zou, C.; Wrighton, M. S.; Laibinis, P. E.; Whitesides, G. M. Selective functionalization of gold microstructures with ferrocenyl derivatives via reaction with thiols or disulfides: characterization by electrochemistry and Auger electron spectroscopy. *Journal of the American Chemical Society*, 1991, **113**, 1128-32.

(83) Hostetler, M. J.; Templeton, A. C.; Murray, R. W. Dynamics of Place-Exchange

Reactions on Monolayer-Protected Gold Cluster Molecules. *Langmuir*, 1999, **15**, 3782-3789.

(84) Kassam, A.; Bremner, G.; Clark, B.; Ulibarri, G.; Lennox, R. B. Place Exchange Reactions of Alkyl Thiols on Gold Nanoparticles. *Journal of the American Chemical Society*, 2006, **128**, 3476-3477.

(85) Donkers, R. L.; Song, Y.; Murray, R. W. Substituent Effects on the Exchange Dynamics of Ligands on 1.6 nm Diameter Gold Nanoparticles. *Langmuir*, 2004, **20**, 4703-4707.

(86) Guo, R.; Song, Y.; Wang, G.; Murray, R. W. Does Core Size Matter in the Kinetics of Ligand Exchanges of Monolayer-Protected Au Clusters? *Journal of the American Chemical Society*, 2005, **127**, 2752-2757.

(87) Song, Y.; Murray, R. W. Dynamics and Extent of Ligand Exchange Depend on Electronic Charge of Metal Nanoparticles. *Journal of the American Chemical Society*, 2002, **124**, 7096-7102.

(88) Everett, W. R.; Welch, T. L.; Reed, L.; Fritsch-Faules, I. Potential-Dependent Stability of Self-Assembled Organothiols on Gold Electrodes in Methylene Chloride. *Analytical Chemistry*, 1995, **67**, 292-8.

(89) Ingram, R. S.; Hostetler, M. J.; Murray, R. W. Poly-hetero-Ï‰-functionalized Alkanethiolate-Stabilized Gold Cluster Compounds. *Journal of the American Chemical Society*, 1997, **119**, 9175-9178.

(90) Labande, A.; Ruiz, J.; Astruc, D. Supramolecular Gold Nanoparticles for the Redox Recognition of Oxoanions: Syntheses, Titrations, Stereoelectronic Effects, and Selectivity. *Journal of the American Chemical Society*, 2002, **124**, 1782-1789.

(91) Green, S. J.; Pietron, J. J.; Stokes, J. J.; Hostetler, M. J.; Vu, H.; Wuelfing, W. P.; Murray, R. W. Three-Dimensional Monolayers: Voltammetry of

Alkanethiolate-Stabilized Gold Cluster Molecules. *Langmuir*, 1998, **14**, 5612-5619.

(92) Miles, D. T.; Murray, R. W. Redox and Double-Layer Charging of Phenothiazine Functionalized Monolayer-Protected Clusters. *Analytical Chemistry*, 2001, **73**, 921-929.

(93) Sudeep, P. K.; Ipe, B. I.; Thomas, K. G.; George, M. V.; Barazzouk, S.; Hotchandani, S.; Kamat, P. V. Fullerene-Functionalized Gold Nanoparticles. A Self-Assembled Photoactive Antenna-Metal Nanocore Assembly. *Nano Letters*, 2002, **2**, 29-35.

(94) Foos, E. E.; Snow, A. W.; Twigg, M. E.; Ancona, M. G. Thiol-Terminated Di-, Tri-, and Tetraethylene Oxide Functionalized Gold Nanoparticles: A Water-Soluble, Charge-Neutral Cluster. *Chemistry of Materials*, 2002, **14**, 2401-2408.

(95) Warner, M. G.; Reed, S. M.; Hutchison, J. E. Small, Water-Soluble, Ligand-Stabilized Gold Nanoparticles Synthesized by Interfacial Ligand Exchange Reactions. *Chemistry of Materials*, 2000, **12**, 3316-3320.

(96) McIntosh, C. M.; Esposito, E. A., III; Boal, A. K.; Simard, J. M.; Martin, C. T.; Rotello, V. M. Inhibition of DNA Transcription Using Cationic Mixed Monolayer Protected Gold Clusters. *Journal of the American Chemical Society*, 2001, **123**, 7626-7629.

(97) Imahori, H.; Arimura, M.; Hanada, T.; Nishimura, Y.; Yamazaki, I.; Sakata, Y.; Fukuzumi, S. Photoactive three-dimensional monolayers: porphyrin-alkanethiolate-stabilized gold clusters. *Journal of the American Chemical Society*, 2001, **123**, 335-6.

(98) Wang, G.; Zhang, J.; Murray Royce, W. DNA binding of an ethidium intercalator attached to a monolayer-protected gold cluster. *Analytical Chemistry*,

2002, **74**, 4320-7.

(99) Aguila, A.; Murray, R. W. Monolayer-Protected Clusters with Fluorescent Dansyl Ligands. *Langmuir*, 2000, **16**, 5949-5954.

(100) Wang, T.; Zhang, D.; Xu, W.; Yang, J.; Han, R.; Zhu, D. Preparation, Characterization, and Photophysical Properties of Alkanethiols with Pyrene Units-Capped Gold Nanoparticles: Unusual Fluorescence Enhancement for the Aged Solutions of These Gold Nanoparticles. *Langmuir*, 2002, **18**, 1840-1848.

(101) Chompoosor, A.; Han, G.; Rotello, V. M. Charge dependence of ligand release and monolayer stability of gold nanoparticles by biogenic thiols. *Bioconjugate Chemistry*, 2008, **19**, 1342-1345.

(102) Thaxton, C. S.; Hill, H. D.; Georganopoulou, D. G.; Stoeva, S. I.; Mirkin, C. A. A Bio-Bar-Code Assay Based upon Dithiothreitol-Induced Oligonucleotide Release. *Analytical Chemistry*, 2005, **77**, 8174-8178.

(103) Letsinger, R. L.; Elghanian, R.; Viswanadham, G.; Mirkin, C. A. Use of a Steroid Cyclic Disulfide Anchor in Constructing Gold Nanoparticle-Oligonucleotide Conjugates. *Bioconjugate Chemistry*, 2000, **11**, 289-291.

(104) Templeton, A. C.; Hostetler, M. J.; Warmoth, E. K.; Chen, S.; Hartshorn, C. M.; Krishnamurthy, V. M.; Forbes, M. D. E.; Murray, R. W. Gateway Reactions to Diverse, Polyfunctional Monolayer-Protected Gold Clusters. *Journal of the American Chemical Society*, 1998, **120**, 4845-4849.

(105) Pengo, P.; Broxterman, Q. B.; Kaptein, B.; Pasquato, L.; Scrimin, P. Synthesis of a Stable Helical Peptide and Grafting on Gold Nanoparticles. *Langmuir*, 2003, **19**, 2521-2524.

(106) Pengo, P.; Polizzi, S.; Pasquato, L.; Scrimin, P. Carboxylate-Imidazole Cooperativity in Dipeptide-Functionalized Gold Nanoparticles with Esterase-like

Activity. *Journal of the American Chemical Society*, 2005, **127**, 1616-1617.

(107) Pasquato, L.; Rancan, F.; Scrimin, P.; Mancin, F.; Frigeri, C. N-Methylimidazole-functionalized gold nanoparticles as catalysts for cleavage of a carboxylic acid ester. *Chemical Communications (Cambridge)*, 2000, 2253-2254.

(108) Ionita, P.; Caragheorgheopol, A.; Gilbert, B. C.; Chechik, V. EPR Study of a Place-Exchange Reaction on Au Nanoparticles: Two Branches of a Disulfide Molecule Do Not Adsorb Adjacent to Each Other. *Journal of the American Chemical Society*, 2002, **124**, 9048-9049.

(109) Li, J.; Wang, X.; Wang, C.; Chen, B.; Dai, Y.; Zhang, R.; Song, M.; Lv, G.; Fu, D. The enhancement effect of gold nanoparticles in drug delivery and as biomarkers of drug-resistant cancer cells. *ChemMedChem*, 2007, **2**, 374-378.

(110) Chen, S.; Kimura, K. Synthesis and Characterization of Carboxylate-Modified Gold Nanoparticle Powders Dispersible in Water. *Langmuir*, 1999, **15**, 1075-1082.

(111) Chen, S. 4-Hydroxythiophenol-Protected Gold Nanoclusters in Aqueous Media. *Langmuir*, 1999, **15**, 7551-7557.

(112) Brust, M.; Fink, J.; Bethell, D.; Schiffrin, D. J.; Kiely, C. Synthesis and reactions of functionalized gold nanoparticles. *Journal of the Chemical Society, Chemical Communications*, 1995, 1655-6.

(113) Chen, S.; Huang, K. Electrochemical and Spectroscopic Studies of Nitrophenyl Moieties Immobilized on Gold Nanoparticles. *Langmuir*, 2000, **16**, 2014-2018.

(114) Johnson, S. R.; Evans, S. D.; Brydson, R. Influence of a Terminal Functionality on the Physical Properties of Surfactant-Stabilized Gold Nanoparticles. *Langmuir*, 1998, **14**, 6639-6647.

(115) Schaaff, T. G.; Knight, G.; Shafigullin, M. N.; Borkman, R. F.; Whetten, R. L. Isolation and Selected Properties of a 10.4 kDa Gold:Glutathione Cluster Compound.

Journal of Physical Chemistry B, 1998, **102**, 10643-10646.

(116) Ackerson, C. J.; Jadzinsky, P. D.; Kornberg, R. D. Thiolate Ligands for Synthesis of Water-Soluble Gold Clusters. *Journal of the American Chemical Society*, 2005, **127**, 6550-6551.

(117) Huang, C.-C.; Hung, Y.-L.; Shiang, Y.-C.; Lin, T.-Y.; Lin, Y.-S.; Chen, C.-T.; Chang, H.-T. Photoassisted Synthesis of Luminescent Mannose-Au Nanodots for the Detection of Thyroglobulin in Serum. *Chemistry--An Asian Journal*, **5**, 334-341.

(118) Naka, K.; Itoh, H.; Tampo, Y.; Chujo, Y. Effect of Gold Nanoparticles as a Support for the Oligomerization of L-Cysteine in an Aqueous Solution. *Langmuir*, 2003, **19**, 5546-5549.

(119) Shon, Y.-S.; Wuelfing, W. P.; Murray, R. W. Water-Soluble, Sulfonic Acid-Functionalized, Monolayer-Protected Nanoparticles and an Ionically Conductive Molten Salt Containing Them. *Langmuir*, 2001, **17**, 1255-1261.

(120) Cliffel, D. E.; Zamborini, F. P.; Gross, S. M.; Murray, R. W. Mercaptoammonium-Monolayer-Protected, Water-Soluble Gold, Silver, and Palladium Clusters. *Langmuir*, 2000, **16**, 9699-9702.

(121) Wuelfing, W. P.; Gross, S. M.; Miles, D. T.; Murray, R. W. Nanometer Gold Clusters Protected by Surface-Bound Monolayers of Thiolated Poly(ethylene glycol) Polymer Electrolyte. *Journal of the American Chemical Society*, 1998, **120**, 12696-12697.

(122) Pengo, P.; Polizzi, S.; Battagliarin, M.; Pasquato, L.; Scrimin, P. Synthesis, characterization and properties of water-soluble gold nanoparticles with tunable core size. *Journal of Materials Chemistry*, 2003, **13**, 2471-2478.

(123) Esumi, K.; Suzuki, A.; Aihara, N.; Usui, K.; Torigoe, K. Preparation of Gold Colloids with UV Irradiation Using Dendrimers as Stabilizer. *Langmuir*, 1998, **14**,

3157-3159.

(124) Zheng, J.; Petty, J. T.; Dickson, R. M. High Quantum Yield Blue Emission from Water-Soluble Au8 Nanodots. *Journal of the American Chemical Society*, 2003, **125**, 7780-7781.

(125) Pellegrino, T.; Manna, L.; Kudera, S.; Liedl, T.; Koktysh, D.; Rogach, A. L.; Keller, S.; Raedler, J.; Natile, G.; Parak, W. J. Hydrophobic Nanocrystals Coated with an Amphiphilic Polymer Shell: A General Route to Water Soluble Nanocrystals. *Nano Letters*, 2004, **4**, 703-707.

(126) Templeton, A. C.; Cliffel, D. E.; Murray, R. W. Redox and Fluorophore Functionalization of Water-Soluble, Tiopronin-Protected Gold Clusters. *Journal of the American Chemical Society*, 1999, **121**, 7081-7089.

(127) Zayats, M.; Pogorelova, S. P.; Kharitonov, A. B.; Lioubashevski, O.; Katz, E.; Willner, I. Au nanoparticle-enhanced surface plasmon resonance sensing of biocatalytic transformations. *Chemistry--A European Journal*, 2003, **9**, 6108-6114.

(128) De la Fuente, J. M.; Berry, C. C. Tat Peptide as an Efficient Molecule To Translocate Gold Nanoparticles into the Cell Nucleus. *Bioconjugate Chemistry*, 2005, **16**, 1176-1180.

(129) Thanh, N. T. K.; Rosenzweig, Z. Development of an aggregation-based immunoassay for anti-protein A using gold nanoparticles. *Analytical Chemistry*, 2002, **74**, 1624-1628.

(130) Zoy, A.; Nassiopoulou, A. G.; Ioannou-Sougleridis, V.; Murugesan, M.; Moore, B. D. Electrical conductivity of Au-nanoparticle-coated K2SO4 microcrystals deposited by DC trapping. *Journal of Physics: Conference Series*, 2005, **10**, 105-108.

(131) Huang, T.; Murray, R. W. Visible Luminescence of Water-Soluble

Monolayer-Protected Gold Clusters. *Journal of Physical Chemistry B*, 2001, **105**, 12498-12502.

(132) Negishi, Y.; Takasugi, Y.; Sato, S.; Yao, H.; Kimura, K.; Tsukuda, T. Magic-Numbered Aun Clusters Protected by Glutathione Monolayers (n = 18, 21, 25, 28, 32, 39): Isolation and Spectroscopic Characterization. *Journal of the American Chemical Society*, 2004, **126**, 6518-6519.

(133) Lin, C.-A. J.; Yang, T.-Y.; Lee, C.-H.; Huang, S. H.; Sperling, R. A.; Zanella, M.; Li, J. K.; Shen, J.-L.; Wang, H.-H.; Yeh, H.-I.; Parak, W. J.; Chang, W. H. Synthesis, Characterization, and Bioconjugation of Fluorescent Gold Nanoclusters toward Biological Labeling Applications. *ACS Nano*, 2009, **3**, 395-401.

(134) Wang, G.; Huang, T.; Murray Royce, W.; Menard, L.; Nuzzo Ralph, G. Near-IR luminescence of monolayer-protected metal clusters. *Journal of the American Chemical Society*, 2005, **127**, 812-3.

(135) Sasaki, E.; Kojima, H.; Nishimatsu, H.; Urano, Y.; Kikuchi, K.; Hirata, Y.; Nagano, T. Highly Sensitive Near-Infrared Fluorescent Probes for Nitric Oxide and Their Application to Isolated Organs. *Journal of the American Chemical Society*, 2005, **127**, 3684-3685.

(136) Chum, H. L.; Koch, V. R.; Miller, L. L.; Osteryoung, R. A. Electrochemical scrutiny of organometallic iron complexes and hexamethylbenzene in a room temperature molten salt. *Journal of the American Chemical Society*, 1975, **97**, 3264-5.

(137) Wilkes, J. S.; Levisky, J. A.; Wilson, R. A.; Hussey, C. L. Dialkylimidazolium chloroaluminate melts: a new class of room-temperature ionic liquids for electrochemistry, spectroscopy and synthesis. *Inorganic Chemistry*, 1982, **21**, 1263-4.

(138) Wilkes, J. S.; Zaworotko, M. J. Air and water stable 1-ethyl-3-methylimidazolium based ionic liquids. *Journal of the Chemical Society, Chemical Communications*, 1992, 965-7.

(139) Earle, M. J.; Seddon, K. R. Ionic liquids. Green solvents for the future. *Pure and Applied Chemistry*, 2000, **72**, 1391-1398.

(140) Lagrost, C.; Carrie, D.; Vaultier, M.; Hapiot, P. Reactivities of Some Electrogenerated Organic Cation Radicals in Room-Temperature Ionic Liquids: Toward an Alternative to Volatile Organic Solvents? *Journal of Physical Chemistry A*, 2003, **107**, 745-752.

(141) Zhao, H.; Xia, S.; Ma, P. Use of ionic liquids as 'green' solvents for extractions. *Journal of Chemical Technology and Biotechnology*, 2005, **80**, 1089-1096.

(142) Davis, J. H., Jr. Task-specific ionic liquids. *Chemistry Letters*, 2004, **33**, 1072-1077.

(143) Pfruender, H.; Jones, R.; Weuster-Botz, D. Water immiscible ionic liquids as solvents for whole cell biocatalysis. *Journal of Biotechnology*, 2006, **124**, 182-190.

(144) Tao, G.-h.; He, L.; Sun, N.; Kou, Y. New generation ionic liquids: cations derived from amino acids. *Chemical communications (Cambridge, England)*, 2005, 3562-4.

(145) Tao, G.-h.; He, L.; Liu, W.-s.; Xu, L.; Xiong, W.; Wang, T.; Kou, Y. Preparation, characterization and application of amino acid-based green ionic liquids. *Green Chemistry*, 2006, **8**, 639-646.

(146) Garcia, M. T.; Gathergood, N.; Scammells, P. J. Biodegradable ionic liquids. Part II. Effect of the anion and toxicology. *Green Chemistry*, 2005, **7**, 9-14.

(147) Suarez, P. A. Z.; Dullius, J. E. L.; Einloft, S.; De Souza, R. F.; Dupont, J. The use of new ionic liquids in two-phase catalytic hydrogenation reaction by rhodium

complexes. *Polyhedron*, 1996, **15**, 1217-19.

(148) Suarez, P. A. Z.; Dullius, J. E. L.; Einloft, S.; de Souza, R. F.; Dupont, J. Two-phase catalytic hydrogenation of olefins by Ru(II) and Co(II) complexes dissolved in 1-n-butyl-3-methylimidazolium tetrafluoroborate ionic liquid. *Inorganica Chimica Acta*, 1997, **255**, 207-209.

(149) Olivier-Bourbigou, H.; Magna, L. Ionic liquids: perspectives for organic and catalytic reactions. *Journal of Molecular Catalysis A: Chemical*, 2002, **182-183**, 419-437.

(150) Cornils, B.; Herrmann, W. A. Concepts in homogeneous catalysis: the industrial view. *Journal of Catalysis*, 2003, **216**, 23-31.

(151) Dominguez de Maria, P. "Nonsolvent" applications of ionic liquids in biotransformations and organocatalysis. *Angewandte Chemie, International Edition*, 2008, **47**, 6960-6968.

(152) Imanishi, A.; Tamura, M.; Kuwabata, S. Formation of Au nanoparticles in an ionic liquid by electron beam irradiation. *Chemical communications (Cambridge, England)*, 2009, 1775-7.

(153) Chen, S.; Liu, Y.; Wu, G. Stabilized and size-tunable gold nanoparticles formed in a quaternary ammonium-based room-temperature ionic liquid under Î³-irradiation. *Nanotechnology*, 2005, **16**, 2360-2364.

(154) Kimura, Y.; Takata, H.; Terazima, M.; Ogawa, T.; Isoda, S. Preparation of gold nanoparticles by the laser ablation in room-temperature ionic liquids. *Chemistry Letters*, 2007, **36**, 1130-1131.

(155) Okazaki, K.-i.; Kiyama, T.; Hirahara, K.; Tanaka, N.; Kuwabata, S.; Torimoto, T. Single-step synthesis of gold-silver alloy nanoparticles in ionic liquids by a sputter deposition technique. *Chemical Communications (Cambridge, United Kingdom)*,

2008, 691-693.

(156) Jin, Y.; Wang, P.; Yin, D.; Liu, J.; Qin, L.; Yu, N.; Xie, G.; Li, B. Gold nanoparticles prepared by sonochemical method in thiol-functionalized ionic liquid. *Colloids and Surfaces, A: Physicochemical and Engineering Aspects*, 2007, **302**, 366-370.

(157) Kim, K.-S.; Demberelnyamba, D.; Lee, H. Size-selective synthesis of gold and platinum nanoparticles using novel thiol-functionalized ionic liquids. *Langmuir*, 2004, **20**, 556-560.

(158) Itoh, H.; Naka, K.; Chujo, Y. Synthesis of Gold Nanoparticles Modified with Ionic Liquid Based on the Imidazolium Cation. *Journal of the American Chemical Society*, 2004, **126**, 3026-3027.

(159) Tatumi, R.; Fujihara, H. Remarkably stable gold nanoparticles functionalized with a zwitterionic liquid based on imidazolium sulfonate in a high concentration of aqueous electrolyte and ionic liquid. *Chemical Communications (Cambridge, United Kingdom)*, 2005, 83-85.

(160) Warren, S. C.; Banholzer, M. J.; Slaughter, L. S.; Giannelis, E. P.; DiSalvo, F. J.; Wiesner, U. B. Generalized Route to Metal Nanoparticles with Liquid Behavior. *Journal of the American Chemical Society*, 2006, **128**, 12074-12075.

(161) Dash, P.; Scott, R. W. J. 1-Methylimidazole stabilization of gold nanoparticles in imidazolium ionic liquids. *Chemical Communications (Cambridge, United Kingdom)*, 2009, 812-814.

(162) Zhao, D.; Fei, Z.; Ang, W. H.; Dyson, P. J. A strategy for the synthesis of transition-metal nanoparticles and their transfer between liquid phases. *Small*, 2006, **2**, 879-883.

(163) Kim, K.-S.; Choi, S.; Cha, J.-H.; Yeon, S.-H.; Lee, H. Facile one-pot synthesis of

gold nanoparticles using alcohol ionic liquids. *Journal of Materials Chemistry*, 2006, **16**, 1315-1317.

(164) Wang, Z.; Zhang, Q.; Kuehner, D.; Ivaska, A.; Niu, L. Green synthesis of 1-2 nm gold nanoparticles stabilized by amine-terminated ionic liquid and their electrocatalytic activity in oxygen reduction. *Green Chemistry*, 2008, **10**, 907-909.

(165) Zhang, H.; Cui, H. Synthesis and Characterization of Functionalized Ionic Liquid-Stabilized Metal (Gold and Platinum) Nanoparticles and Metal Nanoparticle/Carbon Nanotube Hybrids. *Langmuir*, 2009, **25**, 2604-2612.

(166) Wang, Y.; Yang, H. Oleic acid as the capping agent in the synthesis of noble metal nanoparticles in imidazolium-based ionic liquids. *Chemical Communications (Cambridge, United Kingdom)*, 2006, 2545-2547.

(167) Guo, S.; Shi, F.; Gu, Y.; Yang, J.; Deng, Y. Size-controllable synthesis of gold nanoparticles via carbonylation and reduction of hydrochloroauric acid with CO and H2O in ionic liquids. *Chemistry Letters*, 2005, **34**, 830-831.

(168) Templeton, A. C.; Chen, S.; Gross, S. M.; Murray, R. W. Water-soluble, isolable gold clusters protected by tiopronin and coenzyme A monolayers. *Langmuir*, 1999, **15**, 66-76.

(169) Shon, Y.-S.; Choo, H. Organic reactions of monolayer-protected metal nanoparticles. *Comptes Rendus Chimie*, 2003, **6**, 1009-1018.

(170) Hostetler, M. J.; Wingate, J. E.; Zhong, C.-J.; Harris, J. E.; Vachet, R. W.; Clark, M. R.; Londono, J. D.; Green, S. J.; Stokes, J. J.; Wignall, G. D.; Glish, G. L.; Porter, M. D.; Evans, N. D.; Murray, R. W. Alkanethiolate Gold Cluster Molecules with Core Diameters from 1.4 to 5.2 Nanometers: Core and Monolayer Properties as a Function of Core Size. *Langmuir*, 1998, **14**, 17-30.

(171) Alvarez, M. M.; Khoury, J. T.; Schaaff, T. G.; Shafigullin, M. N.; Vezmar, I.;

Whetten, R. L. Optical Absorption Spectra of Nanocrystal Gold Molecules. *Journal of Physical Chemistry B*, 1997, **101**, 3706-3712.

(172) F.Hofmeister. *Arch. Exp. Pathol. Pharmacol*, 1888, **24**, 247 - 260.

(173) Zhou, J.; Ralston, J.; Sedev, R.; Beattie, D. A. Functionalized gold nanoparticles: Synthesis, structure and colloid stability. *Journal of Colloid and Interface Science*, 2009, **331**, 251-262.

(174) Leff, D. V.; Brandt, L.; Heath, J. R. Synthesis and Characterization of Hydrophobic, Organically Soluble Gold Nanocrystals Functionalized with Primary Amines. *Langmuir*, 1996, **12**, 4723-4730.

(175) Carotenuto, G.; Nicolais, L. Size-controlled synthesis of thiol-derivatized gold clusters. *Journal of Materials Chemistry*, 2003, **13**, 1038-1041.

(176) Fabris, L.; Antonello, S.; Armelao, L.; Donkers, R. L.; Polo, F.; Toniolo, C.; Maran, F. Gold Nanoclusters Protected by Conformationally Constrained Peptides. *Journal of the American Chemical Society*, 2006, **128**, 326-336.

(177) Cha, X.; Ariga, K.; Kunitake, T. Inter-peptide hydrogen bonding in monolayers of oligoglycine amphiphiles. *Bulletin of the Chemical Society of Japan*, 1996, **69**, 163-8.

(178) Tam-Chang, S.-W.; Biebuyck, H. A.; Whitesides, G. M.; Jeon, N.; Nuzzo, R. G. Self-Assembled Monolayers on Gold Generated from Alkanethiols with the Structure RNHCOCH2SH. *Langmuir*, 1995, **11**, 4371-82.

(179) Clegg, R. S.; Hutchison, J. E. Hydrogen-Bonding, Self-Assembled Monolayers: Ordered Molecular Films for Study of Through-Peptide Electron Transfer. *Langmuir*, 1996, **12**, 5239-5243.

(180) Boal, A. K.; Rotello, V. M. Intra- and Intermonolayer Hydrogen Bonding in Amide-Functionalized Alkanethiol Self-Assembled Monolayers on Gold

Nanoparticles. *Langmuir*, 2000, **16**, 9527-9532.

(181)Sabapathy, R. C.; Bhattacharyya, S.; Leavy, M. C.; Cleland, W. E., Jr.; Hussey, C. L. Electrochemical and Spectroscopic Characterization of Self-Assembled Monolayers of Ferrocenylalkyl Compounds with Amide Linkages. *Langmuir*, 1998, **14**, 124-136.

(182) Weesie, R. J.; Merlin, J. C.; De Groot, H. J. M.; Britton, G.; Lugtenburg, J.; Jansen, F. J. H. M.; Cornard, J. P. Resonance Raman spectroscopy and quantum chemical modeling studies of protein-astaxanthin interactions in Î±-crustacyanin (major blue carotenoprotein complex in carapace of lobster, Homarus gammarus). *Biospectroscopy*, 1999, **5**, 358-370.

(183) Bourg, M.-C.; Badia, A.; Lennox, R. B. Gold-Sulfur Bonding in 2D and 3D Self-Assembled Monolayers: XPS Characterization. *Journal of Physical Chemistry B*, 2000, **104**, 6562-6567.

(184) Negishi, Y.; Nobusada, K.; Tsukuda, T. Glutathione-Protected Gold Clusters Revisited: Bridging the Gap between Gold(I)-Thiolate Complexes and Thiolate-Protected Gold Nanocrystals. *Journal of the American Chemical Society*, 2005, **127**, 5261-5270.

(185) Jun, S.; Jang, E.; Chung, Y. Alkyl thiols as a sulfur precursor for the preparation of monodisperse metal sulfide nanostructures. *Nanotechnology*, 2006, **17**, 4806-4810.

(186) Zhang, P.; Sham, T. K. X-Ray Studies of the Structure and Electronic Behavior of Alkanethiolate-Capped Gold Nanoparticles: The Interplay of Size and Surface Effects. *Physical Review Letters*, 2004, **92**, 109602/1.

(187) Sham, T. K.; Kim, P. S. G.; Zhang, P. Electronic structure of molecular-capped gold nanoparticles from X-ray spectroscopy studies: Implications for coulomb

blockade, luminescence and non-Fermi behavior. *Solid State Communications*, 2006, **138**, 553-557.

(188) Maye, M. M.; Luo, J.; Lin, Y.; Engelhard, M. H.; Hepel, M.; Zhong, C.-J. X-ray Photoelectron Spectroscopic Study of the Activation of Molecularly-Linked Gold Nanoparticle Catalysts. *Langmuir*, 2003, **19**, 125-131.

(189) Ma, Z.; Han, H. One-step synthesis of cystine-coated gold nanoparticles in aqueous solution. *Colloids and Surfaces, A: Physicochemical and Engineering Aspects*, 2008, **317**, 229-233.

(190) Nuzzo, R. G.; Zegarski, B. R.; Dubois, L. H. Fundamental studies of the chemisorption of organosulfur compounds on gold(111). Implications for molecular self-assembly on gold surfaces. *Journal of the American Chemical Society*, 1987, **109**, 733-40.

(191) Wang, G.; Guo, R.; Kalyuzhny, G.; Choi, J.-P.; Murray Royce, W. NIR luminescence intensities increase linearly with proportion of polar thiolate ligands in protecting monolayers of Au38 and Au140 quantum dots. *The journal of physical chemistry. B*, 2006, **110**, 20282-9.

(192) Shibu, E. S.; Muhammed, M. A. H.; Kimura, K.; Pradeep, T. Fluorescent superlattices of gold nanoparticles: a new class of functional materials. *Nano Research*, 2009, **2**, 220-234.

(193) Kim, Y. J.; Yang, Y. S.; Ha, S.-C.; Cho, S. M.; Kim, Y. S.; Kim, H. Y.; Yang, H.; Kim, Y. T. Mixed-ligand nanoparticles of chlorobenzenemethanethiol and n-octanethiol as chemical sensors. *Sensors and Actuators, B: Chemical*, 2005, **B106**, 189-198.

(194) Kim, J. H.; Chung, B. H. Proteolytic Fluorescent Signal Amplification on Gold Nanoparticles for a Highly Sensitive and Rapid Protease Assay. *Small*, **6**, 126-131.

(195) Nuzzo, R. G.; Dubois, L. H.; Allara, D. L. Fundamental studies of microscopic wetting on organic surfaces. 1. Formation and structural characterization of a self-consistent series of polyfunctional organic monolayers. *Journal of the American Chemical Society*, 1990, **112**, 558-69.

(196) Creager, S. E.; Clarke, J. Contact-Angle Titrations of Mixed ω-Mercaptoalkanoic Acid/Alkanethiol Monolayers on Gold. Reactive vs Nonreactive Spreading, and Chain Length Effects on Surface pKa Values. *Langmuir*, 1994, **10**, 3675-83.

(197) Tajc, S. G.; Tolbert, B. S.; Basavappa, R.; Miller, B. L. Direct Determination of Thiol pKa by Isothermal Titration Microcalorimetry. *Journal of the American Chemical Society*, 2004, **126**, 10508-10509.

(198) Agasti, S. S.; You, C.-C.; Arumugam, P.; Rotello, V. M. Structural control of the monolayer stability of water-soluble gold nanoparticles. *Journal of Materials Chemistry*, 2008, **18**, 70-73.

(199) Donkers Robert, L.; Song, Y.; Murray Royce, W. Substituent effects on the exchange dynamics of ligands on 1.6 nm diameter gold nanoparticles. *Langmuir : the ACS journal of surfaces and colloids*, 2004, **20**, 4703-7.

(200) Collard, D. M.; Fox, M. A. Use of electroactive thiols to study the formation and exchange of alkanethiol monolayers on gold. *Langmuir*, 1991, **7**, 1192-7.

(201) Hong, R.; Fernandez, J. M.; Nakade, H.; Arvizo, R.; Emrick, T.; Rotello, V. M. In situ observation of place exchange reactions of gold nanoparticles. Correlation of monolayer structure and stability. *Chemical Communications (Cambridge, United Kingdom)*, 2006, 2347-2349.

(202) Hostetler, M. J.; Murray, R. W. Colloids and self-assembled monolayers. *Current Opinion in Colloid & Interface Science*, 1997, **2**, 42-50.

(203) Caragheorgheopol, A.; Chechik, V. Mechanistic aspects of ligand exchange in Au nanoparticles. *Physical Chemistry Chemical Physics*, 2008, **10**, 5029-5041.

(204) Hill, H. D.; Millstone, J. E.; Banholzer, M. J.; Mirkin, C. A. The Role Radius of Curvature Plays in Thiolated Oligonucleotide Loading on Gold Nanoparticles. *ACS Nano*, 2009, **3**, 418-424.

(205) Wincel, H. Hydration energies of deprotonated amino acids from gas phase equilibria measurements. *Journal of the American Society for Mass Spectrometry*, 2008, **19**, 1091-1097.

(206) Yan, D.; Saunders, J. A.; Jennings, G. K. Kinetics of Formation for n-Alkanethiolate Self-Assembled Monolayers onto Gold in Aqueous Micellar Solutions of C12E6 and C12E7. *Langmuir*, 2002, **18**, 10202-10212.

(207) Zhu, H.; Tao, C.; Zheng, S.; Wu, S.; Li, J. Effect of alkyl chain length on phase transfer of surfactant capped Au nanoparticles across the water/toluene interface. *Colloids and Surfaces, A: Physicochemical and Engineering Aspects*, 2005, **256**, 17-20.

(208) Cheng, W.; Dong, S.; Wang, E. Synthesis and Self-Assembly of Cetyltrimethylammonium Bromide-Capped Gold Nanoparticles. *Langmuir*, 2003, **19**, 9434-9439.

(209) Fink, J.; Kiely, C. J.; Bethell, D.; Schiffrin, D. J. Self-Organization of Nanosized Gold Particles. *Chemistry of Materials*, 1998, **10**, 922-926.

(210) Su, K. H.; Wei, Q. H.; Zhang, X.; Mock, J. J.; Smith, D. R.; Schultz, S. Interparticle Coupling Effects on Plasmon Resonances of Nanogold Particles. *Nano Letters*, 2003, **3**, 1087-1090.

(211) Wikinson, F. A. C. a. G. *Advanced Inorganic Chemistry*; 5 ed.; Wiley: York, 1988, Chapter 24.

(212) Sturgeon, R. E.; Liu, J.; Boyko, V. J.; Luong, V. T. Determination of Copper in Environmental Matrixes Following Vapor Generation. *Analytical Chemistry*, 1996, **68**, 1883-7.

(213) Luna, A. S.; Sturgeon, R. E.; De Campos, R. C. Chemical Vapor Generation: Atomic Absorption by Ag, Au, Cu, and Zn Following Reduction of Aquo Ions with Sodium Tetrahydroborate(III). *Analytical Chemistry*, 2000, **72**, 3523-3531.

(214) Feng, Y.-L.; Sturgeon, R. E.; Lam, J. W.; D'Ulivo, A. Insights into the mechanism of chemical vapor generation of transition and noble metals. *Journal of Analytical Atomic Spectrometry*, 2005, **20**, 255-265.

(215) Seto, J. Y.; Morbi, Z.; Charron, F.; Lee, S. K.; Bernath, P. F.; Le Roy, R. J. Vibration-rotation emission spectra and combined isotopomer analyses for the coinage metal hydrides: CuH & CuD, AgH & AgD, and AuH & AuD. *Journal of Chemical Physics*, 1999, **110**, 11756-11767.

(216) Xu, S.; Sturgeon, R. E. Flow injection chemical vapor generation of Au using a mixed reductant. *Spectrochimica Acta, Part B: Atomic Spectroscopy*, 2005, **60B**, 101-107.

(217) Zhang, C.; Li, Y.; Wu, P.; Jiang, Y.; Liu, Q.; Yan, X.-P. Effects of room-temperature ionic liquids on the chemical vapor generation of gold: Mechanism and analytical application. *Analytica Chimica Acta*, 2009, **650**, 59-64.

(218) Glavee, G. N.; Klabunde, K. J.; Sorensen, C. M.; Hadjipanayis, G. C. Sodium borohydride reduction of cobalt ions in nonaqueous media. Formation of ultrafine particles (nanoscale) of cobalt metal. *Inorganic Chemistry*, 1993, **32**, 474-7.

(219) Glavee, G. N.; Klabunde, K. J.; Sorensen, C. M.; Hadjipanayis, G. C. Borohydride Reduction of Nickel and Copper Ions in Aqueous and Nonaqueous Media. Controllable Chemistry Leading to Nanoscale Metal and Metal Boride Particles.

Langmuir, 1994, **10**, 4726-30.